Energy, Mines and Resources Canada

Énergie, Mines et Ressources Canada

CANMET

Canada Centre for Mineral and Energy Technology

Centre canadien de la technologie des minéraux et de l'énergie

Energy Research Laboratories

Laboratoires de recherche sur l'énergie

Canada

APPLICATION OF COMPUTER ASSISTED TOMOGRAPHY (CAT) SCANNING IN THE NON-DESTRUCTIVE TESTING OF POROUS MEDIA

FINAL REPORT

by:

A. Kantzas

(Part of Energy, Mines and Resources
Cost-shared Energy Conversion Program
and Part of the Program of the Federal Panel
on Energy R&D [PERD])

April 30, 1990

NOVA HUSKY RESEARCH CORPORATION
2928 - 16 St. N.E.
Calgary, AB T2E 7K7

Work on this project was conducted under the auspices of the Canada Centre for Mineral and Energy Technology, Energy, Mines and Resources Canada.

DSS File No: 06SQ.23440-8-9233

DSS Contract Serial No.: 23440-8-9233/01-SQ

CANMET Scientific Authority: Dr. K. Jha

MICROMEDIA

282 pp

© 1990 NOVA HUSKY RESEARCH CORPORATION

DISTRIBUTION LIST

	No. of Copies
Energy, Mines and Resources Canada:	5
Husky Oil Ltd.:	
I. Adamache	1
R. Davis	1
S. Harding	1
S. Hirowatari	1
L. Jeffries	1
E. Manko	1
R. McKellar	1
K. Miller	1
J. Peggs	1
M. Skalinski	1
NOVA HUSKY RESEARCH CORPORATION:	
B. Erno	1
T. Jack	1
A. Kantzas	1
D. Marentette	1
PanCanadian Petroleum Ltd.	2
NHRC Library	2
Husky Library	1
Files	2
TOTAL	**26**

© 1990 NOVA HUSKY RESEARCH CORPORATION

TABLE OF CONTENTS

Page No.

LIST OF TABLES iv

LIST OF FIGURES v

NOMENCLATURE ix

EXECUTIVE SUMMARY x

1.0 OBJECTIVES 1

2.0 LITERATURE SURVEY 5

3.0 CAT SCANNER CALIBRATION AND MODEL DESCRIPTION 35

4.0 MEASUREMENT OF X-RAY SPECTRA 41

5.0 UNCONSOLIDATED MEDIA 48

6.0 CONSOLIDATED MEDIA 57

7.0 HIGH PRESSURE TESTING 77

8.0 MUD INVASION 81

9.0 DETERMINATION OF SULPHUR 83

10.0 CAPABILITIES AND LIMITATIONS OF COMPUTER ASSISTED TOMOGRAPHY 88

11.0 CONCLUSIONS 90

12.0 ACKNOWLEDGEMENTS 92

13.0 REFERENCES 93

14.0 TABLES 110

15.0 FIGURES 150

© 1990 NOVA HUSKY RESEARCH CORPORATION

LIST OF TABLES - Pages 110-149

Table 2.1:	Principles of Operation of CAT Scanners
Table 2.2:	Classification of Image Reconstruction Methods
Table 4.1:	X-Ray Mean Energies for tube (KeV)
Table 4.2:	X-Ray Mean Energies with Core Holder Assemblies
Table 5.1:	Bulk Density as a Function of Depth for the Cold Lake Cores
Table 5.2:	COLD LAKE CORE A: Porosity vs. Liquid Saturations
Table 5.3:	COLD LAKE CORE B: Porosity vs. Liquid Saturations
Table 5.4:	CAT SCANNER Analysis of PCP Core #1
Table 5.5:	CAT SCANNER Analysis of PCP Core #2
Table 5.6:	CAT SCANNER Analysis of PCP Core #3
Table 5.7:	CAT SCANNER Analysis of PCP Core #4
Table 5.8:	CAT SCANNER Analysis of PCP Core #5
Table 5.9:	CAT SCANNER Analysis of PCP Core #6
Table 6.1:	CAT Scan Petrographic Analysis
Table 6.2:	Comparison of Results
Table 6.3:	Results of CATSCAN Analysis of Bluesky Core
Table 6.4:	CATSCAN Produced Petrographic Results
Table 6.5:	CATSCAN Produced Petrographic Results
Table 6.6:	CATSCAN Analysis of Rainbow Keg River "G" Pool Cores
Table 6.7:	Comparison of Different Core Characterization methods (Trout Reservoir)
Table 6.8:	List of Core Property Data as Determined by CATSCAN (Trout Reservoir)
Table 6.9:	Detailed CAT Scan Analysis of Various Core Samples (Trout Reservoir)
Table 6.10:	Determination of Anhydrite in a Dolomite Core (Trout Reservoir)
Table 6.11:	New Measurements with Reset Photomultiplier Tubes
Table 6.12:	Fracture/Vug vs. Matrix Porosity of Wabamun Core
Table 6.13:	Additional Measurements on Wabamun Core
Table 6.14:	Fracture/Vug vs. Matrix Porosity of the Two Additional Pieces from Wabamun
Table 7.1:	Pressure Response of #3 Sand; Experiment #1
Table 7.2:	Pressure Response of #3 Sand; Effect of Sample Length
Table 7.3:	Pressure Response of #3 Sand; Experiment #2
Table 7.4:	Pressure Response of #3 Sand in Rubber Shrink Tube; Experiment #3
Table 7.5:	Pressure Response of #3 Sand Saturated with Water
Table 7.6:	Pressure Response of #16 Sand; Experiment #5
Table 7.7:	Pressure Response of Berea Sandstone
Table 7.8:	Low Pressure Cycle for Sand #3
Table 8.1:	Bulk Density Comparisons on Core Cleaning
Table 8.2:	Bulk Density of Drilling Muds and Brines
Table 9.1:	A. Core Analysis Data for Core Pieces #12 & #52
	B. Hycal Analysis Data for Core Pieces #12 & #52
Table 9.2:	Characterization of Core #12
Table 9.3:	Characterization of Core #52

© 1990 NOVA HUSKY RESEARCH CORPORATION

LIST OF FIGURES - Pages 150-163

Figure 2.1	Production of Collimated X-ray Beam.
Figure 2.2	Production of Collimated X-ray Beam.
Figure 3.1	Bulk Density (g/cm^3) vs. CT number for all the calibrated standards.
Figure 3.2	Bulk density calibrated for group of line 1 (high atomic number).
Figure 3.3	Bulk density calibrated for group of line 2 (low atomic number).
Figure 3.4	Bulk density calibrated for group of line 3 (very dense standards).
Figure 3.5	Bulk density calibrated for group of line 4. This line is used for all the modelling of this work.
Figure 4.1	X-ray spectrum at 80 kVp, no water ring (annulus)/dosimetry.
Figure 4.2	X-ray spectrum at 100 kVp, no water ring (annulus)/dosimetry.
Figure 4.3	X-ray spectrum at 140 kVp, no water ring (annulus)/dosimetry.
Figure 4.4	X-ray spectrum at 80 kVp, no water ring (annulus)/dosimetry.
Figure 4.5	X-ray spectrum at 110 kVp, no water ring (annulus)/dosimetry.
Figure 4.6	X-ray spectrum at 140 kVp, no water ring (annulus)/dosimetry.
Figure 4.7	Nal crystal-pulseheight analyzer apparatus.
Figure 4.8	X-ray spectrum at 80 kVp, with pulseheight analyzer/3 1/2 in. core in Aluminum core holder.
Figure 4.9	X-ray spectrum at 110 kVp with pulseheight analyzer/3 1/2 in. core in Aluminum core holder.
Figure 4.10	X-ray spectrum at 140 kVp, with pulseheight analyzer/3 1/2 in. core in Aluminum core holder.
Figure 5.1	CT number image of Cold Lake Core. Identification of fractures in uniform sand. The color code at the right hand side indicates the range of CT numbers for each color. It is kept constant throughout the chapter. The range is 100 CT numbers.
Figure 5.2	CT number image of Cold Lake Core. Identification of fractures in a shale barrier.
Figure 5.3	CT number image of Cold Lake Core. Example of core damage. The left hand side of the core is missing.
Figure 5.4	CT number frequency distribution for the image of Figure 5.3.
Figure 5.5	CT number image of Cold Lake Core. Example of a layer where bedding planes meet.
Figure 5.6	CT number frequency distribution for the image of Figure 5.5.
Figure 5.7	CT number image of Cold Lake Core. Idenfication of clay clast inclusions in the boundary between shale and sand. Indication of core damage at the top right side.
Figure 5.8	CT number image of Cold Lake Core 0.01m deeper than the image of Figure 5.7.
Figure 5.9	CT number image of Cold Lake Core. Idenfication of fractures and clay clasts in a uniform sand.
Figure 5.10	Longitudinal reconstruction of Cold Lake Core. Clay clasts, shales and mud invasion can be identified.
Figure 5.11	Longitudinal reconstruction of Cold Lake core. Shales, mud invasion and missing core can be seen.
Figure 5.12	Core from Provost area. Identification of possible bedding planes.
Figure 5.13	CT number image of Provost core. Relatively uniform sand with a presence of clay clast.
Figure 5.14	Core from Provost area. Uniform shale or consolidated sand.
Figure 5.15	CT number image of damaged core from the Provost area.
Figure 5.16	Core from Provost area. Consolidated core broken by unconsolidated material.

© 1990 NOVA HUSKY RESEARCH CORPORATION

Figure 5.17 CT number image of damaged shale piece of core from Provost area.
Figure 5.18 Provost core image. Highly consolidated pieces of rock connected by loose material.
Figure 5.19 CT image of Provost core. Fractured semi-consolidated material.
Figure 5.20 Deudritic fracture pattern of semi-consolidated Provost core.
Figure 5.21 Radial fracture pattern of shale or consolidated core from Provost area.
Figure 5.22 Core from Provost area. Identification of core cracking.
Figure 5.23 CT image of Provost area. Area of very loose sand.
Figure 5.24 Longitudinal representation of Provost core #1; shale laminations and damaged areas are seen.
Figure 5.25 Longitudinal representation of Provost core #2. The consolidated layers and cement material are shown along with core damage.
Figure 5.26 Longitudinal representation of Provost core #3. Two consolidated layers with clay clasts are shown.
Figure 5.27 Longitudinal representation of Provost core #4. Unconsolidated and damaged sand.
Figure 5.28 Longitudinal representation of Provost core #5. Unconsolidated and damaged sand; presence of a shale layer.
Figure 5.29 Longitudinal representation of Provost core #6. Unconsolidated loose and damaged sand.
Figure 5.30 Longitudinal representation of the whole Provost core as a function of depth (in m).
Figure 5.31 Image of sandpack prepared in the laboratory.
Figure 6.1 Schematic of the x-ray scanner gantry.
Figure 6.2 Image of the Halkirk sandstone. Presence of high density inclusions. The color code at the right hand side indicates the range of CT numbers for each color. The range is 100 CT numbers.
Figure 6.3 Image of the Halkirk sandstone. Uniform sample. Color code same as in Figure 6.2.
Figure 6.4 Longitudinal view of Halkirk core #1. Uniform sand. Color code same as in Figure 6.2.
Figure 6.5 Longitudinal view of Halkirk core #2. Color code same as in Figure 6.2.
Figure 6.6 Longitudinal view of Halkirk core #3. Uniform sand with few high density inclusions. Color code as in Figure 6.1.
Figure 6.7 Different longitudinal type views of core samples.
Figure 6.8 CT number image of Bluesky formation. Dolomitic sandstone. Color code same as in Figure 6.2.
Figure 6.9 CT number image of Bluesky formation. Dolomite. Color code as in Figure 6.2.
Figure 6.10 CT number image of Bluesky formation. 2/3 slabbed core with 1/3 Berea Cap. Uniform dolomitic sandstone. Color code as in Figure 6.2.
Figure 6.11 CT number image of Bluesky formation. 2/3 slabbed core with 1/3 Berea cap. Non-uniform dolomitic sandstone. Color code as in Figure 6.2.
Figure 6.12 Saggital view of Rainbow Keg River "A" Pool core 52. Color code as in Figure 6.2.
Figure 6.13 Saggital view of Rainbow Keg River "A" Pool core 56. Color code as in Figure 6.2.
Figure 6.14 Core from Rainbow Keg River "C" Pool. Directional vugs. Evidence of mud invasion. Color code as in Figure 6.2.
Figure 6.15 Rainbow Keg River "C" Pool core. Evidence of mud invasion. Color code as in Figure 6.2.
Figure 6.16 Image of vuggy core in Rainbow Keg River "C" Pool. Color code as in Figure 6.2.

© 1990 NOVA HUSKY RESEARCH CORPORATION

Figure 6.17 Core from Rainbow Keg River "G" Pool. Presence of fracture. Evidence of mud invasion. Color code as in Figure 6.2.

Figure 6.18 Core from Rainbow Keg River "G" Pool. Layered structure (stromatoporoids). Color code as in Figure 6.2.

Figure 6.19 More stromatoporoids from Rainbow Keg River "G" Pool. Color code as in Figure 6.2.

Figure 6.20 Continuation of stromatoporoids from Rainbow Keg River "G" Pool. Color code as in Figure 6.2.

Figure 6.21 Mud invaded piece of Rainbow Keg River "G" Pool core. Color code as in Figure 6.2.

Figure 6.22 Elan analysis of Trout reservoir based on logs. CAT scanning and routine core analysis.

Figure 6.23 Elan analysis of Trout reservoir based on logs. CAT scanning and routine core analysis.

Figure 6.24 Elan analysis of Trout reservoir based on logs. CAT scanning and routine core analysis.

Figure 6.25 Elan analysis of Trout reservoir based on logs. CAT scanning and routine core analysis.

Figure 6.26 Elan analysis of Trout reservoir based on logs. CAT scanning and routine core analysis.

Figure 6.27 Elan analysis of Trout reservoir based on logs. CAT scanning and routine core analysis.

Figure 6.28 Elan analysis of Trout reservoir based on logs. CAT scanning and routine core analysis.

Figure 6.29 Elan analysis of Trout reservoir based on logs. CAT scanning and routine core analysis.

Figure 6.30 Elan analysis of Trout reservoir based on logs. CAT scanning and routine core analysis.

Figure 6.31 Elan analysis of Trout reservoir based on logs. CAT scanning and routine core analysis.

Figure 6.32 Elan analysis of Trout reservoir based on logs. CAT scanning and routine core analysis.

Figure 6.33 Elan analysis of Trout reservoir based on logs. CAT scanning and routine core analysis.

Figure 6.34 Elan analysis of Trout reservoir based on logs. CAT scanning and routine core analysis.

Figure 6.35 Elan analysis of Trout reservoir based on logs. CAT scanning and routine core analysis.

Figure 6.36 Elan analysis of Trout reservoir based on logs. CAT scanning and routine core analysis.

Figure 6.37 Elan analysis of Trout reservoir based on logs. CAT scanning and routine core analysis.

Figure 6.38 Elan analysis of Trout reservoir based on logs. CAT scanning and routine core analysis.

Figure 6.39 Three dimensional fracture map of core #4 from Wabamun formation.

Figure 6.40 Coronal view of Wabamun core #4. Two fractures can be seen. The color code indicates the range of CT numbers (100 CT numbers per color).

Figure 6.41 Image of fracture core from Wabamun formation. Color code as in Figure 6.40. The core is 2/3 slabbed with a 1/3 Berea cap.

Figure 6.42 Coronal view of Wabamun core #5. The core is much more vuggy than #4. Color code as in Figure 6.40.

Figure 6.43 Vuggy core piece from Wabamun formation. Color code is in Figure 6.40.

Figure 6.44 Coronal view of Wabamun core #6. Presence of large vugs. Color code as in Figure 6.40.

Figure 6.45 Image of vuggy and fracture piece from Wabamun core. Color code as in Figure 6.40.

Figure 6.46 Image of vuggy and fractured piece from Wabamun core. Multiple fracture pattern. Color code as in Figure 6.40.

Figure 6.47 Image of fractured piece from Wabamun core. Color code as in Figure 6.40.

Figure 6.48 Bedding planes on Berea sandstone. Each color correponds to CT numbers.

Figure 6.49 More bedding planes on Berea sandstone. Color code as in Figure 6.48.

© 1990 NOVA HUSKY RESEARCH CORPORATION

Figure 6.50 Saggital view of layered Berea sandstone. Color code as in Figure 6.48.
Figure 6.51 Coronal view of layered Berea sandstone. Color code as in Figure 6.48.
Figure 7.1 Effect of overburden pressure on dry sand #3 coarse, high permeability using a teflon shrink tube.
Figure 7.2 Repeat run on sand #3.
Figure 7.3 Repeat run on sand #3 using a rubber shrink tube.
Figure 7.4 Effect of overburden pressure on water saturated sand #3.
Figure 7.5 Effect of overburden pressure on dry sand #16 (fine, low permeability).
Figure 7.6 Effect of overburden pressure on Berea sandstone.
Figure 7.7 Low pressure cycles for sand #3.
Figure 7.8 Effect of overburden pressure on oil saturated sand #3.
Figure 9.1 Bulk density map of the slice of core piece #12 at 18mm from the top face.
Figure 9.2 Bulk density map of the slice of core piece #12 at 20mm from the top face.
Figure 9.3 Bulk density map of the slice of core piece #12 at 21mm from the top face.
Figure 9.4 Bulk density map of the slice of core piece #12 at 24mm from the top face.
Figure 9.5 Bulk density map of the slice of core piece #12 at 25mm from the top face.
Figure 9.6 Bulk density map of the slice of core piece #12 at 27mm from the top face.
Figure 9.7 Bulk density map of the slice of core piece #12 at 30mm from the top face.
Figure 9.8 Bulk density map of the slice of core piece #12 at 15mm from the undamaged face.
Figure 9.9 Bulk density map of the slice of core piece #52 at 35mm from the undamaged face.
Figure 9.10 Bulk density map of the slice of core piece #52 at 55mm from the undamaged face.
Figure 9.11 Bulk density map of the slice of core piece #52 at 75mm from the undamaged face.
Figure 9.12 Bulk density map of the slice of core piece #52 at 95mm from the undamaged face.
Figure 9.13 Bulk density map of the slice of core piece #52 at 115mm from the undamaged face.
Figure 10.1 CAT scanner and core analysis prediction comparisons of bulk density (units in g/cm^3).
Figure 10.2 CAT scanner and core analysis prediction comparison of porosity (units in % pore volume).

© 1990 NOVA HUSKY RESEARCH CORPORATION

NOMENCLATURE:

CAT:	Computer Assisted Tomography
CT:	Computed Tomography
NMRI:	Nuclear Magnetic Resonance Imaging

D:	dose
E:	x-ray energy, mean x-ray energy
e:	x-ray energy limit
I_o:	incident x-ray intensity
I:	transmitted intensity
l:	distance along scan line
N:	Avogadro's Number
p:	projection value
p (l, θ):	ray transmission
P*:	corrected projection
r:	radial coordinate
R:	conjugate Fourier frequency variable
S:	saturation
z:	effective atomic number

GREEK:

ϵ:	detector efficiency
ϕ:	porosity, coordinate system
θ:	angle describing scan line
μ^*:	linear attenuated coefficient
ρ:	bulk density
σ:	photon interaction
Δ:	increment

Subscripts:

b:	bulk
C:	Compton
d:	detector
e:	law
f:	fluid
g:	gas, grain
h:	high
o:	oil
R:	Rayleigh
s:	source
T:	Photoelectric
w:	water

© 1990 NOVA HUSKY RESEARCH CORPORATION

EXECUTIVE SUMMARY

Computer Assisted Tomography (CAT) Scanning has been used as a tool for the development and/or testing of methodologies aiming at the non-destructive characterization of porous media. The present work was equally funded by the core funding program of NOVA HUSKY RESEARCH CORPORATION and the Canadian Centre of Mineral and Energy Technology (CANMET) of Energy, Mines and Resources Canada.

During this work approximately 90 pieces of core were tested. These pieces represent two heavy oil reservoirs (unconsolidated media), two sandstone reservoirs, one dolomitic sandstone, one limestone reservoir and four dolomitic reservoirs (consolidated media). Information on more than 750 rock slices is included. Several hundreds of calibration tests on reservoir rock and other samples were run. Most of the information was analyzed using dual energy scanning. It is estimated that during the course of this work over 2,500 scans were performed.

A computer package, which was developed in NHRC, was used for the analysis of the x-ray images and the prediction of core properties such as bulk density, porosity and effective atomic number. The proposed methods can also be used for characterization of reservoir heterogeneities such as vugs, fractures, shales, bedding planes, clay clasts, stromatoporoids etc. Macroscopic accumulation of minerals such as anhydrite and sulphur can be detected by the scanner. All this information can be mapped in three dimensions with a resolution of 0.000750 m x 0.000750 m x 0.0003 m. The technique is simple and relatively fast. The amount of processed data depends on the expected resolution. The accuracy of the method compared to conventional core analysis is quite satisfactory with the exception of very tight, very dense, full diameter samples which did not give as good results. The reproducibility of the results is also very good.

Improvements on the technique could address increasing resolution and speed. A custom made core analysis CAT scanner could become a routine tool for core analysis in a few years. Complementary use of x-rays with some other source of energy would result in a better characterization of native core material.

Industry has shown interest in the work. Husky Oil and PanCanadian Petroleum assessed the technology and supported the work by providing core material. The computer software has been already transferred to the University of Waterloo for use by the Porous Media Research Institute.

© 1990 NOVA HUSKY RESEARCH CORPORATION

SOMMAIRE

La tomographie scanographique assistée par ordinateur a été utilisée comme technique d'analyse non-destructive des milieux poreux. Les présents travaux ont été financés à part égale par Nova-Husky, le groupe de recherches & développement, et le Centre de technologie des mines et de l'énergie du Canada.

Au cours de ces travaux, environ 90 carottages ont été analysés. Ces échantillons provenaient de deux réservoirs de pétrole bitumineux (milieu friable), deux réservoirs de grès, un réservoir de grès dolomitique, un réservoir calcaire et quatre réservoirs dolomitiques (milieu ferme). Une étude détaillée a porté sur 750 échantillons de carottage. Plusieurs centaines de mesures de calibrage ont été effectuées sur des échantillons de diverses origines (carottages et autres). La plupart des données ont été recueillies par balayage à double faisceaux. On estime qu'au cours de ces travaux, plus de 2500 scanographies ont été effectuées.

Le centre de recherches & développement de Nova Husky a mis au point un logiciel pour analyser les radioscopies et évaluer les caractéristiques de l'échantillon tels que la densité moyenne, la porosité et le numéro atomique des éléments. Cette méthode peut aussi être utilisée pour déterminer les hétérogénéités d'un réservoir (cavités, failles, schistes, plans de stratification, argile friable, stromatoporoïdes, etc.). Les traces macroscopiques de minéraux tels que le soufre et l'anhydrite peuvent être détectées par le scanographe. Toutes les données sont cartographiées en 3 dimensions avec une résolution de 0,75 mm x 0,75 mm x 0,3 mm. La technique est relativement simple et rapide. La vitesse d'analyse dépend du pouvoir de résolution imposé. La précision de cette technique, comparée aux méthodes d'analyse conventionnelles, est tout à fait satisfaisante, sauf pour les échantillons très fermes de gros diamètre et de grande densité, avec lesquels il est plus difficile d'obtenir de bons résultats. La reproductibilité des résultats est également très bonne.

Le taux de résolution et la vitesse d'exécution sont les deux paramètres sur lesquels il faut se concentrer pour améliorer la technique. Il est possible que d'ici quelques années, on aboutisse à un appareil spécialement conçu pour l'analyse de routine des carottes. L'usage complémentaire des rayons X avec d'autres sources d'énergie, résulterait en une meilleure caractérisation des échantillons de carottage.

Le secteur industriel a démontré un certain intérêt pour ces travaux. Les sociétés pétrolières Husky et Pan-Canadian ont évalué cette technologie et ont fourni les échantillons à analyser. Le logiciel a aussi été transféré à l'université de Waterloo aux soins de l'Institut de recherches sur les milieux poreux.

© 1990 NOVA HUSKY RESEARCH CORPORATION

1.0 OBJECTIVES

- To provide a comprehensive review of Computer Assisted Tomography.
- To develop calibration protocols for us of CAT scanners in core analysis.
- To develop a method of measuring the spectrum of the x-rays as detected by the x-ray detector arrays.
- To develop methods of characterizing unconsolidated media using CAT scanners.
- To develop methods of characterizing consolidated media using CAT scanners.
- To assess the effect of overburden pressure on porosity.
- To investigate the potential of studying mud invasion using CAT scanners.
- To determine sulphur deposition in vuggy carbonates.
- To evaluate the capabilities and limitations of CAT scanners.

1.1 Introduction

Computer assisted Tomography (CAT) Scanning is a laboratory technique that can provide two and three dimensional image reconstruction of opaque objects using x-rays. The technique can be used for reconstruction of objects from a few millimeters to several centimeters in diameter. This technique has been successfully used in medical radiology for the detection of cancerous tumors. Recently, CAT Scanners have been used for petroleum engineering applications such as density, porosity, atomic number studies, fracture identification, two and three phase saturation measurements, etc. A number of very important problems can be tackled using the CAT scanners. Of particular interest are the investigation of the effect of drilling mud on the properties of the reservoir rock, and the identification of reservoir heterogeneities. The latter is of great interest for the vuggy carbonate reef type reservoirs of the Rainbow Lake area.

NOVA HUSKY RESEARCH CORPORATION (NHRC) has obtained excellent experience working with CAT scanners for the past five years. An EMI CT5005 fully body scanner, originally designed for medical use, was modified for applications in core analysis and reservoir engineering. The Scanner can scan objects of up to 0.25 m in diameter with a resolution of 0.00075 m by 0.00075 m and a slice thickness of 0.001 m up to 0.015 m. It has been seriously considered that CAT scanning techniques could be used for routine core analysis. Initial calibration work was done to determine the optimum operating conditions for the CAT scanner with respect to energy setting, elimination of artifacts, sample site, choice of dopants, etc. Starting from this point, a number of experiments were performed and used as criteria for the evaluation of CAT scanners as core analysis tools.

© 1990 NOVA HUSKY RESEARCH CORPORATION

1.2 Work Statement

During the initial planning of the project, it was felt that in order to prove the validity of the proposed method, a number of experiments should be performed. The experiments were divided into eight tasks followed by a detailed final report. The initial focus was on unconsolidated rock with only a few experiments on consolidated media. However, due to the low oil prices drilling in unconsolidated reservoirs was kept minimal, and resulted in minimal coring. In order to perform some testing we were assisted by PanCanadian Petroleum, which provided us with 8 m of core to perform some x-ray CAT scanning. Conversely, consolidated core was easily available and a number of Husky geologists and petrophysicists became interested in the project. So we have obtained an abundance of consolidated core material and we used this material for validation of the models we developed. In the following paragraphs the initial work tasks are presented and what modifications had to be made are explained.

The first task was to investigate drilling mud invasion using the CAT scanner. A number of core samples were scanned before and after cleaning. The computer model was used to test change of core characteristics such as porosity, fluid distributions and density distributions due to mud invasion. The conclusions of these tests are given in Chapter 8.

The second task was to design and construct high pressure core holders that transmit x-rays. A number of different options were considered (e.g. aluminum 7075). However, during the initiation of this project new Provincial Government regulations came into effect. These regulations did not allow construction of any high pressure vessels unless the manufacturer meets the Alberta Boilers Branch regulations. Since NHRC could not qualify for such tasks we have decided to consult with one of the qualified companies. Temco of U.S.A. provided us with a satisfactory design for a core holder of 1 m length 0.11 m in diameter made of composite materials. However, in order to obey the law a long and tedious procedure was initiated. This was the first composite core holder built under the Boilers Branch Code and a lot of new procedures had to be investigated. One year has passed since the purchase order was submitted and the core holder has not arrived yet. This unexpected situation has caused us to modify our plans. We used a small aluminum core holder to measure sand and sandstone response to overburden pressure. Because of the size of the core holder, long full diameter core pieces were not used. However, a large number of tests were performed using smaller size cores and the results are presented in chapter 7.

© 1990 NOVA HUSKY RESEARCH CORPORATION

The third task is devoted to the mapping of porosity. A model for porosity mapping has been developed and tested in a variety of samples. The effect of overburden pressure on porosity was demonstrated using sandpacks. Results and discussion on the topic is given in chapters 5 and 7.

A method for evaluation of size, orientation and distribution of "fractures" in unconsolidated media was proposed under task four. Fractures were identified and mapped on a number of occasions. Other types of heterogeneities were also identified and mapped. Explanation of the existence of these "fractures" in unconsolidated media is given in chapter 5. The effect of confining pressure on "fractures" was not tested as sufficiently because of the problems related to the core holder.

In task five it was proposed to use the experience obtained from the previous work to study the possibility of native core characterization. The applicability and limitations of CAT scanning for this purpose is described in chapter 5. In chapter 8 consolidated cores which were tested before and after solvent extraction were compared.

The application of the above findings on consolidated media was proposed under task six and the application in specific carbonate reservoirs of interest to Husky Oil was proposed under task seven. It was proposed to develop a technique for the detailed porosity mapping and the accurate determination of various types of heterogeneities (i.e. bedding planes, cracks, fractures and vugs). It was expected to see a deteriorating accuracy of the developed methodologies against the increased density of the consolidated materials. The possibility of using geo-statistical methods for the core characterization was entertained. The results of these tasks are discussed in chapter 6.

An extension of task seven was the application of CAT scanning in the determination of the distribution of sulphur in a dolomitic reservoir. This unique application was investigated, a method was developed and tested, and the results were implemented in a reservoir in western Alberta. Details are given in chapter 9.

When the initial proposal was made, it was felt that some calibration curves would be created based on the results of this work. Task eight was set for this purpose. An extensive calibration work was performed. This work extended far and beyond the original plan. The findings of this work along with a brief description of the developed model are given in chapters 3 and 4.

Finally, this report is part of the last proposed task (report preparation). Numerous detailed reports have been prepared for the different parts of this project and copies have been submitted to the Government. Three papers were written so far with the results of this work, and more will

© 1990 NOVA HUSKY RESEARCH CORPORATION

follow. A stepwise procedure for core characterization has been established and copies of our software are available. A copy has been already transferred to the University of Waterloo.

The last two chapters of this report provide an assessment of the capabilities and limitations of the CAT scanners followed by some concluding remarks. It is felt that a new era is born in the non-destructive testing of materials and NHRC and Canada can play a leading role.

© 1990 NOVA HUSKY RESEARCH CORPORATION

2.0 LITERATURE SURVEY

2.1 Objective

The material of this chapter has been compiled in order to provide a comprehensive review of the research work done with the aid of Computer Assisted Tomography in the areas of petroleum engineering and materials testing. Moreover, some other very exciting areas of non-destructive testing (NDT) are presented. Emphasis is given in the recent advances of the NDT using Nuclear Magnetic Resonance Imaging (NMRI), while a few highlights of other emerging technologies are presented.

2.2 Background

There is an increasing number of research projects reported in the recent literature that deal with the measurement of the saturation profiles along a core during immiscible and miscible displacement tests. Five methods show a good potential for reliable and non-destructive *in-situ* saturation measurements. These are: i) Radioactive Tracer Measurements, ii) Microwave Attenuation Techniques, iii) Nuclear Magnetic Resonance Imager (NMRI) Techniques, iv) Ultrasound mapping and v) Computer Assisted Tomography (CAT) Techniques. A description of the principles and past history of the various methods is given below. The review starts with detailed discussion about the CAT Scanner followed by a review on the NMR Imager. Finally, other methods are described in the end of this chapter.

2.3 Computer Assisted Tomography Scanning

2.3.1 Principles of Computer Assisted Tomography

The mathematical basis of the reconstruction of an object from the data obtained in a number of views around the object was developed as early as 1917 by Radon (for a list of references for this paragraph see Waggener *et al.* 1984). In 1956, Bracewell developed practical techniques for measuring microwave radiation emitted by the sun. In 1975 Gordon cited over 1500 references related to image reconstruction. The first published attempt at medical application of reconstruction was carried out by Oldendorf in 1961 using a method called "spin migration". Experiments were carried out by Kuhl *et al.* in 1963 utilizing a tomographic image scanner for radionuclide imaging. The first clinically useful CAT system was pioneered by Godfrey Hounsfield of EMI Ltd. in England, and installed in 1971 in the Atkinson Morley Hospital in London. The full

© 1990 NOVA HUSKY RESEARCH CORPORATION

impact of CAT on the medical field is hard to estimate because it is still evolving; however, the profound diagnostic, social and economic impact of the development have already been sufficient for some to compare it to that of the x-ray discovered by Roentgen in 1895.

CAT uses an x-ray source that moves around the sample to obtain one-dimensional projections of x-ray attenuation at different angles. From these projections, a cross-sectional slice through the sample is reconstructed by the computer (Figure 2.1). Finally, a three-dimensional image is reconstructed from sequential transverse cross-sectional slices, taken as the sample is moved through the scanner. To obtain both density and effective atomic number , CAT images are taken at two x-ray energies. One energy is high enough for the x-rays to be predominantly Compton-scattered and one is low enough for them to be mostly photoelectrically absorbed. A combination of the two images in the computer, on a pixel by pixel basis, can be used to generate separate images of bulk density and effective atomic number.

In the first stage of the operation, x-ray transmission data are collected. The data acquisition of the CAT equipment is very sophisticated. The x-ray tube and the detectors are mounted on a moving gantry. The transmitted x-rays which are not scattered or absorbed are detected electronically. Physically dense objects attenuate the beam more than do less dense objects. In one of the systems described by Ayral (1985) the generator/tube combination was operated at 125keV and 30mA. The object is stationary on the x-ray tube and detectors move linearly. A set of parallel beams is generated (Figures 2.1, 2.2). They are all transmitted through volumetric elements, usually called voxels or pixels. Each volumetric element represents 7.6×10^{-4}m by 7.6×10^{-4}m facial surface and 0.01m depth (the depth corresponding to the finite x-ray beam width) for a typical second generation scanner. After one linear scan, the gantry rotates by a degree and the linear scan is repeated. This angular translation is continued until half the periphery of the object is scanned. The scanning is completed in approximately 100 sec. The image is constructed by use of the information accumulated. For a sequence of cross sectional scans, the object is moved along the longitudinal direction of the sample.

In the second stage of the imaging process, the software built into the computer system plays an important role. As the data is collected, each intensity relationship generated for the beams transmitted through individual volumetric elements is linear in the logarithmic scale, described by the equation

$$\mu^{\bullet} = (1/L)\ln(I_o/I) \qquad (2.1)$$

© 1990 NOVA HUSKY RESEARCH CORPORATION

where μ^* is the linear attenuation coefficient, L is the path length, I_o is the incident intensity and I the transmitted intensity. However, numerous linear equations are created and solved simultaneously. The reconstruction of the image is complicated. The sophisticated algorithms in the software of the system are proprietary.

One can actualiy observe the back projection of the image at a CRT terminal. In the video display monitor, controls are incorporated where the range of CT (Computer Tomography) numbers can be adjusted. Thus, the observed image intensities (seen in the monitors or on film) are arbitrary. However, differences in intensities reflect differences in attenuation information based on the present CT number ranges. For example, in the EMI scanner when the gray scale mean value is set for a CT number of 1500 with a deviation of 700 CT numbers, black region display CT numbers of about 1100 and white regions of about 1900. The black areas represent low density regions where a lot of x-rays are transmitted, while the white areas are dense regions where a lot of x-rays are absorbed or scattered. When the film is developed, the opposite colour effect is produced. This qualitative information enables one to visualize the variations in the composition of a cross-section. The information of attenuation coefficients recorded as digital data in the hard copy outputs with a high-speed printer. This data is also stored on magnetic tapes. The digital data enables one to quantitatively analyse the outputs as well. Furthermore, there are subroutines that are built into the proprietary software of the system. Histograms representative of the mean CT numbers of concentric circular regions of a cross-section and the standard deviation about the mean are some of the typical statistical information derived from these subroutines.

Equation (2.1) applies for a narrow monoenergetic beam of x-ray photons which traverses a homogeneous medium. If, instead of a homogeneous medium, the radiation beam traverses a heterogeneous object, such as a body of a patient, the left hand side of equation (2.1) may be replaced by the line integral of the linear attenuation coefficients. If we let the distribution of the linear attenuation coefficients within the two-dimensional cross-section being scanned be represented by $\mu(x,y)$, where x and y are the Cartesian coordinates specifying the location of points in the tomographic slice, the intensity transmitted along a particular path is given by the expression

$$p = \ln(I_o / I) = \int_s^d \mu(x, y)\, dL \qquad (2.2)$$

where dL is the differential of path length along the ray, s is the source, d is the detector and p is called the projection value.

© 1990 NOVA HUSKY RESEARCH CORPORATION

This is the fundamental equation of the CAT process. It states that by taking the logarithm of the ratio of the unattenuated intensity to the transmitted intensity we have measured the line integral of the two-dimensional distribution of linear coefficients. Given a sufficient number of these line integrals or projection values the original distribution can be inferred.

Actually equation (2.2) is a highly idealized portrayal of the actual situation. The x-ray beam utilized in an actual scanner is far from monoenergetic, consisting instead of a spectrum of photons ranging from around 20 KeV up to some peak values, typically 120 keV. In addition to this, the detector system has associated with it an efficiency which is energy dependent. The actual situation, therefore, is more accurately represented as

$$I = \int_{e_l}^{e_h} (dI_o/dE)\epsilon(E)\exp\left[-\int_s^d \mu(x,y,E)ds\right]dE \qquad (2.3)$$

instead of the simpler expression shown in equation (2.2). Here dI_o/dE represents the spectral distribution of intensity, $\epsilon(E)$ is the efficiency of the detector at a particular energy, E, e_l and e_h are the lower energy and higher energy respectively and μ is written not only as a function of spatial coordinates x and y but also of photon energy. In practice, however, the reconstruction algorithm is based on equation (2.2), the assumption being made that the reconstructed coefficients will correspond to some particular effective energy characterizing the attenuation of the beam as a whole. The artifacts which can result from this assumption can be suppressed by correcting the data for beam-hardening effects.

The heart of CAT, the reconstruction process itself, is a special case of a very old problem: given a sufficiently large set of line integrals of an unknown two-dimensional distribution, we wish to determine the distribution. The problem may be solved in a number of ways, each of which could conceivably be incorporated into an algorithm for CAT.

One approach to the problem of reconstruction from projections is based on the work of the 19th century mathematician Fourier. The Fourier methods are derived from a relationship known as the "Central Projection Theorem" or the "Central Slice Theorem", as it is sometimes called. This theorem states that the Fourier transform of a one-dimensional projection of a two-dimensional distribution is mathematically identical to a slice through a two-dimensional Fourier transform of the original distribution. This implies that by taking Fourier transforms of the various one-dimensional profiles obtained using the transmission data, we have calculated the two-dimensional Fourier transform of the unknown distribution in polar coordinates. The Fourier transform of the transmission profiles is described mathematically as,

© 1990 NOVA HUSKY RESEARCH CORPORATION

$$F(R,\theta) = \int_{-\infty}^{+\infty} p(l,\theta)\exp[-2\pi i R l]dl \qquad (2.4)$$

where l is the distance along the scan line, θ is the angle describing the scan line, R is the conjugate Fourier frequency variable and p (l, θ) is the transmission of a particular ray described by (l, θ). The original distribution is recovered by transforming back into real space:

$$f(r,\Phi) = \mu(r,\Phi) = \int_0^{2\pi}\int_0^{\infty} F(R,\theta)\exp[2\pi i R r\cos(\Phi-\theta)]\,|R|\,dR d\theta] \qquad (2.5)$$

where μ (r, ϕ) is the linear attenuation coefficient represented as a function of r and ϕ, the variable r is obtained from l by r = lcos (ϕ- θ), and the term R has arisen from the Jacobian of a coordinate transformation. The angle ϕ is used to describe a point in real space, while the angle θ is used to describe a point in Fourier space. Equations (2.4) and (2.5) are all that is required to reconstruct a two-dimensional object from its one-dimensional projections. Since normal computer methods and display systems are based on rectangular arrays, the Fourier coefficients need to be converted from polar to rectangular grid coordinates and then the two-dimensional Fourier transform needs to be taken to obtain the density distribution on a Cartesian grid. This method is somewhat complex and is not normally used on commercial CAT systems.

A method of reconstruction which, mathematically, is closely related to the two-dimensional Fourier method is the so-called "convolution method" or "filtered back-projection". In the simplest form of back projection, the projection data for each of the various views is thrown back into the reconstruction plane and summed in order to obtain an image. Mathematically we may represent the process of back projection as

$$f(r,\Phi) = \sum_k p[r\cos(\Phi - \Theta_k), \Theta_k]\Delta\Theta_k \qquad (2.6)$$

where p is the projection value and $\Delta\ \theta_k$ is the angular increment between projections. Simple back projection is a very crude approach to the reconstruction problem and it is characterized by "star" artifacts around regions of high density. While the back projection distribution resembles the correct solution distribution (i.e. the image), it is distorted (Waggener *et al.* 1984). The distortion can be removed by the two-dimensional convolution of the degraded image with an appropriate correlation function, or by taking the two-dimensional Fourier transform of the image, multiplying it by a suitable filter, and performing the inverse Fourier transform. These methods require considerable computer time and tend to yield less than optimal results with real data.

© 1990 NOVA HUSKY RESEARCH CORPORATION

An alternative approach is the "filtered back-projection" method which is a technique most commonly used in commercial CAT scanners. With this method the projection data may be corrected or filtered prior to back-projecting. As with other filtering operations this correction may be implemented as a convolution operation in the spatial domain or as a functional multiplication in the Fourier frequency domain. The Fourier filtered back-projection method multiplies the Fourier transform of the projection data by a ramped shaped filter whose magnitude is proportional to R where R is Fourier frequency variable associated with the linear position of the projection data, l . According to the convolution theorem, this spatial frequency filtering is equivalent to convoluting the projection data with a corresponding "filter function" or "kernel" in the spatial domain. This approach is sometimes referred to as the "convolution reconstruction method" and the corrected projection data, $P^*(r_i, j)$ may be obtained from the measured projection data, $p(r_i, \Theta)$, for any given projection angle Θ, by

$$p^*(r_i, \Theta) = (p(r_i, \Theta)/4a) - (1/\Pi^2 a)\left[\sum_j p(r_j, \Theta)/(i-j)^2\right] \qquad (2.7)$$

with (i-j) odd only and where a is the sampling interval. The image can then be formed by back-projecting this corrected projection data onto a suitable two-dimensional matrix by use of equation (2.5). The resultant image will be void of the gross blurring found in the uncorrected back projection method and will be a fairly accurate representation of the linear attenuation coefficients, or density distribution $\mu(x,y)$. The preceding equations describe reconstruction from parallel rays but similar expressions can be derived which are applicable to fan beam configurations.

The major advantage of the filtered back-projection or convolution reconstruction method and the primary reason for its use in commercial scanners is its relatively fast reconstruction time. This is enhanced by the fact that the reconstruction procedure can be implemented as the data is collected (for certain data acquisition geometries) and that the reconstruction process can be compartmentalized, having a separate piece of hardware or computer to perform each phase of the reconstruction. Simultaneous operation between separate computer processors may have one processor normalizing the data for detector imbalances, x-ray output, and beam hardening error as well as taking the logarithm as in equation (2.2), another convoluting the projection data with the appropriate correction function equation (2.7), and a separate processor performing the back-projection operation equation (2.6). By using this reconstruction technique on a slow scanner or by using this technique with multiple processors on a fast scanner, reconstructions can be obtained almost immediately after the scanning process is complete.

© 1990 NOVA HUSKY RESEARCH CORPORATION

The result of the reconstruction process is a two-dimensional array of numbers. The reconstructed matrix can be represented by several different methods including printing out of the matrix values, plotting the values along a line, presenting an average value within the region of interest or simply showing the image as a gray scale display. In the absence of beam hardening artifacts, these matrix values are directly related to the linear attenuation coefficient distribution of the object at a particular effective x-ray energy. The numbers stored in this computer matrix, however, are not the linear attenuation coefficients but are scaled to integer values covering a specified range and usually adjusted so that the value of water is zero. The equation relating the CTnumbers (CTn) to the corresponding linear attenuation coefficients is

$$CTn = K[(\mu - \mu_{water})/\mu_{water}] \tag{2.8}$$

where μ and μ_{water} are the linear attenuation coefficients of the material scanned and of water at the effective energy of the beam and K is a scaling factor equal to the number of CT values between air and water. In the original EMI, K was set at 500 corresponding to -500 to +500 scale between air and dense bone. Most current scanners use a value of 1000 for K. This results in a -1000 to +1000 CTnumber scale with water still a zero and each CTnumber corresponding to 0.1% of the linear attenuation coefficient of water. Some systems extend the CTnumber range to values above +1000 to allow better differentiation of bone densities. The CTnumbers resulting from the K=1000 scale are often referred to as "Hounsfield Units" (HU) in honor of Godfrey Hounsfield, the inventor of the original EMI scanner.

There are five generations of CAT scanners available. The first generation is the oldest and requires the longest x-ray exposure for the sample while the fifth is the newest and fastest. The differences of the five CAT generations are given in Table (2.1). The first and second generation machines collect and reconstruct the data in the form of parallel beams, while the last three generations machines fall in the category of the fan beam data collection. Parallel beam data reconstruction is simpler and less prone to artifacts compared to fan beam data reconstruction. Most industrial scanners are of the second generation configuration. For displacement studies, it is important to achieve good contrast resolution instead of good spatial resolution. Good contrast resolution will aid in distinguishing between different fluids; contrast resolution depends upon the difference in the x-ray photon absorption cross section and photon statistics or photon noise. A review on the theory and the methods of image reconstruction in Computer Assisted Tomography is given by Brooks and Di Chiro (1975) and a brief summary is given in Table (2.2).

© 1990 NOVA HUSKY RESEARCH CORPORATION

2.3.2 *Applications of Computer Assisted Tomography in Petroleum Engineering*

Outside of medical applications, the oil industry is probably most involved with Computer Assisted Tomography. Most of this activity is due to the work at the Shell Bellaire Research Center (BRC) where Vinegar and Wellington started as early as 1979. Now Vinegar and his coworkers are expanding their experience in the domain of Nuclear Magnetic Resonance Imaging (NMRI) and its applications in the petroleum industry. Wellington and Vinegar (1985) presented a study for foam mobility control for CO_2. The scanner they used at that point was a Deltascan 100 second generation scanner with a precision translational table and postprocessing software developed on a VAX 11/780 with a Genisco 6000B color display computer. The software they developed includes ternary color display of three phase saturations, multiplanar reconstruction and video movie capabilities. A CRAY XMP-1 computer was used to run numerical simulations. The imaging of high-pressure high-temperature core floods was achieved by using low x-ray attenuation aluminum pressure vessels. Saturation calculations were done using the linear attenuation coefficients. Dual energy scanning was used to image the three phase fluid saturations using the following equations;

$$\begin{aligned} \mu_{t1} &= \mu_{o1}S_o + \mu_{w1}S_w + \mu_{g1}S_g \\ \mu_{t2} &= \mu_{o2}S_o + \mu_{w2}S_w + \mu_{g2}S_g \\ S_o + S_w + S_g &= 1 \end{aligned} \tag{2.9}$$

In the above equations μ is the total attenuation coefficient for the core with multiple components present. The terms μ_w, μ_o and μ_g are the attenuation coefficients for the core 100% saturated with water, oil and gas respectively. The subscripts 1 and 2 refer to peak acceleration voltages of 120 and 90 KeV. 40% 1-Iodododecane was used as a dopant for the oil phase. This work demonstrated that a surfactant can provide effective mobility control for tertiary CO_2 miscible flooding. On top of that, CAT scanning was demonstrated to be a powerful tool for quantifying the behaviour of multiphase flow in porous media at reservoir temperatures and pressures. Vinegar (1986) gives the first comparative description of CAT scanning and NMRI. He presents some examples of core analysis and multiphase flow testing using both x-ray CAT and NMRI to demonstrate the capabilities of each method. He states that the two techniques can be used in complementary fashion to achieve a better understanding of primary and supplementary oil recovery processes. Vinegar and Wellington (1987) present the theory behind the application of CAT in reservoir engineering. They discuss the equations for phase saturation and the dependance of the linear attenuation coefficient on density and effective atomic number. They suggest optimum energy settings and choice of dopants. Moreover, they provide suggestions for the

© 1990 NOVA HUSKY RESEARCH CORPORATION

design of high pressure core holders and testing of different alloys useful in an x-ray environment. They also provide some measurements of the intensity of x-rays (KeV mean) before and after filtration. Wellington and Vinegar (1987) also show the fundamental equations for use of CAT scanning in porous media research and then proceed to show examples for applications of the novel technology. These examples are:

1) CT measurements of compressibility and compaction;
2) CT scans of core materials;
3) CT correlation of core with well logs; and
4) Multiphase core studies.

The use of CAT scanning techniques for the determination of fluid saturations when measuring relative permeabilities to steam and water at residual oil in natural cores is described in Closmann and Vinegar (1988). The authors conclude that CAT scanning is a viable technique for measuring fluid saturation changes from known initial conditions.

The work of the Belaire researchers provides a comprehensive guide for any new industrial CAT scanner facility. However, there is a large amount of other research work showing the value of CAT scanners in the non-destructive testing of reservoir rocks.

Wang *et al.* (1984a), were the first to publish on the use of Computer Assisted Tomography for the observation of oil displacement in porous media. They used a second generation Deltascan-50 CAT scanner and presented evidence of the saturation distribution across a cross section of Berea sandstone during two phase flow experiments. Wang *et al.* (1984b) discuss the reconstruction of oil saturation distribution histories during immiscible liquid-liquid displacement by the use of CAT scanners. Wang (1985) provides images of viscous fingering, time derivatives of local composition, and residual oil distribution for the case of waterflooding. Cromwell *et al.* (1984) discussed the use of CAT scanners for observing multiphase flow phenomena in porous media. They used Danian chalk and Berea sandstone cores. They used a first generation system and associated software. Water and an organically bound iodine solution were used as the fluids. Honarpour *et al.* (1985) used a fourth generation Picker SD600 for reservoir rock description. They demonstrated rock fabric heterogeneities, macroscopic permeability barriers and fracture system orientations using a North Sea Danian chalk core and a Wyoming Phosphoria Formation core. Their operating conditions were 130kVp at 100mA. Bergosh *et al.* (1985) applied CAT scan testing techniques in the core analysis of naturally fractured reservoirs such as the Monterey Formation. They concluded that CAT scanning is very helpful in analyzing fractured cores before removal from

© 1990 NOVA HUSKY RESEARCH CORPORATION

the inner core barrel liner by characterizing fracture width, spacing, tortuosity, interconnectedness and drilling mud invasion. Hunt *et al.* (1985, 1987) used the scanner to visualize laboratory corefloods. Both immiscible and miscible displacement tests were performed. Fingering and dispersion effects were observed. The testing was done using North Sea sandstones. Oak and Ehrlich (1985) used x-ray absorption methods for the measurement of three phase relative permeability using dual tracers in a fashion very similar to the CAT scan work. Gupta, (1986) discusses the use of CAT scanners as analytical tools in oil recovery. He states that the spatial resolution of an industrial CAT scanner designed for high resolution applications is adequate to resolve mineral distribution within a core.

Fransham and Jelen (1986) used a second generation EMI CT5005 full body scanner to visualize the displacement of heavy oil during a waterflood. They have developed a method to determine saturation changes during the course of a waterflood. Their analysis of CATscan images along a core indicated two scales of fingering. One at a pixel level and one at a zone level. Honarpour *et al.* (1986) used the CATscanner in core characterization studies, using as an example a dolomite sample from the Upper Madison Group. They have used a fourth generation General Electric Scanner at 145kVp and 175mA at successive increments of $3x10^{-3}$m. They were able to identify specific mineral densities and their distribution within the fracture system. Application of CATscan for mineral identification requires both density calibration and contrast. Moreover, verification by other methods was considered necessary by the authors. With respect to fracture infilling CAT scanning indicated that the infilling is variably distributed throughout the fracture. It is often characterized by having variable density and therefore multiple types of mineralization. The fracture may include dolomite, calcite, quartz, anhydrite, gypsum, illite and/or chlorite mineral assemblages. Bergosh and Lord (1987) also used the CAT scanner for the analysis of naturally fractured reservoirs. They found that fracture porosity is very easily determined by the use of CAT scanning. Hunt *et al.* (1986) presented a first comprehensive analysis of the applications and artifact reduction techniques in Computer Assisted Tomography. They conclude that qualitative core analyses can be done quickly and with little or no preparation using CAT. Some of the applications are;

- detection of the extent of drilling mud invasion,
- fracture detection,
- characterization of preserved core,
- screening of core prior to laboratory flow work,
- porosity, mineralogy (also quantitative) and permeability.

© 1990 NOVA HUSKY RESEARCH CORPORATION

Second, third and fourth generation CAT scanners are the most readily available for core work. The effect of image beam hardening can be reduced by surrounding the core with sand or an aqueous KI solution. Sedgwick and Miles Dixon (1987) demonstrated the superiority of CATscan as opposed to x-ray cameras and Xeroradiography in oil sand experiments. Withjack (1987, 1988) describes the use of CAT scanners for the determination of rock properties and the visualization of fluid flow using a General Electric CT9800. He demonstrated linear x-ray attenuation for Berea sandstone and fine-grained dolomite with aqueous concentrations of NaI used in CT coreflood procedures. Beam hardening due to the high concentration of some dopant solutions did not seem to influence significantly the attenuation in the saturated rock samples. The results of the water oil relative permeability studies using CAT scanners were comparable to the conventional methods. The saturation accuracy was greater than 2%. Average porosities were within 1% of other conventional methods. Viscous fingering was observed in miscible floods in Berea sandstone. Manjnath (1988) studied the Buckley - Leverett theory using CT.

Kantzas (1988) and Kantzas *et al.* (1988) presented a first attempt to modify the hardware on a medical CAT scanner aimed at bringing the machine closer to the needs for a core analysis tool. They modified an EMI CT5005 to conduct experiments in long cores positioned at any angle from the horizontal. Kantzas (1988) and Chatzis *et al.* (1988) used the modified CAT scanner to study the physical properties of porous rocks and saturation profiles during two and three phase flow in gravity assisted displacement processes. They were very successful in two phase flow systems. In three phase flow however, the visualizations were only qualitative. Even so, Buckley-Leverett type of profiles were observed. Kantzas (1989) also worked in the modification of the CT5005 to enhance its voltage range and minimize the x-ray thickness. Withjack and Akervoll (1988) used the G.E. CT9800 to study miscible displacement behaviour in 3-D using a 5-spot scaled laboratory model. The 3-D image reconstructions showed the qualitative features of a displacement in an easily interpreted format. Mohanty and Miller (1988) studied the factors that influence unsteady relative permeabilities of a mixed-wet reservoir rock using the CAT scanner. Narayanan and Deans (1988) used a fourth generation Deltascan 2020HR to validate a model for heterogeneous porous media. They visualized flow during high pressure miscible displacement experiments in highly vugular carbonate rock samples. Cuthiell and Sedgwick (1988) applied the CAT scanner to heavy oil corefloods. They discussed a number of experiments including two-phase bitumen/water experiments, steamfloods and foam-based mobility control studies. Wellington and Vinegar (1988) studied the surfactant induced mobility control for carbon dioxide using CAT scanners. The CT images identified several mechanisms that help to explain how mobility control surfactant causes CO_2 to be stable against both gravity and viscous forces during tertiary miscible core flood experiments.

© 1990 NOVA HUSKY RESEARCH CORPORATION

Vinegar *et al.* (1988) discussed the applications of NMRI in core analysis. They have designed a new piece of equipment which is oriented directly to industrial applications, and presented results of core analysis. Earlier Rothwell and Vinegar(1985) had discussed the potential petrographic applications of NMRI.

Ringen and Hove (1987) used three different types of CAT scanners (GE 9800, Philips Tomoscan 310 and Siemens Somatron DR1) to perform core analysis. They studied water imbibition in a dry homogeneous reservoir rock. The visualization study showed a slightly dispersed front, strong end-effects and even distribution of residual gas saturation after breakthrough. A similar test was performed on a composite sample. Strong end effects were also seen as the front passed the boundary between the two plugs. The boundary effect between butted samples is not always the case, as shown in a series of images of oil being displaced by water in a sample composed of two reservoir rock plugs. The effect of reservoir rock sample heterogeneity is demonstrated in two visualization series, gas being displaced by water in a sample with shale barriers and oil being displaced by water in a bioturbated sample. It was shown that the heterogeneity strongly affects the displacement process. Finally, one miscible and one drainage test were compared. The authors found that the main limitations of hospital scanners are filtrations and matrix arithmetics in the image analysis systems. Also the scanner systems set limits to sample size and cell-materials.

Savoie (1988) presented a x-radiographic technique for visualization of heavy oil native cores before any slabbing. He can achieve excellent resolution, but his technique cannot be used for digitization or core analysis of the results due to lack of the proper computer accessories.

Lewis *et al.* (1988) combined a second generation CAT scanner with a multi-electrode resistivity measurement apparatus to study the electrical properties of Berea sandstone cores. The CAT scanner was used for the monitoring of water saturation profiles. The saturation data were combined with four-electrode resistivities to calculate the saturation exponent. Berea sandstone was used as the porous medium. Some cores were used as they were and some other ones were treated with Quilon C, and became oilwet. The CAT scanner showed that the capillary boundary effect is prominent at the outlet end of the core particularly at the final 0.005m before the outlet. The capillary effects were more troublesome during drainage cycles of saturation for both water-wet and oil-wet cores.

© 1990 NOVA HUSKY RESEARCH CORPORATION

Cuthiell and Sedgwick (1988), described a number of applications of X-ray CAT scanning in core flooding of heavy oil reservoir cores. They studied two/phase bitumen/water displacements, steam displacements and foam displacements. Saturation profiles and fingering phenomena were monitored.

Gilliland and Coles (1989) used the CAT scanner to study the damage of unconsolidated cores with reference to the determination of slabbing angle, undamaged sites for future plug and whole core analysis, sample heterogeneity and depositional features. On top of the above core inspection parameters they proceeded in an analysis of different types of core damage and proceeded into speculating about causes of core damage using the CAT scanner as a damage assessment tool.

Sobrie et al. (1989) have presented a tomographic confirmation of flow mechanisms of miscible displacements in heterogeneous core systems. Stratified cores of 0.12m in length were mounted in core holders with aluminum end caps. The CAT scanner was a Siemens Somatom model DRH. A 23% solution of NaCl was displaced by a 23% solution of NaI, which results in a near unity mobility displacement. There is a sharp arrival of the tracer front in the high permeability layer which rises steeply initially and then shows a rounded "shoulder" due to the effects of transverse dispersion of the low permeability layer. The covected front in low permeability arrives later, but ultimately the normalized concentration rises to unity. In a stable viscous displacement, 17 mPas of glycerol was used. In another test 23% NaI was displaced by 10 mPas glycerol. The main effect was that the breakthrough profiles for the high and low permeability layers are brought much closer than has previously been experienced. Perhaps the most powerful single feature of tomography in applying it to stratified systems of this type is that it is able to distinguish genuine flow mechanisms, such as the cross flow effects, from minor artifacts such as the small distortion of the unit mobility front due to minor heterogeneities in the high permeability layer.

Chatzis et al. (1990) discussed their CAT scanner research using a modified EMI CT5005. They have performed a number of tasks including; i) Visualization of flow of heavy oil during gravity drainage conditions, ii) Visualization of fractures in an unconsolidated column, iii) Study of pore structure in vuggy carbonate systems, iv) Study and visualization of finger growth and/or dispersion effects during miscible displacements in glass bead columns and sandstone cores.

2.3.3 Other Industrial Applications

Hangartner and Overton (1982) presented a special purpose isotope CAT scanner for the quantitative measurement of bone density. This translate rotate, second generation machine

© 1990 NOVA HUSKY RESEARCH CORPORATION

employs a ^{125}I "point" photon source and photomultipliers with NaI(Tl) crystals $12.7x10^{-3}$ m thick as detectors. The amplified and energy selected signals are routed to Camac scalers and thence to the computer. The stepping motors for rotation, translation and arm-holder movement are controlled by a M6800 microprocessor. All necessary parameters are loaded from the host computer to the microprocessor through the Camac system. The host computer is a VAX11/750. K_2HPO_4 solutions were used for calibrations. This method is similar to the method of Bone Mineral Content (BMC) by Dual Photon Absorptiometry (DPA) which is a method of scanning the area of interest with a dual photon source and synchronously measuring the attenuated energies from the source (Novo Diagnostic Systems).

Allan *et al.* (1985) presented an overview of the Atomic Energy Canada Limited (AECL) program in CAT scanning. The researchers at AECL have built a first generation translate - rotate test assembly. Test objects are mounted on a turntable that is translated past a collimated beam of radiation. The sources used were a 74-GBq (2Ci) ^{137}Cs source (E = 662 keV) or a 444-GBq (12Ci) ^{60}Co source (E = 1250 keV). Their tests proved that the industrial CAT scanners can be most useful for; i) distinguishing features within complex geometries where other NDT techniques fail because of the complexity of the geometry; ii) detecting small density changes within objects, e.g., void fraction measurements within thick walled vessels and shrink cavities in castings; iii) providing quantitative data that can be used in analyses, e.g., of complex processes or fracture mechanics; iv) providing objective quantitative data that can be used for computer based quality assurance decisions, thereby reducing and in some cases eliminating the present subjectivity often encountered in nondestructive testing.

Abrams and Vinegar (1985) studied the flow of nitrogen and brine in tight Vicksburg "P" Sand cores. The study was performed under field stress conditions. Brine saturations were imaged with a medical CAT scanner. Their laboratory results suggest that water block is not important when drawdown pressures at the fracture face exceed the capillary entry pressure by several thousand kPa. The addition of alcohol / surfactant package to the brine does not significantly increase final gas flow. For the flow studies, the brine was doped with 8% KI. The scanner used was a Deltascan 100 translate rotate head scanner with a tungsten target x-ray tube and three bismuth germanate scintillation detectors.

Spiro *et al.* (1987) studied the bacterial removal of pyritic sulphur from in situ deposits of coal. A CAT scanner was used to follow the dissolution of pyrite inclusions. The scanner used was a GE 9800 scanner. It is of interest to observe that the x-rays were used in conjunction with bacterial action.

© 1990 NOVA HUSKY RESEARCH CORPORATION

Brown (1987) used a GE 9800 CT scanner and a 63.8 MHz, 1.5 T GE medical imager to study water distribution in plants and soils. The experiments included the determination of water holding characteristics of a rigid porous phenolic foam substrate as well as its ability to maintain a constant bulk density during irrigation. Other experiments dealt with the measurement of the water content in porous foam media, the imaging and analysis of the spatial distribution of water in the plant root zone and the nondestructive observation of changes in water content of a split root system.

Johns (1987) discussed the use of a modified GE 9800 CAT scanner for the inspection of engine parts. The CAT scanner is also equipped with a Scoutview, or digital radiography mode of operation. He also compared CAT scanning to Ultrasonic Testing (UT). UT works well in detecting a single, thin, laminar interface parallel to the inspection surface, but it is difficult to apply and interpret on objects with strongly curved external surfaces, while highly reflective subsurface boundaries can hide deeper structures.

Feldcamp (1988) presented a brief description of the use of CAT scanning for gauging of automotive parts. The Ford microscanner is compared with the Exxon synchrotron scanner. Both machines have resolution in the range of a few microns.

Van den Bergen and Jonkers (1988) studied industrial applications of positron emission computerized tomography by performing two experiments; i) the demulsification of a water in oil emulsion, and ii) the displacement of fluid in a core. The technique had a limited performance but it could be used for visualization purposes.

Miller (1988) presented a prototype portable CAT scanner for the inspection of wooden utility poles to determine the extent of internal voiding due to decay or rot. The device weigh 24 kg, is battery powered and fits into two small suitcases. A typical scan provides a low resolution (0.01m) image of an object of 0.30m in diameter with a density of 650 kg/m^3 in eight minutes of imaging and data reconstruction time. The resulting image is displayed in the field on the system's portable computer system. The radiation source is ^{241}Am with a primary x-ray energy of 60 keV. A CdTe semiconductor detector from Radiation Monitoring Devices, Inc was chosen for this application. A Toshiba T1100-Plus personal computer is being used as the main computer for this system, with the software written in BASIC. A Z-8, single board computer is used to control the scanner hardware. The source and detector are moved around the ring using Superior Electric

© 1990 NOVA HUSKY RESEARCH CORPORATION

#MO61-FF-6201B stepper motors. A filtered back-projection technique is used for the reconstruction.

Potet *et al.* (1988) compared computerized vibrothermography and computerized x-ray tomography for the detection and characterization of impact damage in composite materials.

Cannon (1988) gave a short overview of the industrial CAT scanning programs in aerospace and defence industry.

Lien *et al.* (1988) presented a nuclear tomographic technique for the study of multiphase flow in a porous medium at reservoir conditions. They have constructed a long core rig, which operates at reservoir conditions. They used nuclear tracers and detected the emitted γ radiation by a movable germanium detector. The core holder was constructed of reinforced materials. They demonstrated their technique by performing a primary drainage experiment.

Hummel and Wesser (1988) used CAT scanners to evaluate flow patterns in two phase flow by measuring local density noise and tried to display the relevant parameters in the time and frequency domains. Their prototype scanner consists of an x-ray source and six detectors that rotate 360°. They demonstrate that the process is possible.

Miyanishi *et al.* (1988) presented the computerized tomography of a paper roll. They were interested to see the effects of homogeneity of roll compaction and tightness on the quality of a paper roll. They used a Toshiba high resolution , x-ray industrial CAT scanner with an emission energy capacity of 140 kV, a 300 mA x-ray tube and a 512-channel, xenon gas detector. The images were reconstructed in arrays of 320x320 pixels. They found that the average CT value of paper sheets was proportional to sheet density. However, linearity between the CT value and sheet density was not as good with roll samples as it was with sheets showing an effect of the winding tension.

Chu and Sawicka (1988) used γ ray CAT scanning to characterize the internal anomalies of solid insulators in gas insulated equipment. The images of filled epoxy spacers were measured using a first generation, translate-rotate, high resolution (4×10^{-4}m) scanner. The sources used were ^{192}Ir (average energy 460 keV) and ^{60}Co (average energy 1.2 MeV).

Tollner and Verma (1989) used an EMI 5005 scanner to predict imbibition and drainage in a sand media. They developed calibration equations based on the water content at the end of their six

© 1990 NOVA HUSKY RESEARCH CORPORATION

day study, and these equations successfully predicted initial water content. A NOVA analysis was performed on the results to identify potential causes of error. They concluded that Scan artifacts are probably the most serious cause of error.

Kanamori *et al.* (1989) presented a prototype high energy (12 MeV) x-ray CAT scanner by using a linear accelerator. As a demonstration test slits of 2 x 10^{-3}m width inside a 0.25m diameter iron object were imaged.

Sawicka and Palmer (1989) reported the recent work on γ ray CAT scanning in the Chalk River Nuclear Laboratories. The first generation scanner equipped with ^{60}Co and ^{192}Ir was used in testing of potential applications of CAT scanning to ceramic processing and materials development. The examples sited describe the measurement of density gradients in green and signeted parts, determination of the density and distribution of second phases, identification of cracks and voids and evaluation of structural details in composites and complex assemblies. The samples were; one unsintered, biaxially-pressed alumina pellet; biaxially-pressed urania pellets; light ceramic boards formed of fibers and inorganic binders; a small piece of ceramic foam; signeted zirconia/alumina composite pellets; two defective ceramic rotors (a silicon carbide one and a silicon nitride one); one gold rich mineral sample; a damaged nuclear fuel bundle; zirconia pellets with infiltrated alumina; a monolithic oxide fuel cell constructed of a stack of cross-oriented, corrugated ceramic layers; ceramic tool bits made of alumina reinforced with silicon carbide whiskers; and polymer matrix composites containing ceramic particles, such as composite electrical insulators. The Atomic Energy of Canada scanner is very slow but it resolution is excellent (down to 1 x 10^{-4}m). Also the γ ray beam is almost monochromatic and this improves the contrast and eliminates artifacts.

Fryar and McCarthy (1989) have presented an experimental and theoretical study for the imaging of several atomic elements in a single CT scan using a tube source of x-rays. They considered the total transmission of x-ray photons through a cylindrical matrix and developed an equation by which minimum analyte concentrations, within the matrix, can be determined. The parameters used in this equation are easily obtained from published data or they are easily determined functions of the apparatus. Several elements can be detected in a single scan.

Phogat and Aylmore (1989) used γ ray CAT scanning as a method for the direct measurement of the spatial distribution of soil macroporosity and for monitoring changes which occur during wetting and drying processes. They used a ^{137}Cs source and a single detector with a resolution of

© 1990 NOVA HUSKY RESEARCH CORPORATION

0.002 x 0.002 x 0.002m. Surface soil samples were collected and the bulk densities measured were in the range of 1,141 - 1,516 kg/m^3.

Norman and Crose (1989) investigated the integration of quantitative x-ray CAT scanning with finite element analysis to develop a quantitative non-destructive evaluation technique. Software was developed which links data from CAT systems to their finite element model (ROSAAS). Failure predictions were made based on anomaly distribution and variable material properties. The correlation was excellent with specimens containing severe anomalies. Specimens with minor anomalies did not correlate well.

Anderson and Gantzer (1989) used both CAT scanning and NMR imaging for the determination of soil water content. Soil cores of Mexico silty loam and Crider silty clay were used. The bulk densities tested varied from 1200 kg/m^3 to 1600 kg/cm^3. Although they were very successful with the CAT scanner, they had problems with the NMR Imager. They used a Philips Tomoscan 310 (third generation scanner rotate/rotate type with 576 xenon detectors and 120 kV peak energy) and a Technicare Teslacon MRI scanner (25.5 MHz, 0.6 T). Cu solutions were used to enhance the NMR images.

Mossotti and Castanier (1989) used an EMI CT5005 to dynamically monitor the transport of water through the interior of Salem Limestone test briquettes. The study was aiming in understanding the incremental dose-response function of limestone and marble to acid rain. It was found that water transport in limestone during drying is controlled by capillarity. The only other significant parameter is the presence of wind.

Warner *et al.* (1989) scanned cross sections of a 0.203m soil core taken from a site under Kentucky bluegrass to determine if macropores such as cracks, earthworm holes and root channels could be distinguished and characterized. The images were compared to physical sections. A wet bulk density and an air-filled macroporosity were calculated for scans. The scanner was a Siemens Somatom DR3/F2 with a voltage set to 125 peak kV 700 mA and 14-s scan time. Pixel size was 5.36 x 10^{-4}m by 5.36 x 10^{-4}m and slice thickness that was 0.002m or 0.008m. The authors determine that the practical spatial resolution of the scanner is twice the predicted value because of boundary effects.

Cesareo (1989) presented a first generation CAT-miniscanner which is characterized by monoenergetic scanning radiation both from an X-ray tube with secondary targets and from radioactive sources (10 - 120 keV), a single NaI(Tl) detector and a PC Apple IIE with a

© 1990 NOVA HUSKY RESEARCH CORPORATION

reconstruction program working in Pascal. The use of energy dispersive photon detectors with multienergy gamma sources offers the possibility of being able to record images at a number of energies simultaneously. In some cases, in which the presence of a given element is to be enhanced, a pair of x- or γ-rays can be used, whose energy brackets the energy of the photoelectric discontinuity of the element.

Vinegar *et al.* (1989) patented a novel apparatus for the analysis of failure of materials using a CAT scanner or a NMRI. A uniaxial special core holder is used and the x-ray or magnetic field data can be analyzed to provide information such as; bulk compressibility, Poisson's ratio, Young's modulus, Lame parameters.

2.3.4 Samples of Theoretical Work on Computer Assisted Tomography

Goodennough *et al.* (1975) presented some potential flaws in the original EMI head scanner reconstruction algorithm. These possible artifacts would result in missing parts of the head in the imaging process. It is not known whether these type of artifacts were eliminated in the more recent versions of the EMI software, but from our experience it seems that it has been corrected.

Alvarez and Macovski (1976) presented the theory of a technique for obtaining essentially complete energy dependent information in a computerized tomography system, by making simple, low resolution energy spectrum measurements. They use a model that includes the effect of Compton Scattering and Photoelectric absorption for each pixel. The effects are tied together through some constants. The image reconstruction is then deduced to the reconstruction of the coefficient maps given a set energy. Their methodology is very interesting and it is very similar to the technique used for the effective atomic number determination from the CT number data.

Snyder and Cox (1977) presented an overview of the mathematical foundations of reconstructive tomography. They focused on the problem of relating the number of angular views to other parameters in the design of the reconstruction procedure. Their analytical findings support the argument that the number of angular views and the number of transverse measurements should be in a ratio of about $\pi/2$.

Christ (1984) outlined a procedure for treatment of dual energy polyenergetic spectra that takes into account the changes of the two x-ray spectra through the absorber. Thus it is possible to determine the absolute values of the linear attenuation coefficient of two polychromatic spectra and to calculate the exact values of the effective atomic number (Z_{eff}) and the electron density (D).

© 1990 NOVA HUSKY RESEARCH CORPORATION

This is achieved by an iteration procedure in which preliminary values of Z_{eff} and D resulting from a dual energy measurement are used to compute the linear attenuation coefficient for the given absorber. From the comparison with their measured values an iterative correction is derived which leads to a convergent result for Z_{eff} and D. This procedure requires the knowledge of the spectra of the incident radiation.

Chen *et al.* (1984) discussed a software package for three dimensional display from Computer Tomograms. The software package was designed for the G.E. 8800 CT scanner.

Heffeman and Robb (1985) discussed the use of filtered back projection to reconstruct only the defects in objects where the ideal (unflawed) object is known. This technique is of potential importance when limited views are available.

Kalender *et al.* (1986) presented phantom studies for the evaluation of a prototype dual energy implementation using rapid kVp switching on a Siemens Somatom DR3. The rapid kVp switching allows simultaneous dual energy data acquisition in a single scan.

Collick *et al.* (1987) presented a new K-edge filtered x-ray scanning system for dual-photon absorptiometry.

Herman (1988) proposed that three dimensional imaging on a CAT or NMRI scanner has a very low cost per patient, when used appropriately. He also discusses a 3-D imaging strategy for the GE CT 9800 scanner.

Lewis (1988) presented a list of representative publications for image reconstruction that have appeared since 1980, which provide introductions to both the mathematical foundations of CAT scanning and to the research literature on image reconstruction from projections.

Levoy (1988) showed how to use the so called direct volume visualization for the presentation of three dimensional CAT scanner data. He also discussed the problems associated with this technique.

Tonner and Taylor (1989) patented a method of region of interest tomography which employs a differential scanning technique. With this technique, only the region of interest is scanned, i.e. it is not necessary to scan the whole sample. Reference data for the region of interest of a complete reference object that is a relatively good match to the sample outside the region of interest and

© 1990 NOVA HUSKY RESEARCH CORPORATION

has a known attenuation distribution inside the region of interest is first obtained. This can be done by scanning only the region of interest of an actual complete reference object or by constructing a digital image of the reference object and mathematically scanning only the region of interest of the image. A differential image is reconstructed from the differential data. The authors claim that the proposed method is simpler, more compact and less costly that conventional CAT equipment. From the claims of the patent it is clear that this technique could be useful in eliminating artifacts due to sample holders and other features outside the scanned sample. However, the proposed method does not offer any increased resolution.

Vontz *et al.* (1989) proposed methods for the theoretical determination for small defects in different materials that can be scanned given a CAT scanner and the interdependent contrast and spatial resolutions. The tradeoff between these two factors was discussed. It was also shown how to estimate the smallest detectable flaw sizes for a given material, and how to enhance the quality of a tomogram with respect to resolution, noise, flaw detection and artifacts. The method was developed on the Delta Scan 50, with regard to NDT of technical materials and parts (ceramics, light metals, polymers, composites). The work was continued with a high resolution system using a FEINFOCUS microfocus x-ray tube and a THOMSON image intensifier (normally used in microradiography).

2.4 NMR Imaging

2.4.1 Petroleum Engineering Applications

Rothwell and Vinegar (1985) presented petrophysical applications of NMRI. They used a prototype built by Bruker Instruments. This system is based on a CXP-200 spectrometer console utilizing a 0.84 T electromagnet. Gradients of 1.4 kHz/mm can be produced in all three orthogonal directions to generate the projections. Rock data collection for a typical cross section took appr. 5 min. The cross-sectional image reconstruction was performed in a dedicated Aspect 2000A minicomputer interfaced to the NMR imager. Carr-Purcell type pulse sequences were applied. These first presented results show images of Berea Sandstone with porosity variations and Lion Mountain Sandstone with a sand/shale transition.

Blackband *et al.* (1986) used Nuclear Magnetic Resonance Imaging techniques to study the mobile proton content in prepared samples containing mixtures of crude oil, water and sand. The samples were 0.05m in diameter and the measurements were made with proton resonances at 30MHz and a steady state, free precession technique for the imaging process. They got an

© 1990 NOVA HUSKY RESEARCH CORPORATION

estimation of the fraction of water and heavy crude oil in a prepared sand/water/oil sample. The method is still under development.

Baldwin and Yamanashi (1988) presented a NMRI study of fluid dynamics in reservoir core. They have modified a medical NMR Imager to image water and oil in reservoir rocks by the construction of a new receiving coil. Both oil and water inside the core produced detectable proton NMR signals, while the rock matrix produced no signal. Because of similar T_2 NMR relaxation times, the water was doped with a paramagnetic ion, Mn^{+2}, to reduce its relaxation time. Flood fronts in Berea Sandstone were readily observed. Saturation measurements closely approximated the results of Dean-Stark extraction. The modified equipment was a Picker International Model MR VISTA 2055. They found that the water phase is generally easier to dope because ionic paramagnetic ions are readily soluble in it yet insoluble in the oil phase. In a water-wet Berea Sandstone core the waterfront was generally sharp, however, the images suggested that in some areas oil may be bypassed and isolated behind the water front. In a treated, partially oil-wet, Berea Sandstone core the water took a path which appeared to leave oil behind in the center of the core.

Chen *et al.* (1988) used NMRI to study oil and water invasion in a model porous medium. The residual oil saturation state was studied. The porous medium was unconsolidated crushed Pyrex particles. The fluids were an aqueous solution of 0.04477 kg of $NiSO_4*6H_2O$ per 10^{-3}m of deionized water and Soltrol 100. Drainage and imbibition experiments were performed at conditions controlled by capillarity and gravity only. The proton NMR images were obtained at 1.9 T in a 0.31m bore Oxford superconducting magnet.

Edelstein *et al.* (1988) have adapted a 2 Tesla, 0.305m horizontal bore NMR system for imaging / spectroscopy of oil cores. Strong and fast shielded gradients (up to 0.18 G/m with a settling time of less than a few hundred microseconds have been developed to produce good quality images of cores with very short relaxation times. Accurate and rapid spectroscopic porosity measurements have been made on carbonate and sandstone whole cores, including some shaly samples. Porosity images have been made of carbonates and clean sandstones. Oil/water saturation has been determined spectroscopically in carbonates and clean sandstones, and selective water and oil images have been produced. Other NMR nuclei, such as ^{2}H (deuterium), ^{13}C, ^{19}F and ^{23}Na can be used for a variety of oil core applications. In particular, they have produced ^{13}C spectra of oil in many different rocks; these spectra can potentially determine oil saturation in shaly materials where the proton NMR lines of oil and water overlap. The porosity of water filled cores can in principle be determined in the laboratory by a measurement of the proton signal strength of the

© 1990 NOVA HUSKY RESEARCH CORPORATION

sample at time zero compared to the proton signal of a known standard. One way to do this measurement is to first Fourier transform the time domain NMR data and then integrate the area under the corresponding spectral line. This approach allows a separate determination of oil and water saturation in rocks with narrow spectral lines. Core samples of known porosity and $H_2O/D_2O/CuSO_4$ aragose gels were used as standards. One way to get porosity images is to produce multiple echo images and then project back to t=0 to obtain the total spin density. The saturation images can be produced by using a narrow frequency RF excitation pulse to selectively excite either the water or the oil protons to produce water or oil images respectively. In a different approach, the use of an inversion recovery pulse sequence takes advantage of different T_1 relaxation times for the protons in the oil and water phases. An inversion pulse is applied followed by a time delay so that the signal from the faster relaxing species decays to zero net longitudinal spin. A 90° observe pulse is then applied and only signal from the more slowly relaxing phase appears.

Vinegar and Tutunjian (1988) patented a method for the determination of multiphase saturations by NMR Imaging of Multiple nuclides. The patent explains how to use various nuclear radio frequency signals to monitor fluid saturations. Materials for core holders and custom made coils for this type of application are also explained.

Vinegar *et al.* (1989) presented a whole core NMR system. The system enables rapid nondestructive measurements of bulk volume of movable oil, aliphatic/aromatic ratio, oil viscosity, and organic versus carbonate carbon. A 0.133m $^{13}C/^{1}H$ NMR coil has been installed on a General Electric CSI-2T NMR imager / spectrometer. With a 0.10m OD whole core, good ^{13}C signal to oil ratio is obtained within minutes, while ^{1}H spectra are obtained in seconds. The oil viscosity predictions were accurate for viscosities up to 100 mPa.s. ^{13}C NMR measures only the movable hydrocarbon content of the cores. In carbonates, the ^{13}C spectrum also contains a carbonate powder pattern useful in quantifying inorganic carbon. ^{13}C NMR can be used in cores where the ^{1}H NMR spectrum is too broad to separately resolve oil and water resonances. It should be noted that kerogen is not detected by ^{13}C NMR, but it should be measured using solid-state NMR methods such as cross polarization / magic angle spinning.

Doughty and Maerefat (1989) have modified a Fourier transform, multinuclear, magnetic resonance spectrometer into a NMRI for use in core analysis studies. They started with a JEOL GX-270, 270MHz spectrometer. The design changes mainly involved the construction of an X-, Y-, Z-gradient coil / RF probe assembly and a gradient control board. The new equipment has a much stronger magnetic field (6.34 Tesla) and higher operating frequency (270 MHz for protons). As a

© 1990 NOVA HUSKY RESEARCH CORPORATION

result it potentially provides increased sensitivity and resolution over that of medical NMRI machines. Their first results indicate the high frequencies may not be the best for petrophysical applications of NMRI. The authors are currently working on changing the operating frequency to 60MHz and to include multislice imaging capability.

Larmous *et al.* (1989) showed that the medical NMRI Bruker BMT 100 scanner can be used for the determination of local and overall porosities. They also used the scanner to study the clogging of a column of glass beads by a suspension of microparticles. The NMRI predicted porosities are 2% lower than the porosities which were calculated theoretically. The imaging of the clogging process showed in homogeneity of pore clogging with more clogging at the upper part of the porous medium.

Dereppe and Schenker (1990) used a BIOSPEC BMT 47/30 NMR equipped with a B-G 15/A gradient system to study the oil/water displacement in limestone. When H_2O and oil were used, Chemical shift tests were necessary to be done in order to separate the phases. However, when D_2O was used the contrast of the phases was very clear without any need for chemical shift.

A potential use of the NMR imager would be to map the permeability of a core. Some initial work of predicting core permeability using NMR spectroscopy comes from the well logging tools. A few relatively accurate tests are given in Kenyon *et al.* (1986) and Banavar and Schwartz (1987).

2.4.2 Other Industrial Applications

Samoilenko *et al.* (1987) applied NMRI to the study of the structure of objects containing ^1H nuclei. They used a modified Bruker CXP-200T proton NMR spectrometer. The time taken to obtain images with 64x64 resolution elements was about 2400 s. They provided images of a polyethylene gear wheel, a tree branch, a hyposulphide crystal and a poly(methyl methacrylate) block with one polypropylene and two polyurethane pieces inserted into it. Different types of nonuniformities were observed. Moreover, they studied the diffusion of acetone into a poly(methyl methacrylate) block at room temperature.

Mareci *et al.* (1988) performed an NMR imaging and relaxation study of polymer swelling and fluid dynamics. They used a GE CSI-2 imager/spectrometer at 23°C. They studied the swelling process of poly(methyl methacrylate) in chloroform and the dynamics of the swollen polymer chain. They have shown that the swelling process occurs in a way similar to surface melting, through a kind of first-order phase transition which generates a layer of mobile polymer chains around the solid,

© 1990 NOVA HUSKY RESEARCH CORPORATION

without divergent behaviour of the spin-lattice relaxation rate. Insights into the dynamics of the polymer chains in the region being swollen is provided by local T_1 measurements.

Gaigalas *et al.* (1988) used a 0.15 T resistive magnet whole-body imaging system to visualize flow in porous media with applications in nuclear wastes management. They monitored flow of water with and without paramagnetic dopants in alpha alumina, purified bentonite and kaolin.

Nieminen and Koenig (1988) used NMRI to study the nature of the adhesive bond formed by using a water based poly(vinyl acetate) (PVAC) adhesive to glue together Finnish pine wood blocks. They used a Bruker MSL-300 FT-NMR spectrometer with a mini-imaging accessory. The spatial resolution of the NMR image at 300 MHz is $< 1 \times 10^{-4}$m As the drying occurred, voids were observed to form in the adhesive layer as a consequence of the loss of water and the shrinkage of the adhesive. Their results indicated that NMRI will find many applications in adhesive studies, since one can view the action of the adhesive system in the form of images which are easily interpreted.

Briguet (1988) presented a general review of the use of NMRI to study liquids and solids with a few examples.

Miller and Garroway (1988) discussed the problem of NMRI of solids. They stated that the standard NMRI techniques would not work for the general case of NMRI of solids. They focused on the description of ^{1}H NMRI of solid organic materials where the dominant line-broadening mechanism is the homonuclear magnetic dipole-dipole interaction. They proposed as an improvement the use of surface coils.

Assink *et al.* (1988) used a Nalorac imager/spectrometer with a 1.89 T Oxford magnet to study density profiles of a draining foam by NMRI. They proved the feasibility of the process but fell short of clarifying the various problems in this preliminary work.

Runge *et al.* (1988) presented a computer optimized radio-frequency (RF) pulse for sharper section definition. This improvement was tested on a Siemens 1.0 T Magnetom and resulted in improved tissue contrast.

Chang *et al.* (1989) used a Siemens 0.5 T Magnetom whole body medical imager NMRI to image the internal features of wood. Two white oak logs and one black cherry log were examined. As a result of inherent moisture variations associated with various characteristics of the log, clear

© 1990 NOVA HUSKY RESEARCH CORPORATION

images were obtained to reveal not only normal features such as sapwood - heartwood, earlywood - latewood, and wood rays but also defects as varied as reaction wood, wetwood, gum spots and knots.

Clough and Koenig (1989) used the same NMRI machine as above to study the swelling of polybutadiene rubber in 1,4-dioxane. They observed a nonuniformity of the signal intensities and T_2 relaxation times through the sample, which indicates that the rubber is spatially heterogeneous. This heterogeneity may have several sources. For example, poor mixing of the sulphur and polybutadiene or large thermal gradients during mixing or molding would result in areas of different crosslink density. The vulcanization reactions themselves may result in areas of different crosslink density.

Weisenberger and Koenig (1989a) used NMRI to monitor the various aspects of Case II diffusion without interrupting the processes. They used a Bruker MSL-300 spectrometer with a 7.0 T super-wide bore (0.15m) superconducting magnet. They found that the images of poly(methyl methacrylate) (PMMA) in methanol clearly show the three characteristics of Case II diffusion (i.e. a sharp concentration gradient at the front, no concentration gradient behind the front and constant front velocity). They found that the advance of the sharp concentration front is linear with time and has a velocity comparable to other studies. The equilibrium volume fraction also agrees well with previous investigations.

The same authors (Weisenberger and Koenig, 1989b) discussed the NMRI of solvent diffusion in polymers. The constraints on the imaging experiment imposed by the diffusion process were discussed with respect to sample geometry and the rate of diffusion. A fast imaging scheme known as FLASH is described as an alternative method which reduces the influence of the diffusion rate and NMR relaxation parameters. The case II diffusion examples were also presented here.

Chang and Komoroski (1989) examined a number of elastomeric materials of similar glass transition temperature but differing chain segmental mobilities. Examples include cis-polybutadiene, natural rubber and a cured carbon-black-filled cis-polybutadiene. Proton NMR images were obtained at ambient temperature at 200.1 MHz on a General Electric CSI-4.7 system with a 0.33m room temperature horizontal bore, and a 0.75m imaging bore. Several images were also obtained on a GE Sigma clinical NMR imaging system at 64 MHz (1.5 T) using the 0.15m extremity coil provided. The low frequency results were clearly superior.

© 1990 NOVA HUSKY RESEARCH CORPORATION

Ellingson *et al.* (1989a) compared the X-ray CAT scanner and the NMR hospital imagers in the detection of the distribution of the organic binder materials used in the injection molding of ceramics. They found that x-ray CT is a more sensitive method and it can detect variations of 1% wt in binder content.

Ellingson *et al.* (1989b) studied the potential of NMRI as a characterization technique for advanced ceramics using a 1 T imager. The applications included optimization of slip casting rates of Al_2O_3, quantifying distribution of organic materials during injection molding of Si_3N_4 and mapping of porosity in partially sintered Al_2O_3 disks.

Garrido and Mark (1989) used solid state ^1H NMR imaging with chemical shift selective excitation to couple directly spectroscopic information (chemical shift) with image information (space) in rubber-like materials. The equipment used was a Bruker MSL 400 spectrometer/imager equipped with an Oxford 9.4 T 0.089m vertical bore superconducting magnet.

Guillot *et al.* (1989) used a home made NMRI for the monitoring of drying in a porous rock. The drying kinetics were studied. They have found evidence of a threshold saturation which can be interpreted as the irreducible saturation S_o. Images showed that under this threshold, two compartments appear, a central heart where the remaining liquid water is concentrated and lateral shoulders in which the physicochemical state of protons is not yet clarified.

Karuhanithy and Mooibroek (1989) used NMRI to detect physical flaws in fibre-reinforced ceramics in the green state. Alumina-SiC fibre composites were fabricated by slipcasting, and NMR Imaging was applied to identify physical flaws in the green state, using water already present in the material. The two dimensional spin-wrap method was employed. A Bruker MSL 400 MHz spectrometer equipped with a micro-imaging accessory from the University of British Columbia was used. The resolution was 7×10^{-5}m by 7×10^{-5}m by 8×10^{-4}m.

2.4.3 Theoretical

A number of theoretical papers that deal with different aspects of the NMR technology and imaging methods have appeared. For reference purposes let us include a few introductory papers (Hinshaw and Lent, 1983; Rothwell, 1985), a tutorial on tomography of materials that bend rays (Vest, 1985) and a recent article on NMRI of materials that focuses on the theory behind solid state NMRI with applications in advanced materials. A Bruker CXP-200 and a MSL 200 NMR spectrometers was used. Examples of applications included a cross-linked rubber impregnated

© 1990 NOVA HUSKY RESEARCH CORPORATION

with aluminum particles, a piece of solid-filled phenolic resin surrounded by round wooden sticks and wrapped with Teflon tape and a three-day old tobacco horn worm.

2.5 Ultrasonic Technology

Soucemarianadin *et al.* (1987 a) presented an application of an ultrasound method for saturation mapping in porous media. Advantages of this method compared to other non-destructive methods include the lack of safety hazards and the absence of dopants that could modify phase behaviour, miscibility and interfacial tension. Soucemarianadin *et al.* (1987 b) applied the same technique in order to study sweep efficiency of multilayered porous media, during stable and unstable flow.

Justice *et al.* (1989) discussed the potential of acoustic tomography for monitoring Enhanced Oil Recovery. The authors state that it is quite possible to obtain geophysical tomographic data of sufficient quality to produce interpretable tomograms for thermal EOR monitoring of heavy oil reservoirs.

Wolf (1988) used ultrasonic tomography to measure the spatial distribution of the gas phase in a cross section of a gas/liquid flow line. In this application the projection data are obtained from measurement of the extinction along a set of ultrasonic rays in this cross section, using piezo-ceramic ultrasonic transducers. The transducers are arranged in a circular sensor array which is directly integrated in a pipe wall of the flow; instead of mechanical rotation, the sensors are sequentially switched.

Acoustic imaging has also attracted a great deal of research attention. A history of acoustic imaging is given by Wade (1986). Although the imaging in microscopy is very advanced, tomographic acoustic imaging has not been developed yet. The most serious drawback is the lack of resolution.

Some recent advances in image enhancement for the NDE of composite materials using Acoustical Imaging is given in Frock and Martin (1986). Mak *et al.* (1986) have developed an immersion method for the imaging of internal defects in solids. The method takes into account the effects of surface refraction. The technique requires the exterior surface of the object being inspected to be known a priori.

© 1990 NOVA HUSKY RESEARCH CORPORATION

2.6 Other

Snyder and Hesselink (1985) used Optical CAT scanning for use in a nonsteady fluid or combusting flow. Lasers are used as the beam source.

Allen and Puckett (1986) used radioactive tracers to test the reliability of their waterflooding simulation package. ^{59}Fe in the form of radioactive ferrocene was used as a tracer in cores of Clashach sandstone 1m long, 0.045m in diameter. The radiation was collimated by a lead collimator and it was detected by a NaI crystal and photomultiplier tube assembly. The measurements were done using a slit width of $6x10^{-3}m$.

Wexler *et al.* (1985) presented an electrical impedance-based method and apparatus for imaging the interior of a structure, such as a mineral or human body, having regions of differing impedance. The technique involves impressing a number of excitation patterns on the body and measuring the resulting voltages at a number of sites. Because voltages need not be measured at current injection sites, contact resistance problems are ameliorated. This impedance computed tomography reconstruction process employs the solution of the Poisson equation and makes no assumptions of raylike behaviour of the current flow paths.

Tamburi *et al.* (1987) used the commercial technique called Electroscan to map subsurface pollution plumes. Electroscan has been developed after the principles described in the above paper. So far that inventors focused in geophysical type applications rather that core analysis.

The microwave attenuation technique was developed to measure water saturations in laboratory porous media experiments by Parsons (1975). Microwaves are electromagnetic radiation occupying the spectrum between infrared and radiowaves (0.3 - 300 GHz). Microwave energy is absorbed by the water molecule dipole. Energy is dissipated as heat but not enough to raise the temperature noticeably. The resulting electrical-field (intensity of the transmitted radiation) decays exponentially, as radiation traverses the absorbing medium, and obeys the Beer-Lambert absorption law. Substances such as oil, gas, consolidated rock and epoxy resins are nearly transparent compared to water. Parsons performed waterflooding and oilflooding experiments on Berea cores 1.20m long, 0.10m wide and 0.025m thick. The saturation snapshots obtained show the typical Buckley-Leverett saturation behaviour for both oilfloods and waterfloods. Bentsen and Saeedi (1981) performed waterflooding experiments in unconsolidated media using a similar microwave technique for the saturation profile measurements. Islam and Bentsen (1986) used this technique as a basis to develop an apparatus for measuring relative permeability.

© 1990 NOVA HUSKY RESEARCH CORPORATION

Huand *et al.* (1989) described a method for the tomographic imaging of two-component flow using capacitance sensors. The prototype system uses eight capacitance sensors to perform a 'body scan' of the fluid-conveying pipe, and a linear back projection algorithm is developed to reconstruct the cross-sectional image of the two component flow from the measured capacitance values. Capacitance sensing methods are suitable for imaging flows consisting of two components of very different permitivities, such as water/oil, gas/oil and solids/gas flows. Capacitance sensors have the advantage of being non-invasive, inexpensive, simple to construct and fast in measurement speed.

© 1990 NOVA HUSKY RESEARCH CORPORATION

3.0 CAT SCANNER CALIBRATION AND MODEL DESCRIPTION

3.1 Scope and Hardware Setup

The EMI CAT scanner has been built to serve in radiology. Trying to use it for core analysis involves operation at conditions far from the design stage. This in turn incorporates a number of other problems which cannot be addressed without drastically modifying the scanner. For the objectives of this work we have decided to keep things as simple as possible and work with a standard set of conditions. Therefore, the machine was calibrated for operation at a constant setting of photomultiplier tubes and reference voltage. Frequent testing of the response of the photomultiplier tubes is required. Wedge correction scans are required for each operating voltage. We have decided to operate at 140 kVp as the high energy setting and as low as possible for the low energy setting. The lowest setting that can be set by the machine is 80 kVp. The same core holder is to be used in all samples and good centering is required for elimination of artifacts. We have found that the scanner software does not "like" irregular objects. Effort was made to scan only cylindrical pieces. The work in this chapter is related to task 8.

3.2.1 Description of Scanning Process

The scanning experiments were performed in the CT-5005 full body scanner. All scans were done using slow scanning mode which requires 72 seconds for scanning and 50 seconds for image reconstruction. The machine is a second generation scanner and the scanning sequence is of the translation rotation type. The x-ray apparatus consists of a tungsten fan x-ray tube with an array of 30 detectors across the x-ray gantry. The core holder is an aluminum pipe of 0.635×10^{-2}m thickness and 10.16×10^{-2}m inside diameter. Full diameter cores are put inside the core holder which is centered inside the gantry. Core plugs are analyzed by using a Plexiglass annulus which is full of water. There is one annulus of 3.81×10^{-2}m and one annulus of 5.08×10^{-2}m available for different sizes of plugs. All the useful data is stored on magnetic tapes and can be viewed at any time for inspection or re-evaluation. The images are stored in matrices of 320x320 elements. This corresponds to a pixel size of 7.5×10^{-4}m x 7.5×10^{-4}m per matrix element. The slice thickness was 3×10^{-3}m along the long axis of the core. The images are displayed on a monochrome screen in the Scanner room. Black and white Polaroid pictures are generated on the spot for visualization purposes.

© 1990 NOVA HUSKY RESEARCH CORPORATION

3.2.2 *Modelling of Physical Properties Using the CAT Scanner*

The CAT scanner produces two dimensional arrays of data that are called the CT numbers. These are integer numbers and correspond to the linear attenuation coefficient of each voxel through equation (3.1)

$$CT_n = K\frac{\mu - \mu_{water}}{\mu_{water}} \tag{3.1}$$

Where μ is the linear attenuation coefficient, μ_w the linear attenuation coefficient of water and k a constant. The linear attenuation coefficient is given by equation (3.2)

$$\mu^* = \frac{1}{L}\ln\frac{I_o}{I} \tag{3.2}$$

Where I is the transmitted intensity, I_o the incident intensity and L the path length. In order to correlate the CT number to specific physical properties of a core sample one must see the dependance of the linear attenuation coefficient on other physical properties. Vinegar and Wellington (1987), and Wellington and Vinegar (1987) gave a detailed discussion on the topic. They stated that the linear attenuation coefficient is a function of the bulk density and the effective atomic number of the sample as dictated by equation (3.3)

$$\mu = \rho\left(\alpha + \beta\frac{\overline{Z}^{3.8}}{E^{3.2}}\right) \tag{3.3}$$

where a,b are constants, E is the mean photon energy in keV, ρ is the bulk density and Z is the effective number of the sample. For energies above about 100keV, x-rays interact with matter predominantly by Compton scattering which is dependent on electron (bulk) density. For x-ray energies well below 100keV, photoelectric absorption becomes dominant. The latter type of interaction is strongly dependent on the effective atomic number of each voxel. This theoretical principle is the main idea behind what is called dual energy scanning. The low energy scans can be used for bulk density determination and the high energy set can be used for effective atomic number determination. Knowledge of the effective atomic number of each voxel can be used to characterize the nature of the mineral of each voxel. The term "effective atomic number" is used instead of the term "atomic number" for voxel characterization because each voxel is a mixture of at least two compounds (rock and air). The effective atomic number is heavily weighted towards the heaviest compounds in the mixture (i.e. solids). The rock is also a mixture of elements. The effective atomic number of the rock is heavily weighted towards the heaviest element. Therefore

© 1990 NOVA HUSKY RESEARCH CORPORATION

one should be in the position to identify different minerals based on the effective atomic number analysis. When the minerals are identified, one can proceed with an estimate of the voxel porosity using equation (3.4)

$$\phi = \frac{\rho_g - \rho_b}{\rho_g - \rho_f} \tag{3.4}$$

where ρ_b is the bulk density, ρ_g is the mineral or grain density and ρ_f is the fluid density. Having done two CT scans of the same slice one can get an estimate of the bulk density, effective atomic number, grain density (mineralogy) and porosity. Furthermore one can visualize heterogeneities in different places throughout the core.

2.3 Description of Postprocessing Algorithm

The data from the magnetic tapes are transferred to a SUN workstation for computer analysis using a comprehensive computer software package developed at NHRC. The package includes algorithms for array rearrangement and slicing, region of interest algorithms, statistical analysis for frequency distribution and mean values of the estimated properties, core analysis models and fluid saturation models. As of October 1st, 1989 the NHRC CAT scanner postprocessing software version 1.0 was in use. This version operates using a number of interactive programs written in the "C SHELL" command language of the UNIX operation system. These programs are in turn calling FORTRAN routines for data manipulation and graphics generation. The graphics are generated using the Graphics Kernel System (GKS). All color images are generated on a graphics screen and then transferred to a TECTRONIX color printer. At various times the calibration equations used in the software have changed because of improvements in our hardware setup. Currently, equations are:
For bulk density,

$$\text{Density} = 0.00163 * \text{CT number} + 1.119 \tag{3.5}$$

(for derivation see the next section)
The mean x-ray energy as used for the effective atomic number calculations is

$$\text{KeV} = 19.7219 + 0.520186 * \text{kVp} \tag{3.6}$$

© 1990 NOVA HUSKY RESEARCH CORPORATION

where kVp is the peak x-ray energy in KV and corresponds to the low energy scan. This is usually done at energize of 80 - 100 kVp, while the high energy scan is done at 140 kVp. Mean energies were estimated using a spectrum measurement technique developed at NHRC (see the next chapter). The mineral discrimination is based on comparing the bulk density and effective number of each pixel to a data set which is given as an input. In the current software version a pixel is assigned an index for a mineral 'x' when both its bulk density and its effective atomic number are within the specified limits for the mineral 'x'. Each pixel can be assigned only one mineral. There are not enough equations for the quantitative discrimination of a mixture of minerals within a single pixel.

3.3.0 Bulk Density Calibration of the CAT Scanner

According to the model of equation (3.3) when the x-ray energy is higher than 100 keV the linear attenuation coefficient is proportional to the bulk density. One could then write that

$$CT_n = \alpha \rho + \beta \qquad (3.7)$$

where α and β are coefficients and ρ the bulk density. The CT number is proportional to the linear attenuation coefficient through equation (3.1). In order to verify equation (3.7) a series of tests were performed. During these tests a number of samples were scanned at the highest possible energy (140 kVp). At the same time their bulk density was determined using weight and volume measurements. The measured bulk density was plotted against the average CT number as measured through the region of interest algorithm of the EMI Scanner. Two groups of tests were performed.

The first test consists of twenty three (23) samples which were collected in-house. These samples are liquid (heptane, water, different crude oils) and solids (teflon, sulphur, gypsum, illite, calcite, kaolin, and a collection of sandstones and dolomites).

The second test consists of one hundred and twelve (112) ward standards composed of a wide variety of rocks and minerals (e.g. feldspars, pyroxenes, volcanic rocks, carbonates, silicates, pyrogenic, non-clastic rocks, metamorphic rocks, etc.).

When all the rocks were scanned and plotted, the graph of Figure 3.1 was formed. It can be seen from the graph that the points do follow a linear behaviour but the bulk density, CT number linear

© 1990 NOVA HUSKY RESEARCH CORPORATION

relationship has a considerable scatter. A linear regression test on all the points gives a correlation of coefficients of 0.92 which is low for the purpose of calibration.

The next step was a classification according to certain characteristics. Four distinct lines were identified. Line 1 (Figure 3.2) is the line which includes samples of high CT number for relative low density. In this group sulphur, calcite, chlorinated materials and some carbonates are included. The best fitting straight line for sets of line 1 is

$$\rho = 0.00138\ CT_n + 0.728 \tag{3.8}$$

with a correlation of 0.996 which is an excellent coefficient. The samples of low CT number for relatively low density formed the line 2 and it also includes teflon. The best fitting line was

$$\rho = 0.00158\ CT_n + 1.375 \tag{3.9}$$

with a correlation of 0.998 which is also excellent. Line 3 consists of materials with very high density and very high CT numbers. The best fitting line is

$$\rho = 0.00140\ CT_n + 0.963 \tag{3.10}$$

with a correlation of coefficient of 0.99. The data for line 2 are shown in Figure 3.3 while the data for line 3 is Figure 3.4. Because there were only very few points in line 3, the fourth line was used for the remaining points, including the points of line 3. The best fitting line for the remainder of the points was

$$\rho = 0.00163\ CT_n + 1.019 \tag{3.11}$$

with a correlation of coefficients of 0.986.
Equation (3.11) was used on a number of rock tests. It was found that the bulk density estimates were always smaller than the measured values by approximately 100 kg/m^3 (0.1 g/cm^3). To compensate for this the line was corrected by 0.1 in the coefficient thus giving

$$\rho = 0.00163\ CT_n + 1.119 \tag{3.12}$$

which was the final calibration line.

© 1990 NOVA HUSKY RESEARCH CORPORATION

From the calibration and the existing information, it was not possible to group the rock samples through some geological criteria. Since there were no chemical compositions for many of these rocks it was difficult to come up with any solid classification. There are only indications that there is an effect of atomic number which is still strong at 140 kVp energy. This is strengthened by the fact that the points of line 1 (equation 3.8) have higher atomic numbers than the rest of the samples.

This is consistent with equation (3.3). The problem is that we cannot achieve any higher energy from the existing equipment to correct the effective atomic number effect. In order to compensate for this we had to correct for the bulk densities of different materials when it was considered necessary. For example, although the bulk densities of dolomites and sandstones are predicted accurately, the predictions for sulphur were not accurate. Our postprocessing software cannot handle two different calibration curves and as a result, when sulphur was expected to be present in bulk quantities in a rock sample, the input sulphur grain density and effective atomic number were taken from predictions of pure sulphur analysis. Pure sulphur was scanned and its bulk density and effective atomic numbers were calculated using the model. Then the predictions were used as input data for the system.

This parameter correction is not very accurate. However, it was adopted on two occasions out of the numerous tests performed during this project and the results were considered satisfactory. There are two ways to improve on this area. One is to use a higher energy source and eliminate the atomic number effect or develop a better model which provides for a high energy effect of the effective atomic number coupled by calibrations where both density and effective atomic number are taken into account. The first task involves redesigning of the hardware and the second an in depth study of the x-ray absorption at the nucleus level. Both tasks offer a great potential, but they are both beyond the scope of this project.

© 1990 NOVA HUSKY RESEARCH CORPORATION

4.0 MEASUREMENT OF THE X-RAY SPECTRA

4.1 Objective

This part of the project was designed to measure the x-ray energy spectrum detected by the CAT scanner detector arrays. The results are used in an improved algorithm for the measurement of effective atomic number calculations in the CAT scanner postprocessing software package. The work was done as an extension of task 8.

4.2 Background

McCullough *et al.* (1974) showed that at the 120 kVp (73 keV) setup, the EMI head scanner provides numbers which are related to keV coefficient values with an agreement of better than 0.5%. Fewell and Shuping (1977) described a method to determine primary x-ray spectra over the 45-90 kVp section. Vinegar and Wellington (1987) describe the algorithm of calculation of rock properties and fluid saturations. One of the important parameters necessary for a quantitative core analysis package is the mean energy of the x-rays. This energy can be calculated through measurement of the half value length or through calculating the relative amounts of Compton and Photoelectric effects present. Wellington and Vinegar (1987) provided spectra for x-rays at various peak acceleration voltages (kVp settings) as detected by the CAT scanner detectors and for a tungsten x-ray tube. The spectra were measured with and without a core assembly present. Moreover, Wellington and Vinegar (1987) provided a plot of mean x-ray energy as a function of peak energy for the above two cases. In this chapter the corresponding results for NHRC CAT scanner system are calculated and the measured mean energy values are incorporated in the postprocessing software package.

4.3 Photon Attenuation in Computer Tomography

This section presents the calculations of the linear attenuation coefficient as a function of physical properties and the mean x-ray energy (Weber and Van den Berge, 1969, McCullough, 1975). The mass attenuation coefficient of a compound is given by:

$$\frac{\mu}{\rho} = \sum_i w_i \frac{\mu_i}{\rho_i} \qquad (4.1)$$

© 1990 NOVA HUSKY RESEARCH CORPORATION

Where μ,μ_i are the linear attenuation coefficients of a compound and its constituents, ρ,ρ_i are the corresponding densities and the weight fractions of each constituent. This is the so-called "mixing" rule and it ignores changes in the atomic wave function resulting from changes in the molecular, chemical, or crystalline environment of an atom. Above 10 keV, errors from this approximation are expected to be less than a few percent.

The mass attenuation coefficient μ/ρ is also proportional to the total photon interaction cross section per atom, σ^{α}_{tot}, that is the sum of the cross sections for all the elementary scattering and absorption processes. The appropriate relation is:

$$\frac{\mu}{\rho}\left[\frac{cm^2}{g}\right] = \sigma^{a}_{tot}\left[\frac{cm^2}{atom}\right]\cdot\left(\frac{N_A}{A}\right)\left[\frac{atoms}{g}\right] \tag{4.2}$$

where $N_A = 6.02310^{-23}$ in the Avogadro's number and A is the atomic mass of the absorber. Hubbell (1969) has tabulated σ^{α}_{tot} [barns/atom] and the factor $(N_A/A) \times 10^{-24}$ for a wide variety of elements and compounds. Since there are Z electrons per atom, Eq. (4.2) can be written in terms of the total cross section per electron, σ^{α}_{tot}, as:

$$\frac{\mu}{\rho}\left[\frac{cm^2}{g}\right] = \sigma^{e}_{tot}\left[\frac{cm^2}{electron}\right]\cdot\left(\frac{N_A z}{A}\right)\left[\frac{electrons}{g}\right] \tag{4.3}$$

where N_AZ/A = Ng the mass electron the mass electron density. For all elements except H_2, Ng approximately equals $N_A/2$. This indicates that atomic composition dependence of μ/ρ is principally related to that of σ^{e}_{tot}.

The energy and atomic composition dependence of the mass attenuation coefficients μ/ρ in the photon energy range of interest in CT scanning is related to the three modes of photon interaction: (i) coherent scattering, (ii) photoelectric effect, and (iii) Compton effect. The effect of coherent scattering is quite small. It is estimated that at 100 KeV, coherent scattering is about 2.5% of the total attenuation σ^{e}_{tot} can be written as:

$$\sigma^{e}_{tot} = \sigma^{e}_{T} + \sigma^{e}_{R} + \sigma^{e}_{C} \tag{4.4}$$

where R denotes Rayleigh (coherent) scattering, T denotes the photoelectric effect and C denotes the Compton Scattering.

© 1990 NOVA HUSKY RESEARCH CORPORATION

Analytical expressions which provides a good approximation for the terms of equation (4.4) for $30 \leq E \leq 100$ kev and $1 \leq Z \leq 20$ are as follows:

$$\sigma_T^e = 9.8 \quad 10^{-24} \frac{Z^{3.8}}{E^{3.2}} \left[\frac{cm^2}{electron} \right] \tag{4.5}$$

$$\sigma_R^e = 1.25 \quad 10^{-24} \frac{Z^{2.0}}{E^{1.9}} \left[\frac{cm^2}{electron} \right] \tag{4.6}$$

$$\sigma_C^e = 0.597 \quad 10^{-24} e^{-0.0028(E-30)} \left[\frac{cm^2}{electron} \right] \tag{4.7}$$

where Z is the effective atomic number of the component and E the mean x-ray energy.

From equations (4.1) to (4.7) one can write:

$$\frac{\mu}{\rho} = 6.023 \; 10^{23} \frac{1}{2} \left(9.8 \; 10^{-24} \frac{Z^{3.8}}{E^{3.2}} + 1.25 \; 10^{-24} \frac{Z^{2.0}}{E^{1.9}} + 0.597 \; 10^{-24} e^{-0.0028(E-30)} \right) \tag{4.8}$$

or if one does the arithmetic calculation:

$$\frac{\mu}{\rho} = 2.95127 \frac{Z^{3.8}}{E^{3.2}} + 0.3764 \frac{Z^{2.0}}{E^{1.9}} + 0.17979 e^{-0.0028(E-30)} \tag{4.9}$$

Equation (4.9) is the equation to solve for Z when μ, ρ and E are known. If one drops the Raleigh term, then equation (4.9) becomes

$$\frac{\mu}{\rho} = 2.95127 \frac{Z^{3.8}}{E^{3.2}} + 0.17979 e^{-0.0028(E-30)} \tag{4.10}$$

which is of the same form as in Vinegar and Wellington (1987). In order to calculate Z from (4.9) or (4.10) the value of E is necessary. The mean energy, E, equals the photon energy only when the x-ray beam is monoenergetic. This is not the case in commercial x-ray sources which emit a wide spectrum of x-rays from 20 keV to the peak acceleration energy (80 - 140 kVp) for the CAT scanner tube.

© 1990 NOVA HUSKY RESEARCH CORPORATION

4.4 Calculation of Mean X-Ray Energy

The x-ray energy of a polyenergetic source is the sum (spectrum) of all the monoenergetic beams that compose the source. If the full spectrum is known, the mean energy can be calculated by:

$$\bar{E} = \frac{\int_o^{E_{max}} E D(E) dE}{\int_o^{E_{max}} D(E) dE} \qquad (4.11)$$

Therefore, in order to measure the mean energy, one must have measurements of the full x-ray spectrum. Two methods have been proposed for the measurement of the x-ray spectrum; both methods were tested.

4.5 Ionization Chamber Approach

Following the recommendation of Dr. K. Vij of NHRC, Tomotechnology Inc. of Calgary was contracted to measure the x-ray spectrum of the x-ray tube in our CAT scanner. The measurements were done by Dr. Hahn of the Foothills Hospital in Calgary. The method used dosimetry with an ionization chamber. Dosimetric measurements of aluminum HVLs (Half Value Lengths) were carried out for tube peak potentials of 80, 110 and 140 kVps. Two sets of measurements were taken. One involved the inherent spectrum (no core or core holder) and the other involved the water annulus (doughnut). Each set of measurements gave a group of sets of data $\{D_k, t_k\}$ where D_k and t_k were respective dose and thickness values in the kth measurements for k = 1, 2, 3, ..., 24. Using normalized values of these D_k values and published data of the linear absorption coefficients of aluminum, spectra were obtained.

The suggested procedure is based on the measurement of radiation doses attenuated through the absorber. The relation of the attenuation dose to the material thickness can be expressed as:

$$D = k \sum_{i=1}^{m} \phi_i e^{\mu(E_i)} \Delta E \qquad (4.12)$$

where D is the dose, k is a constant, ϕ_i is the normalized intensity, μ is the linear attenuation coefficient and E is the energy. Measurement of doses for different thickness of material allows a system of linear equations to be set up from which the values of intensities of radiation for

© 1990 NOVA HUSKY RESEARCH CORPORATION

respective energies can be calculated. Half value lengths (HVL) are tabulated for several materials with their relations to the x-ray energies. It is advantageous to interpolate the measured doses and to equate them with the appropriate HVL. The procedure then consists of the dosimetry measurements, auxiliary calculations using published material and solving the system of linear equations for discrete radiation intensities. The following steps may be followed:

a) Radiation dose measurement
- set a fixed tube peak voltage
- measure radiation dose varying the thickness of the absorber
- normalize results to the measurement without the absorber
- establish region of interest for x-ray energy axis

b) Auxiliary calculations
- decide on the starting energy, E_1
- decide on the energy step ΔE
- for energies $E_i = E_1 + (i-1)\,\Delta E$ find the linear attenuation coefficients $\mu(E_i)$ of the absorber and calculate $HVL_i = (l_n 2)/\mu(E_i)$
- interpolate normalized doses δ_i to correspond to their respective HVL_i
- set a coefficient matrix [A] where $a_{ij} = e^{-\mu(Ej)HVLi}$

c) Spectra calculations $$[A]\left[\int_{\Phi_n}^{\Phi_i}\right] = \frac{1}{k\Delta E}\left[\int_{\delta_m}^{\delta_i}\right], \quad \Phi_i = \frac{I_i}{D_o E_i} \qquad (4.13)$$

4.6 NaI Crystal Approach

This approach involves the use of a NaI with a photomultiplier tube and a scintillation counter similar to the detector system which runs in the CAT scanner. The detector assembly is connected to a pulse height analyzer which automatically produces the number of counts per energy channel and directly provides the x-ray spectrum. The auxiliary work related to this method is a calibration of the keV energy/channel relation by using known monoenergetic sources. Also care must be taken not to saturate the crystal. An oscilloscope can be used for detecting whether the x-rays saturate the detector or not. Although this approach sounds a lot simpler than dosimetry, it requires a considerable amount of calibration work for the design of a proper housing for the NaI crystal. A lead cylinder was especially designed for this purpose with a small opening at the top to allow the least amount of x-rays to go through without saturating the crystal. A long trial and error

© 1990 NOVA HUSKY RESEARCH CORPORATION

process was used to design and drill the optimum opening for the x-ray path. A simplified schematic of the apparatus is given in Figure 4.1.

4.7 Results

4.7.1 Ionization Chamber Approach

The results of Dr. Hahn's work are given in Figures 4.2 - 4.7. The results of the mean energies are given in Table 4.1. Please note that the results from Vinegar and Wellington are the data for the spectrum without a core present.

It can be seen from the table that all the measurements are reasonably close to each other. During the measurements; however, we observed that when dealing with the water ring doughnut at 80 kVp the ionization chamber was not giving reproducible readings due to high absorption from the water ring. As a result, the value of 56.024 for the mean energy is questionable, and it is expected to be inaccurate.

Consequently, the x-ray spectrum was remeasured using an aluminum core used in routine work in place of the water ring. A computer program was written for the auxiliary calculations and ISML subroutines were used for the solution of the linear sets of equations. HVL measurements were taken using a new ionization chamber. However, the analysis of the data gave a matrix which was too ill-conditioned for any accurate spectrum measurements. It is possible that this problem occurred because of the significant absorption from the core and housing assembly. This is consistent with the problems encountered by Dr. Hahn. In any event, this method was not pursued further.

4.7.2 NaI Crystal Approach

The longest part of this experiment was to calibrate the electronics and make sure that the detector was not saturated by the x-rays. Different sensitivity detectors were tested and an optimum of housing opening and NaI crystal size was obtained. A computer program was written to transform the output of the pulse height analyzer to x-ray energy. Equation (4.11) was used for the calculations of the mean x-ray energy. The results are given in Table 4.2. The actual spectra are shown in Figures 4.8-4.10 and they correspond to an aluminum core holder and a 0.10m diameter Berea core. The results of Wellington and Vinegar are the ones with core holder and an 0.05m diameter Berea core.

© 1990 NOVA HUSKY RESEARCH CORPORATION

It must be noted that there was always a blank run for background radiation done using the lead housing without any opening. It was also found that positioning of the crystal was crucial for a successful spectrum measurement. The results of the mean energies compare well with the results of Vinegar and Wellington if one takes into account that the setups and the scanners were different (the x-ray tubes were of the same type). Regression analysis gave the following equation for the total keV/kVp line:

$$keV = 19.7219 + 0.520186*kVp \qquad (4.14)$$

This equation was used for the calculation of the mean energy in the CAT scanner postprocessing software package. Equations (4.1) to (4.10) were used to back calculate the effective atomic number starting from the measured linear attenuation coefficients. As a check, we have calculated the linear attenuation coefficient of water at 80 kVp (62.27 keV). The value of 0.204 cm^{-1} relates very well to the calculated value of 0.206 cm^{-1} reported at 60 keV by McCullough. This agreement gave us confidence in the calculations of the postprocessing package regarding effective atomic number calculations.

4.8 Conclusions

The x-ray spectra for different kVp values were measured using two different techniques. The estimated mean x-ray energies were in good agreement with the reported values in the literature. The NaI crystal method proved more useful and mean energies provided by this method will be used to generate values for this parameter in CAT scan analysis.

© 1990 NOVA HUSKY RESEARCH CORPORATION

5.0 UNCONSOLIDATED MEDIA

This chapter deals with the applications of Computer Assisted Tomography in the testing of unconsolidated core. The importance of CAT scanning for characterization of heavy oil core is evaluated. This chapter was developed from the work done for tasks 1,3,4 and 6. It was found that although the scanner can be used very effectively for identification of core damage and reservoir heterogeneities, a complete analysis of native heavy oil core is not possible because of too many unknown parameters.

5.1 Experimental Work

Two different formations were tested using the CAT scanner. Firstly, core material from the "B" member of the Clearwater Formation of the Lower Cretaceous Mannville Group in the Cold Lake area was scanned. Two pieces of core, each approximately 0.3m long were used. Scans were taken at 0.01m intervals at a resolution of 0.00075m x 0.00075m x 0.005m. The second set of scans was done using six cores from the same well in the Provost are a courtesy of PanCanadian Petroleum. Four of the cores were 1.5m long and two cores were 1m long. They were scanned at 0.05m intervals at a resolution of 0.00075m x 0.00075m x 0.003m. The post processing software package which was developed in-house for the analysis of CAT scanner data was used for data analysis and graphics presentation. 55 single energy scans were taken for the Cold Lake core and 88 dual energy scans (equivalent of 176 single energy scans) were taken for the Provost core.

Longitudinal reconstruction of the core images can show the distribution of features in the third direction. This "stacked" slice representation gave more realistic features description of the Cold Lake samples rather than the Provost ones since the scans were taken so much closer in the Cold Lake cores than the Provost cores. The results are presented as color CT number Images. The colour code bar at the right side of the images shows the CT number range that is depicted by one colour. For example, CT numbers between 500 and 600 are depicted as green; this can be translated linearly to bulk density images. What is expected to be seen from a CT scan of a homogeneous sand is a uniform image with a narrow CT number distribution. This was achieved when sandpacks were packed and scanned. However, when the cores were scanned things were quite different. The following figures show some examples.

Figure 5.1 shows an image of a slice from one piece of the Cold Lake core. The slice consists of a uniform body of sand which is separated into pieces by lower density streaks which are almost radial in direction. The perimeter of the core also shows lower density than the bulk body. The

© 1990 NOVA HUSKY RESEARCH CORPORATION

perimeter of the core shows evidence of core damage with a few small pieces missing. The low density streaks are unconsolidated "fractures".

Figure 5.2 shows an image of the slice taken 0.01m deeper than the slice of Figure 5.1. There are two distinct features in this image. Firstly, the fracture pattern is the same and it is even more profound in a few points. Secondly, the CT numbers have shifted to a higher value. The post processing software indicated average shift upwards of 55 CT numbers or 0.09 g/cm^3 (90 kg/m^3). This is a clear indication that there is a different layer present than in the previous slice. This may be a different bedding plane or more probably a shale lamination.

Figure 5.3 shows an image from the second core from Cold Lake. The image reveals an area of relatively high density (shale?) to the right half of the image and a very low density are to the left half of the image. Figure 5.4 is the CT number frequency distribution of Figure 5.3. Each colour of Figure 5.3 is the same as in Figure 5.4. The low density (low CT number) part of the slice is an indication of severe core damage. The frequency distribution shows three different peaks which can be translated as three different CT number distributions. Note that a uniform piece of sand should give a narrow normal distribution of CT numbers. Inspection of any of the two figures can provide the information about the core damage.

Figure 5.5 shows a different type of heterogeneity. The slice can be divided into three different areas. A relatively lower density area is the centre where the trace of a "fracture" is present, a relatively high density area to the right and a far higher density area to the left. The frequency distribution plot (Figure 5.6), shows a clear bimodal distribution with two peaks of approximately 480 CT number and 610 CT number. Viewing of the two figures indicates the slice was taken exactly at the merging point of two different density planes which may be bedding planes or the boundary of a shale and a sand layer. It is very interesting to observe the distinct separation of the two layers in the frequency plot. A point of interest is that Figures 5.3 and 5.5 are only 0.04m apart from each other.

The slice of Figure 5.7 was taken 0.06m below the slice of Figure 5.5. A completely different picture is shown. The bottom left piece of the core is of higher density which is progressively reduced as we move from bottom left to top right. At top right evidence of core damage is clear. A new feature which is shown in this figure is the presence of small clusters of very high CT numbers. The difference of the CT numbers from the rest of the high density area is between 200 and 300 CT numbers. These have been identified as clay clasts by the geologist who was cooperating with us in these core tests.

© 1990 NOVA HUSKY RESEARCH CORPORATION

Figure 5.8 is the scan of a slice taken 0.01m lower than the previous slice. The characteristics of this slice are similar to the previous one and a variety of high density clusters is also shown. Using the images of Figures 5.7 and 5.8 one can come up with the determination of sizes and size distributions of these inclusions. The location of the inclusions can be correlated with depth and these areas can be omitted when a plug is to be selected. All this can be achieved simply be viewing the core prior to slabbing.

Figure 5.9 shows the image of a slice 0.11m lower than the previous slice and close to the bottom of the core piece. A few high density clusters are present but the main feature of this image is the maze of fractures which have a general radial direction but often spread in dendritic structures. From the two core pieces investigated so far it seems that these fractures are more profound in the ends of the pieces. The core holds better at the middle section.

Figures 5.10 and 5.11 are two longitudinal representations of the second piece from Cold Lake which are taken approximately 0.04m apart. Both figures show the high density areas depicted clearly in two distinct layers at the bottom of the picture (green colour). The depth of some fractures can also be seen. Figure 5.11 shows very clearly the area where the core was severely damaged (grey colour) and Figure 5.12 shows some of the high density inclusions. Although the slices were taken with an 0.005m gap of each other, the different features of the core are clear. The gap between the slices is responsible for the "stretching of the core features in the longitudinal direction. Another very interesting feature as observed by the longitudinal sections is the presence of high density streaks that run along the length of the core and close to the perimeter. Such a feature can only be attributed to circulation of fines due to the coring process. These particles come from the higher density layers or shales and are deposited in the perimeter of the core. The extent of mud invasion can vary from a few millimeters to several centimeters. Samples where mud invasion has taken place are not representative any more. The CAT scanner can be of great help in identifying such areas of mud invasion.

A number of images from cores coming from the Provost North Bodo area are presented next. The core was taken from the McLaren Member of the Upper Mannville Group and it is generally described as a semiconsolidated sand. PanCanadian Petroleum has provided eight meters of frozen core kept in rubber sleeves. The core came in six pieces, three of these were 1.5m each and three 1m each. It was decided to scan each piece in approximately 0.05m intervals with a slice thickness of 0.003m. Selected images are presented.

© 1990 NOVA HUSKY RESEARCH CORPORATION

Figure 5.12 shows the first of the Provost examples. There are two interesting features in this image. First the core is not round, with some pieces missing on the left side of it. Secondly, there are two diagonally arranged streaks of low density in a higher density background. This could be bedding planes or damage due to fracturing.

Figure 5.13 is taken at 0.15m lower than the previous slice. The sand is more uniform and looks pretty much like the uniform pieces of the Cold Lake samples. However, damage is still evident (the core is not round) and some higher density areas around the perimeter indicate mud invasion. A high density cluster (clay clast or siderite) is also observed.

At a slice scanned 0.05m lower in the picture is completely different (Figure 5.14). The bulk of the core at this level is far denser. The image looks like the shale barriers of the Cold Lake area and there is some damage due to core erosion and mud invasion in the perimeter.

The picture is again much different in Figure 5.15. The core is damaged with large chunks missing from the top and left side and some pieces missing in the middle (looks like holes). The average CT number is far lower than in previous slices.

The next two figures are from the second core piece approximately 0.6m apart. Figure 5.16 shows an image where large pieces of consolidated material are held together by lower density pieces. There are a couple of void areas (vug like structures) showing a core piece missing. The perimeter of the piece is well defined indicating that the whole core is there.

On the contrary, there is a significant piece of core missing on the image of Figure 5.17. Large cracks, "vug" type structures and low density areas showing erosion of core material are present. Some small pieces of semiconsolidated material (or shale) are also present.

Figure 5.18 is taken from the third piece of core approximately 1.5m lower than the slice of Figure 5.16. Again, large clusters of consolidated material are held together by less dense material. There is a relatively small piece of damaged core at the very end of the left side of the core.

Radial type fractures are the main characteristics of the next slice as presented in Figure 5.19. The fractures vary in size and these are from almost "vug" type structures down to barely visible "hair" like fractures. The bulk of the core looks like a higher density sand or shale.

© 1990 NOVA HUSKY RESEARCH CORPORATION

Figure 5.20 is the image of a slice of core piece #3. It is a radially fractured medium density sand with some missing pieces. Figure 5.22 which is the image of a slice approximately 0.10m deeper in the reservoir has also the same type fracture pattern but the material is far more compact than the previous image and its density is also higher.

Figure 5.22 shows a slice from piece #4. Here the core has been cracked at the top right end but the damage is significantly less in the rest of the image.

Figure 5.23 shows a very loose sand piece from core #6. The perimeter of the piece is severely damaged and probably the freezing of the core kept the piece together.

The next set of figures shows the longitudinal representation of each of the six pieces. Figure 5.24 shows the longitudinal cut for the middle of the first core piece. The top of the core is shown at the bottom of the image (picture as viewed from top). The first part of the core is almost lost. It is followed by a layer of relatively high densities. There are two layers of relatively high density interrupted by a layer of unconsolidated sand. The rest of the core is unconsolidated sand with varying degrees of damage.

In Figure 5.25 the longitudinal representation or core piece #2 is shown. Layers of loose unconsolidated sand are mixed with layers of highly consolidated material. Pieces of sand are missing in "vug" like structures while close to the upper right part of the image there is a consolidated piece of rock which is so dense that the x-rays could not go through (density around 3000 kg/cm^3). It may be cement or siderite.

The longitudinal representation of piece #3 shows an unconsolidated sand layer in the middle packed in between two consolidated layers. High density clusters are shown inside the top layer. The unconsolidated layer is damaged in the centre and there is evidence of mud invasion on the sides (perimeter of the core) while at the same time the perimeter of the consolidated layers is damaged. A possible explanation is that particles from the high density area were entrained in the lower density area.

The fourth piece is clearly unconsolidated with only a small semiconsolidated piece at the bottom of the image. There is some damage of the core and various degrees of density in the unconsolidated layer with some evidence of erosion in the core perimeter. The image of the fourth piece is shown in Figure 5.27.

© 1990 NOVA HUSKY RESEARCH CORPORATION

Going on to the fifth piece (Figure 5.28) we observe a similar picture. One layer of semiconsolidated (or higher density material surrounded by unconsolidated sand). A large piece of core is missing at the bottom left part of the image.

Finally, Figure 5.29 shows the sixth and last piece; it is an unconsolidated sand which is very loose and/or highly damaged with big chunks of core missing.

The composite picture of the whole core is given in Figure 5.30. In this composite picture one can see the relative size and importance of the different layers. Up to eight different high density zones are shown with unconsolidated sand of different densities in between. The bottom of the reservoir is far more uniform and loosely packed than the top. Very few areas of the core are uniform and smooth enough for representative core plugging.

For comparison purposes, Figure 5.31 shows a loosely and tightly packed dry sand. The average CT number on the loose sand is 401 and the average CT number on the packed sand is 418. The sandpack was prepared by packing sand in a shrink tube and putting it under pressure.

5.2 Modelling and Discussion

The CT number arrays which were used for the generation of the presented images were also used as input for the post processing packages. The cores from Cold Lake were scanned only at one energy (140 kVp) while the cores from the Provost area were scanned at two energy levels (140 kVp and 85 kVp). The Cold Lake data were processed for bulk density only. The bulk density results were then used for the calculation of porosity assuming only quartz grain density. The Provost data were processed for bulk density, effective atomic number and porosity. In both cases the results are subject to interpretation and speculation and are not as clear as was expected. The reason is that we cannot measure the fluid content and the solid content simultaneously using the CAT scanner.

In order to measure both fluids and solids we need at least four independent measurements for density, effective atomic number and fluid saturations. With x-ray scanning we can at best obtain two. When a dry core is scanned, then the fluid is assumed to be air with bulk density approximately equal to zero. When a core is fully saturated with a single fluid, an independent measurement of the fluid density can help in quantifying the porosity map. However, for a two or three phase system where the saturations are not known, the information is simply not enough.

© 1990 NOVA HUSKY RESEARCH CORPORATION

Another problem associated with the correct measurement of porosity is the fact that the core is depressurized when it comes to the ground and gas comes out of solution. Although we will consider the effect of overburden pressure on a sandpack later, it is worth stating that if the sand is not round and uniform and/or there is gas present in the core, the effect of pressure on porosity is significant. The fact that the core is also frozen can alter the porosity due to expansion of water.

As a result the non-destructive characterization of unconsolidated core is not easy. However, it is not impossible. A more sophisticated approach needs to be taken. One way of tackling this problem is parallel measurement of some other properties of the core such as fluid content through an independent source. Nuclear Magnetic Resonance Imaging offers the best promise at the moment. Calibration of pressure response to pressure can provide correction factors for porosity due to the lack of pressure. Both of these tasks were beyond the scope of this project but they will be pursued in the future. Although these limitations are serious, one cannot deny the invaluable help of the CAT scanner as a tool for viewing the core in three dimensions and through different directions and for the preliminary estimation of various physical properties in a non-destructive way. A preliminary evaluation of the physical properties is given in the following paragraphs.

The bulk density results for the Cold Lake cores are given in Table 5.1 coupled with some plug measurements which were done on some representative uniform plugs. The agreement is very good. Tables 5.2 and 5.3 show porosity calculations given a total liquid saturation of oil and water. It was assumed that oil and water have the same bulk density, an assumption which is reasonable for heavy oil reservoirs. The results were not corrected for the effect of pressure.

Similar results are presented for the Provost cores in Tables 5.4 to 5.9. From all of these results the only non-ambiguous numbers are the ones of bulk density. The rest are subject to interpretation and correction, depending on the amount of fluids present.

From the aforementioned results the most reliable application of CAT scanning at the moment is the 3-D viewing of unconsolidated cores and the quantification of heterogeneities and core damage. The only physical properties that can be accurately quantified are the bulk density and the effective atomic number. The CAT scanner can have detailed applications as a core damage analysis tool. Such an assessment is presented in the next session.

© 1990 NOVA HUSKY RESEARCH CORPORATION

5.3 Assessment of Core Damage Using Computer Assisted Tomography Scanning

The importance of the CT scan technique in the inspection and analysis of cores is enhanced by its value as a damage assessment tool. Determination of the magnitude and cause of damage to this fragile material is often the first step in prevention or reduction of future alteration. A number of examples of damaged core with accompanying hypotheses of cause are presented.

The most frequent alteration of the core is mechanical separation with accompanying mud invasion. The longitudinal or surview scan (e.g. Figures 5.10, 5.11) of core section typifies the separation of a laminated sand-shale sequence at the shale boundaries. Inspection of the slabbed core from these sections usually confirms that the core indeed separated at a sand shale interface rather than within the shale itself. Separations of this type are more common in thinly bedded sands and shales rather than in thicker, more structurally stable shale beds. Invasion of barite weighted drilling mud into the cracks may suggest that this separation occurred downhole during the coring operation. Prevention of this type of damage is very difficult due to the fact that the material is so fragile.

Cases of mechanical damage are often seen when inspecting recovered cores shock induced fractures may or may not traverse the core. Mud invasion patterns can also help in identifying the extent of the damage. The fractures can be caused by stamp failures, possibly caused by the weight of the core, triggered by a rough treatment of the core during surfacing or while in vertical position. A number of mechanical shocks and torque stresses applied to the core as it is being cut. If the core barrel is not circulated clean just off the bottom before commencing the coring process, it is possible to leave an accumulation of cuttings, shale slough, and drilling mud in the core barrel. In some cases, this rubble can jam the barrel preventing the core from entering. A mixture of large clasts and fill material can be attributed to rubble. The sand clasts may be further surrounded by drilling mud indicating non-competent core material. This part of the core could be useful for stratigraphic and petrographic analysis in the event that it can be correctly depth correlated.

In order to obtain parameters for reservoir properties from a core, plug samples are generally taken for cleaning and quantitative analyses. It is imperative that these plug samples reflect the reservoir as accurately as possible both in representation of the reservoir character and in quantitative results. Taking plugs in unconsolidated cores is difficult at best and sometimes results in serious damage to the plug sample and remaining core.

© 1990 NOVA HUSKY RESEARCH CORPORATION

The invasion of mud filtrate and especially mud solids into cores represents a common and often serious problem in the subsequent analysis of the core. The use of the CT scan is an invaluable aid in detecting the presence and location of such damage. Closer inspection of the damaged areas reveal both mud filtrate and, more seriously, mud solids invading in some cases. These mud particles are difficult to clean from the core and will cause inaccuracies in subsequent core analysis work. The best cure in such a case is obviously prevention of the invasion if possible by the use of face discharge coring bits and low fluid loss mud systems. Lost circulation material can be added in some cases to aid in this effort.

One of the more common occurrences of damage to sections of clean, massive unconsolidated cores is that of concentric fracturing or separation inside the inner barrel. This deterioration is thought to be a result of freezing, transportation shock, torque applied while coring or a combination of all these factors. Very little evidence of radial fractures has been found at the rig site by visually inspecting tube ends of the one meter sections of recovered material. Close inspection of mud invasion and fluorescence patterns show that in most cases, the separation point coincides with the depth of mud invasion. Since the mud filtrate is water and is replacing mostly hydrocarbons in the invaded zone, it provides a cement to hold the sand together as it is frozen, whereas the oil or gas saturated portion of the core does not freeze as completely or at the same rate. In core sections which were originally water wet in the formation, the concentric separation tends to be less severe or not present. However, some samples have been observed to exhibit this type of failure having never been frozen, suggesting that torque on the sample while it was being cored followed by transport shock may have been caused the damage. Again these samples were oil saturated *in situ* and invaded by fresh water drilling mud.

The fragile nature of unconsolidated formations makes them difficult to core and even more difficult to analyze and preserve without significant damage to the recovered material. Once the decision is made to attempt to core an unconsolidated reservoir, a number of precautions can be made to improve the success of the project. These preparations should begin early in the life of the well in determining compatible mud systems, well deviation, hole size and bottom hole assemblies which will increase the chance of good core recovery. Care must be exercised as well in wellsite handling, transportation, laboratory techniques used while slabbing and sample taking, and finally in the analysis procedures themselves.

© 1990 NOVA HUSKY RESEARCH CORPORATION

6.0 CONSOLIDATED MEDIA

6.1 Introduction

This chapter describes the efforts of applying Computer Assisted Tomography for the characterization of consolidated media. A number of different areas were evaluated. These areas included core visualization, identification of heterogeneities, mapping of bulk density, porosity, effective atomic number, vugs and fractures.

Seven different reservoirs were tested. The results of six of them are presented here while the seventh one is discussed in chapter 9. The six tested reservoirs are; i) Halkirk, a sandstone reservoir; ii) Bluesky, a dolomitic sandstone reservoir; iii) Rainbow Keg River "A" Pool, iv) Rainbow Keg River "G" Pool, v) Trout vi) Wabamun and vii) Berea. Each of these reservoirs are discussed separately:

6.2 Characterization of the Halkirk Reservoir

6.2.1 Sample Description of the Halkirk Reservoir

Three full diameter core pieces ranging from 0.10m to 0.20m in length were mounted inside the water ring core holder. The water ring core holder was initially used to reduce beam hardening, a common artifact in the images of consolidated material. The cores were marked with their location numbers (8,9 and 29) and were oriented with these numbers facing forward and upwards in the tunnel (Figure 6.1). The first slice of each core was 0.005m inside from the face marked with these location numbers. Scans were taken along the length of the cores every 0.005m. Dual energy scans were performed at 140kVp and 85kVp respectively, with core piece #8 scanned at eight (8) locations, core #9 was scanned at twelve (12) locations and core #29 was scanned at twenty (20) locations at each kVp level. All scans were archived on tape and processed using the NHRC post processing package. The black and white photographs for each slice are shown in the associated NHRC report. Typical samples are presented here.

6.2.2 Results

The first piece scanned was Core #8. The overall picture of this core shows a very homogeneous piece with the majority of the CT numbers within a close range (in the black and white pictures). There are one or two high density inclusions which show as whiter spots in virtually all of the

© 1990 NOVA HUSKY RESEARCH CORPORATION

slices scanned. A typical example is given in Figure 6.2. The density calculated from the CT data throughout this core ranged from 2,080 to 2,140 kg/m^3 with an average of 2,100 kg/m^3 (Table 6.1). The average density given by the service company for this core section was 2,120 g/m^3 (Table 6.2). The determined porosities from the CT data of this core range from 19.36% to 21.41% with an average of 20.93% (Table 6.1). The service lab results show 20.2% porosity (Table 6.2).

The analysis continued with Core #3. Again this core was very homogeneous and a uniform colour scheme was observed which encompassed the full diameter of the core. There are a few higher density inclusions but they are relatively small in area. The CT derived densities range from 1,960 to 2,020 kg/m^3 with an average of 1,980 g/m^3 (Table 6.1) while the service lab result was 2,030 g/m^3 (Table 6.2). The CT porosity ranged from 24.0% to 25.9% with an average of 25.1% (Table 1) and the service lab porosity was 23.6% (Table 6.2).

Finally, core #29 was tested. The same trend exists in this section of core which is also very homogeneous and with an even colour across the entire core diameter. There are a couple of lower density areas (possibly the ends of a different layer) which showed up. An example is shown in Figure 6.3. The CT density range was from 1,950 to 2,040 kg/m^3 with an average of 1,970 kg/m^3 (Table 6.1), while the service lab density result was 2,030 kg/m^3 (Table 6.2). The CT data porosity ranged from 22.7% to 26.2% with an average value of 25.5% (Table 1) and the service lab porosity was 23.9% (Table 6.2).

6.2.3 Discussion

The CAT scan derived petrographic analyses had a very good agreement with the independent service lab results. The longitudinal data from the CT scans are presented as colour graphs in Figures 6.4 to 6.6. In these graphs different density ranges are represented as different colours within a set scale of 100 CT units. These graphs are a compilation of all the individual slices stacked upon each other in a "coronal" type mode (Figure 6.7). The region of interest may be moved up and down the core diameter if a specific characteristic needs to be investigated. This allows the identification of cracks, fissures, high density inclusions with respect to the location inside the core in both length and diameter.

The colour scheme for core #8 has only two colours green and yellow (Figure 6.4). This represents a CT number range of 200 CT units and consequently a tight range or homogeneous density range also. One can see that this trend is consistent both across the core diameter and the core length scanned. Core #9 has an even tighter density range as the colour scheme is

© 1990 NOVA HUSKY RESEARCH CORPORATION

predominantly dark green (Figure 6.5). In core #29 one can see an area where there seems to be a higher density inclusion with respect to the rest of the core (Figure 6.6). This shows as a yellow patch half way up the core in amongst the larger areas of dark green. The trend of this inclusion can be followed with continuous scanning and graphs such as Figure 6.6.

In comparing these two methods, CT and service lab, one must take into account the difference in techniques. The CT method analyzes the core in very small sections calculating the petrographic properties in small increments and then taking an average of all of these small sub- sections, whereas the service lab method is a single measurement of the whole core at once. In comparing the performance of the CT core method to industry accepted routine methods, the CT method runs between 1% to 6% difference in the values for bulk density and porosity (Table 6.2).

6.3 Core Characterization from the Bluesky Reservoir

6.3.1 Sample Description and Scanning Technique

The Bluesky reservoir is a dolomitic sandstone with areas of pure dolomite. Nine sections of core from three wells each about 0.20m long were borrowed from the ERCB storage lab for CAT scanning. The cores were given code names representing location and depth and they were scanned in approximately 0.05m intervals. The cores were mounted inside an 0.10m OD, 0.0063m thick aluminum pipe inside the scanner gantry. The cores were scanned at energies of 140kVp and 85kVp. Some of the cores were 2/3 slabbed. In these cases, a small 1/3 piece of Berea sandstone was put on top of the 2/3 section to fill the void and give a cylindrical object. This trick reduces shape artifacts in the reconstruction process.

6.3.2 Experimental Results

Black and white photographs for all the slices are given in the related report and they are not presented here with the exception of typical examples which are given as colour graphics. A brief description of each core piece is given below.

- **Core A3**

Five scans (identified as slices #1 to #5) were done with slices at the 0.03, 0.08, 0.13, 0.18 and 0.23 m marks starting at the face marked A3 with the arrow pointing up and facing forward. Slices #1 and #3 showed relative homogeneity across the diameter as evident by a consistent grey

© 1990 NOVA HUSKY RESEARCH CORPORATION

colour. Slice #2 had an extra large white spot in the upper left-hand portion that suggests the presence of a higher density material. Slices #4 and #5 showed that a low density area is present, as indicated by darker black areas. This may be a vug, fracture, or just lower density sand. A typical example of the high density core is shown in Figure 6.8.

o **Core B2**

Five scans (slices #6 to #10) were done at locations 0.02, 0.07, 0.12, 0.17 and 0.22 m marks with the arrow pointing up and the face with the arrow put on front. Slices #6 and #8 showed good homogeneity but in picture #7 there was evidence of very small high density regions indicated as white spots. Slices #9 and #10 showed a homogeneous sand with several low density areas. Slice #10 was typical of core breakup at the very end of the core length. A typical example is shown in Figure 6.9. As seen in the figure the density (CT number) of this slice is far denser than the one in Figure 6.8.

o **Core B3**

Two scans (#11, #12) were taken, one at the 0.06 m mark and the second at the 0.11 m mark. Slices #11 and #12 showed reasonable homogeneity.

o **Core B6**

Two scans (#13, #14) were done at the 0.04 and 0.09 m marks. Slices #13 and #14 showed that there could be two zones of varying density along the length of the core. A possible explanation could be different bedding planes. These two planes were shown by the difference in grey colour in the two slices. Slice #13 had a much darker colour scheme than slice #14 (i.e. the average density in slice #13 is lower than that of slice #14). Moreover the familiar high density spots were very clear in slice #14.

o **Core C2**

Three scans (#15-#17) were taken at the 0.03, 0.08 and 0.13 m marks. There was good homogeneity across the 2/3 section (pictures #15, #16 and #17). An example is shown in Figure 6.10. The 1/3 piece of Berea is show as green is colour while the rock piece is red.

© 1990 NOVA HUSKY RESEARCH CORPORATION

o **Core D3**

Three scans (#18-#20) were completed at the 0.05, 0.10 and 0.15 m marks along the core length. This piece had a wide variety of densities indicated by the varying shades of grey colour. Slices #18, #19 and #20 showed these colour variations quite clearly. The density variations covered the full area of the 2/3 slabbed section. Figure 6.11 shows an example of this more heterogeneous sand.

o **Core D5**

Three scans (#21-#23) were done at the 0.05, 0.10 and 0.15 cm marks. This core had relatively good homogeneity because of the consistent grey colour scheme shown in slices #21, #22 and #23. Some low density features are seen in slices #22 and #23.

o **Core C1B2**

Four scans were taken on this piece at the 0.04, 0.08, 0.12 and 0.16 m marks. Slices #24, #25, #26 and #27 showed that this core had a variable density section in the first half and low density regions in the second half. Its density was considerably lower than the previous pieces, as evidenced by lower CT numbers.

o **Core C1B6**

Three scans (#28-#30) were taken at the 0.03, 0.06 and 0.09 m marks. Slices #28, #29 and #30 showed the presence of a low density line, most probably a crack, running through the middle of the core in the top half section of the core. Otherwise, the core was quite homogeneous.

6.3.3 Data Analysis and Interpretation

The raw CT data consists of an array of numbers, each number coinciding with a volume element (or voxel) of dimensions 7.5×10^{-4} x 7.5×10^{-4} x 3.0×10^{-3} m, the sum of which make up a single CT slice or scanned segment. To begin the analysis, that portion of the data which corresponds to the object of interest is selected. In the present case, this region of interest is circular, and includes only the 0.09 m diameter rock section.

© 1990 NOVA HUSKY RESEARCH CORPORATION

The CT numbers are next converted to bulk density values, using a previously derived correlation (Kantzas, 1989). For the first seven core sections, from two wells, the average bulk densities vary from 2,150 to 2,290 kg/m^3, with little variation within the section except in piece C2. The two pieces from the third well, have consistently lower bulk density averaging 2,050 kg/m^3.

If the mineralogy is known, simple, and homogeneous, then the grain density of the dominant mineral can be obtained directly from reference tables, and combined with the bulk densities to calculate porosities at each location. For this study, the rock was initially assumed to be primarily quartz, and thus a grain density of 2,650 kg/m^3 was chosen. Calculations based on this grain density led to either very low or negative values for the porosity. This implies that the actual grain density, as seen by the CT scanner, is higher than that expected for quartz.

The most direct approach is to determine the mineralogy by a separate technique, and then select an average grain density consistent with that mineralogy. Results of an XRD analysis of a small portion of core from section B2 show that the rock is mostly quartz (71%), dolomite (14%) and clay minerals (12%). Using values 2,650, 2,830, and 2,650 kg/m^3 for these three components respectively, a weighted average of 2,680 kg/m^3 is calculated as the average grain density of this "dolomitic sandstone".

When this grain density was combined with the bulk densities derived from the CT data, to determine porosities, some of the values were still anomalously low or negative. This implies that the grain density in these locations is higher than the average value. The ideal solution to this problem would be to have an independent way of determining grain density (or mineralogy) in each volume element, and then that specific value could be used to calculate porosity.

One possible way of doing this uses the data obtained from a CT scan at lower energy to calculate the "effective atomic number" (Z_{eff}) of the material in the voxel. Values of Z_{eff} calculated from CT numbers obtained from low energy scans of Bluesky core sections vary from 13.9 to 14.5. Z_{eff} values can be determined for pure minerals as a weighted mean of the atomic numbers of the constituent elements.

Unfortunately, in this rock at least, the Z_{eff} does not provide an unambiguous distinction among the minerals present. An approximation was made, based on a directly measured value of Z_{eff} of a sample of natural dolomite, and assuming the rock to be a mixture of dolomitic sandstone (with grain density 2,680 kg/m^3 and natural dolomite. Although this approach gave fairly consistent

© 1990 NOVA HUSKY RESEARCH CORPORATION

porosities for most of the core sections, the values are significantly higher than values obtained from routine core analysis.

To resolve this more definitively, we proceeded to select and cut two plugs from one core section (B2). Location was based on the homogeneity of the bulk density values, and on the black and white pictures. Pore volume was measured directly with nitrogen using Boyle's law, and bulk volume and mass were also determined directly, allowing calculation of overall bulk density and porosity.

The CT values of bulk density appear to be 100 kg/m^3 (0.1 g/cm^3) lower than directly measured values. Similar comparisons on plugs cut from Berea sandstone and various dolomites showed a discrepancy of similar magnitude. To correct this, a small change was made in the correlation coefficient relating CT number with bulk density, and corrected values of bulk density and porosity were obtained as shown in Table 6.3. Increasing the bulk density by 100 kg/m^3 results in a porosity change of 3.8% so that the corrected average porosity of the section from which the plug was cut becomes 14.2%. This compares fairly well with the directly measured value of 12.8%. The corrected coefficients were used for bulk density calculations presented throughout this work.

6.4 Characterization of Core from the Rainbow and Keg River "A" Pool

6.4.1 Sampling Description and Scanning Technique

Two cores from the Rainbow Keg River "A" Pool were brought for x-ray scanning. The objective was to identify which of the two cores was more uniform so it could be used for a coreflood experiment. The two cores (coded C56 and C52 respectively) were full diameter cores of approximately 0.25m length each. They were scanned while mounted in the water ring at energies of 140kVp and 105kVp. The scans were further processed for bulk density and porosity estimations. Seventeen slices were taken from each core.

6.4.2 Experimental Results

Core #56

This section of core has the same features all the way through it as these slices did not show much deviation in shading. There seems to be the same density distribution, area wise, as evident from the white to dark ratio from picture to picture. The calculated densities of each slice is shown in

© 1990 NOVA HUSKY RESEARCH CORPORATION

Table 6.4. One can see from Table 6.4 that there is a very tight bulk density gradient from 2,300 to 2,400 kg/m^3. This is also consistent with the porosity values listed in Table 6.4. The range of porosities slice by slice was 0.15 to 0.19. The average bulk density derived from the CT data was 2,3579 kg/m^3 and the average porosity was 0.17.

Core #52

The petrographic properties of this section can be found in Table 6.5. The range of bulk density slice by slice for the core length was 2,1515 to 2,4314 kg/m^3 and the porosity of 0.14 to 0.24. The black and white figures clearly show evidence of a wider range in these two properties. The ratio of white to dark shading changes near the center of the core length towards the end that was scanned. The core analysis results are shown in Table 6.5. The average bulk density was reported as 2,380 kg/m^3 and the average porosity of 0.162. The CT produced averages for bulk density of 2,3579 kg/m^3 and porosity of 0.17 (Table 6.5).

6.4.3 Discussion

The petrographic analysis based on CT produced images agreed closely with the standard core analysis methods. The two properties, bulk density and porosity, for both cores had very good agreement at the two decimal place accuracy. The original calculated results were corrected after other core scan studies revealed that there was a consistent difference between standard core analysis and CT analysis of 100 kg/m^3 in the bulk densities. Therefore the calibration line used in the algorithm of the NHRC software was adjusted to compensate for this deviation.

Core #52 had the widest range of bulk density (2,1515 to 2,4413 kg/m^3) along the length that was scanned. This also affects the porosity range (0.14 to 0.24). The ratio of white to black shading in the CT image photographs changes along the core length.

The colour graphics (Figures 6.12 and 6.13) are produced from the in-house software using the individual slices. They represent an interpolation of individual slices stacked side by side in the "coronal " mode. This graphic representation of core #52 (Figure 6.12) provides a method of looking at the pattern of density change along the core length at right angles to the original slices. The colour scale on the right side shows that this core's range is from 100 to 900 CT units. There are two small areas of lower CT units, one in the lower left corner and the other in the upper right

© 1990 NOVA HUSKY RESEARCH CORPORATION

corner. These two areas are most likely vugs as they have CT numbers in the order of 100 units, which is characteristic of holes with either a small air pocket or very loosely packed grains.

Core #56 had the smallest or tightest range of bulk density, 2,3153 to 2,4037 kg/m^3. Consequently the porosity range was also tighter, 0.15 to 0.18. Since the range of the petrographic properties is small then the conclusion derived from the CT images is that this core is more homogeneous than core #52.

The colour coronal image of core #56 (Figure 6.13) confirms this conclusion. The CT number range, from the colour scale, indicates that we have CT numbers ranging from 500 to 800. There is one anomaly in the upper left side of the black and white picture. This higher density area, 900 to 1100 units, is indicative of a high density inclusion most probably an anhydrite type of nodule. This small enclosure is at the surface and could be seen visually. Overall the remainder of the core had an evenly spread density as the colour distribution from Figure 6.13 shows. Thus core #56 would be a good source for a core plug anywhere along the length with the exception of its area where the anhydrite inclusion shows at the surface.

6.5 Characterization of Core from the Rainbow Keg River "G" Pool

6.5.1 Sample Description and Scanning Technique

Mr. Rick Davies of Husky Oil brought nine boxes of Canterra Mobil Rainbow cores of the Keg River "G" Pool horizontal well to NHRC for CAT scanning, looking for possible bedding planes as a key to the core orientation in the formation.

These cores were received directly from the coring company before cleaning and cutting. Initial scans were done on the cores at an energy of 140 kVp. Some dual energy scans were also performed for further analysis. Most of the core pieces were long i.e. 0.10 to 0.60 m, and were scanned at such distances as to achieve four to five slices per length of core. They were then sent to AGAT Laboratories for cleaning and cutting into smaller sections. Dual scans at 140 and 85 kVp were done on the cleaned core sections. Fifty black and white photographs of the scans were taken. They are included in the original report. Here only representative samples are presented. Every attempt was made to duplicate the scan locations done in the previous 140 kVp scans.

Results showed that this core section has numerous vuggy areas in varying proportions and size to the core area. One section of core gave a trace indication of possible planes, but further

© 1990 NOVA HUSKY RESEARCH CORPORATION

investigation confirmed that these were in fact areas of stromatoporoids and not bedding planes. Consequently no orientation of the core could be made. All scans were archived on magnetic tape and processed on in house software for petrographic properties, including bulk density, porosity, and effective atomic number.

6.5.2 Results

In general the fifty black and white pictures showed that this section of core has numerous vuggy areas both small and large and with varying distributions in the core area. Some examples are shown in Figures 6.14 to 6.21. A common characteristic of all images is the higher density perimeter. This can be attributed to hardening effects but it is not uniform. It could also be attributed to accumulation of fines due to mud invasion. Probably both causes are the contributing. Figure 6.14 shows a sample with oriented vugs. In Figure 6.15 the core is divided into two "lower" density clusters which are separated by higher density material. A highly vuggy core section is shown in Figure 6.16. Figure 6.17 shows two relatively lower density regions (red, black) and two higher density regions (light blue tones) separated by a line of three vugs that look almost like a fracture. Figure 6.17 looks like a mud invaded sample while Figure 6.16 is more typical of a hardening effect. However, since the core is not too thick or too dense it is concluded that what we observe is related to fines invasion. Figure 6.18 to 6.20 show the layer structure which was attributed to stromatoporoids. Note the red streaks which are parallel to each other. Finally, Figure 6.21 shows a distinct density layering which is also typical of mud invasion type phenomena.

Some of the slices showed that larger vugs are elliptical and trend towards a north-south direction in relation to the core orientation in the CT instrument. These vugs do not occur consistently throughout the core section. Other sections have pieces missing on the edges or larger vugs or holes which take up bigger percentages of the core area.

Additional analysis on these scans yielded the petrographic properties found in Table 6.6. The bulk densities ranged from 2,100 to 2,500 kg/m^3 and the porosity ranged from 7.3 % to 22.8 %. The predicted properties agree reasonably well with the conventional core analysis data. It must be noted that the bulk density predictions had to be adjusted to correct for the deviation of limestone from the calibration line. It must be also noted that the CAT scanner predictions are averages on single slices while the core analysis predictions are averages over the whole core piece. It is not expected to get a perfect match unless the whole core is scanned.

© 1990 NOVA HUSKY RESEARCH CORPORATION

6.6 Core Characterization from the Trout Reservoir

6.6.1 Background

This section deals with the examination of applications of CAT Scanner technology in the more accurate description of carbonate reservoirs. In particular, the potential of complementing well logging with Computer-Assisted Tomography on core specimens was tested. The example was a core from the Canterra *et al.* Trout in the Keg River Formation. The CAT Scanner postprocessing software package was used for predictions on bulk density, effective atomic number and porosity. These predictions were compared to the results from routine core analyses. The ELAN software package was used for the interpretation of well logs.

CAT Scanning gives a higher resolution description of parameters such as bulk density and porosity than is obtained by routine core analyses using procedures which give average values for the selected sample tested. CAT Scanning uniquely provides three-dimensional mapping of these parameters as well as the distributions for heterogeneities and mineral inclusions throughout the core. As such it is a powerful assistance in the overall description of core scanning for bulk density, is excellent for high porosity samples, but less satisfactory for high density low porosity cases. This may be due in part to the fact that CAT Scanning measures total porosity while routine methods give only inter-connected porosity values.

6.6.2 CATscan Analysis

The core section brought for analysis was approximately 5.5m long and it was cut in forty five pieces. An analytical laboratory had already extracted and analyzed part of the core. The following strategy was used for the scanning work. All pieces were scanned in two different energy levels namely 140 and 85 kVp. Because of the potentially enormous amount of data involved only one slice was taken from each piece. In addition, 7 pieces of core underwent a more detailed examination by scanning every $5x10^{-3}$ m with a slice thickness of $3x10^{-3}$ m. Although this strategy gave a $2x10^{-3}$ m gap in between slices, it provided a fairly detailed description of these core pieces. All dual scanning work was processed to give predictions of bulk density and porosity. At the same time CT number and bulk density maps were prepared in different planes (Figure 6.23 to 6.38).

Table 6.7 provides a comparison of the core analysis and the CATscan analysis results for the pieces that have been analyzed in the core laboratory. The porosity and bulk density are given as

© 1990 NOVA HUSKY RESEARCH CORPORATION

a function of depth. The physical property which is directly measured in the CATscanner is the bulk density. Comparison of bulk densities with the core analysis laboratory gives excellent agreement with the exception of the very last piece which has a difference of 7%. For the rest of the samples the difference is better than 4%. For the grain density a value of 2,830 kg/m^3 was used. The core laboratory measures the porosity directly, then extracts a value for grain density from the measured bulk density and porosity. We measure the bulk density, introduce grain density into the input data and the porosity is then calculated from the two values of density. It can be seen (again with the exception of the very last piece) that the agreement is excellent in all samples with porosity greater than 10% while the agreement becomes worse as the porosity reaches the value of zero (Table 6.7). In most cases the deviation in porosity can be attributed to bulk density differences. In some cases the difference can be attributed to grain density discrepancies.

The deviation in the bulk densities may indicate an inherent weakness in the CAT scan procedures for high density samples. The bulk density is measured in CAT scan using a calibration curve of CT number versus bulk density. The deviation of the two different methods at high densities may indicate that more calibration samples are needed in the high density range. On the other hand, it must be recognized that core laboratory analysis only measures the interconnected porosity, while the CAT scan provides both interconnected and isolated porosity. This is consistent with CT porosity being generally greater than routine core analysis (Table 6.7). This is also evident from the fact that logs of total porosity are in closer agreement with CAT scan predictions than core lab analyses for low porosity samples. Comparative results between log analysis, core data and CAT scan are given in Figure 6.22.

Figures 6.23 to 6.26 are graphical illustrations of four slices of the core. Each colour shows a different bulk density level. Vugs, fractures and high density areas (e.g. anhydrite) can be easily identified. Table 6.8 shows a complete listing of all single slice pieces scanned. Mean values of bulk density and porosity are presented. Table 6.9 shows the detailed scanning results on a number of pieces of core from the same reservoir. The scans were performed in 0.005m intervals with a 0.003m collimator thickness. These scans show how higher resolution of physical property distributions can be obtained through the scanning technique. Note that four and five % porosity units differences are common within the length of a single piece of rock. Routine core analysis presents an average value for meter connected porosity over the sample tested.

© 1990 NOVA HUSKY RESEARCH CORPORATION

6.6.3 *Use of CATscan Data in Log Analysis*

The well log analysis was performed by Dr. Mark Skalinski of Husky Oil. The well was logged using: DLL*-MSFL*, LDT*-CNL*-GR, BHC* and Formation MicroScanner (FMS*) logs. The reservoir is dolomitic, locally anhydritic or shaly, displaying varying degrees of secondary (mainly vuggy) porosity.

The log interpretation was performed using an ELAN* program from the Schlumberger ELITE Workstation. The ELAN* solves the interpretation problem by minimization of the incoherence function. This function is defined as the quadratic sum of squares of the differences between the observed log readings and the reconstructed logs for a given model. The interpretation models which are based on geological information, core description and information obtained from CATscan can be defined as follows:

MODEL	DESCRIPTION	COMPONENTS
1	Vuggy Dolomite	DOLOMITE, SHALE, VUGS, WATER, OIL
2	Fractured dolomite	DOLOMITE, SHALE, FRAC, WATER, OIL
3	Anhydritic dolomite	DOLOMITE, SHALE, ANH, WATER, OIL

The log response of isolated vugs was defined assuming that they are bypassed by sonic waves i.e. $DT_{vug} = DT_{ma}$ and that their conductivity is low. Resistivity, therefore, is responding mainly to the intergranular pore water volume regardless of the fluid saturation of the vugs. Fracture response was mainly driven by high conductivity of the flushed zone obtained from MSFL.

The models were combined using probability logic switching to MODEL 2 or 3 respectively when fracture or anhydrite volume was significant. Figure 6.22 shows the ELAN* output combined with standard core analysis and CATscan porosity. Note the very good agreement between core, CATscan and log porosities (track 3), where log porosity is treated as the sum of intergranular and secondary components.

---

* Trademark of Schlumberger

© 1990 NOVA HUSKY RESEARCH CORPORATION

The CATscan slices on Figures 6.23 and 6.26 illustrate: intergranular and pin point vugs (Figure 6.23), leached fossil porosity (Figure 6.24), leached vugs and anhydrite (Figure 6.26) and fractures (Figure 6.25).

The rest of the examples show some additional features that can be derived from the study of the images. Figure 6.27 is the same map as Figure 6.26 put in CT number units. This is the initial step for all the CT postprocessing work. Figure 6.28 describes the effective atomic number map. Having the bulk density and effective atomic number maps one can proceed in evaluating grain densities and porosities. Figures 6.29 - 6.36 show bulk density maps for different parts of the core. Different types and sizes of vugs and anhydrite inclusions can be identified. Finally, Figures 6.37 to 6.38 show the longitudinal representation of two core pieces, a uniform one and a vuggy one. By using this type of representation, one can follow the core features along the length of the core.

6.7 Core Characterization of the Wabamun Formation

6.7.1 Introduction

This section deals with the x-ray CAT Scanning of three core pieces from a NUMAC PCP TANGENT well. The cores were taken from the dolomitic Wabamun Formation. All of the pieces were slabbed prior to scanning. The 2/3 pieces were used for the scanning process.

The cores were mounted inside an aluminum core holder in the CT tunnel and scanned at two energies. Black and white photographs were taken. They are included in the original report. Longitudinal colour graphs of the CT data results are presented here. The CT data were processed using the postprocessing software developed at NHRC and were compared to standard core analysis for bulk density, porosity and mineralogy.

The very high bulk density of the core samples was probably the cause of beam hardening artifacts. These artifacts show a reduction in the CT numbers of the core perimeter. A simple linear smoothing filter was written to compensate for this artifact. The filter was tested with these cores and gave a small improvement of the image quality.

The comparison of the results of the core analysis to the results of CAT scanning showed that the agreement was excellent with core #5 poor with core #6 and extremely poor with core #4. When

© 1990 NOVA HUSKY RESEARCH CORPORATION

the porosity of the core approached zero, the disagreement between the methods became very large. However, the methodology of testing and the core sampling may have an effect on the deviation of the results. In order to verify this the core samples were scanned again. Effort was made to keep the scanner setting as close to the calibration settings as possible. The quality of the picture was not the best but the core analysis predictions improved significantly. The consistent setting of the photomultipier tubes is affecting the quality of the results.

One of the pieces, core #4, was used for creating a map of the observed fractures. The density and orientation of fractures of the core was recorded and drawn. It was observed that the fractures follow discrete patterns but this observation could not be generalized by the presented results due to lack of sufficient data. It is proposed that a number of different cores from a fractured reservoir should be scanned, and the fractures should be mapped for the whole reservoir. Then the fracture density and orientation could be analyzed and a general fracture pattern could be extracted.

6.7.2 Sample Description and Scanning Technique

Three 2/3 slabbed cores ranging from 0.10 to 0.20 m were mounted inside an aluminum core holder which aids in reducing beam hardening, a common artifact in CT produced images. One 1/3 slabbed piece of Berea sandstone was put on top of the each of the Wabamun pieces to reduce possible artifacts from the sharp angles of the slabbed piece. The cores were marked as Wabamun #4, #5 and #6 respectively.

The first slice or picture of cores #4 and #5 was 0.02 m in from the face marked "T", while the first slice of core #6 was 0.06 m from the face marked "T". Scans were taken along the length of the cores every 0.005 m with a slice thickness of 0.003 m. Dual energy scans were done (at 140kVp and 110kVp) with core #4 having 20 slices at each kVp level, core #5 having 18 and core #6 having 20 slices at each kVp level. All scans were then archived on magnetic tape for further processing.

The second set of scans consisted of re-scanning the three pieces at intervals of 0.005 m starting at 0.005 m from the face marked "T" and scanning of two additional pieces marked Wabamun #2 and #3. There were 37 slices for Wabamun #2, 38 slices for #3, 30 for #4, 27 for #5 and 33 for #6.

© 1990 NOVA HUSKY RESEARCH CORPORATION

6.7.3 *First Results*

Wabamun piece #4

Twenty (20) slices were taken from piece #4. As it was seen from the photographs, the images were far brighter in the centre than in the perimeter. This is an artifact that is common when very dense objects are scanned. This type of artifact can be damaging when an estimate of the rock physical properties is attempted. The images of this core show that the core is a tight piece of dolomite which is fractured. The fractures are partially filled with lighter density material (calcite ?) and partially open. The fractures show a distinct orientation and the fracture density varies along the core. In a couple of consecutive slices the fractures become almost invisible. This area is the bottle neck for any flow path that may be drawn through this core sample. An interesting observation is the fact that the fractures cut the rock in directions which are almost perpendicular to each other. Many parallel fractures are also shown. Finally fractures that start almost parallel to each other but then converge to form an "alpha" type structure are evident. The author is not in the position to explain why the fractures are formed in this way, but it would be very interesting to extract more information of this type from the reservoir and try to explain the fracture orientation. Figure 6.39 shows the fracture map for the Wabamun core #4. Figure 6.40 is a longitudinal image for piece #4. A long wide fracture is seen in the left part of the image, while a few hairline fractures are shown close to the centre of the core (700 - 800 CT number range). Figure 6.41 shows a slice of core #4. The artifacts due to density are shown as well as fracture patterns.

Wabamun piece #5

Eighteen slices were taken for piece #5. The same type of artifacts as in piece #4 are present in piece #5 although the effect is not as strong. Piece #5 is a very vuggy piece, with a continuum of big vugs along the core. Although is difficult to detect a direction for the vugs it seems that vugs tend to be formed parallel to two lines at 45° and 135°. In some slices hair line fractures are shown to connect larger vugs. The directions that these hair line fractures are following are the same as the directions in piece #4, although there is no evidence that the core orientation was maintained. Figure 6.42 shows a longitudinal image for piece #5. The connectivity paths and some hair line structures are evident. A typical slice is shown in Figure 6.43.

© 1990 NOVA HUSKY RESEARCH CORPORATION

Wabamun piece #6

Piece #6 was scanned at twenty locations. This core is covered with a mixture of vugs and fractures. There is one extremely large fracture (which could also be classified as a very long vug) and hair line fractures that again follow two almost perpendicular directions. "Alpha" type fracture structures are also clear. Figure 6.44 shows the longitudinal representation for piece #6 The large openings at the right side are what in the images shows as the big fracture. Figures 6.45 to 6.47 show slices where vugs and fractures can be clearly seen.

6.7.4 Smoothing of the CAT scanner data

The initial CAT scanner estimates were not satisfactory. The visual observations had shown that the artifacts due to hardening were significant. For this reason, a simple filter was designed to smooth the data. The filter is using a simple linear model to rise the peripheral data compared to the CT data in the centre of the core. A small FORTRAN program was written and incorporated into the existing CAT scanner postprocessing software. The program reads the CT number arrays and identifies the highest value in each row. All the other CT numbers of this row are increased proportionally to their distance from the maximum point and their difference from the maximum value. With this simple trick all the rock features remain unaltered relatively to each other. The same algorithm is repeated using all the columns. So the filter is a double pass filter, since each pixel is adjusted twice, once through its row maximum and once through its column maximum.

The filter was applied to both high and low energy CT number arrays. The filtered data were then used as input for the CAT scanner postprocessing software. The results of the bulk density and porosity were better but still not satisfactory.

Since the quality of the results and the smoothing algorithm did not produce the desired accuracy a new set of experiments was attempted. With this new set of experiments the focus was in eliminating the hardening effect by adjusting the photomultiplier (PM) energy in the CAT scanner console. At the same time a sensitivity analysis of the CT number data as a function of the photomultiplier tube setting was performed. It was observed that the CT number array is extremely sensitive to the PM tube setting. Adjustment of $\pm$ 40 volts on the PM tubes can change the mean CT number value by 200 units or more. These core pieces were very dense and it was initially felt that adjusting the PM tubes would improve the contrast. This is true and for visualization purposes tube adjustment serves well. However, when physical properties are to be estimated, the scans have to be taken at the PM setting which is the same with the setting of the

© 1990 NOVA HUSKY RESEARCH CORPORATION

PM tubes when the calibration line was estimated. Adjustments on the PM tubes causes the calibration line to shift and reduces the accuracy of the physical property predictions. Effort was taken to stay as close to the calibration settings as possible. The quality of the pictures (contrast) was not as good as in the first set of runs but the hardening rings were not present. The scans were taken at 140 and 110 kVp energies and the physical properties of the core were recalculated.

Table 6.11 shows the bulk density and porosity results for the first three pieces of rock. The average bulk density for core piece #4 is 2,710 kg/m^3 (error of 2.87%) and the average porosity is 4.34% (error 190%). For piece #5 the bulk density is 2,580 kg/m^3 (error 1.17%) and the average porosity is 8.42% (error 19.0%). Finally, the predictions for core piece #6 are for bulk density 2,630 kg/m^3 (error 1.13%) and for the porosity 6.78% (error 23.27%). It is evident by the results that the relative error was significantly reduced. The CAT scanner is still underestimating the bulk density and at very low porosities the error is still large, but the predictions are much better. The reason that piece #5 shows actually lower porosity than the core analysis is because the region of interest was taken in the middle of the core while the largest vugs are in the perimeter.

Table 6.12 shows how the porosity can be divided to fracture/vug porosity and matrix porosity keeping the same threshold as before. Being encouraged from these last results we run two additional sets of scans as described in table 6.13. The comparison of vug-fracture and matrix porosity is given in Table 6.14.

6.7.5 Discussion

The main objective of this section was to try and map the fractures in the core samples. The mapping of vugs and the prediction of physical properties are also important, but the CAT scanner method was proved to be successful in the previous examples. Let us focus our discussion first on the fracture mapping.

A successful fracture map should address two issues; i) the identification of a fracture system; and ii) the orientation of the major planes. When core is used for this task, a number of parameters affect the quality of the results. The expected information is often compromised by the sampling process or drilling damage of the core. The resolution in 3-D is often poor and although the principle axes in the core can be identified with respect to each other, it is difficult to extract information about these axes with respect to the reservoir unless the core is oriented.

© 1990 NOVA HUSKY RESEARCH CORPORATION

With regards to the physical characteristics of the fractures in a core sample, one can extract information on extent of a plane in two dimensions, width of the plane, and whether or not the fracture is filled or open. This information can suffer because of the sample size and the lack of the proper overburden pressure. The information on the infill material can also be compromised by lack of adequate resolution.

However, a good description of the fracture patterns in a reservoir is of great importance for the design of a successful production strategy. The use of logging tools can be of great help in assessing the fracture patterns. Also additional information such as material anisotropy can provide information on possible stress axes which are based on the crystalline structure of the reservoir and are independent of position. Deposition anisotropies are important in identifying potential fracture patterns which are position dependent. Finally post depositional information (macrogeological data such as mountain lines etc.) can also help in the identification of fracture patterns.

Certainly, it is the combination of all the available data and not an individual piece of information that can provide us with a good fracture map. The CAT scanner, because of its finer resolution, compared to the logging tools, can add invaluable information in the overall characterization strategy. However, a large number of samples representing different depths and different wells should be tested before any interpretation is attempted. Such a project, although quite ambitious, could help characterize larger pools (such as those of Rainbow) but it might prove to be more difficult in smaller pools like those of the Wabamun Formation.

With respect to the prediction of physical properties and elimination of artifacts, testing of numerous samples had proved that there is a definite correlation between position of the sample in the CAT scanner gantry, setting of the detectors and quality of the produced image. Moreover, even at the perfect setup, large and very dense objects still are prone to artifacts. It seems that there is a density length correlation which dictates the maximum length (i.e. diameter) of sample that the x-rays can go through, for a given sample density. This is evident also from the principle equation of x-ray absorption (the Beer - Lambert law), but it is not always evident to the CAT scanner operator before scanning a sample. Work in this area is continued. Currently, we are focusing on keeping all parameters (i.e. core holder, positioning, photomultiplier tube setting etc.) as constant as possible. We will consider later the option of creating multiple correlation curves for different experimental setups.

© 1990 NOVA HUSKY RESEARCH CORPORATION

6.8 Berea Sandstone

In order to complete the picture on consolidated media we present a few images of Berea sandstone. The images show the clear bedding planes. Figures 6.48 and 6.49 show two scans on the same piece of core approximately 0.05m apart. The bedding planes can be shown as black and red layers which run parallel to each other. Figures 6.50 and 6.51 show the saggital and coronal views of the whole core (28 slices). The bedding planes are shown to go through the whole length of the core. Please note that the colour interval has been reduced to 50 CT units to magnify the presence of the bedding planes.

6.9 Summary

Several hundreds of slices were scanned in the course of this investigation. Seven different reservoirs were characterized with respect to one feature or another. Predictions about bulk density, effective atomic number, porosity and mineralogy were obtained for a variety of conditions. The CAT scanner proved to be an excellent tool for viewing and identification of various heterogeneities but also for the quantitative prediction of reservoir properties. Adjustments had to be made to quantify the results in various cases. Confidence has been built on the potential use of the CAT scanner.

© 1990 NOVA HUSKY RESEARCH CORPORATION

7.0 HIGH PRESSURE TESTING

7.1 Background

In order to assess the effect of overburden pressure on porosity, a number of simple tests were performed. The objective was to investigate whether some correction can be introduced to the postprocessing software so that we can correlate the sandpack porosity of the native core to the porosity at reservoir conditions.

7.2 Experimental

7.2.1 Experiment #1

A dry sandpack of 0.05m in diameter and approximately 0.13m in length was prepared using a teflon shrink tube to hold it together. The sandpack was put inside an aluminum core holder and pressurized using water for the overburden pressure. The sand was a typical silica sand with air permeability of 80 darcy ($8x10^{11}$ m^2) and it will be noted further on as sand #3.

The x-ray scanning was done at a single energy 140kVp. The post processing algorithm was used for the calculation of bulk density and porosity. One slice was scanned per pressure step. The pressure intervals were from 0 psi (0KPa) to 2500 psi (17238 KPa) with a step of 500 psi (3448 KPa).

After the core was scanned at 2500 psi (17238 KPa) the pressure was reduced back to zero. The core was left overnight and the same process was repeated the next day. After each pressure increase, the core was left for one hour to equilibrate before testing.

7.2.2 Experiment #2

The second experiment involved the same type of sand and packing and the same procedure, only this time during the first pressure cycle, pressurizing was followed by scanning of the core at ten slices. Only one slice per step was scanned during the second pressure cycle.

© 1990 NOVA HUSKY RESEARCH CORPORATION

7.2.3 Experiment #3

The third experiment was the same as experiment #1 with the exception of the shrink tube. It was felt that the shrink tube type may affect the packing of the sand after pressurizing. Instead of the teflon shrink tube, a rubber shrink tube, was used. Only one pressure cycle was attempted.

7.2.4 Experiment #4

In this experiment the same sand was used but the core was now saturated with distilled water. During the first pressure cycle, there was some water production. This water was not replaced during the second cycle. Single slices were scanned.

7.2.5 Experiment #5

The experiment was the same as #1, but a different sand was now used. The new sand (designated as sand #16) was finer and of air permeability of approximately 2.5 Darcy (2.5×10^{-12} m^{12}). Single slices were scanned.

7.2.6 Experiment #7

Since the sands in the heavy oil reservoirs are not at more than a few hundred psi pressure it was decided to repeat experiment #1 but change the pressure cycle from 0-2500 psi (0-17238 KPa) to 0-500 (0-3448 KPa) psi with a step of 125 psi (862 KPa). Two pressure cycles were attempted and single slices were scanned.

7.2.7 Experiment #8

This experiment was supposed to bring the sandpack to conditions close to unconsolidated core. The sand was saturated with a brine and then displaced by a 3000 mPa.s oil to connate water. The sand was scanned in single slices through two pressure cycles. Then it was subject to shocks and scanned again to observe possible fracturing.

7.3 Results and Discussion

The results of the aforementioned experiments are presented in Tables 7.1 to 7.8 in the form of CT numbers, bulk densities and porosities. The results of the first experiment are shown in Table 7.1.

© 1990 NOVA HUSKY RESEARCH CORPORATION

The porosity of the sandpack decreases from 35.63% at 0 psi pressure down to 31.45% at 2500 psi pressure which is 11.73% reduction of porosity. However, depressurizing to 0 psi (0 KPa) increases the pressure to 33.60% only. This yields a 5.7% permanent porosity reduction. The second pressure cycle is not as smooth as the first one but at 2500 psi (17238 KPa) reduces the porosity to 31.07% which is quite close to the first cycle.

The ten slice scans are presented in Table 7.2. The first observation is that the side of the sandpack (slice 1) is tighter than the centre (slice 10). As the pressure increases, the CT numbers increase as in the first experiments. At 2500 psi (17238 KPa) the CT numbers are almost the same in all slices. The compression makes the packing more uniform. However, when depressurizing, the core does not depressurize uniformly. The porosity change of slice #5 goes down from 37.72% to 32.25% (i.e. a porosity reduction of 14.50%). The porosity reduction in the second cycle for the same slice is from 34.21% to 31.20% (i.e. a porosity reduction of 8.80%).

Similar behaviour is observed in experiment #3 (Table 7.4). The porosity is reduced from 36.66% to 31.88% (i.e. reduction of 13.04%). There was no evidence of any effect of the shrink tube type. All the experiments reveal a considerable porosity reduction which is actually due to packing of the sand because of the overburden.

In experiment #4 the presence of water in the packing results in a somewhat different behaviour. To begin with, the porosity at 0. psi is far higher (43.79%). This is reduced to 37.96% at 2500 psi (17238 KPa), i.e. a porosity reduction of 13.31%, which is still higher than the initial porosity with air present even at zero pressure. It is tempting to think that the porosity algorithm is not accurate. However, the porosities measured in this experiment are in close agreement with previous independent results with the same type of sand. The second cycle might be somewhat in error. This is due to the fact that some water, which was produced from the core holder during the compression was not re-injected during the production.

In experiment #5 (Table 7.6) another sand is tested. This finer sand has a far smoother response to pressure. The initial pressure of 32.62% is reduced to 30.83% at 2500 psi (17238 KPa) i.e. reduction of 5.49%. In the second cycle the reduction is similar (i.e. 5.59%). The actual porosity values are also far closer to each other than with sand #3.

The response of Berea Sandstone on compression was much smoother than the sands. The porosity was reduced from 24.19% and 23.63% at zero pressure to 23.37% in both cases at 1500

© 1990 NOVA HUSKY RESEARCH CORPORATION

psi (10343 KPa), i.e. porosity reduction of 3.8% and 1.5% respectively. Because of overburden leaks during this test, a second cycle was not attempted. (Table 7.7).

The results of Table 7.8 for the two low pressure cycles with sand #3 also indicate porosity reductions of 3.9% and 3.93% respectively with an overall reduction of 4.87% respectively.

Figures 7.1 to 7.8 show the porosity vs. pressure plots for all the experiments. The most interesting observation is the presence of a hysteresis between cycles. This raises questions on what type of protocol should be used for adjusting the porosity estimates for pressure. The results also clearly indicate that the effect of pressure is more profound in coarser sands. Whatever type of correlation is to be developed it needs to be done for each specific sand separately. Results from one type of sand cannot be related to another sand without care. The other quite interesting observation is that the porosity of a dry sand and the porosity of a saturated sand seem to be different even under overburden. This result is quite strange and further investigation is needed towards this direction.

© 1990 NOVA HUSKY RESEARCH CORPORATION

8.0 MUD INVASION

8.1 Background

One of the most important initial plans of this project was the monitoring of mud invasion. In order to assess this task, three avenues were explored. At first, all the cores that were scanned were viewed for traces of mud invasion. Second, designing of experiments that would simulate the mud invasion conditioner were considered. Schlumberger of U.K. was thought to be an ideal partner for performing such experiments. However, Husky did not show any interest in this type of work and the idea was abandoned. Finally, a number of cores were scanned before and after extraction in an effort to observe any changes in the bulk density of the cores before and after the extraction.

8.2 Core Inspection

A large number of scans were performed during the course of this project. In all cases, the images were inspected for evidence of mud invasion. There were a lot of cases where core damage due to invasion of drilling fluids was quantified.

In unconsolidated cores evidence of mud invasion were shown through three different occurrences. Firstly, pieces of shale have been broken and dissolved in the drilling fluids (Figures 5.10-5.11). At the same time the perimeter of the core shows evidence of higher density material. This high density material forms a narrow annulus that has a direction parallel to the coring and flow of drilling fluids (Figure 5.11). In other cases, fluids have invaded a sand layer and caused significant reduction in the tightness of the formation resulting in a very poorly packed sand (Figure 5.29). As a result of the effect of mud invasion can be seen both as an increase or a decrease of the expected CT numbers depending on the location and condition of the sand.

On the contrary, in high density consolidated media, the presence of mud is shown as a bright ring in the perimeter of the core. This is due to the accumulation of fines which are entrained during the mud circulation and they are deposited inside the core. It can be easily confused with a common beam hardening artifact where again the perimeter of the core looks brighter than the center of the core. An easy way to distinguish between the two cases is to observe the shape of the ring. If it's uniform and symmetrical it is an artifact. If it is not symmetrical and spreads through the core in different locations then it is probably related to mud invasion. This phenomenon was evident in Figures 6.15 - 6.21.

© 1990 NOVA HUSKY RESEARCH CORPORATION

8.3 Core Cleaning

In order to investigate whether or not the cleaning has any effect on the mud invasion problem, a number of cores were scanned before and after cleaning. The core was analyzed using the post processing software and the bulk density averages before and after cleaning were compared. The drilling muds were also scanned. Four pieces of core were tested. One from the Trout reservoir, two from the Sundre reservoir and one from the Worsley reservoir. The results were shown in Table 8.1.

The Trout core was scanned at eight locations. There was no apparent change in the bulk density. The two Sundre cores were scanned in eight locations each. Again, there was no apparent density change. The Worsley core was scanned in fifteen (15) locations. No apparent density change was observed either. The results in Table 8.1 show a density difference between the pre and post extraction stage of approximately 30 kg/m^3 or less, which is within the experimental error in the range of densities used. Therefore, it is not considered to be significant.

Table 8.2 shows the CAT scanner estimated bulk density for some of the brines and muds. The mud densities are far higher than the brines which indicates a considerable amount of particles. Some of these particles are deposited in the core. If this is the case, the cleaning of the core does not remove any of this material.

8.4 Summary

Observations of the CAT scanning images can help in drawing conclusions about the degree of core damage due to mud invasion.

© 1990 NOVA HUSKY RESEARCH CORPORATION

9.0 DETERMINATION OF SULPHUR

9.1 Objective

This work aimed at developing a technique which allows the quantitative determination of the sulphur deposits in the Peppers reservoir, using Computer Assisted Tomography (CAT) scanning. The findings of this report were to be used as initial information for more detailed reservoir characterization and further sulphur determination work, which was conducted as a contract with Husky Oil. Although the results of the contract are confidential, one sample is provided for demonstration purposes.

9.2 Background

Husky *et al.* Peppers is a dolomitic reservoir which contains large amounts of sulphur. Analysis of the sulphur phase diagrams and reservoir conditions lead to the conclusion that the sulphur is in the liquid state. It is therefore a candidate for recovery by a fluid recovery method as if it was an oil reservoir. However, in order to initiate such a recovery scheme, one should have a good estimate of the amount of sulphur in place. Husky initiated a research program for the evaluation of this reservoir which involved, in various stages, Hycal, Tomotechnology and recently NHRC. This section will focus on the work done in NHRC with other work being used for comparative purposes.

9.3 Methods

9.3.1 Sample Description

For the method development stage two pieces of core were obtained. They were taken from the core drilled in the Husky *et al.* Peppers well and they were designated as pieces #12 and #52. The reservoir is a dolomite of the Leduc Formation. A summary of the core analysis of these two pieces is given in Table 9.1. Both of the pieces were received after they had been extracted with carbon disulfide (CS_2) and dimethyldisulfide (DMDS) in an effort to determine the amount of sulphur present. Piece #12 was brought to NHRC by Ion Adamache of Husky, who also arranged for piece #52 to be brought to the laboratory from Hycal Energy. Piece #12 was in excellent condition. On the contrary, piece #52 was in a very poor shape. It was wrapped in an aluminum foil and it was broken. The two largest parts where then re-wrapped in masking tape and used in

© 1990 NOVA HUSKY RESEARCH CORPORATION

the scanning tests. The core was not completely dry and had a very strong smell. Moreover, it was very brittle indicating that the prolonged exposure to the solvents had affected the rock texture.

9.3.2 Scanning Procedure

The scanning algorithm and calibration technique were developed at NHRC (Kantzas, 1989 a,b). This particular project helped us evaluate some aspects of our methodology. The cores were scanned at two nominal energies namely 140 kVp and 100kVp. Core #12 was scanned in over 0.015 m length at 0.001 m intervals with a collimator that gives 0.001 m thickness of the x-ray beam. The scanning started 1.5 10^{-2} m from the face marked 'top'. Core #52 was scanned using the 0.001 m thickness collimator but the scans were 0.02 m apart and the first scan was taken 0.015 m from the solid end of the core.

9.3.3 Postprocessing Algorithm

The CAT scanner data were analyzed for bulk density, porosity, effective atomic number, and mineral distribution. Region of interest tests were performed to estimate the average slice value of each property.

9.4 Results and Discussion

The results are presented in Tables 9.2 and 9.3. Colour graphics of the bulk density maps for a number of slices are given in Figures 9.1 to 9.13. The color code is the same for all the figures and covers densities of 1,000 to 4,000 kg/m^3. Each color corresponds to a 200 kg/m^3 density interval. The first piece (core #12) was in very good shape and there was no problem in the analysis of the results. The second piece (core #52) was not as easy to handle because of the damage and smell. During the analysis, we have observed that a very critical parameter for a quantitative core characterization was the value of the mean energy (in keV) which is used for the determination of the Effective Atomic Number of each pixel. This observation initiated another project for the exact measurement of the mean x-ray energy which was described in chapter 4. The results of this report are based on estimates of the mean x-ray energy, using literature values for the same type of tubes.

Figures 9.1-9.13 represent only parts of each slice. In particular, they are the regions of interest on which the core analysis estimates were determined.

© 1990 NOVA HUSKY RESEARCH CORPORATION

9.4.1 Core #12 - Description

Figure 9.1 shows the bulk density image for the slice of core piece #12 which was taken at 0.018 m from the top face. As seen from the color range of the image, bulk densities vary from 1,400-1,600 kg/m^3, to 3,400-3,600 kg/m^3. The low density areas are the areas with high porosity (matrix or vugs), while the very high density areas are anhydrite or cementing material. Colors up to yellow (i.e. densities up to 2,200 kg/m^3) could be considered as vugs. The vugs seem to run through the core diagonally. Unfortunately, there was no care taken to orient the core with respect to the reservoir. Therefore we cannot comment on the direction of the vugs inside the reservoir.

Figure 9.2 shows the slice which is 0.002 m lower than the one of Figure 9.1. The same pattern of vugs is shown, although the higher densities indicate that the vugs are reduced in size. The anhydrite piece at the 11 o'clock mark is still visible. Another piece of anhydrite appears at the 7 o'clock mark.

Going 0.001 m lower in the core (Figure 9.3) the two anhydrite pieces are still evident. Also some new vugs are appearing at the 2 o'clock mark. If a threshold value were assigned for the density where a vug starts, a vug size distribution can be obtained. However, it must be noted that the threshold value selection is quite arbitrary. A vug will never be an exact cylinder so that it can be treated as void space. Figure 9.3 and the following Figure 9.4, which is 0.003 m lower than the previous one, do follow the same pattern in the distribution of vugs and high porosity areas. The occasional piece of anhydrite is present but the high porosity areas seem to be within the same range and quite well connected. The same pattern is followed in Figure 9.5, while in the last two figures from piece #12, which are 0.027 m and 0.03 m from the top face respectively, the density pattern changes. The vugs are becoming larger in size and their distribution shifts to the 12 to 3 o'clock quadrant. However, good connectivity is maintained.

9.4.2 Core #12 - Derived Parameters

The results of the postprocessing algorithm for the core piece #12 are given in Table 9.2. The average bulk density as estimated from the CAT scanner is lower than the density given by the physical testing (2,500 kg/m^3 compared to 2,640 g/m^3 respectively), but the difference is easily explained by the fact that the core laboratory performed the analysis before the solvent extraction. The same applies for the porosity (5.5% from core laboratory and 10.97% from CAT scanner). However, if the porosity value from the CAT scanner is compared to the one reported by Hycal the

© 1990 NOVA HUSKY RESEARCH CORPORATION

agreement is excellent (10.97% to 11.5% respectively). Moreover, Table 9.2 gives the areal percentage of vugs, sulphur and dolomite for each slice. The core laboratory, and solvent extraction techniques cannot provide such information.

The scans from Tomotechnology did provide similar information; however, direct comparison is very difficult because it is impossible to scan at exactly the same place when going from one laboratory to the next. In their interpretation Tomotechnology presents a higher percentage of remaining sulphur and considerable amount of anhydrite which was not detected here. The images revealed some traces of anhydrite, which were incorporated with the dolomite, but nothing close to the 15% average areal saturation as shown in the Tomotechnology report. Since we have no access to the algorithm used by Tomotechnology we cannot comment any further on their results.

Comparing our results with the efficiency of the sulphur recovery by Hycal, we feel confident to say that the extraction process was very successful and the amount of total solids recovered corresponds to almost all the sulphur in the core. The good connectivity of the high porosity areas as shown in the CAT scanner images is probably responsible for this high recovery. However, the low value of the permeability of the core in relation to the permeability of core piece #52 is somewhat contradictory to the good sulphur recovery.

9.4.3 Core #52 - Description

Bulk density images are presented in Figures 9.8 to 9.13. Figure 9.8 shows the bulk density map of the first slice, 0.020 m in from the undamaged phase end. The average bulk density is relatively low, as opposed to the previous core piece and a large number of vugs are present. The largest portion of the map is of bulk density of 2,400 kg/m^3 or less. This is an indication of high porosity and probably high permeability.

The next figure (Figure 9.9) is taken 0.020 m further inside in the core. The picture is quite different now. Larger vugs are present and the lower density region is mixed with a region of high density. It seems that the upper part of the slice belongs to a higher density layer than the lower part. Some anhydrite is present at the 4 o'clock mark of the area of interest.

Figure 9.10, which is 0.020 m further inside the core, shows that the lower density region is not there anymore. The slice is predominantly high density, low porosity dolomite with small vugs

© 1990 NOVA HUSKY RESEARCH CORPORATION

distributed through its surface. This low porosity area should act as a barrier to any kind of vertical flow (such as the solvent extraction floods performed at Hycal).

In Figure 9.11 (again 0.020 m further inside the core), we see larger vugs mixed with very low porosity areas and some traces of anhydrite at the eight o'clock and twelve o'clock marks.

In Figure 9.12 (0.020 m further inside the core) the vug presence is reduced again compared to the high density area. However the vugs are distributed throughout the cross section of the slice indicating good connectivity although the cross section porosity is expected to be low.

Finally, Figure 9.13 shows the extend of the core damage and the existence of very large vugs. We are not in the position to comment whether the vugs were present in the core initially or whether they were caused by the solvent extraction of subsequent damage of the core is not clear. The fact is that these vugs increase the mean value of the estimated porosity quite significantly.

9.4.4 Core #52 - Derived Parameters

Table 9.3 provides the core property estimates for the slices of core piece #52. It is far more heterogeneous than core #12, with porosities varying from 4.36% up to 18.70%. The amount of sulphur present is significantly higher then in core piece #12. The average bulk density (2,380 kg/m^3) is again lower than the core analysis value (2,520 kg/m^3) which can be explained because of the presence of additional sulphur and core damage subsequent to core laboratory testing. The estimated average porosity (12.54%) by CAT scanner is again higher than Core Laboratory's and Hycal's estimates (11.4% and 9.2% respectively). However, taking into account that both these porosities were measured BEFORE the solvent extraction we feel confident that our estimate is realistic. Please note that the difference between the core laboratory measurements is quite significant.

The poorer sulphur recovery by Hycal is in good agreement with the higher residual sulphur in core piece #52. However, it is not very clear why the core piece with higher permeability and higher porosity (core #52), which was also deeper in the reservoir, gave lower sulphur recovery and higher residual sulphur. This piece also has the higher water saturation (see Table 9.1).

© 1990 NOVA HUSKY RESEARCH CORPORATION

10.0 CAPABILITIES AND LIMITATIONS OF COMPUTER ASSISTED TOMOGRAPHY

During this project a number of tests were performed and showed that Computer Assisted Tomography can be used in a variety of applications related to core analysis and reservoir characterization. These tests were described in the previous chapters and the results indicate that the CAT scanner will become an integral part of all core laboratories in a few years. However, there is a lot of work and research to be done to improve the quality of information. Some of the aspects and concerns for future work are described in this chapter. The following points need to be addressed.

i) Resolution: The resolution of the EMI Scanner is not bad. Other modified hospital machines have up to four times higher resolution. However, this is not enough for pore level visualization. New machines need to be designed to perform three dimensional pore mapping. These machines could work with drilling cuts, since mapping of a full diameter core at this level would be an enormous data analysis task.

ii) Energy expansion: It has been show that even at 140kVp energy there is an effect of the effective atomic number on density. To compensate for this the high energy output should be increased further, closer to 200kVp. On the contrary, the low energy should be decreased to 60kVp or less so that effective atomic number and k edge effects can be maximized. In order to do this, the hardware of the scanner needs to be redesigned. Moreover, since the energies will be so much different, in order to use a single reliable set of detectors, different scanning times need to be considered.

iii) Native core: For a full characterization of a native core the dual energy scanning cannot provide enough information. Independent physical property measurements are required. These properties could reflect the fluid content (ultrasonic, microwave or spin-echo). NMR imaging could be used as a prime candidate.

iv) Speed: A successful core analysis must be fast. The EMI 5005 Scanner is slow. More recent generations have far better speeds. The hardware must be totally redesigned to provide faster readings. It should also be automated to perform with minimum supervision.

v) Permeability: A core analysis tool will be successful only if permeability can be measured. This cannot be done by CAT scanners alone. A number of different measurements need to be combined (as in log analysis for example) to show permeability estimates.

© 1990 NOVA HUSKY RESEARCH CORPORATION

The above comments can be used as arguments that it is time to start considering the design of a core analysis scanner. However, even in its present condition, the scanner can be an extremely efficient tool to complement microscopic and log information.

© 1990 NOVA HUSKY RESEARCH CORPORATION

11.0 CONCLUSIONS

- Computer Assisted Tomography has been successfully used in the characterization of porous media.

- Extensive calibration is needed for quantitative prediction of porous media properties.

- A method for the measurement of the x-ray spectrum and the mean x-ray energy was developed, tested and implemented.

- The CAT scanner can be used for the characterization of unconsolidated media in the following ways:

    - core viewing
    - plug selection prior to slabbing
    - identification and mapping of heterogeneities (bedding planes, inclusions, shales)
    - bulk density
    - effective atomic number
    - porosity (if the fluid content is known)
    - fluid content (if porosity is known)

- The CAT scanner can be used for the characterization of consolidated media in the following ways:

    - core viewing
    - fracture mapping
    - vug mapping
    - identification and mapping of macroscopic mineral distribution such as dolomite in sandstone, sulphur in dolomite, anhydrite in dolomite, etc.
    - bulk density
    - effective atomic number
    - porosity
    - identification and mapping of bedding planes and stromatoporoids
    - mud invasion

© 1990 NOVA HUSKY RESEARCH CORPORATION

- Mud invasion can be traced and mapped. The extent of mud invasion cannot be quantified without further experimental work.

- The porosity of unconsolidated media is profoundly affected by the presence of fluids and the magnitude of the overburden pressure.

- CAT Scanners could be used as routine core analysis tools if some technical improvements are made on the existing equipment which was designed for medical use.

© 1990 NOVA HUSKY RESEARCH CORPORATION

12.0 ACKNOWLEDGEMENTS

The author would like to thank Energy, Mines and Resources Canada for partial funding of this project through the CANMET contract 23440-8-9233 named "Application of CAT Scanning in the Non-destructive Testing of Porous Media" and especially the Scientific Authority, Dr. Kamal Jha.

The author would also like to thank the following people for helping, in one way or another, with the completion of this project: T. Jack, D.F. Marentette, J. Chriest, B. Erno, P. Siska (NHRC), M. Stalinski, R.L. McKellar, S. Harding, S. Hirowatari, L. Rosenneger, N. Van Regen, I. Adamache (Husky Oil), R. Tiberio (PanCanadian Petroleum) and P. Wan (U. of Waterloo).

© 1990 NOVA HUSKY RESEARCH CORPORATION

13.0 REFERENCES

Abrams, A. and Vinegar, H.J., "Impairment Mechanisms in Vicksburg Tight Gas Sands", SPE 13883 presented at the SPE/DOE 1985 Low Permeability Gas Reservoirs held in Denver, Colorado, May 19-22,1985.

Alvarez, R.E. and Macovski, A., "Energy-selective Reconstructions in X-ray Computerized Tomography", Phys. Med. Biol., 21(5), p.733, 1976.

Allan, C.J., Keller, N.A., Lupton, L.R., Taylor, T. and Tonner P.D., "Tomography: an Overview of the AECL Program", Applied Optics, 24(23), p.4067, 1985.

Anderson, S.H. and Gantzer, C.J., "Determination of Soil Water Content by X-ray Computed Tomography and Magnetic Resonance Imaging", Irrig Sci, 10, p.63, 1989.

Ayral, S., "Computed Tomography: A Novel Technique Applied to Displacement Phenomena in Porous Media". Ph.D. Thesis, Columbia University, 1985.

Assink, R.A., Caprihan, A. and Fukushima, E., "Density Profiles of a Draining Foam by Nuclear Magnetic Resonance Imaging", AIChE J, 34(12), p.2077, 1988.

Baldwin, B.A. and Yamanashi, W.S., "Determining Fluid Saturation Distribution in Cores Using NMR Imaging", Paper SCA 8714, presented in the Society of Core Analysts Conference, 1987.

Baldwin, B.A. and Yamanashi, W.S., "Detecting Fluid Movement and Isolation in Reservoir Cores Using Medical NMR Imaging Techniques", SPE/DOE 14884 presented at the SPE/DOE Fifth Symposium on Enhanced Oil Recovery of the Society of Petroleum Engineers and the Department of Energy held in Tulsa, OK, April 20-23, 1986, SPERE, 4 , p.207, May 1989.

Baldwin, B.A. and Yamanashi, W.S., "NMR Imaging of Fluid Dynamics in Reservoir Core", Magnetic Resonance Imaging, 6, p.493, 1988.

Banavar, J.R. and Schwartz, M., "Magnetic Resonance as a Probe of Permeability in Porous Media", Phys Rev Let, 58(14), p.1411, 1987.

Bentsen, R.G. and Saeedi, J., "Liquid-Liquid Immiscible Displacement in Unconsolidated Porous Media" J. Can. Pet. T 20(1), P.3, 1981.

© 1990 NOVA HUSKY RESEARCH CORPORATION

Bergosh, J.L., Marks, T.R. and Mitkus, A.F., "New Core Analysis Techniques for Naturally Fractured Reservoirs". SPE 13653 presented at the SPE 1985 California Regional Meeting, held in Bakersfield, California, March 27-29, 1985.

Bergosh, J.L. and Lord, G.D., "New Developments in the Analysis of Cores From Naturally Fractured Reservoirs". SPE 16805 presented at the 62nd Annual Technical Conference and Exhibition of the Society of Petroleum Engineers held in Dallas, TX, September 27-30, 1987.

Bergosh, J.L. and Lord, G.D., "New Developments in the Analysis of Cores From Naturally Fractured Reservoirs". SPE 17479 (abstract only) presented at the SPE California Regional Meeting held in Long Beach, California, March 23-25, 1988.

Blackband, S., Mansfield, P., Barnes, J.R., Clague, A.D.H. and Rice, S.A., "Discrimination of Crude Oil and Water in Sand and in Bore Cores with nmr Imaging". SPEFE, 1(1), 31, 1986.

van den Bergen, E.A. and Jonkers, G., "Industrial Applications of Positron Emission Computerized Tomography" American Nuclear Society Conference on Industrial Radiation and Radioisotope Measurement Applications, Pinehurst, NC, p.10, 1988.

Briguet, A., "Imagerie par Resonance Magnetique Nucleaire dans les Materiaux Composites", Mol. Cryst. Liq. Cryst. Inc. Nonlin. Opt., 161, p.413, 1988.

Brooks, A.R. and Di Chiro, G., "Theory of Image Reconstruction in Computed Tomography". Radiology, 117, p.561, 1975.

Brown, J.M., "Computed Tomography and Magnetic Resonance Imaging of Water Distribution in Plants and Soils", Ph.D. Thesis, North Carolina State University, 1987.

Brown, L.D., "NMR Imaging: Principles and Recent Progress" Paper SCA 8812, presented at the Society of Core Analysts Conference, 1988.

Cannon, P., "CT Scanners Diagnosed as Good Medicine for Industry", Electronic Imaging '88, International Imaging Exposition and Confernce, p.451, 1988.

Cesareo, R., "Using a Computed Tomography Scanner for Nonmedical Applications", Nuc. Instr. and Meth. in Phys. Res., A275, p.420, 1989.

Chang, C. and Komoroski, R.A., "NMR Imaging of Elastomeric Meterials", Marcomolecules, 22, p.600, 1989.

© 1990 NOVA HUSKY RESEARCH CORPORATION

Chang, S.J., Oison, J.R. and Wang, P.C., "NMR Imaging of Internal Features of Wood", Forest Products Journal, 39(6), p.43, 1989.

Chatzis, I., Kantzas, A. and Dullien, F.A.L., "On the Investigation of Gravity Assisted Inert Gas Injection Using Micromodels, Long Berea Sandstone Core and Computer Assisted Tomography" SPE 18284, presented at the SPE Annual Technical Conference and Exhibition, held in Houston, Texas, October 2-5, 1988.

Chatzis, I., Macdonald, I.F. and Dullien, F.A.L., "Application of a Modified CAT Scanner in Non Medical Research", URIF Final Report, University of Waterloo, Jan 1990.

Chen, J.D., Diaz, M.M., Patz, S. and Lawrence, S.W., "Magnetic Resonance Imaging of Immiscible-Fluid Displacement in Porous Media", Phys. Rev. Letters, 61(13), p.1489, 1988.

Chen, J.D. and Wada, N., "A New Technique for Visualizing the Distribution of Oil Water and Quartz Grains in a Transparent, Three Dimensional, Porous Medium". SPEFE, 1, p.205, 1986.

Chen, L.S., Herman, G.T., Meyer, C.R., Reynolds, R.A. and Udupa, J.K., "3D83 - An Easy-to-use Software Package for Three-Dimensional Display from Computed Tomograms", Proc ISMII '84, IEEE Computer Soc. Int. Symp. on Medical Images and Icons, 515, p.309, 1984.

Christ, G., "Exact Treatment of the Dual-energy Method in CT Using Polyenergetic x-ray Spectra", Phys. Med. Biol., 29(12), p.1501, 1984.

Chu, F.Y. and Sawicka, B.D., "The Application of Gamma-ray Computed Tomography in Solid Insulator Diagnostics", Presented at the IEEE International Symposium on Electrical Insulation, held in Boston MA, June 5-8, 1988.

Closmann, P.J. and Vinegar, H.J., "Relative Permeabilities to Steam and Water at Residual Oil in Natural Cores: CT Scan Saturations". SPE 17449 presented at the SPE California Regional Meeting held in Long Beach, California, March 23-25, 1988.

Clough, R.S. and Koenig, J.L., "Observation of Polybutadiene Rubber Structure Using NMR Imaging", Journal of Polymer Science: Part C: Polymer Letters, 27, p.451, 1989.

Cowdrey, E.J.K., "Principles and Practices for the Safe Handling of Radioactive Materials in WNRE Laboratories", Atomic Energy Canada Limited, 1980.

© 1990 NOVA HUSKY RESEARCH CORPORATION

Cromwell, V., Kortum, D.J. and Bradley, D.J., "The Use of a Medical Computer Tomography (CT) System to Observe Multiphase Flow in Porous Media", SPE 13098 presented at the 59th Annual Technical Conference and Exhibition held in Houston, TX, September 16-19, 1984.

Cuthiell, D. and Sedgwick, G., "X-ray CT Applied to Heavy Oil Corefloods", Proceedings, The Fourth UNITAR/UNDP International Conference on Heavy Crude and Tar Sands, Volume 2 - Geology, Chemistry - Paper No 9, p.727, Edmonton, Alberta, Canada, August 7-12, 1988.

Dechter, J.J., Komoroski, R.A. and Ramaprasad, S., "NMR Chemical Shift Selective Imaging of Individual Fluids in Sandstone and Dolomite Cores", Paper SCA 8903, presented at the Society of Core Analysts Conference, 1989.

Dereppe, J.M. and Schenker, K.V., "Analysis of Oil-Water Replacement in Limestone by MR Imaging", Bruker Report #2, 1989.

Doughty, D.A. and Maerefat N.L., "Preliminary Transformation of an NMR Spectrometer into an NMR Imager for Evaluating Fluid Content and Rock Properties of Core Samples" The Log Analyst, 30, p.78, March-April, 1989.

Edelstein, W.A., Vinegar, H.J., Tutunjian, P.N., Roemer, P.B. and Mueller, O.M., "NMR Imaging for Core Analysis", SPE 18272 presented at the 63rd Annual Technical Conference and Exhibition of the Society of Petroleum Engineers held in Houston, TX, October 2-5, 1988.

Ellingson, W.A., Wong, P.S. Dieckman, S.L., Pollinger, J.P., Yeh, H. and Vannier, M.W., "An Initial Comparison of X-ray and NMR Computed Tomography for Detection of Organic Binder Distribution", Ceram Eng Sci Proc, 10(7-8), p.1022, 1989.

Ellingson, W.A., Wong, P.S., Dieckman, S.L., Ackerman, J.L. and Garrido, L., "Magnetic Resonance Imaging: A New Characterization Technique for Advanced Ceramics", Am Ceram Soc Bull, 68(6), p.1180, 1989.

Evans, R.D., "The Atomic Nucleus", McGraw Hill, 1955.

Feldkamp, L.A. and Jesion, G., "3-D x-ray Computed Tomography" Review of Progress in Quantitative Non-destructive Evaluation, 5A, p.555, 1986.

Feldkamp, L.A., "New Approaches to X-ray Computed Tomography", in Physics News in 1987 - Physics in Industry, Physics Today, p.48, Jan 1988.

© 1990 NOVA HUSKY RESEARCH CORPORATION

Fewell, T.R. and Shuping, R.E., "Photon Energy Distribution of Some Typical Diagnostic X-ray Beams" Med. Phys., 4 (3), p. 187, May/June 1971.

Fincke, J.R., Berggren, M.J. and Johnson, S.A., "The Application of Reconstructive Tomography to the Measurement of Density Distribution in Two-Phase Flow". ISA, ISBN 87664-473-6, p235, 1980.

Flannery, B.P., Deckman, H.W., Roberge, W.G. and D'Amico, K.L., "Three Dimensional X-ray Microtomography". Science, 237, p.1439, 1987.

Fryar, J., McCarthy, K.J. and Fenelon, A., "Multielement Imaging in Computerized X-Ray Tomography" Nucl Instr Meth Phys Res, A271, p.671, 1988.

Fransham, P.B. and Jelen, J., "Displacement of Heavy Oil Visualized by CAT Scan" CIM 86-37-80 presented at the 37th Annual Technical Meeting of the Petroleum Society of CIM held in Calgary, June 8-11, 1986.

Frock, B.E. and Martin, R.W., "Applications of Digital Image Enhancement Techniques to the Ultrasonic NDE of Composite Materials", 15th International Symposium on Acoustical Imaging, Halifax, N.S., p.461, 1986.

Fryar, J. and McCarthy, K.J., "Multi-elememnt Imaging in CT Using a Tube Source of X-rays", IEEE Trans on Nucl Sci, 36(1), p.1138, 1989.

Gaigalas, A.K., Van Orden, A.C. and Robertson, B., "Application of Magnetic Resonance Imaging to Visualization of FLow in Porous Media", Nuclear Technology, 84, p.113, 1989.

Garrido, L. and Mark, J.E., "NMR Chemical Shift Imaging of Polymeric Materials", Polymer Preprints, 30(2), p.217, 1989.

Gilliland, R.E. and Coles, M.E., "Use of CT Scanning in the Investigation of Damage to Unconsolidated Materials", Paper 8902, Proceedings, Society of Core Analysts Conference, 1989.

Goudenough, D.J. and Weaver, K.E., "Overview of Computed Tomography". IEEE Trans Nuc Sci, NS26(1), p.1661, 1979.

Goodenhough, D.J., Weaver, M.S. and Davis, D.O., "Potential Artifacts Associated with the Scanning Pattern of the EMI Scanner", Radiology, 117, p.615, Dec. 1975.

© 1990 NOVA HUSKY RESEARCH CORPORATION

Guillot, G., Trokiner, A., Darrasse, L. and H., Saint-Jaimes, "Drying of a Porous Rock Monitored by NMR Imaging", J. Phys. D: Appl. Phys., 22, p. 1646, 1989.

Gupta, N.K., "Computed Tomography as an Analytical Tool in Oil Recovery". Presented at the 1986 Fall Conference of the American Society for Non-destructive Testing, New Orleans, LA, Sept. 29 - Oct. 3, 1986.

Hangartner, T.N. and Overton, T.R., "Quantitative Measurement of Bone Density Using Gamma-Ray Computed Tomography", J Com Ass Tom, 6(6), p.1156, 1982.

Hefferman, P.B. and Robb, R.A., "Difference Image Reconstruction from a Few Projections for Nondestructive Materials Inspection",
Applied Optics, 24(23), p.4105, 1985.

Herman, G.T. "Image Reconstruction from Projections. The Fundamentals of Computerized Tomography". Academic Press, 1980. Hinshaw, W.S. and Lent, A.H., "An Introduction to NMR Imaging: From the Block Equation to the Imaging Equation". Proceedings of the IEEE, 71(3), p.338, 1983.

Herman, G.T., "Three-Dimensional Imaging on a CT or MR Scanner" J Com Ass Tom, 12(3) p.450, 1988.

Hinshaw, W.S. and Lent, A.H., "An Introduction to NMR Imaging: From the Bloch Equation to the Imaging Equation", Proc. IEEE, 71(3), p.338, 1983.

Honarpour, M.M., Cromwell, V., Hatton, D. and Satchwell, R., "Reservoir Rock Descriptions Using Computed Tomography". SPE 14272 presented at the 60th Annual Technical Conference and Exhibition of the Society of Petroleum Engineers held in Las Vegas, NV,September 22-25, 1985.

Honarpour, M.M., McGee, K.R., Crocker, M.E., Maerefat, N.L. and Sharma, B., "Detailed Core Description of a Dolomite Sample from the Upper Madison Limestone Group". SPE 15174 presented at the Rocky Mountain Regional Meeting of the Society of Petroleum Engineers held in Billings, MT, May 19-21, 1986.

Hove, A.O., Ringen, J.K. and Read, P.A., "Visualization of Laboratory Corefloods With the Aid of Computerized Tomography of X-rays". SPEFE, 2, p.148, 1987. SPE 13654 presented at the SPE 1985 California Regional Meeting, held in Bakersfield, California, March 27-29, 1985.

© 1990 NOVA HUSKY RESEARCH CORPORATION

Hove, A.O., Nilsen,V. and Jenkes, A., "Visualization of Xanthan Flood Behaviour in Core Samples by Means of X-ray Tomography". SPE 17342 presented at the SPE/DOE Enhanced Oil Recovery Symposium held in Tulsa, OK, April 17-20, 1988.

Huang, S.M., Plaskowski, A.B., Xie, C.G. and Beck, M.S., "Tomographic Imaging of Two-component Flow Using Capacitance Sensors", J. Phys. E: Sci. Instrum., 22, p.173, 1989.

Hubbell, J.H., "Photon Cross Sections, Attenuation Coefficients and Energy Absorption Coefficients from 10 keV to 100 GeV", NSRDS-NBS 29 (U.S. GPO, Washington, D.C., 1969)

Hummel, R. and Wesser, U., "Determination of Density Noise in a Two-Phase-Flow by x-ray Computer Tomography", Progres in Nuclear Energy, 21, p.333, 1988.

Hunt, P.K., Engler, P. and Bajsarowicz, C., "Computed Tomography as a Core Analysis Tool: Applications and Artifact Reduction Techniques". SPE 16952 presented at the 62nd Annual Technical Conference and Exhibition of the Society of Petroleum Engineers held in Dallas, TX, September 27-30, 1987.

Islam, R.M. and Bentsen, R.G., "A Dynamic Method for Measuring Relative Permeability". J Can Pet T, 25(1), p.39, 1986.

Johns, C., "Medical CAT Scanning for Aircraft Engine Components", Leading Edge, p.27, Fall 1987.

Justice, J.H., Vassiliou A.A., Singh, S., Logel, J.D., Hansen, P.A., Hall, B.R., Hutt, P.R. and Solanki, J.J., "Acoustic Tomography for Monitoring Enhanced Oil Recovery", Geophysics, p.12, Feb. 1989.

Kalender, W.A., Perman, W.H., Vetter, J.R. and Klotz, E., "Evaluation of a Prototype Dual-energy Computed Tomographic Apparatus. I. Phantom Studies", Med. Phys. 13(3), p.334, May/Jun 1986.

Kanamori, T., Kamata, S. and Ito, S., "Cross-Sectional Imaging of Large and Dense Materials by High Energy X-Ray CT Using Linear Accelerator", Journal of Nuclear Science and Technology, 26(9), p.826, 1989.

Kantzas, A., "A Theoretical and Experimental Study of Gravity Assisted Inert Gas Injection as a Method of Oil Recovery". Ph.D. Thesis, University of Waterloo, 1988.

© 1990 NOVA HUSKY RESEARCH CORPORATION

Kantzas, A., "Investigation of Physical Properties of Porous Rocks and Fluid Flow Phenomena in Porous Media Using Computer Assisted Tomography". *In Situ*, 14(1), p. 77, (1990).

Kantzas, A., Marentette, D.F., Erno, B. and Harding S., "Characterization of a Heavy Oil Reservoir Using Computer Assisted Tomography of Core Material". Presented at the Third Petroleum Conference of the South Saskatchewan Section of the Petroleum Society of CIM held in Regina, Sask., Sept. 25-27, 1989.

Kantzas, A., Marentette, D.F. and Skalinski, M., "Computer Assisted Tomography as a Complementary Tool to Well logging". Presented at the Twelfth Formation Evaluation Symposium of the Canadian Well Logging Society held in Calgary, Alberta, Sept. 26-28, 1989.

Kantzas, A., Chatzis, I., Macdonald, I.F. and Dullien, F.A.L., "Using a Vertical Scanner for Horizontal Scanning in Non-Medical Applications of Computer Assisted Tomography", CSNDT Journal p. 20, Mar/Apr 1988.

Kantzas, A., "Upgrading and Tuning up the CT5005 Scanner (Software and Hardware), NHRC Report #401, December 1988.

Kantzas, A., "CAT Scanner Calibration Part I", NHRC Report #405, December 1988.

Kantzas, A., "Development of Postprocessing Software Package for the Data of the CAT Scanner Tests", NHRC Report #411, January 1989.

Kantzas, A., "Computer Assisted Tomography Industrial Applications", A Literature Survey", NHRC Report #412, January 1989.

Kantzas, A., "CAT Scanner Calibration Part II", NHRC Report #418, January 1989.

Kantzas, A., "Sulphur Determination in Reservoir Rocks - Canterra *et al.* Peppers 10-27-52-24W5 - Preliminary Work", NHRC Report #480, October 1989.

Kantzas, and D.F. Marentette, "CAT Scanner Examination of Core Samples from Bluesky Formation", NHRC Report #485, November 1989.

Kantzas, A. and P. Siska, "On the Measurement of the X-ray Spectrum Detected by the CAT Scanner Detectors", NHRC Report #492, November 1989.

© 1990 NOVA HUSKY RESEARCH CORPORATION

Kawasaki, S., Kondo, M., Izumi, S. and Kikuchi M., "Radioactivity Measurement of Drum Package by Computed Tomography" Industrial Tomography II, p.85, 1988.

Karunanithy, S. and Mooibroek, S., "Detection of Physical Flaws in Alumina Reinforced with SiC Fibres by NMR Imaging in the Green State", J Mat Sci, 24, p.3686, 1989.

Kenyon, W.E., Day, R.I., Straley, C. and Willemsen, J.F., "Compact and Consistent Representation of Rock NMR Data for Permeability Estimation", SPE 15643, presented at the 61st Annual Technical Conference and Exhibition of the Society of Petroleum Engineers held in New Orleans, LA, October 5-8, 1986.

Lamrous, O., Houi, D., Zarcone, C. and Pradere, J., "Magnetic Resonance Imaging Application to Study of Porous Media", Revue Phys. Appl., 24, p.607, 1989.

Levoy, M., "Direct Visualization of Surfaces from Computed Tomography Data", Comp. Sci. Dept, Univ. South Carolina, 1988.

Lewis, M.G., Sharma, M.M., Dunlap, H.F., and Dorfman, M.H., "Techniques for Measuring the Electrical Properties of Sandstone Cores", SPE 18178, presented at the 63rd Annual Technical Conference and Exhibition of the Society of Petroleum Engineers held in Houston, TX, October 2-5, 1988.

Lewitt, R.M., "Mathematical Foundations of Computed Tomography: An Introduction to the literature", Review of Progress in Quantitative Non-destructive Evaluation, 7A, p. 367, 1988.

Lien, J.R., Graue, A. and Kolltveit, K., "A Nuclear Imaging Technique for Studying Multiphase Flow in a Porous Medium at Oil Reservoir Conditions", Nuclear Instruments and Methods in Physics Research, A271, p.693, 1988.

Listerud, J.M., Sinton, S.W. and Drobny, G.P., "NMR Imaging of Materials", Anal Chem, 61(1), p.23A, Jan 1989.

Liu, D., Castanier, L.M. and Bringham, W.E., "Analysis of Transient Foam Flow in 1-D Porous Media with CT", SPE 20071, presented at the 60th California Regional Meeting held in Ventura, California, April 4-6, 1990.

Louis, A.K. and Natterer, F., "Mathematical Problems in Computerized Tomography". Proceedings of the IEEE, 71(3), p.379, 1983.

© 1990 NOVA HUSKY RESEARCH CORPORATION

MacCuaig, N., Seville, J.P.K., Gilboy, W.B. and Clift, R., "Application of Gamma-ray Tomography to Gas Fluidized Beds" Applied Optics, 24(23), p.4083, 1985.

Macovski, A.,"Physical Problems of Computerized Tomography". Proceedings of the IEEE, 71(3), p.1533, 1987.

Mak, D.K., Macecek, M. and Kovacs, A., "Ultrasonic Defect Visualization in a Metal Block", 15th International Symposium on Acoustical Imaging, Halifax, N.S., p.503, 1986.

Manjnath, A., "Examination of the Buckley-Leverett Theory Using Computerized Tomography". SPE 17491 (abstract only) presented at the SPE California Regional Meeting held in long Beach, California, March 23-25, 1988.

Mareci, T.H., Donstrup, S. and Rigamonti, A., "NMR Imaging and Relaxation Study of Polymer Swelling and Chain Dynamics" J Molecular Liquids, 38, p.185, 1988.

Marentette, D.F and A. Kantzas, "CAT Scanner Analysis of Cores from Rainbow Keg River Pools" NHRC Report #486, November 1989.

Marentette, D.F. and A. Kantzas, "CAT Scan Analysis of Sandstone Cores - Husky Halkirk Field", NHRC Report #501, December 1989.

Marentette, D.F. and A. Kantzas, "CATSCAN Analysis of Husky AEC Caribou Lake Lease Part I 8D-26-69-5W4", NHRC Report #425, March 1989.

Marentette, D.F. and A. Kantzas, "CATSCAN Analysis of Husky AEC Caribou Lake Lease Part II 8C-9-69-5W4", NHRC Report #430, March 1989.

McClean B.A., Overton, T.R., Hangartner, T.N. and Rathee, S., "A Special Purpose X-ray Fan Beam CT Scanner for Trabecular Bone Density Measurement in the Appendicular Skeleton", Phys Med Biol, 35(1), p.11, 1990.

McCollough, E.C., "Photon Attenuation in Computed Tomography". Medical Physics, 2(6), p.307, 1975.

McCullough, E.C., Baker, H.L., Jr., Houser, O.W., and Reese, D.F., "An Evaluation of the Quantitative and Radiation Features of a Scanning X-ray Transverse Axial Tomograph: The EMI Scanner", Rad. Phys. 111, p. 709, June 1974.

© 1990 NOVA HUSKY RESEARCH CORPORATION

Miller, J.B. and Garroway, A.N., "NMR Imaging of Solids", Review of Progress in Quantitative Nondestructive Evaluation, 7A, p.287, 1988.

Miller, W.H., "Design and Implementation of a Portable Computerized Axial Tomography System for Field Use", Nucl. Instr. and Meth. in Phys. Res., A270, p.590, 1988.

Miyanishi, T., Iida, K. and Sotobayashi, H., "Computerized Tomography of a Paper Roll", TAPPI J, 71(10), p.167, 1988.

Mohanty, K.K. and Miller, A.E., "Factors Influencing Unsteady Relative Permeability of a Mixed-Wet Reservoir Rock". SPE 18292 presented at the 63rd Annual Technical Conference and Exhibition of the Society of Petroleum Engineers held in Houston, TX, October 2-5, 1988.

Morgan, D.R. and Lingenfelter, D.E., "Introducing Industrial CAT Scan Inspection". ASQC Quality Congress Transaction - Anaheim, p.671, 1986.

Mossiti, V.G. and Castanier L.M., "Water Transport in Limestone by X-ray CAT Scanning", Proc. of the Sessions related to structural materials at Structures Congress, San Francisco, May 1-5, 1989.

Muller, M. and Fink, D., "Reconstruction of Submicron Size Spatial Distributions of Implanted Particles in Solids by Computer Tomography" Nuc Instr Meth Phys Res, B34, p.162, 1988.

Narayanan, K. and Deans, H.A., "A Flow Model Based on the Structure of Heterogeneous Porous Media". SPE 18328 presented at the 63rd Annual Technical Conference and Exhibition of the Society of Petroleum Engineers held in Houston, TX, October 2-5, 1988.

Nicholls, C.I. and Heaviside, J., "Gamma Ray Absorption Techniques Improve Analysis of Core Displacement Tests". SPE 14421 presented at the 60th Annual Technical Conference and Exhibition of the Society of Petroleum Engineers held in Las Vegas, NV, September 22-25, 1985.

Nieminen, A.O.K. and Koenig, J.L., "NMR Imaging - A Promising New Adhesive Evaluation Technique", J. Adhesion Sci. Technol., 2(6), p407, 1988.

Norman, J.P. and Crose, J.G., "A Finite Element Method for Defect Evaluation Based on Quantitative NDE Data", 88-WA/CIE-1 presented at the Winter Annual Meeting of the ASME, held in CHicago, Illinois, Nov. 27 - Dec. 2, 1988.

Novo Diagnostic Systems Manuals, 1985.

© 1990 NOVA HUSKY RESEARCH CORPORATION

Nzekwu, B.I. and Bennion, D.G., "Mobility Control in Dynamic Gravity Segregation Flow Systems". J Can Pet T, 26, p.80, 1987.

Oak, M.J. and Ehrlich, R,. "A New X-Ray Absorption Method for Measurement of Three Phase Relative Permeability". SPE 14420 presented at the 60th Annual Technical Conference and Exhibition of the Society of Petroleum Engineers held in Las Vegas, NV, September 22-25, 1985.

Parsons, R.W., "Microwave Attenuation - A New Tool for Monitoring Saturations in Laboratory Flooding Experiments". Soc Pet Eng J, 15, p.320, 1975.

Peck, H.E., "Computed Tomography for Imaging and Measuring Material Properties". ANTEC '87, p.1055, 1987.

Persson, S. and Ostman, E., "Use of Computed Tomography in Non-destructive Testing of Polymeric Materials". Applied Optics, 24(23), p.4095, 1985.

Persson, S. and Ostman, E., "Determination of Crosslink Density Gradients in Vulcanized Rubber Products by Computed Tomography". PGI Science AB, Vamamo Sweden, 2, p.527, 1986.

Persson S., "How Computed X-ray Tomography Can be Used to Study Crosslink Density in Non-filled Peroxide Cured Polyisoprene Rubber", Polymer, 29(5), p.802, 1988.

Phogat, V.K. and Aylmore, L.A.G., "Evaluation of Soil Structure by Using Computer Assisted Tomography", Aust. J. Soil Res., 27, p.313, 1989.

Potet, P., Bathias, C. and Degrigny, B., "Quantitative Characterization of Impact Damage in Composite Materials: A Comparison of Computerized Vibrothermography and X-ray Tomography", Materials Evaluation, 46, p.1050, July 1988.

Reimers, P., Gilboy, W.B. and Goebbels, J., "Recent Developments in the Industrial Application of Computerized Tomography with Ionizing Radiation". NDT International, 17(4), p197, 1984.

Ringen, J.K. and Hove, A., "The Use of x-ray Tomography in Core Analysis", Ch. 15, North Sea Oil and Gas Reservoirs, p.209, 1987.

Rothwell, W.P., "Nuclear Magnetic Resonance Imaging", Applied Optics, 24(23), p.3958, 1985.

Rothwell, W.P. and Vinegar, H.J., "Petrophysical Applications of NMR Imaging", Applied Optics, 24(23), p.3969, 1985.

© 1990 NOVA HUSKY RESEARCH CORPORATION

Runge, V.M., Wood, M.L., Kaufman, D.M. and Silver, M.S., "MR Imaging Section Profile Optimization: Improved Contrast and Detection of Lesions", Radiology, 167(3), p.831, 1988.

Samoilenko, A.A., Artemov, D.Y. and Sibel'dina, L.A., "The Application of NMR Imaging to the Study of the Internal Structures of Solids", Russian Journal of Physical Chemistry, 61(11), p.1623, 1987.

Sasov, A.Y., "Investigation of Soil Microstructure by Methods of Computerized Tomography". Vestnik Moskovskogo Universiteta. Geologiya, 42(3), p56, 1987.

Sawicka, B.D. and Tapping, R.L., "CAT Scanning of Hydrogen Induced Cracks in Steel". Nuclear Instruments and Methods in Physics Research, A256, p.103, 1987.

Sawicka, B.D. and Palmer, B.J.F., "Application of COmputed Tomography to the Development of Advanced Ceramics", C S N D T J, 10(2), p.24, 1989.

Savoie, C.L., "Practical Applications of X-radiography Techniques in Tar Sands", Proceedings, The Fourth UNITAR/UNDP International Conference on Heavy Crude and Tar Sands, Volume 2 - Geology, Chemistry - Paper No 70, p.523, Edmonton, Alberta, Canada, August 7-12, 1988.

Sedgwick, G.E. and Miles-Dixon, E.W.A., "Application of x-Ray Imaging Techniques to Oil Sands Experiments". CIM 87-38-84 presented at the 38th Annual Technical Meeting of the Petroleum Society of CIM held in Calgary, June 7-10, 1987.

Sequin, F.H., Burstein, P., Bjorkholm, P.J., Homburger, F. and Adams,A., "X-ray Computed Tomography with 50-um Resolution". Applied Optics, 24(23), p.4117, 1985.

Seville, J.P.K., Morgan, J.E.P. and Clift, R., "Tomographic Determination of the Voidage Structure of Gas Fluidized Beds in the Jet Region". Fluidization V, p.87.

Shani, U., "Understanding Three Dimensional Images". UMI Research Press, 1984.

Snyder, D.L. and Cox, J.R.Jr., "An Overview of Reconstructive Tomography and Limitations Imposed by a Finite Number of Projections", in Reconstruction Tomography in Diagnostic Radiology and Nuclear Medicine, Editted by M.M. Ter-Pogossian *et al.*, 1987.

Snyder, R. and Hesselink, L., "High Speed Optical Tomography for Flow Visualization", Applied Optics, 24(23), p.4046, 1985.

© 1990 NOVA HUSKY RESEARCH CORPORATION

Sobrie, K.S., Wat, R.M.S., Hove, A.O., Nilsen, V. and Leknes, J., "Miscible Displacements in Heterogeneous Core Systems: Tomographic Conformation of Flow Mechanisms" SPE 18493 presented at the SPE International Symposium on Oilfield Chemistry held in Houston, TX, February 8-10, 1989.

Somasundaran, P., Huang, Y.B. and Gryte, C.C., "CAT Scan Characterization of Sedimentation and Floccs". Pwdr Techn, 53, p.73, 1987.

Soucemarianadin, A., Bourlion, M. and Lenormand, R., "Ultrasonic Saturation Mapping in Porous Media". SPE 16953 presented at the 62nd Annual Technical Conference and Exhibition of the Society of Petroleum Engineers held in Dallas, TX, September 27-30, 1987.

Soucemarianadin, A., Touboul, E., Bourlion, M., Nittmann, J. and Lenormand, R., "Sweep Efficiency in Multilayered Porous Media: Contrast Between Stable and Unstable Flow". SPE 16955 presented at the 62nd Annual Technical Conference and Exhibition of the Society of Petroleum Engineers held in Dallas, TX, September 27-30, 1987.

Spiro, C.L., Holmes, D.S., Lobos, J. and Maylotte, D.H., "Use of X-ray Computed Tomography to Examine Microbial Desulfurization of Lump Coal", Energy and Fuels, 1, p.76, 1987.

Storm, E. and Israel, H.I., "Photon Cross Sections from 0.001 to 100 MeV for Elements 1 to 100", LA-3753, Los Alamos Scientific Laboratory, 1967.

Sullivan, J.D., Root,J.H., Sawicka, B.D. and Class, S.J., "Non-destructive Evaluation of Infiltration-toughened Ceramics", Atomic Energy of Canada Limited report #9728, Nov. 1988.

Taguchi, I. and Tanaka, K., "Development of High-energy X-ray Computed Tomographic Scanner and Its Application to Analysis of Iron and Steel". NIPPON Steel Technical Report No33, p.22, April 1987.

Tamburi, A., Roeper, U. and Wexler, A., "An Application of Impedance-Computed Tomography to Subsurface Imaging of Pollution Plumes", Ground-Water Contamination: Field Methods, ASTM STP 963, 1987.

Tapping, R.L. and Sawicka, D.B., "Computer-Assisted Tomography for the Non-destructive Evaluation of Hydrogen-Induced Cracking in Steel". Materials Performance, p.46, December, 1987.

© 1990 NOVA HUSKY RESEARCH CORPORATION

Tonner, P.D. and Taylor, T., "Region of Interest Tomography Employing a Differential Scanning Technique", U.S.A Patent #4,878,169, 1989.

Vannier, M.W., Knapp, R.H., Gayou, D.E., Butterfield, R.L., Larson J.W.and Sammon P.N., "Three Dimensional Surface Reconstruction for Industrial Computed Tomography". Applied Optics, 24(23), p.4075, 1985.

Vest, C.M., "Tomography for Properties of Materials that Bend Rays: a Tutorial", Applied Optics, 24(23), p.4089, 1985.

Vinegar, H.J., and Wellington, S.L., "Tomographic Imaging of Three-Phase Flow Experiments", Rev. Sci. Ingstrum. 58(1), p. 96, Jan. 1987

Vinegar, H.J. and Tutunjian, P.N., "Determining Multiphase Saturations by NMR Imaging of Multiple Nuclides", U.S.A. Patent #4,769,602, 1988.

Vinegar, H.J., Tutunjian, P.N., Edelstein, W.A. and Roemer, P.B., "Determining Carbonate Content of Cores by 13C NMR", Paper SCA 8901, presented at the Society of Core Analysts Conference, 1989.

Vinegar, H.J., Wellington, S.L. and de Waal, J.A., "Apparatus for Analysis of Failure of Material", U.S.A. Patent #4,856,341, 1989.

Vinegar, H.J., "X-Ray CT and NMR Imaging of Rocks". JPT, 38(3), p.257, 1986.

Vinegar, H.J. and Wellington, S.L., "Tomographic Imaging of Three-phase Flow Experiments". Rev.Sci.Instrum. 58(1), p.96, 1987.

Vontz, T., Goebbels, K., Maisl, M., Reiter, H. and Hirserkorn, S., "NDT for Small Defects by X-ray Tomography", Review of Progress in Quantitative Nondestructive Evaluation, 7A, p.389, 1988.

Wade, G., "A History of Acoustical Imaging", 15th International Symposium on Acoustical Imaging, Halifax, N.S. p.1, 1986.

Waggener, R.G., Kereiakes, J.G. and Shalek, R.J., (editors) "CRC Handbook of Medical Physics Volume II" CRC Press (1984).

Wang, S.Y., Ayral, S. and Gryte, C.C., "Computer-Assisted Tomography for the Observation of Oil Displacement in Porous Media". Soc Pet Eng J, 24, p.53, 1984.

© 1990 NOVA HUSKY RESEARCH CORPORATION

Wang, S.Y., Ayral, S., Castellana, F.S. and Gryte, C.C., "Reconstruction of Oil Saturation Distribution Histories During Immiscible Liquid-Liquid Displacement by Computer-Assisted Tomography". AIChE J, 30(4), p.642, 1984.

Wang, S.Y., Huang, Y.B., Pereira, V. and Gryte, C.C., "Application of Computed Tomography to Oil Recovery from Porous Media". Applied Optics, 24(23), p.4021, 1985.

Warner, G.S., Nieber, J.L., Moore, I.D. and Geise, R.A., "Characterizing Macropores in Soil by Computed Tomography", Soil Science Society of America Journal, Div. S-1-Soil Physics, 53(3), p.653, 1989.

Weber, J. and van den Berge, D.J., "The Effective Atomic Number and the Calculation of the Composition of Phantom Materials", Br.F.Radioil., 42, p. 378, 1969.

Weisenberger, L.A. and Koenig, J.L., "NMR Imaging of Case II Diffusion in Glassy Polymers", J Pol Sci C: Pol. Letters, 27, p.55, 1989.

Weisenberger, L.A. and Koenig, J.L., "NMR Imaging of Solvent Diffusion in Polymers", Applied Spectroscopy, 43(7), p.1117, (1989).

Wellington, S.L. and Vinegar, H.J., "CT Studies of Surfactant-Induced CO2 Mobility Control". SPE 14393 presented at the 60th Annual Technical Conference and Exhibition of the Society of Petroleum Engineers held in Las Vegas, NV, September 22-25, 1985.

Wellington, S.L. and Vinegar, H.J., "X-Ray Computerized Tomography". JPT, 39(8), p.885, 1987.

Wellington, S.L. and Vinegar, H.J., "Surfactant-Induced Mobility Control for Carbon Dioxide Studied with Computerized Tomography". Surfactant-Based Mobility Control Chapter 17, ACS, 1988.

Wexler, A., Fry, B. and Neuman, M.R., "Impedance-Computed Tomography Algorithm and System", Applied Optics, 24(23), p.3985, 1985.

Withjack, E.M., "Computed Tomography for Rock-Property Determination and Fluid Flow visualization". SPE 16951 presented at the 62nd Annual Technical Conference and Exhibition of the Society of Petroleum Engineers held in Dallas, TX, September 27-30, 1987.

© 1990 NOVA HUSKY RESEARCH CORPORATION

Withjack, E.M. and Akervoll, I., "Computed Tomography Studies of a 3-D Miscible Displacement Behavior in a Laboratory Five-Spot Model". SPE 18096 presented at the 63rd Annual Technical Conference and Exhibition of the Society of Petroleum Engineers held in Houston, TX,October 2-5, 1988.

Wolf, J., "Investigation of Bubbly Flow by Ultrasonic Tomography", Part. Part. Syst. Charact., 5, p.170, (1988).

© 1990 NOVA HUSKY RESEARCH CORPORATION

14.0 TABLES

© 1990 NOVA HUSKY RESEARCH CORPORATION

TABLE 2.1: Principles of Operation of CAT Scanners

Generation	Source	Detector	Scan. Time	Rotation
First	Pencil x-ray beam	One detector	10 min/sl	180 deg.
Second	Parallel x-ray beam	Linear array of multiple detectors	20 sec/sl	180 deg.
Third	Fan x-ray beam	Linear array of multiple detectors	5 sec/sl	360 deg.
Fourth	Fan x-ray beam	Linear array forming a continuous cycle	1 sec/sl	None for detector 360 deg. for tube
Fifth	Tungsten rings, rotating beam	Linear array forming a continuous cycle	50-100 msec/sl	None

© 1990 NOVA HUSKY RESEARCH CORPORATION

Table 2.2: Classification of Image Reconstruction Methods

I. BACK PROJECTIONS

II. ITERATIVE METHODS

A. Simultaneous Iterative Reconstruction Technique (SIRT).
B. Algebraic Reconstruction Technique (ART).
C. Iterative Least Squares Technique (ILST).

III. ANALYTIC METHODS

A. Filtered Back-projection (Convolution Radon's Method, Fourier Filtering).
B. Two-dimensional Fourier Reconstruction.

© 1990 NOVA HUSKY RESEARCH CORPORATION

TABLE 4.1 X-Ray Mean Energies for tube (keV)				
kVp	No Water Ring	With Water Ring	McCullough (1975)	Vinegar/ Wellington (1987)
80	48.126	56.024	-	48.8
90	-	-	-	53.3
100	-	-	62.0	56.7
110	56.669	63.322	-	-
120	-	-	72.0	63.3
130	-	-	-	-
140	67.798	76.942	79.0	-

TABLE 4.2 X-Ray Mean Energies with Core Holder Assemblies		
		Vinegar/Wellington
kVp	NHRC	(1987)
80	62.27	68.9
90	69.55	74.3
100	75.45	79.9
110	80.45	-
120	86.82	90.5
130	-	-
140	96.82	-

© 1990 NOVA HUSKY RESEARCH CORPORATION

TABLE 5.1

Bulk Density as a Function of Depth for the Cold Lake Cores

CORE A		CORE B		PLUGS
Depth(cm)	B.D.*(g/cm^3)	Depth(cm)	B.D.(g/cm^3)	B.D.(g/cm^3)
2.0	1.72	1.0	1.75	1.77
3.0	1.72	2.0	1.74	1.77
4.0	1.81	3.0	1.72	1.66
5.0	1.74	4.0	1.79	
6.0	1.78	5.0	1.83	
7.0	1.94	6.0	1.80	
8.0	1.84	7.0	1.84	
9.0	1.80	8.0	1.96	
10.0	1.74	9.0	1.94	
11.0	1.72	10.0	1.91	
12.0	1.71	11.0	1.84	
13.0	1.72	12.0	1.77	
14.0	1.69	13.0	1.84	
15.0	1.68	14.0	1.78	
16.0	1.67	15.0	1.76	
17.0	1.67	16.0	1.76	
18.0	1.68	17.0	1.76	
19.0	1.72	18.0	1.77	
20.0	1.68	19.0	1.75	
21.0	1.67	20.0	1.76	
22.0	1.67	21.0	1.75	
23.0	1.66	22.0	1.76	
24.0	1.64	23.0	1.76	
25.0	1.59	24.0	1.73	
26.0	1.31	25.0	1.73	
27.0	0.85	26.0	1.79	
		27.0	1.76	
		28.0	1.57	

* B.D. = Bulk Density

© 1990 NOVA HUSKY RESEARCH CORPORATION

TABLE 5.2

COLD LAKE CORE A: Porosity vs. Liquid Saturations

Slice #'s	B.D.* (g/cm^3)	Liquid Saturations (%) 0	10	20	30	40	50	60	70	80	90	100
1	1.72	0.35	0.36	0.38	0.40	0.41	0.43	0.45	0.48	0.50	0.53	0.56
2	1.72	0.35	0.36	0.38	0.40	0.41	0.43	0.45	0.48	0.50	0.53	0.56
3	1.81	0.32	0.33	0.34	0.36	0.37	0.39	0.41	0.43	0.45	0.48	0.51
4	1.74	0.34	0.36	0.37	0.39	0.40	0.42	0.44	0.47	0.49	0.52	0.55
5	1.78	0.33	0.34	0.36	0.37	0.39	0.40	0.42	0.45	0.47	0.50	0.53
6	1.94	0.27	0.28	0.29	0.30	0.32	0.33	0.35	0.36	0.38	0.41	0.43
7	1.84	0.31	0.32	0.33	0.34	0.36	0.38	0.40	0.42	0.44	0.46	0.49
8	1.80	0.32	0.33	0.35	0.36	0.38	0.40	0.41	0.44	0.46	0.49	0.52
9	1.74	0.34	0.36	0.37	0.39	0.40	0.42	0.44	0.47	0.49	0.52	0.55
10	1.72	0.35	0.36	0.38	0.40	0.41	0.43	0.45	0.48	0.50.	0.53	0.56
11	1.71	0.35	0.37	0.38	0.40	0.42	0.44	0.46	0.48	0.50	0.53	0.56
12	1.72	0.35	0.36	0.38	0.40	0.41	0.43	0.45	0.48	0.50	0.53	0.56
13	1.69	0.36	0.38	0.39	0.41	0.43	0.45	0.47	0.49	0.52	0.55	0.58
14	1.68	0.37	0.38	0.40	0.41	0.43	0.45	0.47	0.50	0.52	0.55	0.59
15	1.67	0.37	0.38	0.40	0.42	0.44	0.46	0.48	0.50	0.53	0.56	0.59
16	1.67	0.37	0.38	0.40	0.42	0.44	0.46	0.48	0.50	0.53	0.56	0.59
17	1.68	0.37	0.38	0.40	0.41	0.43	0.45	0.47	0.50	0.52	0.55	0.59
18	1.72	0.35	0.36	0.38	0.40	0.41	0.43	0.45	0.48	0.50	0.53	0.56
19	1.68	0.37	0.38	0.40	0.41	0.43	0.45	0.48	0.50	0.52	0.55	0.59
20	1.67	0.37	0.38	0.40	0.42	0.44	0.46	0.48	0.50	0.53	0.56	0.59
21	1.67	0.37	0.38	0.40	0.42	0.44	0.46	0.48	0.50	0.53	0.56	0.59
22	1.66	0.37	0.39	0.40	0.42	0.44	0.46	0.48	0.51	0.54	0.57	0.60
23	1.64	0.38	0.40	0.41	0.43	0.45	0.47	0.49	0.52	0.55	0.58	0.61
24	1.59	0.40	0.42	0.43	0.45	0.47	0.49	0.52	0.54	0.57	0.61	0.64
25	1.31	0.51	0.53	0.55	0.57	0.60	0.62	0.65	0.69	0.72	0.77	0.81
26	0.85	0.68	0.71	0.73	0.77	0.80	0.84	0.88	0.91	0.97	1.03	1.09

* B.D. = Bulk Density

© 1990 NOVA HUSKY RESEARCH CORPORATION

TABLE 5.3

COLD LAKE CORE B: Porosity vs. Liquid Saturations

Slice #'s	B.D.* (g/cm^3)	Liquid Saturations (%) 0	10	20	30	40	50	60	70	80	90	100
1	1.75	0.34	0.35	0.37	0.38	0.40	0.42	0.44	0.46	0.48	0.51	0.54
2	1.74	0.34	0.36	0.37	0.39	0.40	0.42	0.44	0.46	0.49	0.51	0.54
3	1.72	0.35	0.36	0.38	0.39	0.41	0.43	0.45	0.47	0.50	0.53	0.56
4	1.79	0.32	0.34	0.35	0.37	0.38	0.40	0.42	0.44	0.46	0.49	0.51
5	1.83	0.31	0.32	0.33	0.35	0.36	0.38	0.40	0.42	0.44	0.46	0.49
6	1.80	0.32	0.33	0.35	0.36	0.38	0.39	0.41	0.43	0.46	0.48	0.51
7	1.84	0.31	0.32	0.33	0.34	0.36	0.38	0.39	0.41	0.43	0.46	0.49
8	1.96	0.26	0.27	0.28	0.29	0.31	0.32	0.33	0.35	0.37	0.39	0.41
9	1.94	0.27	0.28	0.29	0.30	0.31	0.33	0.34	0.36	0.38	0.40	0.43
10	1.91	0.28	0.29	0.30	0.31	0.33	0.34	0.36	0.38	0.40	0.42	0.44
11	1.84	0.31	0.32	0.33	0.34	0.36	0.38	0.39	0.41	0.43	0.46	0.49
12	1.77	0.33	0.34	0.36	0.37	0.39	0.41	0.43	0.45	0.47	0.50	0.53
13	1.84	0.31	0.32	0.33	0.34	0.36	0.38	0.39	0.41	0.43	0.46	0.49
14	1.78	0.33	0.34	0.35	0.37	0.39	0.40	0.42	0.44	0.47	0.49	0.52
15	1.76	0.34	0.35	0.36	0.38	0.39	0.41	0.43	0.45	0.48	0.50	0.53
16	1.76	0.34	0.35	0.36	0.38	0.39	0.41	0.43	0.45	0.48	0.50	0.53
17	1.76	0.34	0.35	0.36	0.38	0.39	0.41	0.43	0.45	0.48	0.50	0.53
18	1.77	0.33	0.34	0.36	0.37	0.39	0.41	0.43	0.45	0.47	0.50	0.53
19	1.75	0.34	0.35	0.37	0.38	0.40	0.42	0.44	0.46	0.48	0.51	0.54
20	1.76	0.34	0.35	0.36	0.38	0.39	0.41	0.43	0.45	0.48	0.50	0.53
21	1.75	0.34	0.35	0.37	0.38	0.40	0.42	0.44	0.46	0.48	0.51	0.54
22	1.76	0.34	0.35	0.36	0.38	0.39	0.41	0.43	0.45	0.48	0.50	0.53
23	1.76	0.34	0.35	0.36	0.38	0.39	0.41	0.43	0.45	0.48	0.50	0.53
24	1.73	0.35	0.36	0.37	0.39	0.41	0.43	0.45	0.47	0.49	0.52	0.55
25	1.73	0.35	0.36	0.37	0.39	0.41	0.43	0.45	0.47	0.49	0.52	0.55
26	1.79	0.32	0.34	0.35	0.37	0.38	0.40	0.42	0.44	0.46	1.49	0.51
27	1.76	0.34	0.35	0.36	0.38	0.39	0.41	0.43	0.45	0.48	0.50	0.53
28	1.57	0.41	0.42	0.44	0.46	0.48	0.50	0.52	0.55	0.58	0.61	0.65

* B.D. = Bulk Density

© 1990 NOVA HUSKY RESEARCH CORPORATION

Table 5.4
CAT SCANNER Analysis of PCP Core #1

Slice No.	Bulk Density (g/cm^3)	Effective Atomic Number	Porosity dry (density $0.0 g/cm^3$)	Porosity liquid (density $1.0 g/cm^3$)	air (%)	sandstone (%)	cement (%)
1	0.6601	2.58	0.40	0.65	78.69	21.31	0.00
2	1.9501	7.06	0.38	0.60	46.09	53.91	0.00
3	1.7828	12.48	0.32	0.52	1.09	98.91	0.00
4	1.9061	12.85	0.28	0.45	0.00	100.00	0.00
5	1.9865	12.81	0.25	0.40	0.00	100.00	0.00
6	1.9324	12.86	0.27	0.43	0.00	100.00	0.00
7	1.8505	12.84	0.30	0.48	0.00	99.84	0.16
8	2.0594	13.21	0.22	0.36	0.00	100.00	0.00
9	1.7798	12.69	0.33	0.53	0.00	100.00	0.00
10	1.7816	12.63	0.33	0.52	0.00	100.00	0.00
11	1.7909	12.62	0.32	0.52	0.00	100.00	0.00
12	1.8122	12.66	0.32	0.51	0.00	100.00	0.00
13	1.6951	12.55	0.36	0.58	0.00	100.00	0.00
14	1.7128	12.33	0.35	0.56	0.85	99.15	0.00
15	1.7566	12.49	0.34	0.54	0.00	100.00	0.00
avg	1.7067	11.64	0.31	0.50	8.45	91.54	0.01

© 1990 NOVA HUSKY RESEARCH CORPORATION

Table 5.5
CAT SCANNER Analysis of PCP Core #2

Slice No.	Bulk Density (g/cm^3)	Effective Atomic Number	Porosity dry (density $0.0g/cm^3$)	Porosity liquid (density $1.0g/cm^3$)	air (%)	sandstone (%)	cement (%)
1	1.2054	7.12	0.09	0.16	59.54	40.46	0.00
2	2.2353	13.57	0.16	0.25	0.00	100.00	0.00
3	2.1927	13.40	0.17	0.28	0.00	100.00	0.00
4	2.4364	13.92	0.08	0.13	0.00	100.00	0.00
5	1.9100	13.10	0.28	0.45	0.00	99.97	0.03
6	1.8180	12.81	0.31	0.50	0.00	100.00	0.00
7	1.6721	10.04	0.29	0.48	20.27	79.73	0.00
8	2.1639	13.56	0.18	0.30	0.00	99.23	0.77
9	2.0276	13.22	0.23	0.38	0.00	100.00	0.00
10	2.2467	13.51	0.15	0.24	0.00	100.00	0.00
11	2.3133	13.06	0.16	0.25	0.85	91.03	8.12
12	1.5921	12.25	0.40	0.64	0.19	99.81	0.00
13	1.8845	12.89	0.29	0.46	0.00	100.00	0.00
14	1.7389	12.53	0.34	0.55	1.03	98.97	0.00
15	1.7996	12.75	0.32	0.51	0.00	100.00	0.00
avg	1.9491	12.51	0.24	0.39	5.46	93.95	0.59

© 1990 NOVA HUSKY RESEARCH CORPORATION

Table 5.6
CAT SCANNER Analysis of PCP Core #3

Slice No.	Bulk Density (g/cm^3)	Effective Atomic Number	Porosity dry (density $0.0 g/cm^3$)	Porosity liquid (density $1.0 g/cm^3$)	air (%)	sandstone (%)	cement (%)
1	2.2818	12.43	0.14	0.23	0.00	82.52	17.48
2	2.2020	13.37	0.17	0.27	0.00	100.00	0.00
3	2.2158	13.32	0.16	0.26	0.00	100.00	0.00
4	1.9527	12.66	0.25	0.42	0.82	99.18	0.00
5	1.8342	12.72	0.31	0.49	0.00	100.00	0.00
6	1.8372	12.74	0.31	0.49	0.00	100.00	0.00
7	1.8627	12.73	0.29	0.47	0.61	99.39	0.00
8	1.8499	12.73	0.30	0.48	0.00	100.00	0.00
9	1.9524	12.97	0.26	0.42	0.29	99.71	0.00
10	1.9467	12.95	0.27	0.43	0.00	100.00	0.00
11	1.9467	13.32	0.19	0.30	0.00	100.00	0.00
12	2.1473	13.30	0.17	0.28	0.00	99.26	0.74
13	2.2002	13.40	0.17	0.27	0.00	100.00	0.00
14	2.2311	13.49	0.17	0.27	0.00	92.76	7.24
15	2.1648	13.36	0.18	0.30	0.00	99.34	0.66
avg	2.0577	13.03	0.22	0.36	0.11	98.14	1.74

© 1990 NOVA HUSKY RESEARCH CORPORATION

Table 5.7
CAT SCANNER Analysis of PCP Core #4

Slice No.	Bulk Density (g/cm^3)	Effective Atomic Number	Porosity dry (density $0.0g/cm^3$)	Porosity liquid (density $1.0g/cm^3$)	air (%)	sandstone (%)	cement (%)
1	1.6463	11.79	0.36	0.57	5.33	94.67	0.00
2	1.7215	12.44	0.35	0.56	0.00	100.00	0.00
3	1.8935	12.79	0.29	0.46	0.00	100.00	0.00
4	1.8999	12.79	0.28	0.45	0.00	100.00	0.00
5	1.9028	12.76	0.28	0.45	0.00	100.00	0.00
6	1.7277	12.41	0.35	0.58	0.00	100.00	0.00
7	1.7824	12.60	0.33	0.52	0.00	100.00	0.00
8	1.6716	12.31	0.37	0.59	0.00	100.00	0.00
9	1.6676	12.31	0.37	0.59	0.00	100.00	0.00
10	1.7791	10.61	0.33	0.53	0.00	100.00	0.00
11	1.8037	12.66	0.32	0.51	0.00	100.00	0.00
12	1.8121	12.70	0.32	0.51	0.00	100.00	0.00
13	1.6202	12.23	0.39	0.62	0.00	100.00	0.00
14	1.7716	12.58	0.33	0.53	0.00	100.00	0.00
15	1.7638	12.58	0.33	0.54	0.00	100.00	0.00
16	1.9152	12.98	0.29	0.46	0.00	89.20	10.80
avg	1.7737	12.53	0.33	0.53	0.33	98.99	0.67

© 1990 NOVA HUSKY RESEARCH CORPORATION

Table 5.8
CAT SCANNER Analysis of PCP Core #5

Slice No.	Bulk Density (g/cm^3)	Effective Atomic Number	Porosity dry (density $0.0 g/cm^3$)	Porosity liquid (density $1.0 g/cm^3$)	air (%)	sandstone (%)	cement (%)
1	1.3708	9.25	0.36	0.58	25.58	74.42	0.00
2	1.4179	9.39	0.33	0.54	25.21	74.79	0.00
3	1.7208	12.38	0.35	0.56	0.50	99.50	0.00
4	1.5522	11.53	0.39	0.62	6.45	93.55	0.00
5	1.6063	11.68	0.36	0.58	7.56	92.44	0.00
6	1.9056	12.61	0.26	0.42	3.66	96.34	0.00
7	1.8125	12.73	0.31	0.50	0.88	99.12	0.00
8	2.0642	13.12	0.22	0.35	0.00	100.00	0.00
9	1.7229	12.47	0.35	0.56	0.00	100.00	0.00
10	1.7582	12.55	0.34	0.54	0.00	100.00	0.00
11	1.7555	12.55	0.34	0.54	0.00	100.00	0.00
12	1.7522	12.49	0.34	0.54	0.00	100.00	0.00
13	1.7114	12.44	0.35	0.57	0.00	100.00	0.00
14	1.7403	12.47	0.34	0.55	0.00	100.00	0.00
15	1.6118	12.39	0.39	0.63	0.00	100.00	0.00
avg	1.7002	12.00	0.33	0.54	4.66	95.34	0.00

© 1990 NOVA HUSKY RESEARCH CORPORATION

Table 5.9
CAT SCANNER Analysis of PCP Core #6

Slice No.	Bulk Density (g/cm^3)	Effective Atomic Number	Porosity dry (density $0.0 g/cm^3$)	Porosity liquid (density $1.0 g/cm^3$)	air (%)	sandstone (%)	cement (%)
1	1.1394	7.32	0.38	0.60	43.51	56.49	0.00
2	1.7857	12.67	0.33	0.52	0.00	100.00	0.00
3	1.7458	12.46	0.34	0.55	0.00	100.00	0.00
4	1.7641	12.53	0.33	0.54	0.00	100.00	0.00
5	1.4263	11.68	0.46	0.74	0.58	99.42	0.00
6	1.5873	12.15	0.40	0.64	0.82	99.18	0.00
7	1.6506	12.29	0.38	0.60	0.00	100.00	0.00
8	1.5729	12.15	0.41	0.65	0.00	100.00	0.00
9	1.4459	11.76	0.45	0.73	1.46	98.54	0.00
10	1.4911	12.04	0.44	0.70	0.05	99.95	0.00
11	1.5055	11.99	0.43	0.69	0.34	99.66	0.00
12	1.6029	12.13	0.39	0.63	1.27	98.73	0.00
avg	1.5598	11.76	0.39	0.63	4.00	96.00	0.00

© 1990 NOVA HUSKY RESEARCH CORPORATION

TABLE 6.1

CAT Scan Petrographic Analysis

Slice #	Bulk Density (g/cm^3)	Porosity (%)	Z_{eff}	Air	Mineralogical Analysis (Area %) Sandstone	High Density
			Halkirk-8-612			
1	2.1313	19.49	13.72	-	100.0	-
2	2.1439	19.36	13.56	-	100.00	-
3	2.1025	20.79	13.45	-	97.74	2.26
4	2.0918	21.11	13.47	-	97.68	2.32
5	2.0809	21.41	13.43	-	99.66	0.34
6	2.0977	20.93	13.49	-	97.11	2.89
7	2.0988	20.87	13.50	-	97.42	2.58
8	2.0886	21.06	13.43	-	100.00	-
Avg.	**2.1044**	**20.93**	**13.51**	**-**	**98.39**	**1.61**
			Halkirk-9-612			
1	1.9755	25.46	13.66	-	100.00	-
2	2.0279	23.47	13.34	-	99.87	0.13
3	2.0148	24.00	13.32	-	100.00	-
4	2.0028	24.51	13.27	-	100.00	-
5	1.9858	25.12	13.26	-	100.00	-
6	1.9772	25.46	13.24	-	100.00	-
7	1.9765	25.48	13.27	-	100.00	-
8	1.9672	25.78	13.24	-	100.00	-
9	1.9766	25.47	13.29	-	100.00	-
10	1.9884	25.09	13.27	-	100.00	-
11	1.9797	25.38	13.26	-	100.00	-
12	1.9611	25.96	13.19	-	100.00	-
Avg.	**1.9861**	**25.10**	**13.30**	**-**	**99.99**	**0.01**
			Halkirk-29-612			
1	1.9842	25.24	13.29	-	100.00	-
2	1.9618	25.93	13.22	-	100.00	-
3	1.9538	26.21	13.22	-	100.00	-
4	1.9544	26.18	13.21	-	100.00	-
5	1.9601	25.98	13.24	-	100.00	-
6	1.9611	25.94	13.22	-	100.00	-
7	1.9611	25.94	13.23	-	100.00	-
8	1.9609	25.95	13.23	-	100.00	-
9	1.9614	25.94	13.22	-	100.00	-
10	1.9759	25.49	13.31	-	100.00	-
11	2.0200	23.79	13.51	-	100.00	-
12	2.0470	22.73	13.61	-	100.00	-
13	2.0082	24.27	13.27	-	100.00	-
14	1.9754	25.50	13.24	-	100.00	-
15	1.9690	25.69	13.24	-	100.00	-
16	1.9647	25.83	13.24	-	100.00	-
17	1.9650	25.83	13.25	-	100.00	-
18	1.9667	25.78	13.25	-	100.00	-
19	1.9686	25.73	13.26	-	100.00	-
20	1.9707	25.69	13.26	-	100.00	-
Avg.	**1.9745**	**25.48**	**13.28**	**-**	**100.00**	**-**

© 1990 NOVA HUSKY RESEARCH CORPORATION

TABLE 6.2

Comparison of Results

Core No.	CT RESULTS		SERVICE LAB RESULTS		DIFFERENCE (%)	
	Bulk Density	Porosity	Bulk Density	Porosity	Bulk Density	Porosity
Halkirk 8-612	2.1044	20.93	2.120	20.20	0.74	3.4
Halkirk 9-612	1.9861	25.10	2.030	23.60	2.10	5.9
Halkirk 29-612	1.9745	25.48	2.030	23.90	2.70	6.2

© 1990 NOVA HUSKY RESEARCH CORPORATION

TABLE 6.3

Results of CATSCAN Analysis of Bluesky Core

Slice #		Bulk Density (g/cm^3)	Porosity (%)	Slice #		Bulk Density (g/cm^3)	Porosity (%)
A3	1	2.23	16.79	B6	1	2.29	14.55
	2	2.25	16.04		2	2.32	13.43
	3	2.26	15.67		**Avg**	**2.30**	**14.18**
	4	2.26	15.67				
	5	2.23	6.79	C2	1	2.27	15.30
	Avg.	2.25	16.04		2	2.41	10.08
					3	2.48	7.46
B2	1	2.30	14.18		**Avg**	**2.39**	**10.82**
	2	2.30	14.18				
	3	2.29	14.55	D3	1	2.29	14.55
	4	2.29	14.55		2	2.30	14.18
	5	2.22	17.16		3	2.34	12.69
	Avg.	**2.28**	**14.92**		**Avg.**	**2.31**	**13.80**
B3	1	2.34	12.69	D5	1	2.30	14.18
	2	2.33	13.06		2	2.32	13.43
	Avg.	2.33	13.06		3	2.31	13.80
					Avg	**2.31**	**13.80**
CHRC1B2	1	2.13	20.52				
	2	2.14	20.15				
	3	2.12	20.89				
	4	2.12	20.89				
	Avg.	**2.13**	**20.52**				
CHRC1B6	1	2.18	18.66				
	2	2.17	19.03				
	3	2.18	18.66				
	Avg.	**2.18**	**18.66**				

© 1990 NOVA HUSKY RESEARCH CORPORATION

TABLE 6.4

CATSCAN Produced Petrographic Results

Core #56

Slice #	Bulk Density (g/cm^3)	Porosity
1	2.3362	0.17
2	2.3153	0.18
3	2.3337	0.18
4	2.3382	0.17
5	2.3421	0.17
6	2.3677	0.16
7	2.3445	0.17
8	2.3366	0.17
9	2.3261	0.18
10	2.3400	0.17
11	2.3476	0.17
12	2.3639	0.16
13	2.3826	0.16
14	2.3789	0.16
15	2.4037	0.15
16	2.3779	0.16
17	2.4016	0.15
AVERAGE	**2.3510**	**0.17**
Core Analysis	**2.36**	**0.167**

© 1990 NOVA HUSKY RESEARCH CORPORATION

TABLE 6.5

CATSCAN Produced Petrographic Results

Core #52

Slice #	Bulk Density (g/cm^3)	Porosity
1	2.3519	0.17
2	2.3813	0.16
3	2.3507	0.17
4	2.3886	0.16
5	2.3963	0.15
6	2.3965	0.15
7	2.4259	0.14
8	2.3696	0.16
9	2.3431	0.17
10	2.3217	0.18
11	2.2959	0.19
12	2.3157	0.18
13	2.3597	0.17
14	2.3889	0.16
15	2.4413	0.14
16	2.4050	0.15
17	2.1515	0.24
Average	**2.3579**	**0.17**
Core Analysis	**2.38**	**0.162**

© 1990 NOVA HUSKY RESEARCH CORPORATION

Table 6.6

CATSCAN Analysis of Rainbow Keg River "G" Pool Cores

Picture Location*	Bulk** Density (g/cm^3)	Porosity (%)	Mineralogy Area (%) air	limestone	high density
		Box 1 Core 4			
5	2.4880	8.19	-	100.00	-
6	2.4316	10.27	0.32	99.68	-
average	**2.4598**	**9.23**	**0.16**	**99.84**	-
core analysis	**2.3890**	**12.60**			
		Box 2 Core 10			
7	2.4142	10.91	-	100.00	-
8	2.4233	10.58	-	100.00	-
9	2.4422	9.88	0.11	99.89	-
average	**2.4265**	**10.46**	**0.04**	**99.96**	-
core analysis	**2.4230**	**11.00**			
		Box 3 Core 15			
13	2.3875	11.90	-	100.00	-
14	2.4230	10.59	-	100.00	-
15	2.2469	17.09	-	100.00	-
average	**2.3525**	**13.19**	-	**100.00**	-
core analysis	**2.3650**	**13.40**			
		Box 4 Core 23			
16	2.4787	8.53	-	100.00	-
17	2.3965	11.57	-	100.00	-
average	**2.4373**	**10.06**	-	**100.00**	-
core analysis	**2.3810**	**12.80**			
		Box 5 Core 30			
26	2.1491	20.70	-	100.00	-
27	2.1140	21.99	-	100.00	-
28	2.1078	22.22	-	100.00	-
average	**2.1236**	**21.63**	-	**100.00**	-
core analysis	**2.0240**	**25.40**			
		Box 6 Core 34			
29	2.4807	8.46	-	100.00	-
30	2.5259	6.79	-	100.00	-
31	2.5333	6.52	-	99.97	0.03
average	**2.5133**	**7.26**	-	**99.99**	**0.01**
core analysis	**2.4830**	**8.50**			
		Box 7 Core 40			

© 1990 NOVA HUSKY RESEARCH CORPORATION

32	2.5033	7.63	-	99.81	0.19
33	2.4495	9.61	-	100.00	-
34	2.3627	12.81	-	100.00	-
35	2.3666	12.67	-	100.00	-
average	**2.4215**	**10.64**	-	**99.95**	**0.05**
core analysis	**2.3850**	**12.40**			
			Box 8 Core 45		
45	2.4567	9.34	-	100.00	-
46	2.4172	10.80	-	100.00	-
47	2.2327	17.61	-	100.00	-
average	**2.3687**	**12.59**	-	**100.00**	-
core analysis	**2.3260**	**14.80**			
			Box 9 Core 46		
48	2.0960	22.66	-	100.00	-
49	2.1257	21.56	-	100.00	-
50	2.0974	22.60	-	100.00	-
average	**2.1064**	**22.27**	-	**100.00**	-
core analysis	**1.9910**	**26.80**			

* as marked in core box

** grain density 2.71 g/cm^3

© 1990 NOVA HUSKY RESEARCH CORPORATION

TABLE 6.7: Comparison of different core characterization methods (Trout Reservoir)

Depth [m]	Routine Core Analysis			CATSCAN		
	poros. (frac.)	bulk dens. g/cm^3	grain dens. g/cm^3	poros. (frac.)	bulk dens. g/cm^3	grain dens. g/cm^3
1463.40-1463.67	0.027	2.730	2.806	0.072	2.636	2.83
1463.67-1463.84	0.025	2.752	2.824	0.042	2.604	2.83
1463.84-1464.02	0.080	2.617	2.843	0.088	2.584	2.83
1464.02-1464.40	0.114	2.502	2.824	0.113	2.512	2.83
1464.40-1464.64	0.108	2.516	2.821	0.105	2.530	2.83
1464.64-1464.82	0.139	2.430	2.823	0.128	2.464	2.83
1464.82-1465.06	0.128	2.462	2.822	0.127	2.464	2.83
1465.06-1465.26	0.132	2.453	2.827	0.139	2.436	2.83
1465.26-1465.49	0.114	2.494	2.816	0.118	2.496	2.83
1465.49-1465.78	0.101	2.528	2.811	0.093	2.523	2.83
1465.78-1465.98	0.095	2.545	2.811	0.097	2.485	2.83
1465.98-1466.17	0.080	2.582	2.805	0.084	2.595	2.83
1466.17-1466.37	0.099	2.531	2.810	0.087	2.582	2.83
1466.37-1466.51	0.099	2.531	2.809	0.106	2.529	2.83
1466.51-1466.66	0.141	2.386	2.778	0.151	2.394	2.83
1466.66-1466.83	0.095	2.548	2.816	0.107	2.528	2.83
1466.83-1467.01	0.094	2.551	2.818	0.090	2.465	2.83
1467.01-1467.22	0.114	2.494	2.816	0.099	2.551	2.83
1467.22-1467.42	0.035	2.700	2.799	0.049	2.713	2.83
1467.42-1467.67	0.044	2.684	2.808	0.065	2.673	2.83
1467.67-1468.00	0.076	2.585	2.796	0.107	2.554	2.83
1468.00-1468.21	0.015	2.727	2.766	0.053	2.652	2.83
1468.21-1468.42	0.086	2.562	2.802	0.101	2.557	2.83
1468.42-1468.57	0.095	2.534	2.800	0.087	2.598	2.83
1468.57-1468.83	0.120	2.475	2.812	0.066	2.660	2.83

poros. = porosity
dens. = density
frac. = fraction

© 1990 NOVA HUSKY RESEARCH CORPORATION

TABLE 6.8: List of Core Property Data as Determined by CATSCAN (Trout Reservoir)

Core #	name	bulk density (g/cm^3)	porosity (fraction)
1	sample-1t	2.666	0.061
2	sample-1	2.636	0.072
3	sample-1b	2.653	0.067
4	sample-2	2.742	0.042
5	sample-3t	2.604	0.080
6	sample-3	2.584	0.088
7	sample-3b	2.593	0.085
8	sample-4	2.512	0.113
9	sample-4b	2.552	0.097
10	sample-1tp	2.542	0.102
11	sample-1p	2.530	0.105
12	sample-1bp	2.639	0.070
13	sample-5	2.464	0.128
14	sample-6t	2.471	0.125
15	sample-6	2.467	0.127
16	sample-6b	2.287	0.185
17	sample-2p	2.436	0.139
18	sample-7	2.496	0.118
19	sample-8	2.523	0.093
20	sample-8b	2.495	0.108
21	sample-3p	2.485	0.097
22	sample-3bp	2.593	0.085
23	sample-9	2.595	0.084

© 1990 NOVA HUSKY RESEARCH CORPORATION

TABLE 6.8 continued...

Core #	name	bulk density (g/cm^3)	porosity (fraction)
24	sample-4p	2.582	0.087
25	sample-10	2.529	0.106
26	sample-5p	2.394	0.151
27	sample-11	2.528	0.107
28	sample-12t	2.543	0.102
29	sample-12	2.465	0.090
30	sample-6tp	2.348	0.158
31	sample-6p	2.551	0.099
32	sample-13t	2.660	0.073
33	sample-13	2.713	0.049
34	sample-13b	2.551	0.097
35	sample-14t	2.658	0.066
36	sample-14	2.673	0.065
37	sample-14b	2.710	0.052
38	sample-7p	2.554	0.107
39	sample-15	2.652	0.053
40	sample-8tp	2.636	0.070
41	sample-8p	2.557	0.101
42	sample-8bp	2.472	0.129
43	sample-16	2.598	0.087
44	sample-9p	2.660	0.066
45	sample-9bp	2.589	0.078

© 1990 NOVA HUSKY RESEARCH CORPORATION

TABLE 6.9: Detailed CAT Scan Analysis of Various Core Samples (Trout Reservoir)

Slice #	Sample 4		Sample 2p		Sample 7		Sample 3p	
	b.den. (frac.)	poros. g/cm^3	b.den (frac.)	poros. g/cm^3	b.den (frac.)	poros.	b.den. (frac.)	poros. g/cm^3
1			2.424	0.141	2.176	0.231	2.495	0.119
2	2.660	0.066	2.436	0.136	2.407	0.149	2.523	0.109
3			2.434	0.137	2.455	0.132	2.487	0.118
4	2.589	0.093	2.508	0.112	2.511	0.113	2.539	0.099
5			2.485	0.120	2.512	0.112	2.551	0.086
6	2.357	0.167	2.506	0.113	2.500	0.117	2.576	0.086
7	2.425	0.142	2.505	0.114	2.485	0.122	2.568	0.087
8	2.458	0.131	2.532	0.105	2.494	0.118	2.559	0.088
9	2.527	0.107	2.536	0.104	2.507	0.114	2.523	0.092
10	2.534	0.105	2.450	0.133	2.504	0.115	2.484	0.097
11	2.530	0.106	2.434	0.139	2.500	0.116	2.495	0.096
12	2.540	0.103	2.442	0.137	2.511	0.112	2.544	0.089
13	2.533	0.105	2.443	0.136	2.508	0.114	2.588	0.083
14	2.531	0.106	2.408	0.149	2.488	0.121	2.622	0.075
15	2.530	0.106	2.427	0.142	2.492	0.119	2.609	0.081
16			2.461	0.130	2.509	0.113	2.602	0.082
17			2.477	0.126	2.501	0.116	2.605	0.081
18			2.479	0.127	2.495	0.118	2.598	0.083
19			2.466	0.129	2.496	0.118	2.598	0.083
20			2.474	0.126	2.499	0.117	2.579	0.089
21			2.470	0.127	2.492	0.119	2.556	0.097
22			2.459	0.131			2.511	0.110
23			2.475	0.125				
24			2.482	0.123				
25			2.488	0.121				
26			2.436	0.139				
overall	2.518	0.114	2.467	0.128	2.478	0.124	2.555	0.092
corelab	2.502	0.114	2.453	0.132	2.477	0.117	2.545	0.095

poros. = porosity
dens. = density
frac. = fraction

© 1990 NOVA HUSKY RESEARCH CORPORATION

Table 6.9 continued...

Slice #	Sample 6p b.den. (frac.)	Sample 6p poros. g/cm^3	Sample 9p b.den (frac.)	Sample 9p poros. g/cm^3
1	2.389	0.162	2.142	0.237
2	2.397	0.157	2.398	0.138
3	2.392	0.156	2.389	0.139
4	2.554	0.098	2.466	0.108
5	2.537	0.102	2.495	0.110
6	2.516	0.112	2.430	0.138
7	2.373	0.129	2.423	0.140
8	2.313	0.140	2.517	0.107
9	2.395	0.145	2.431	0.132
10	2.514	0.112	2.480	0.115
11	2.552	0.098	2.524	0.102
12	2.556	0.097	2.507	0.102
13	2.559	0.096	2.539	0.090
14	2.554	0.098	2.499	0.105
15	2.554	0.098	2.361	0.144
16	2.543	0.102	2.559	0.089
17	2.534	0.104	2.657	0.065
18	2.382	0.158	2.555	0.124
19			2.383	0.128
20			2.310	0.139
21			2.333	0.128
22			2.494	0.097
23			2.584	0.086
24			2.523	0.124
25			2.465	0.098
26			2.488	0.092
overall	2.479	0.120	2.399	0.115
corelab	2.494	0.114	2.475	0.120

poros. = porosity
dens. = density
frac. = fraction

© 1990 NOVA HUSKY RESEARCH CORPORATION

TABLE 6.10: Determination of Anhydrite in a Dolomite Core (Trout Reservoir)

Name	slice	b.den	zeff	porosity	g.den dolomite	anhydrite	air (vugs)
sample 7p	1	2.569	12.955	0.095	0.9814	0.0186	
	2	2.570	13.038	0.096	0.9868	0.0132	
	3	2.641	13.359	0.078	0.9061	0.0939	
	4	2.655	13.392	0.073	0.9075	0.0925	
	5	2.503	12.937	0.112	0.9308	0.0499	0.0194
	6	2.291	12.515	0.159	0.8810	0.0616	0.0574
	7	2.263	12.694	0.177	0.8284	0.1232	0.0484
	8	2.317	12.973	0.168	0.8238	0.1426	0.0335
	9	2.357	13.217	0.172	0.8509	0.1386	0.0105
	10	2.493	13.045	0.131	0.8457	0.1490	0.0053
	11	2.555	13.168	0.109	0.8588	0.1367	0.0045
	12	2.541	13.325	0.109	0.9160	0.0822	0.0018
	13	2.590	13.311	0.091	0.9349	0.0642	0.0009
	14	2.633	13.384	0.077	0.9103	0.0897	
	15	2.637	13.338	0.076	0.9244	0.0753	0.0003
	16	2.664	13.370	0.067	0.9150	0.0848	0.0002
	17	2.692	13.434	0.061	0.8587	0.1412	0.0001
	18	2.704	13.390	0.057	0.8659	0.1326	0.0015
	19	2.682	13.371	0.061	0.9035	0.0952	0.0013
	20	2.663	13.219	0.064	0.9426	0.0535	0.0039
	overall	2.551	13.172	0.102	0.8986	0.0919	0.0095
	corelab	2.585		0.076			

b.den = bulk density
g. den = grain density

© 1990 NOVA HUSKY RESEARCH CORPORATION

TABLE 6.11
New Measurements with Reset Photomultiplier Tubes

Slice#	Wabamun #4 Bulk Density (g/cm^3)	Wabamun #4 Porosity (fr)	Wabamun #5 Bulk Density (g/cm^3)	Wabamun #5 Porosity (fr)	Wabamun #6 Bulk Density (g/cm^3	Wabamun #6 Porosity (fr)
1	2.52973	0.10599	2.49460	0.11826	2.53902	0.10275
2	2.55210	0.09820	2.63314	0.07003	2.59292	0.08364
3	2.71451	0.04213	2.68125	0.05321	0.04938	
4	2.72718	0.03821	2.65477	0.06247	2.67694	0.05480
5	2.73082	0.03696	2.59996	0.08148	2.68115	0.05331
6	2.71794	0.04106	2.61633	0.07579	2.67567	0.05482
7	2.72473	0.03886	2.62317	0.07357	2.67689	0.05486
8	2.71481	0.04181	2.66304	0.05936	2.67351	0.05596
9	2.72551	0.03900	2.70033	0.04633	2.68458	0.05220
10	2.71760	0.04114	2.65993	0.06044	2.65372	0.06256
11	2.72098	0.03998	2.64096	0.06696	2.64561	0.06563
12	2.71218	0.04295	2.64138	0.06683	2.60387	0.07981
13	2.72156	0.04008	2.62790	0.07133	2.58667	0.07867
14	2.71117	0.04316	2.60146	0.07722	2.59809	0.07734
15	2.72181	0.03969	2.59836	0.08231	2.54387	0.09554
16	2.71563	0.04225	2.62019	0.07384	2.50472	0.09892
17	2.74020	0.03669	2.66576	0.05910	2.55135	0.08979
18	2.73331	0.03811	2.63546	0.06921	2.58277	0.07936
19	2.74086	0.03531	2.62352	0.07296	2.63505	0.06781
20	2.72602	0.03906	2.43652	0.13224	2.63505	0.06781
21	2.73639	0.03614	2.52449	0.09197	2.71755	0.04109
22	2.73082	0.03716	2.57825	0.08493	2.72093	0.04156
23	2.73758	0.03543	2.52947	0.08706	2.69903	0.04913
24	2.73006	0.03764	2.38484	0.13600	2.70275	0.04773
25	2.74089	0.03422	2.38971	0.15066	2.69738	0.04898
26	2.73056	0.03754	2.42133	0.13920	2.65061	0.06566
27	2.73753	0.03471	2.50201	0.11429	2.62274	0.06814
28	2.72539	0.03840			2.58738	0.08013
29	2.72123	0.03930			2.58702	0.07954
30	2.68329	0.05218			2.65311	0.06078
31	2.72123				2.61930	0.07058
32	2.68329				2.55631	0.09259
33					2.60186	0.08056
Average	2.71241	0.04345	2.58326	0.08419	2.63295	0.06784
Core Analysis	2.7900	0.0110	2.5500	0.1040	2.6600	0.0550

© 1990 NOVA HUSKY RESEARCH CORPORATION

TABLE 6.12
Fracture/Vug vs. Matrix Porosity of Wabamun Core

Slice#	Wabamun #4		Wabamun #5		Wabamun #6	
	(frac/gm (%)	matrix (%)	frac/vug (%)	matrix (%)	frac/vug (%)	matrix (%)
1	2.03078	8.56829	4.62775	7.19797	1.87397	8.40089
2	1.21756	8.60226	1.95383	5.04964	0.53383	7.83020
3	0.00000	4.21305	0.25153	5.06979	0.06845	4.86946
4	0.00000	3.82064	1.63373	4.61355	0.05386	5.42612
5	0.00000	3.69594	3.61216	4.53703	0.03078	5.30036
6	0.00000	4.10640	3.02149	4.55878	0.01539	5.46700
7	0.00371	3.88246	3.02043	4.33670	0.00769	5.47842
8	0.00000	4.18095	1.33643	4.59937	0.05598	5.53970
9	0.00000	3.90024	0.21571	4.41682	0.22261	4.99710
10	0.00000	4.11409	0.91112	5.13321	0.71664	5.53968
11	0.01963	3.97851	1.80817	4.88832	1.67737	4.88592
12	0.00796	4.28681	1.62032	5.06317	3.29862	4.68359
13	0.01910	3.98912	2.11388	5.01886	2.84663	5.02203
14	0.00371	4.31202	3.25247	4.47101	2.58802	5.14768
15	0.00769	3.96100	4.06502	4.16640	4.73197	4.82579
16	0.02733	4.19741	2.85498	4.52909	5.37997	4.51418
17	0.03953	3.62908	1.46511	4.44468	4.97065	4.01103
18	0.02414	3.78642	2.08358	4.83789	3.91790	4.02018
19	0.00371	3.52746	2.68393	4.61274	3.01358	3.76890
20	0.00743	3.89891	9.22582	4.00081	2.02308	3.69805
21	0.00743	3.60679	4.45142	4.74947	0.64102	3.46749
22	0.05174	3.66437	4.27360	4.22145	1.06898	3.08676
23	0.00000	3.54312	5.14117	3.56826	1.84716	3.06751
24	0.00000	3.76386	9.74678	3.85765	1.44097	3.33244
25	0.00000	3.42186	11.38770	3.68112	1.85889	3.03987
26	0.13054	3.62350	9.94399	3.97910	3.39581	3.17123
27	0.00000	3.47148	6.48522	4.94414	3.91183	2.90538
28	0.00000	3.83975			4.86568	3.14986
29	0.00000	3.93022			3.02600	2.98576
30	0.01194	5.20616			4.03083	3.05387
31					5.33208	3.02895
32					1.94269	3.93069
33						6.11306
Average	**0.12047**	**4.22407**	**3.45138**	**4.96762**	**2.19277**	**4.59123**

© 1990 NOVA HUSKY RESEARCH CORPORATION

TABLE 6.13
Additional Measurements on Wabamun Core

Slice#	Wabamun #2 Bulk Density (g/cm^3)	Wabamun #2 Porosity (fr)	Wabamun #3 Bulk Density	Wabamun #3 Porosity (fr) (g/cm^3)
1	2.54592	0.10019	2.48484	0.12180
2	2.64395	0.06583	2.52851	0.10631
3	2.73647	0.03555	2.67656	0.05492
4	2.81949	0.02137	2.66613	0.05862
5	2.81577	0.02294	2.69115	0.05016
6	2.81510	0.02012	2.68530	0.05190
7	2.80296	0.02335	2.66671	0.05807
8	2.81400	0.02220	2.67753	0.05419
9	2.81836	0.02185	2.65524	0.06237
10	2.81190	0.02258	2.63476	0.06938
11	2.80272	0.02440	2.64109	0.06565
12	2.81777	0.02099	2.63384	0.06862
13	2.80626	0.02212	2.69734	0.04827
14	2.82274	0.02044	2.69027	0.05141
15	2.82456	0.02212	2.69734	0.04827
16	2.82420	0.02112	2.67428	0.05583
17	2.81635	0.02250	2.66611	0.05855
18	2.81075	0.02213	2.65446	0.06325
19	2.82000	0.02291	2.68199	0.05263
20	2.82593	0.02299	2.66036	0.06031
21	2.82593	0.02299	2.66638	0.05795
22	2.82172	0.02151	2.66035	0.06017
23	2.80910	0.02452	2.66636	0.05798
24	2.80545	0.02191	2.67295	0.05578
25	2.81656	0.02524	2.66071	0.06011
26	2.81056	0.02292	2.64105	0.06683
27	2.81542	0.02215	2.64399	0.06571
28	2.82066	0.02204	2.63367	0.06937
29	2.80779	0.02393	2.62240	0.07333
30	2.82725	0.01774	2.62822	0.07130
31	2.80877	0.02006	2.59413	0.08319'
32	2.82041	0.02008	2.58585	0.08610
33	2.81574	0.02169	2.59940	0.08144
34	2.82051	0.01969	2.60399	0.07982
35	2.80876	0.02335	2.62029	0.07401
36	2.80553	0.02080	2.62898	0.07102
37	2.76081	0.02994	2.61451	0.07609
38			2.54745	0.09968
Average	2.80001	0.02587	2.63856	0.06789
Core Analysis	2.7700	0.0280	2.7300	0.0390

© 1990 NOVA HUSKY RESEARCH CORPORATION

TABLE 6.14: FRACTURE/VUG VERSUS MATRIX POROSITY OF THE TWO ADDITIONAL PIECES FROM WABAMUN

	Wabamun #5		Wabamun #6	
Slice#	frac/vug (%)	matrix (%)	frac/vug (%)	matrix (%)
1	3.29796	6.72118	4.45052	7.72964
2	0.20218	6.38075	2.40594	8.22525
3	0.00371	3.55134	0.30194	5.18998
4	0.00000	2.13743	0.86150	5.00001
5	0.00000	2.29397	0.34651	4.66913
6	0.00000	2.01167	0.52693	4.66305
7	0.00371	2.33112	0.97506	4.83205
8	0.00000	2.22021	0.40515	5.01353
9	0.00000	2.18545	1.84452	4.39294
10	0.00000	2.25762	2.35341	4.58531
11	0.00849	2.43141	2.18552	4.38010
12	0.00000	2.09949	2.94678	3.91565
13	0.00000	2.38179	3.88850	3.87041
14	0.00371	2.04006	1.09684	4.04458
15	0.00000	2.21172	0.99204	3.83524
16	0.00000	2.11169	1.34253	4.24038
17	0.00000	2.24966	1.13186	4.72275
18	0.00371	2.20960	1.94614	4.37916
19	0.00000	2.29105	0.49589	4.76759
20	0.00478	2.01061	1.20801	4.82252
21	0.00478	2.29450	0.65747	5.13745
22	0.00000	2.15096	0.65296	5.36380
23	0.00000	2.45237	0.28124	5.51635
24	0.00000	2.19076	0.04484	5.53360
25	0.01518	2.50783	0.38949	5.62196
26	0.00743	2.28442	0.71451	5.96901
27	0.00000	2.21491	1.17140	5.39934
28	0.00000	2.20350	1.01565	5.92151
29	0.00000	2.39294	1.92438	5.40863
30	0.00000	1.77446	0.94189	6.18817
31	0.00000	2.00609	2.21650	6.10300
32	0.00000	2.00822	1.99310	6.61721
33	0.00000	2.16874	1.06341	7.08098
34	0.00000	1.96922	1.39772	6.58483
35	0.00000	2.33510	1.19475	6.20622
36	0.00000	2.08012	1.11223	5.98944
37	0.00000	2.99390	1.25922	6.35029
38			1.86415	8.10402
Average	**0.09613**	**2.49070**	**135791**	**5.43092**

© 1990 NOVA HUSKY RESEARCH CORPORATION

TABLE 7.1

Pressure Response of #3 Sand; Experiment #1

Pressure (psi)	Mean CT Number	Bulk Density (g/cm^3)	Porosity (%)
0	360	1.7058	35.63
500	372	1.7254	34.89
1000	385	1.7465	34.09
1500	399	1.7694	33.23
2000	413	1.7922	32.37
2500	428	1.8166	31.45
1000	417	1.7987	32.12
0	393	1.7596	33.60
500	423	1.8085	31.75
1000	433	1.8248	31.14
1500	436	1.8297	30.95
2000	429	1.8183	31.39
25000	434	1.8264	31.07
0	397	1.7661	33.35

TABLE 7.2

Pressure Response of #3 Sand; Effect of Sample Length

Slice Number	0 psi	500 psi	1000 psi	1500 psi	2000 psi	2500 psi	1000 psi	0 psi
1	338	358	374	388	409	417	427	401
2	331	350	367	384	405	417	423	391
3	331	349	366	382	400	417	420	389
4	329	346	364	381	399	418	418	385
5	326	345	362	379	397	415	416	383
6	327	345	362	379	396	418	414	378
7	327	345	363	379	395	412	414	378
8	323	344	361	378	395	418	413	376
9	324	343	360	377	394	419	413	376
10	323	340	357	374	391	413	410	372

© 1990 NOVA HUSKY RESEARCH CORPORATION

TABLE 7.3

Pressure Response of #3 Sand; Experiment #2

Pressure (psi)	Mean CT Number	Bulk Density (g/cm^3)	Porosity (%)
0	326	1.6504	37.72
500	345	1.6813	36.55
1000	362	1.7091	35.51
1500	379	1.7368	34.46
2000	397	1.7661	33.35
2500	415	1.7954	32.25
1000	416	1.7971	32.19
0	383	1.7433	34.21
500	412	1.7906	32.43
1000	415	1.7954	32.25
1500	423	1.8085	31.75
2000	427	1.8150	31.51
2500	432	1.8232	31.20

TABLE 7.4

Pressure Response of #3 Sand in Rubber Shrink Tube; Experiment #3

Pressure (psi)	Mean CT Number	Bulk Density (g/cm^3)	Porosity (%)
0	343	1.6781	36.66
500	361	1.7074	35.57
1000	378	1.7351	34.52
1500	392	1.7580	33.66
2000	408	1.7840	32.68
2500	421	1.8052	31.88

© 1990 NOVA HUSKY RESEARCH CORPORATION

TABLE 7.5

Pressure Response of #3 Sand Saturated with Water

Pressure (psi)	Mean CT Number	Bulk Density (g/cm^3)	Porosity (%)
0	496	1.9275	43.79
500	524	1.9731	41.02
1000	541	2.0008	39.34
1500	556	2.0253	37.86
2000	568	2.0448	36.68
2500	555	2.0236	37.96
1000	553	2.0204	38.16
0	518	1.9633	41.62
500	543	2.0041	39.15
1000	544	2.0058	39.05
1500	545	2.0073	38.95
2000	546	2.0090	38.85
2500	546	2.0090	38.85

TABLE 7.6

Pressure Response of #16 Sand; Experiment #5

Pressure (psi)	Mean CT Number	Bulk Density (g/cm^3)	Porosity (%)
0	409	1.7857	32.62
500	425	1.8117	31.63
1000	431	1.8215	31.26
1500	433	1.8248	31.14
2000	437	1.8313	30.89
2500	438	1.8329	30.83
1000	432	1.8232	31.20
0	404	1.7775	32.92
500	421	1.8052	31.88
1000	425	1.8117	31.63
1500	428	1.8166	31.45
2000	432	1.8232	31.20
2500	434	1.8264	31.08

© 1990 NOVA HUSKY RESEARCH CORPORATION

TABLE 7.7

Pressure Response of Berea Sandstone

Pressure (psi)	Mean CT Number		Bulk Density (g/cm^3)		Porosity (%)	
0	546	555	2.0090	2.0236	24.19	23.63
500	559	558	2.0302	2.0285	23.39	23.45
1000	560	560	2.0318	2.0318	23.33	23.33
1500	561	561	2.0334	2.0334	23.27	23.27

TABLE 7.8

Low Pressure Cycle for Sand #3

Pressure (psi)	Mean CT Number	Bulk Density (g/cm^3)	Porosity (%)
0	326	1.6504	37.72
125	335	1.6650	37.17
250	340	1.6732	36.86
375	345	1.6813	36.55
500	350	1.6895	36.24
0	332	1.6602	37.35
125	341	1.6748	36.80
250	345	1.6813	36.55
375	348	1.6862	36.37
500	356	1.6993	35.88

© 1990 NOVA HUSKY RESEARCH CORPORATION

TABLE 8.1

Bulk Density Comparisons on Core Cleaning

1) Trout Core

Slice #	Bulk Density before cleaning (g/cm^3)	Bulk Density after cleaning (g/cm^3)
1	2.3862	2.3323
2	2.4868	2.5038
3	2.4957	2.5036
4	2.5674	2.5708
Avg	2.4840	2.4776

2) Sundre Core #1

Slice #	Bulk Density before cleaning (g/cm^3)	Bulk Density after cleaning (g/cm^3)
1	2.5282	2.5453
2	2.6033	2.6023
3	2.6318	2.7175
4	2.7339	2.7229
5	2.7240	2.7135
6	2.7166	2.7048
7	2.6977	2.6840
8	2.6809	2.6318
Avg	2.6645	2.6653

© 1990 NOVA HUSKY RESEARCH CORPORATION

3) Sundre Core #2

Slice #	Bulk Density before cleaning (g/cm^3)	Bulk Density after cleaning (g/cm^3)
1	2.4608	2.4596
2	2.5177	2.4801
3	2.5484	2.5682
4	2.6482	2.6056
5	2.6629	2.6176
6	2.6565	2.5861
7	2.6086	2.5573
8	2.5808	
Avg	2.5854	2.5535

4) Colgas Worsley

Slice #	Bulk Density before cleaning (g/cm^3)	Bulk Density after cleaning (g/cm^3)
1	2.2193	2.1923
2	2.2457	2.2179
3	2.3044	2.2861
4	2.3444	2.3076
5	2.3416	2.2933
6	2.3337	2.2942
7	2.3465	2.3355
8	2.4652	2.4702
9	2.5402	2.5211
10	2.5616	2.5336
11	2.5455	2.4919
12	2.4978	2.4576
13	2.4751	2.4122
14	2.4240	2.3705
15	2.3807	
Avg	2.4017	2.3702

© 1990 NOVA HUSKY RESEARCH CORPORATION

TABLE 8.2

Bulk Density of Drilling Muds and Brines

Bulk Density g/cm^3	Filename
1.3655	Trout brine
1.6061	Trout mud
1.3059	Sun brine
1.9848	Sun mud
1.1190	Colgas Mud
1.1213	Rainbow brine
1.6279	Rainbow mud

© 1990 NOVA HUSKY RESEARCH CORPORATION

TABLE 9.1

A. CORE ANALYSIS DATA FOR CORE PIECES #12 AND #52

	CORE #12	CORE #52
Permeability (Air)		
Maximum (mD)	4.59	19.0
90 Deg. (mD)	1.61	18.0
Vertical (mD)	0.4	5.56
Porosity	0.055	0.114
Bulk Density (kg/m^3)	2640.	2520.
Grain Density (kg/m^3)	2800.	2840.
Water fraction	0.182	0.653

B. HYCAL ANALYSIS DATA FOR CORE PIECES #12 AND #52

	CORE #12	CORE #52
Initial Permeability to CS_2 (mD)	1.40	11.60
Solids recovered prior to heatup (g)	78.73	19.70
Permeability after first heatup (mD)	0.41	1.30
Solids recovered prior to second heatup (g)	5.85	0.70
Permeability after second heatup (mD)	0.31	0.90
Solids recovered after second heatup (g)	0.12	0.00
Pre-test porosity (%)	*6.6	9.2
Post-test porosity (%)	11.5	*10.5

*calculated based on mass balance

© 1990 NOVA HUSKY RESEARCH CORPORATION

TABLE 9.2

Characterization of core #12

Slice #	Bulk Density (gr/cm^3)	Eff. Atomic Number	Porosity(%)	Area %	Air	Sulphur	Dolomite
1	2.45	13.19	12.76		0.00	0.14	99.86
2	2.47	13.20	11.92		0.00	0.08	99.92
3	2.49	13.15	11.13		0.00	0.10	99.90
4	2.53	13.11	10.12		0.00	0.06	99.94
5	2.54	13.19	9.47		0.00	0.08	99.92
6	2.56	13.28	8.84		0.00	0.10	99.90
7	2.57	13.24	8.49		0.00	0.18	99.82
8	2.58	13.26	8.26		0.00	0.02	99.98
9	2.59	13.21	7.94		0.00	0.04	99.96
10	2.59	13.27	7.84		0.00	0.22	99.78
11	2.56	13.31	8.58		0.00	0.61	99.39
12	2.51	13.16	10.62		0.16	0.02	99.82
13	2.42	13.05	13.93		0.37	0.00	99.63
14	2.35	12.84	16.19		0.34	0.04	99.61
15	2.29	12.90	18.29		0.28	0.10	99.61
Ave	**2.50**	**13.16**	**10.97**		**0.08**	**0.12**	**99.80**

© 1990 NOVA HUSKY RESEARCH CORPORATION

TABLE 9.3

Characterization of core #52

Slice #	Bulk Density (gr/cm^3)	Eff. Atomic Number	Porosity(%)	Area %	Air	Sulphur	Dolomite
1	2.25	12.74	17.34		0.12	12.29	87.58
2	2.33	12.92	18.49		0.73	17.67	81.60
3	2.70	13.33	4.36		0.00	0.10	99.90
4	2.54	12.98	10.47		0.02	0.83	99.15
5	2.67	13.27	5.60		0.02	0.32	99.66
6	1.90	10.25	18.70		20.47	3.73	75.80
Ave	**2.38**	**12.58**	**12.54**		**3.56**	**5.83**	**90.61**

© 1990 NOVA HUSKY RESEARCH CORPORATION

15.0 FIGURES

© 1990 NOVA HUSKY RESEARCH CORPORATION

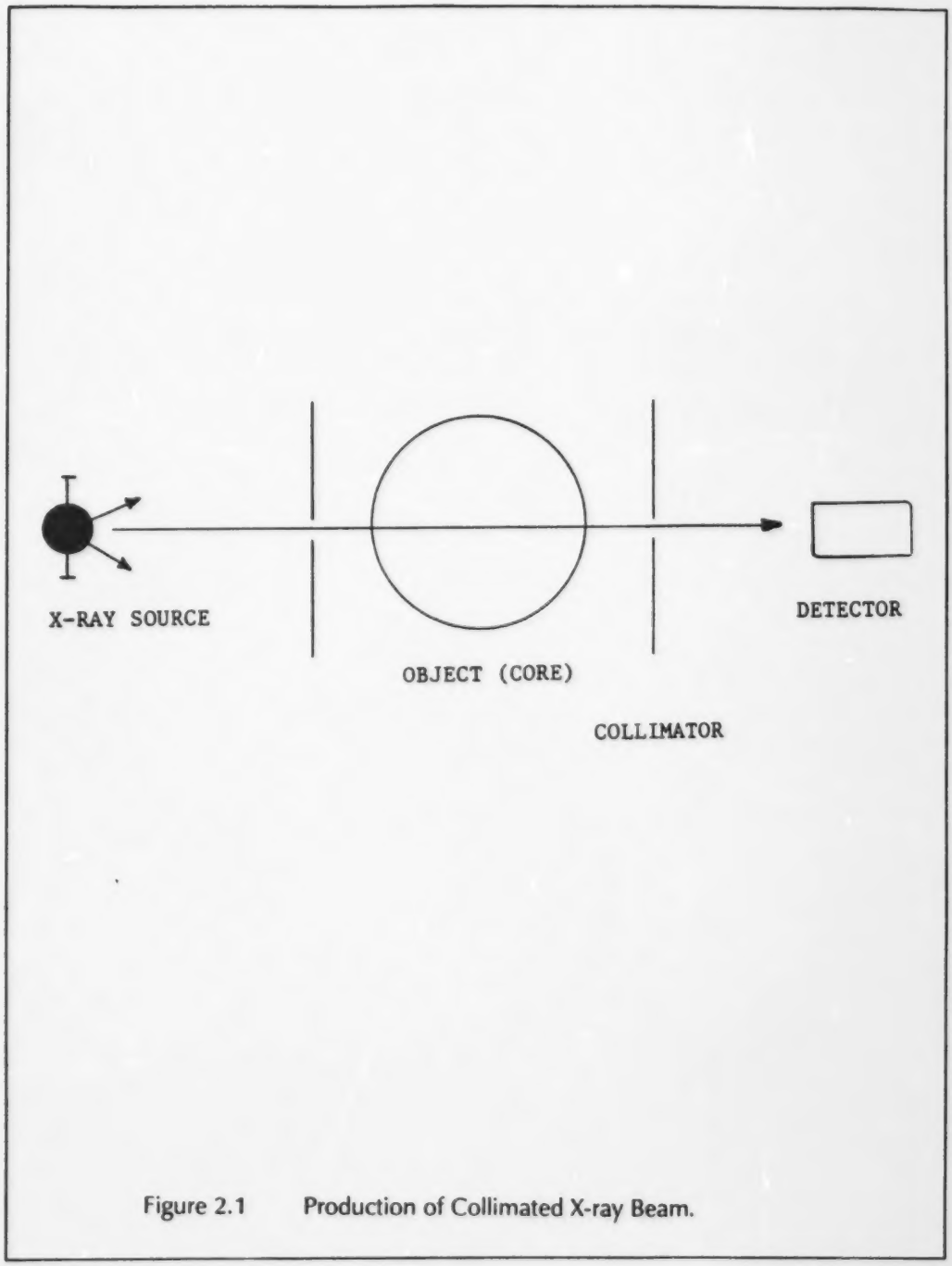

Figure 2.1 Production of Collimated X-ray Beam.

© 1990 NOVA HUSKY RESEARCH CORPORATION

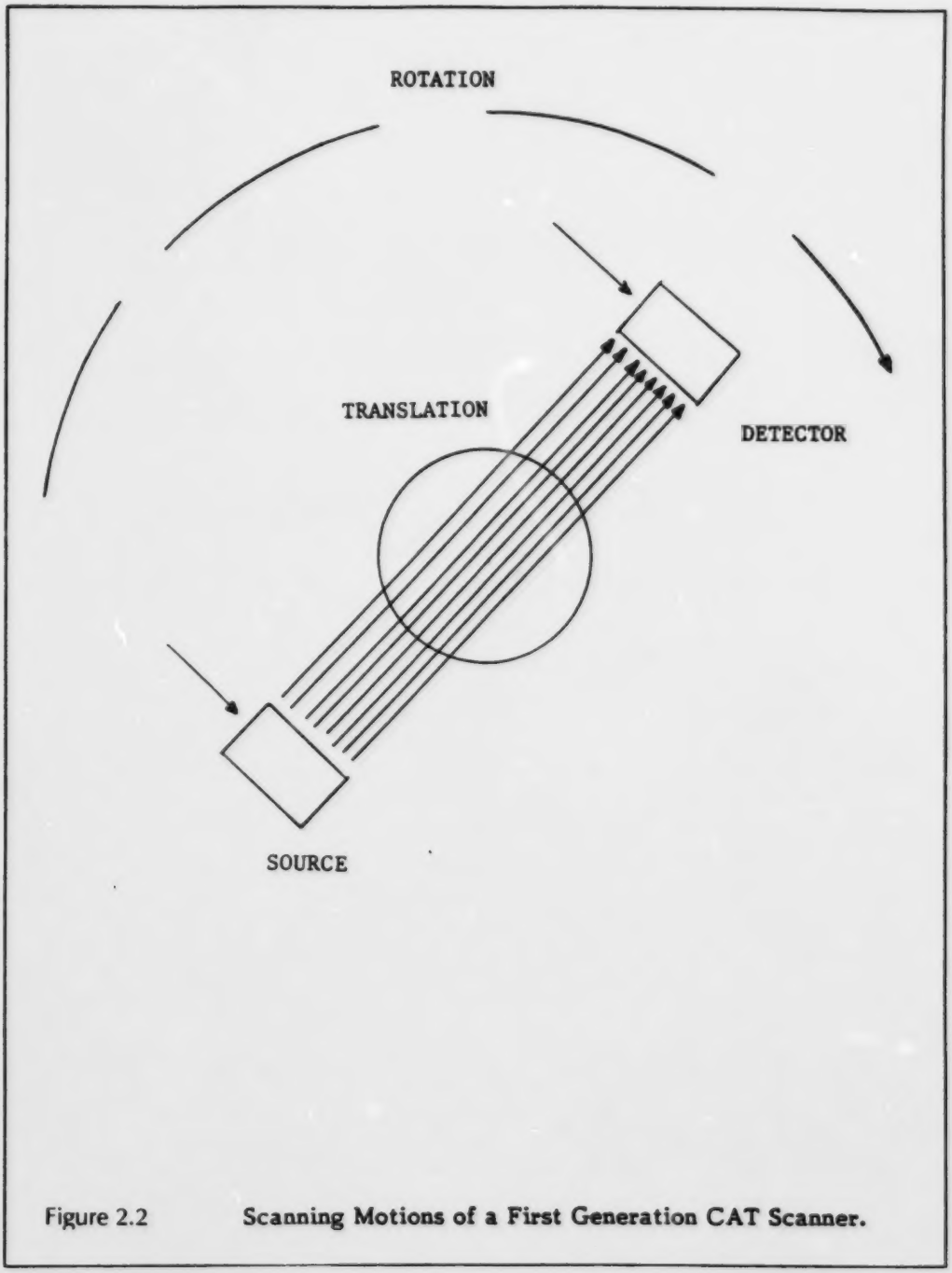

Figure 2.2 **Scanning Motions of a First Generation CAT Scanner.**

© 1990 NOVA HUSKY RESEARCH CORPORATION

Figure 3.1 Bulk Density (g/cm^3) vs. CT number for all the calibrated standards.

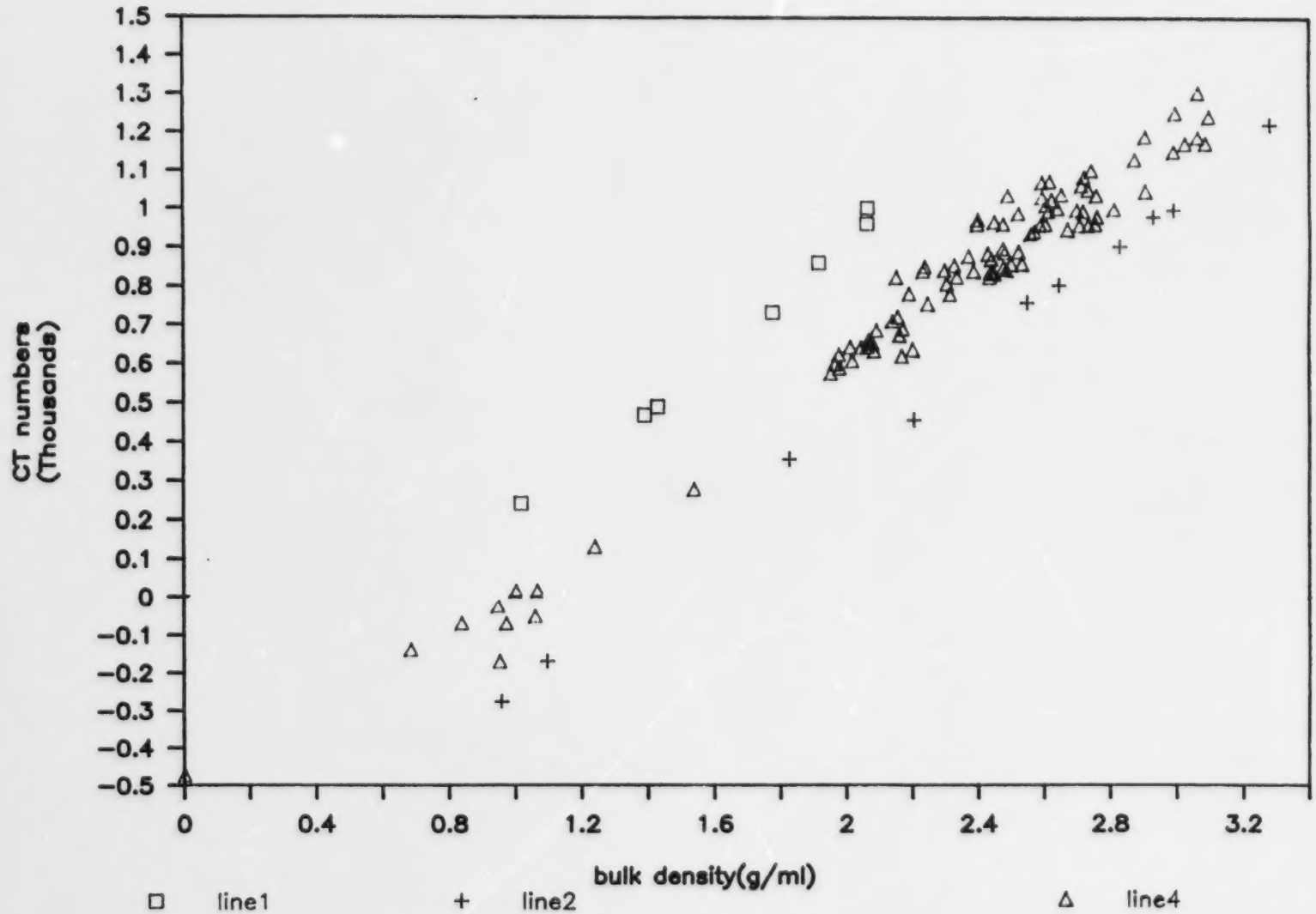

Figure 3.2 Bulk density calibrated for group of line 1 (high atomic number).

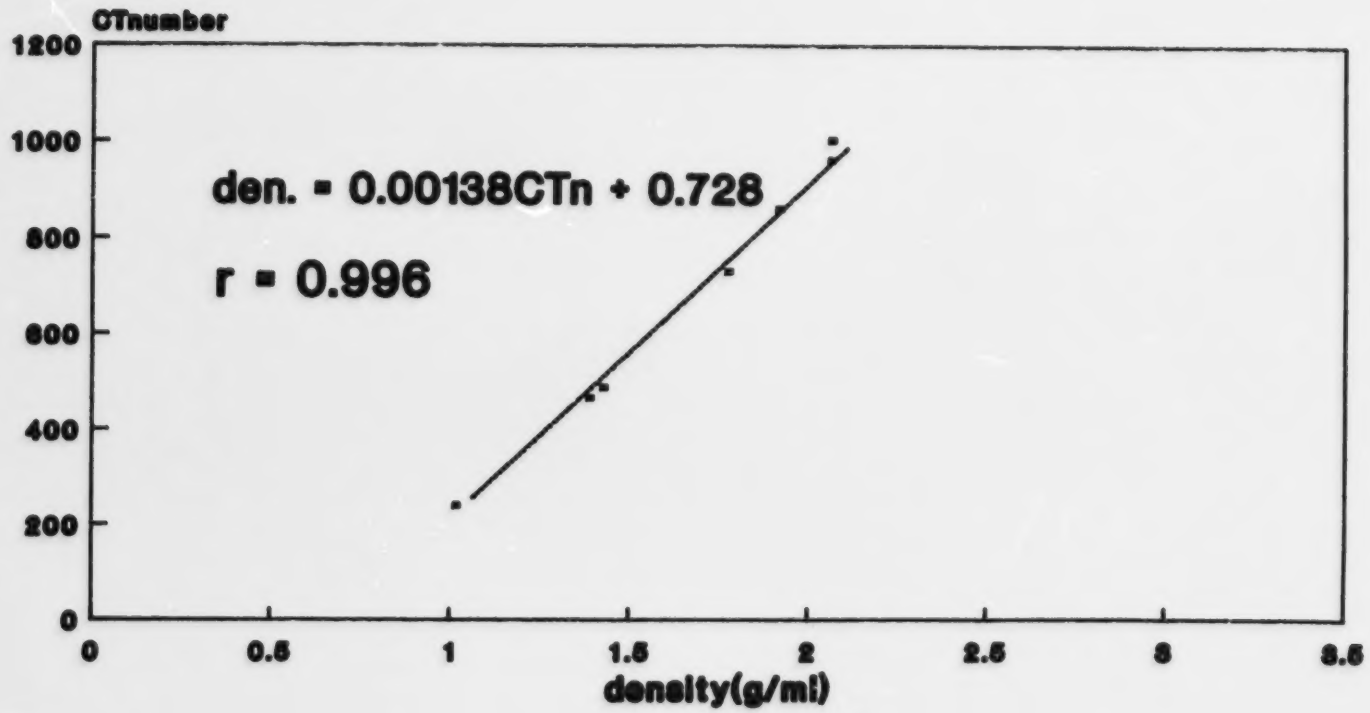

© 1988 NOVA HUSKY RESEARCH CORPORATION

Figure 3.3 Bulk density calibrated for group of line 2 (low atomic number).

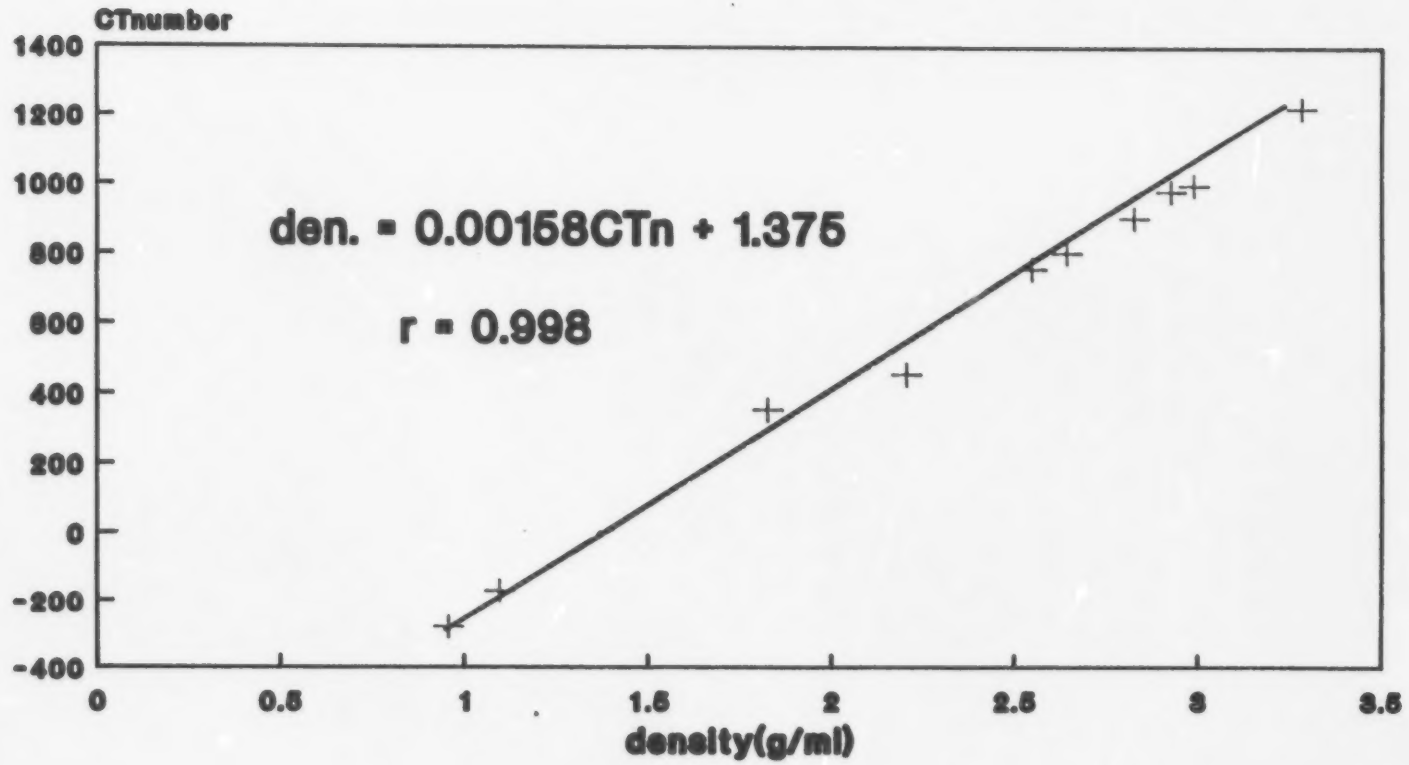

© 1988 NOVA HUSKY RESEARCH CORPORATION

Figure 3.4 Bulk density calibrated for group of line 3 (very dense standards).

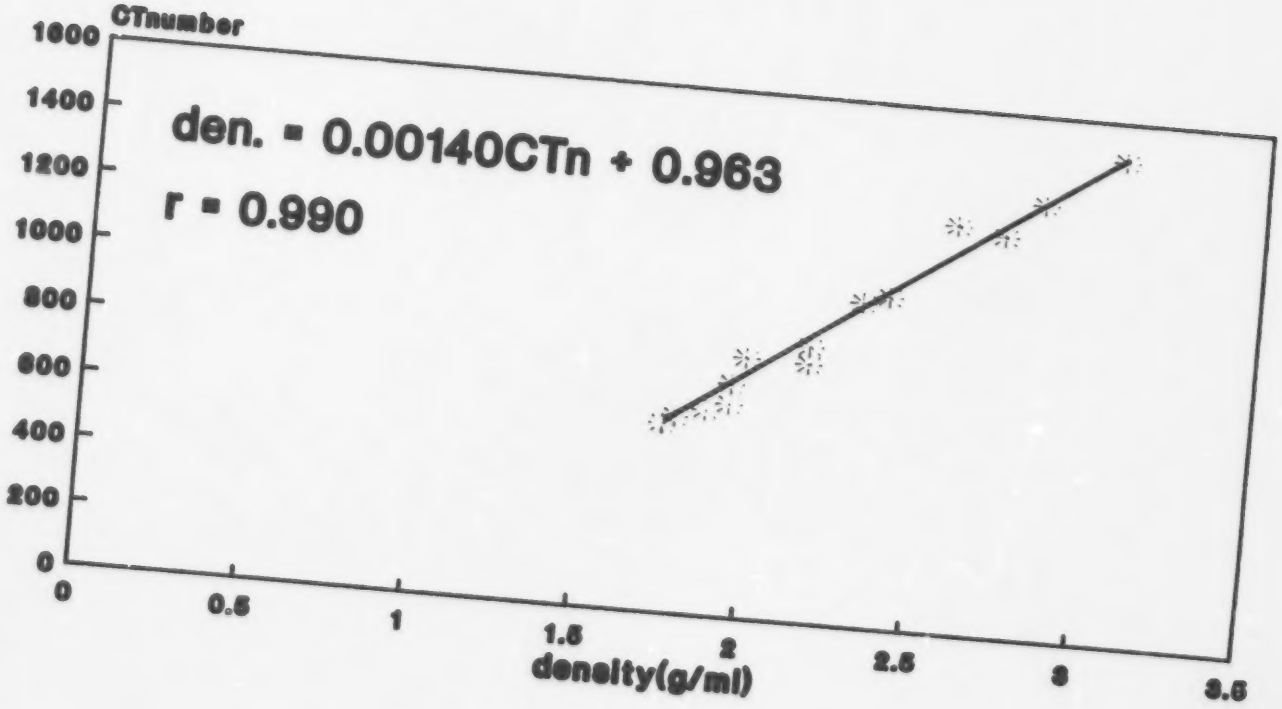

© 1988 NOVA HUSKY RESEARCH CORPORATION

Figure 3.5 Bulk density calibrated for group of line 4. This line is used for all the modelling of this work.

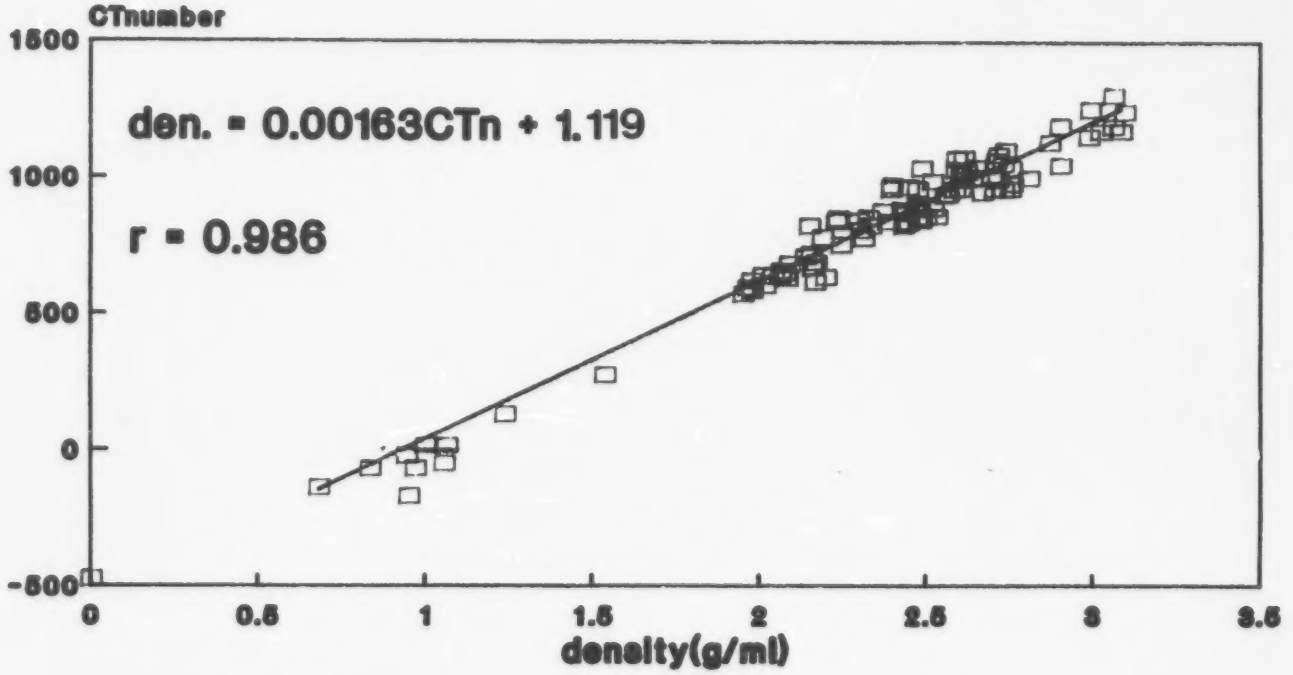

© 1988 NOVA HUSKY RESEARCH CORPORATION

Figure 4.1 X-ray spectrum at 80 kVp, no water ring (annulus)/ dosimetry

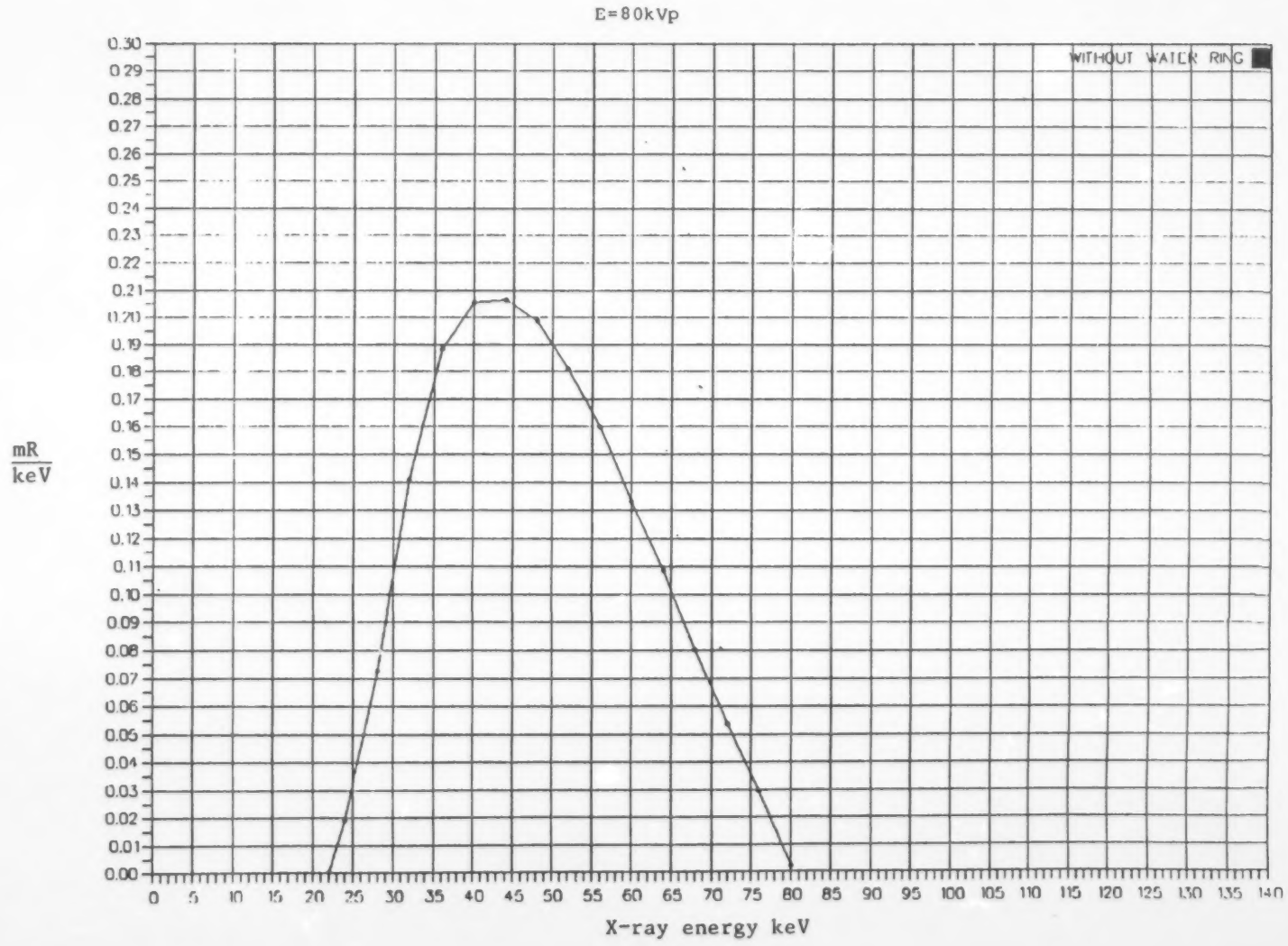

© 1988 NOVA HUSKY RESEARCH CORPORATION

Figure 4.2 X-ray spectrum at 110 kVp, no water ring (annulus)/ dosimetry

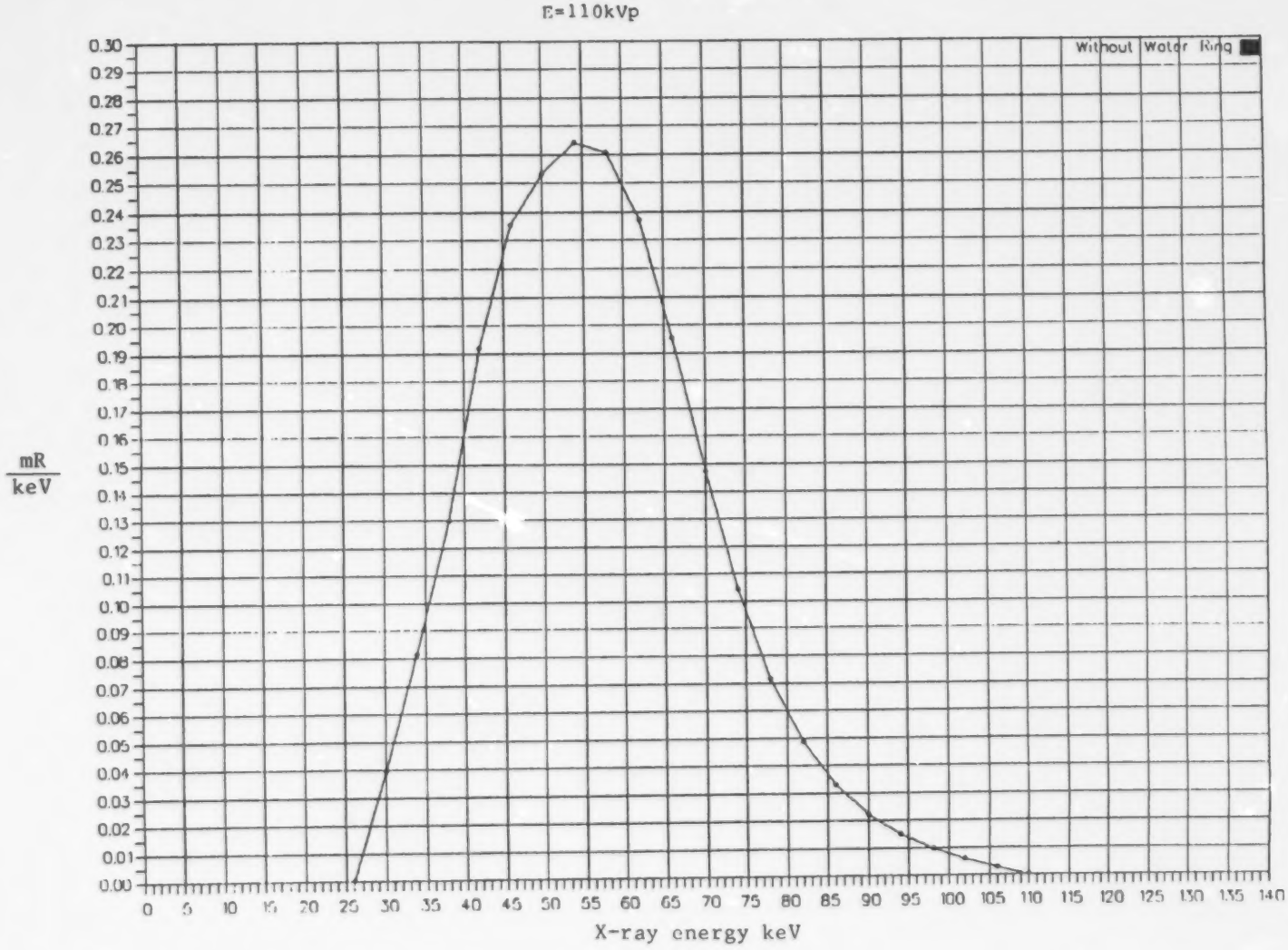

© 1988 NOVA HUSKY RESEARCH CORPORATION

Figure 4.3 X-ray spectrum at 140 kVp, no water ring (annulus)/ dosimetry

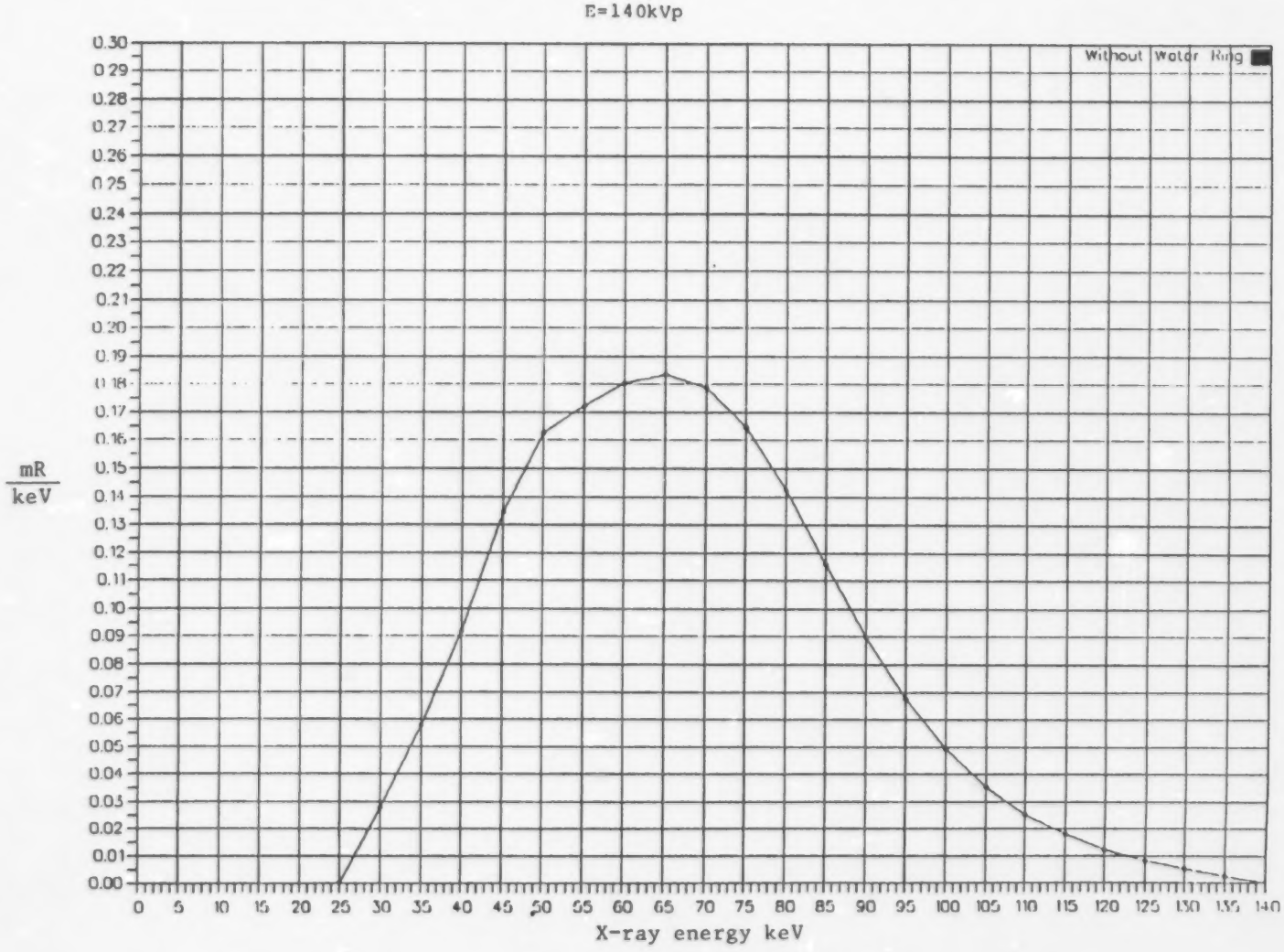

© 1988 NOVA HUSKY RESEARCH CORPORATION

Figure 4.4 X-ray spectrum at 80 kVp, with water ring (annulus)/ dosimetry

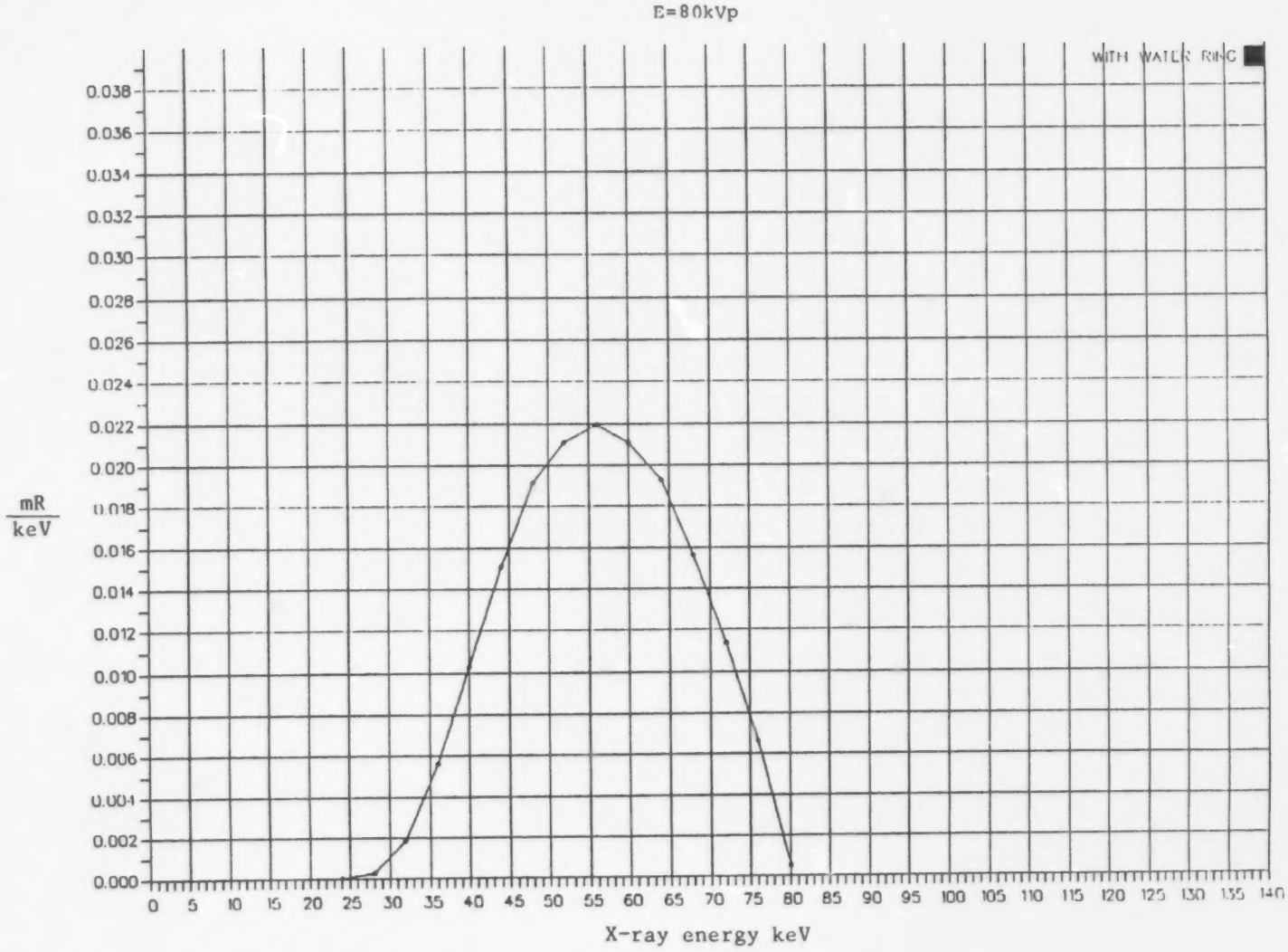

© 1988 NOVA HUSKY RESEARCH CORPORATION

Figure 4.5 X-ray spectrum at 110 kVp, with water ring (annulus)/ dosimetry

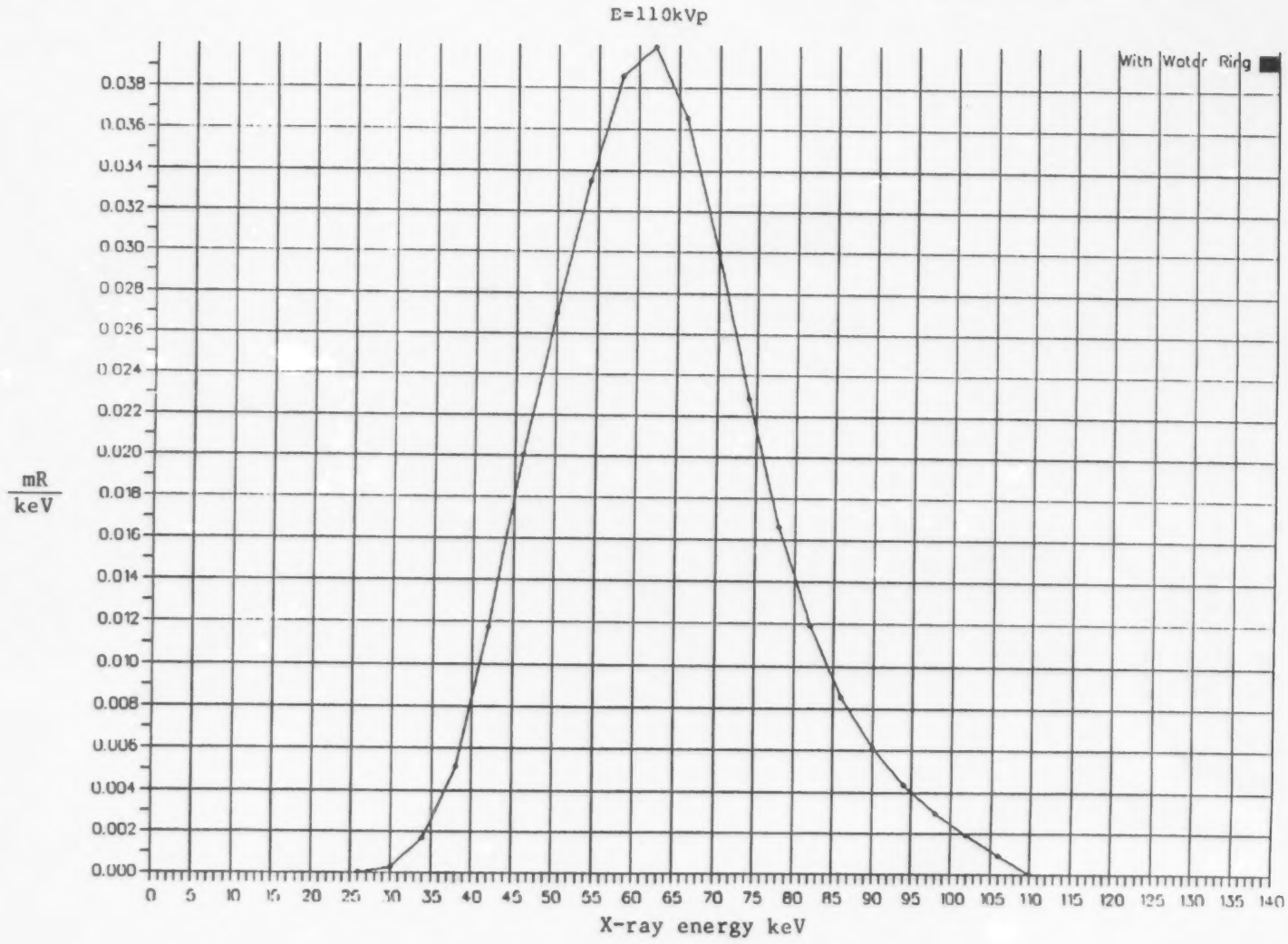

© 1988 NOVA HUSKY RESEARCH CORPORATION

Figure 4.6 X-ray spectrum at 140 kVp, with water ring (annulus)/ dosimetry

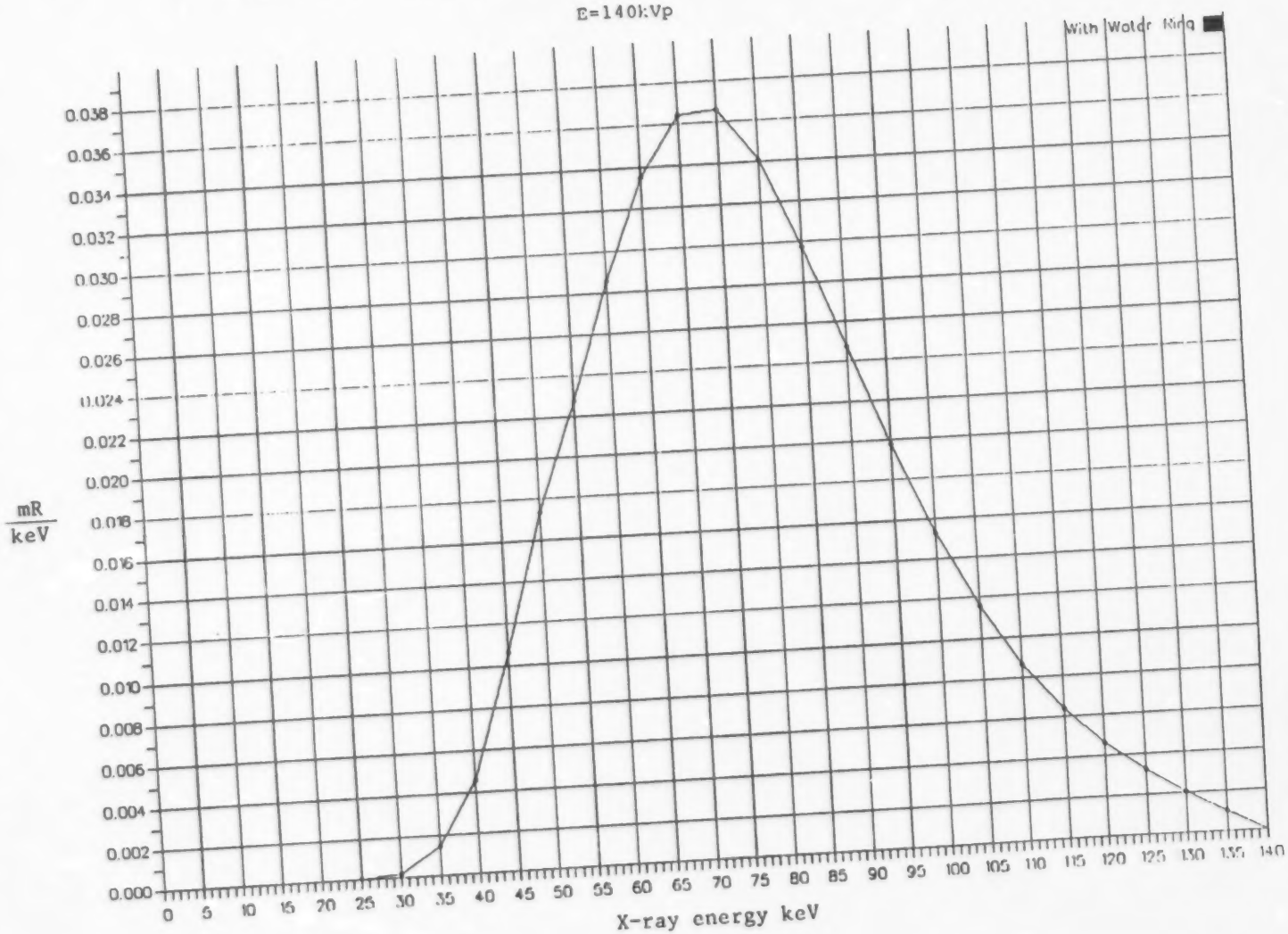

© 1988 NOVA HUSKY RESEARCH CORPORATION

Figure 4.7 NaI crystal-pulseheight analyzer apparatus.

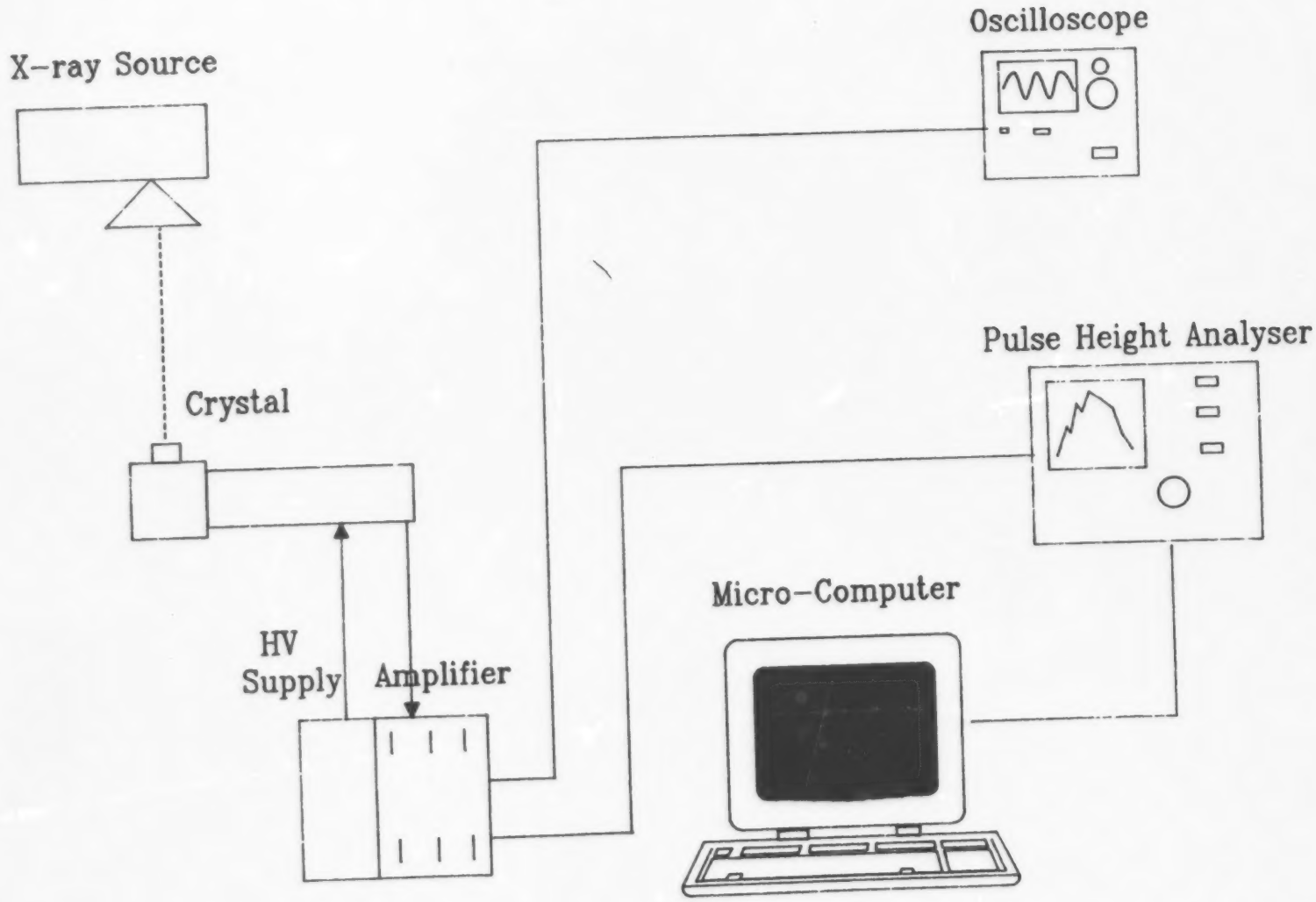

© 1988 NOVA HUSKY RESEARCH CORPORATION

Figure 4.8 X-ray spectrum at 80 kVp, with pulseheight analyzer/3 1/2 in. core in Aluminum core holder

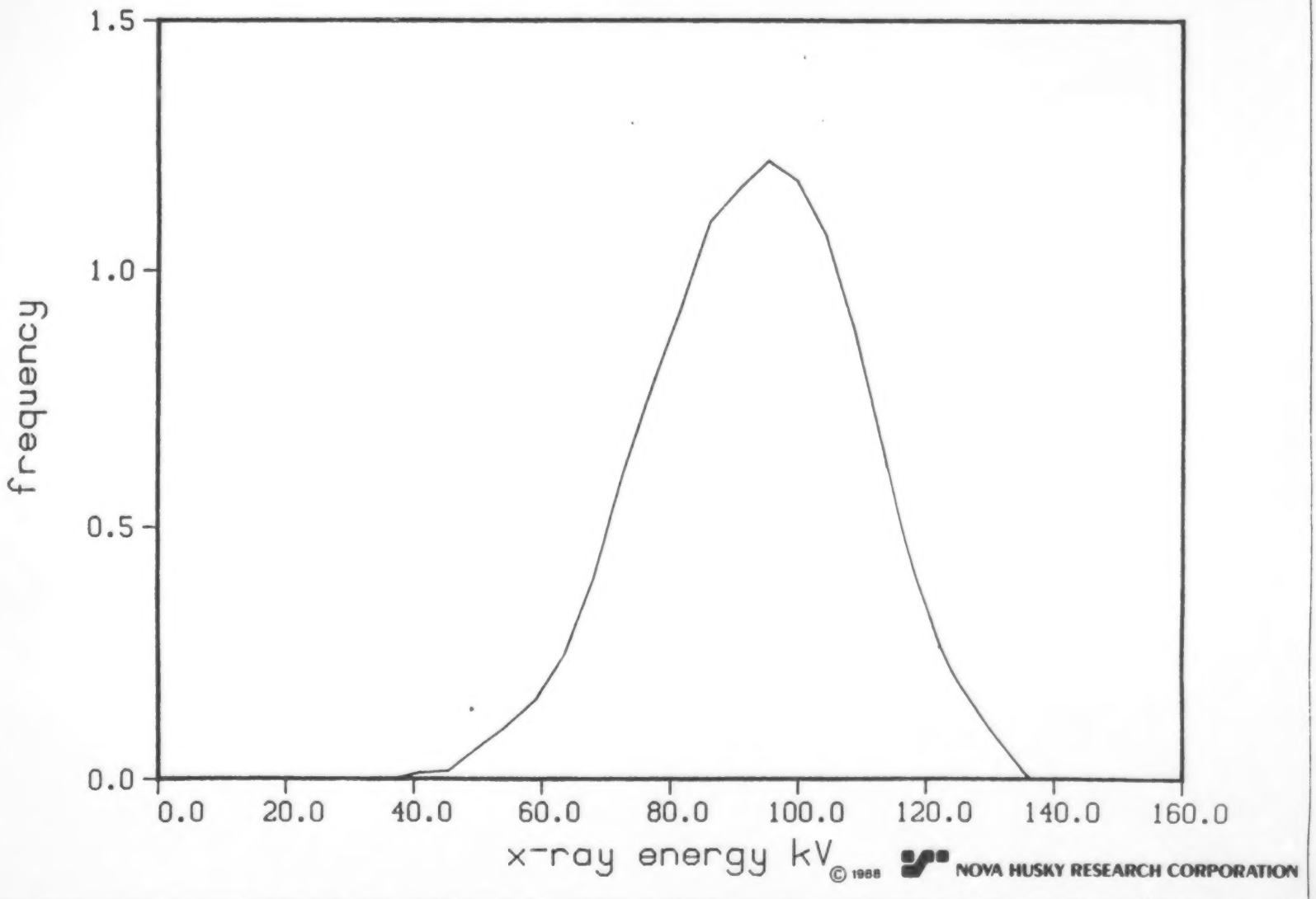

Figure 4.9 X-ray spectrum at 110 kVp, with pulseheight analyzer/3 1/2 in. core in Aluminum core holder

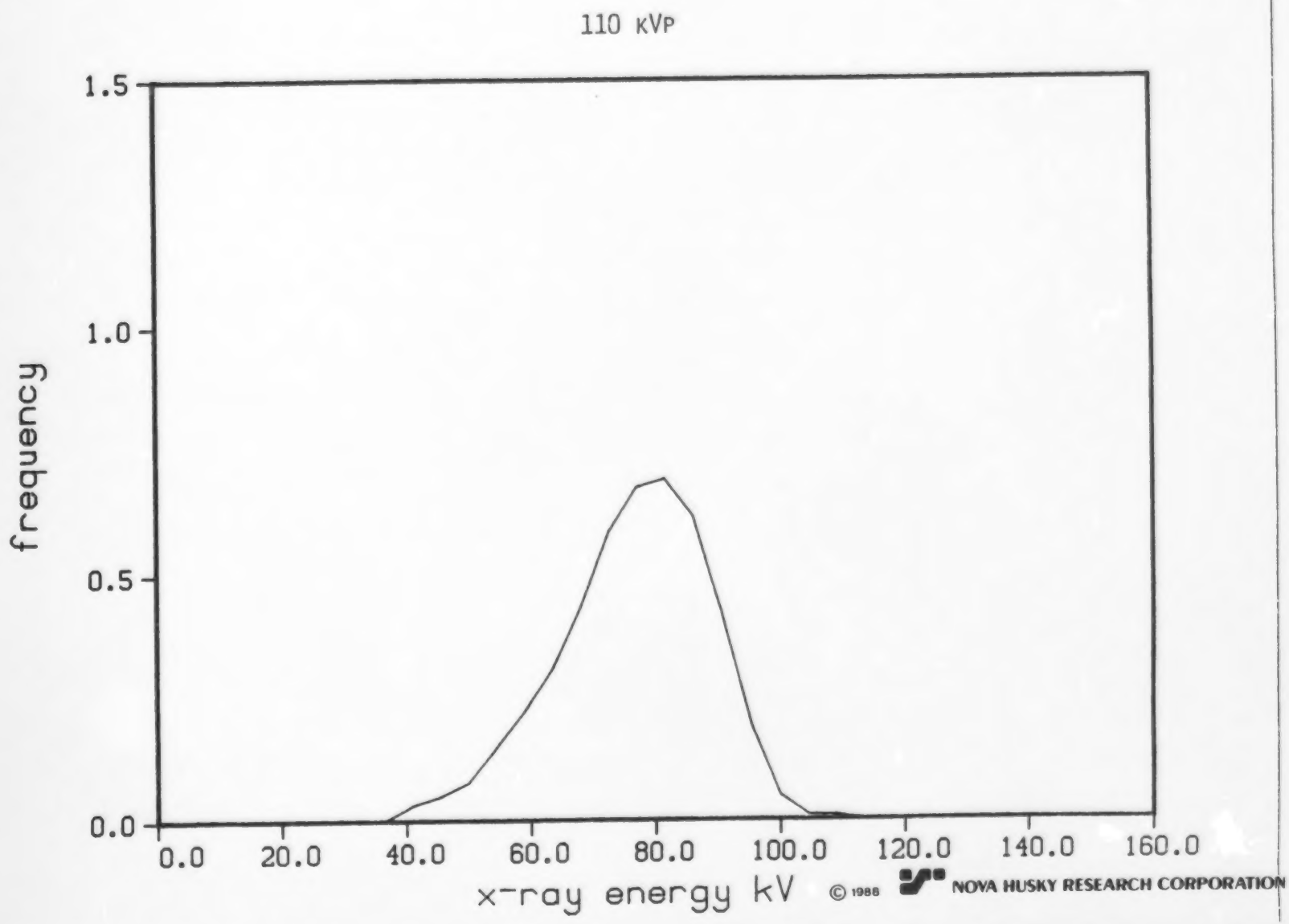

Figure 4.10 X-ray spectrum at 140 kVp, with pulseheight analyzer/3 1/2 in. core in Aluminum core holder

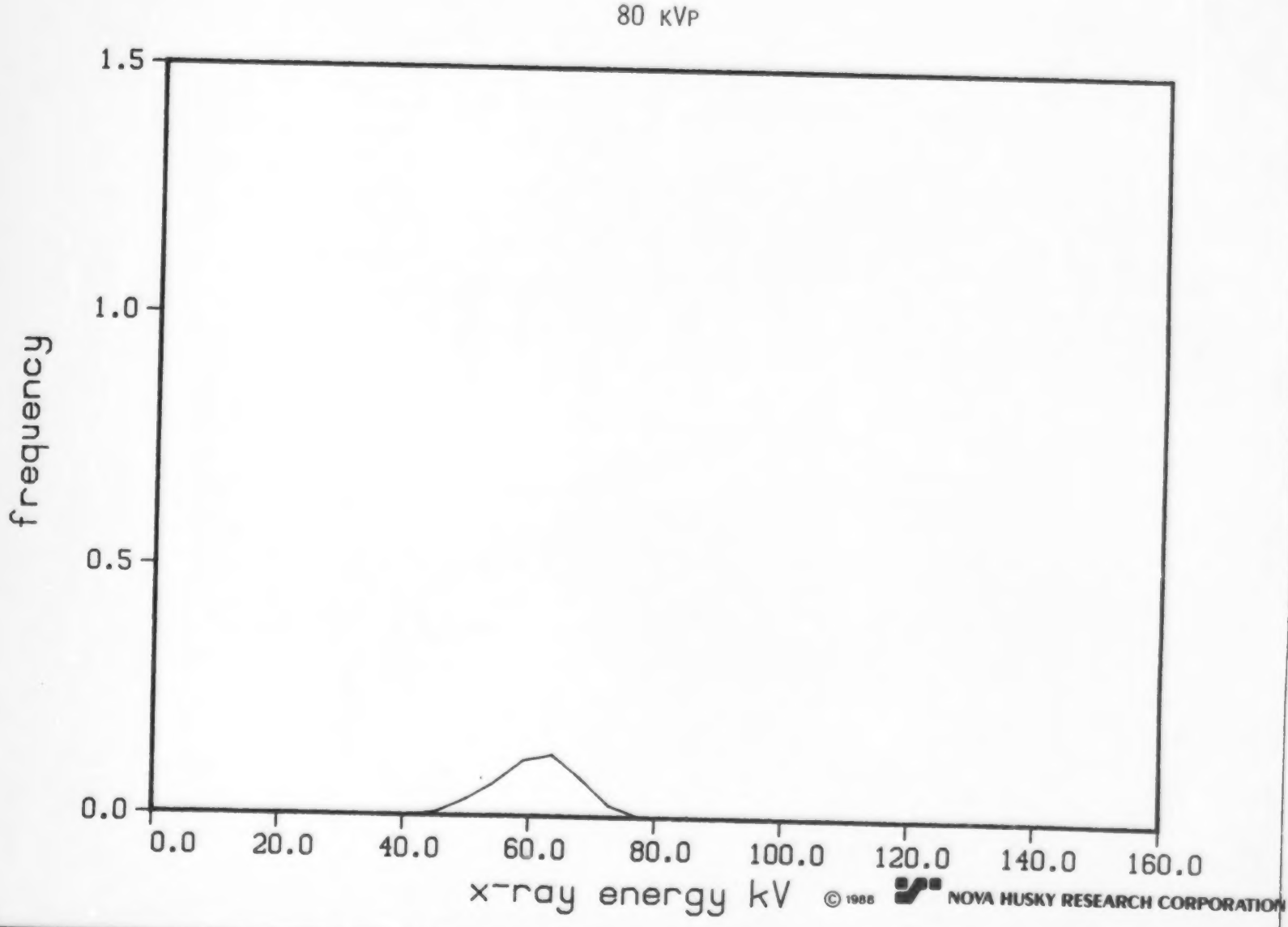

Figure 5.1 CT number image of Cold Lake Core. Identification of fractures in uniform sand. The color code at the right hand side indicates the range of CT numbers for each color. It is kept constant throughout the chapter. The range is 100 CT numbers.

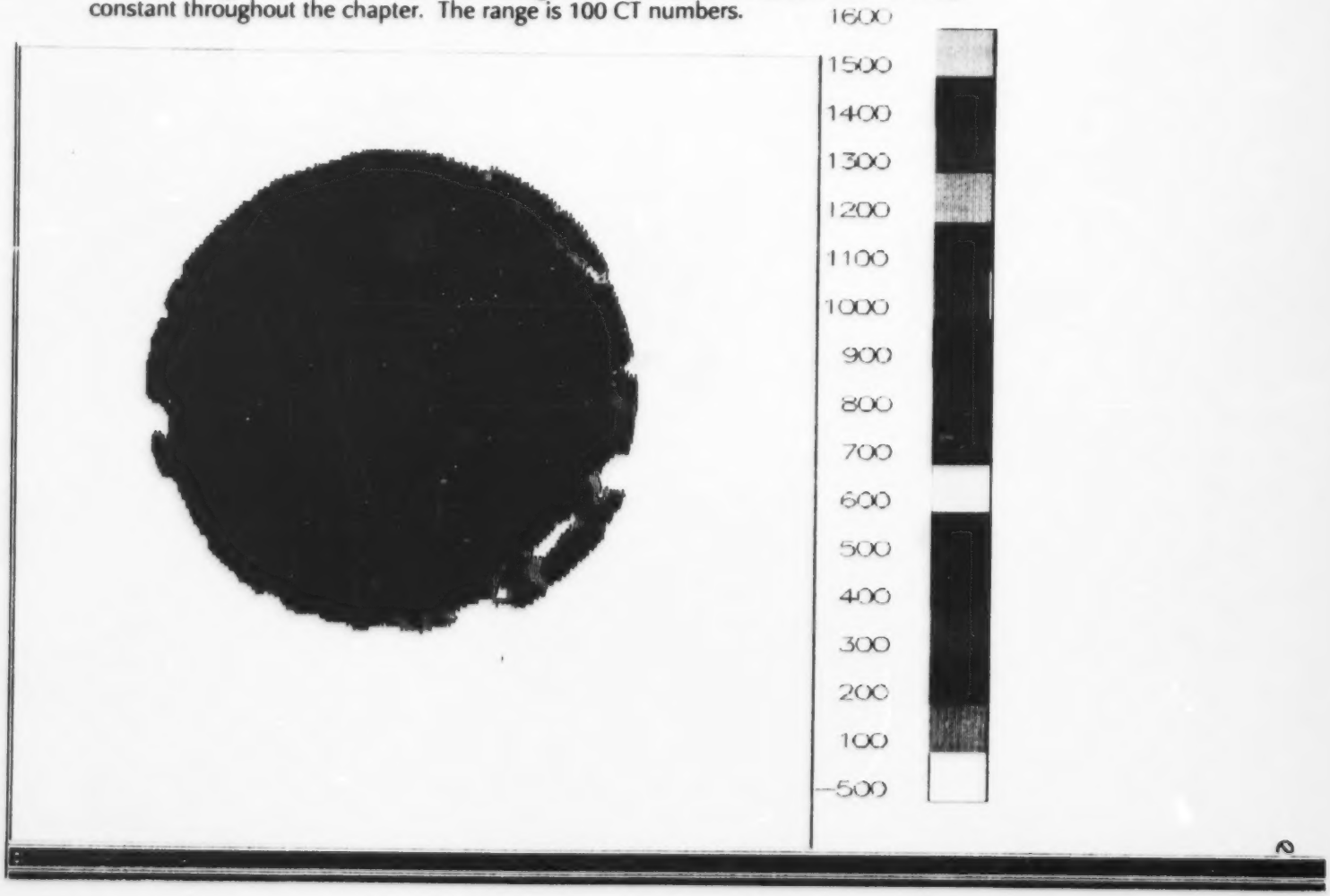

© 1988 NOVA HUSKY RESEARCH CORPORATION

Figure 5.2 CT number image of Cold Lake Core. Identification of fractures in a shale barrier.

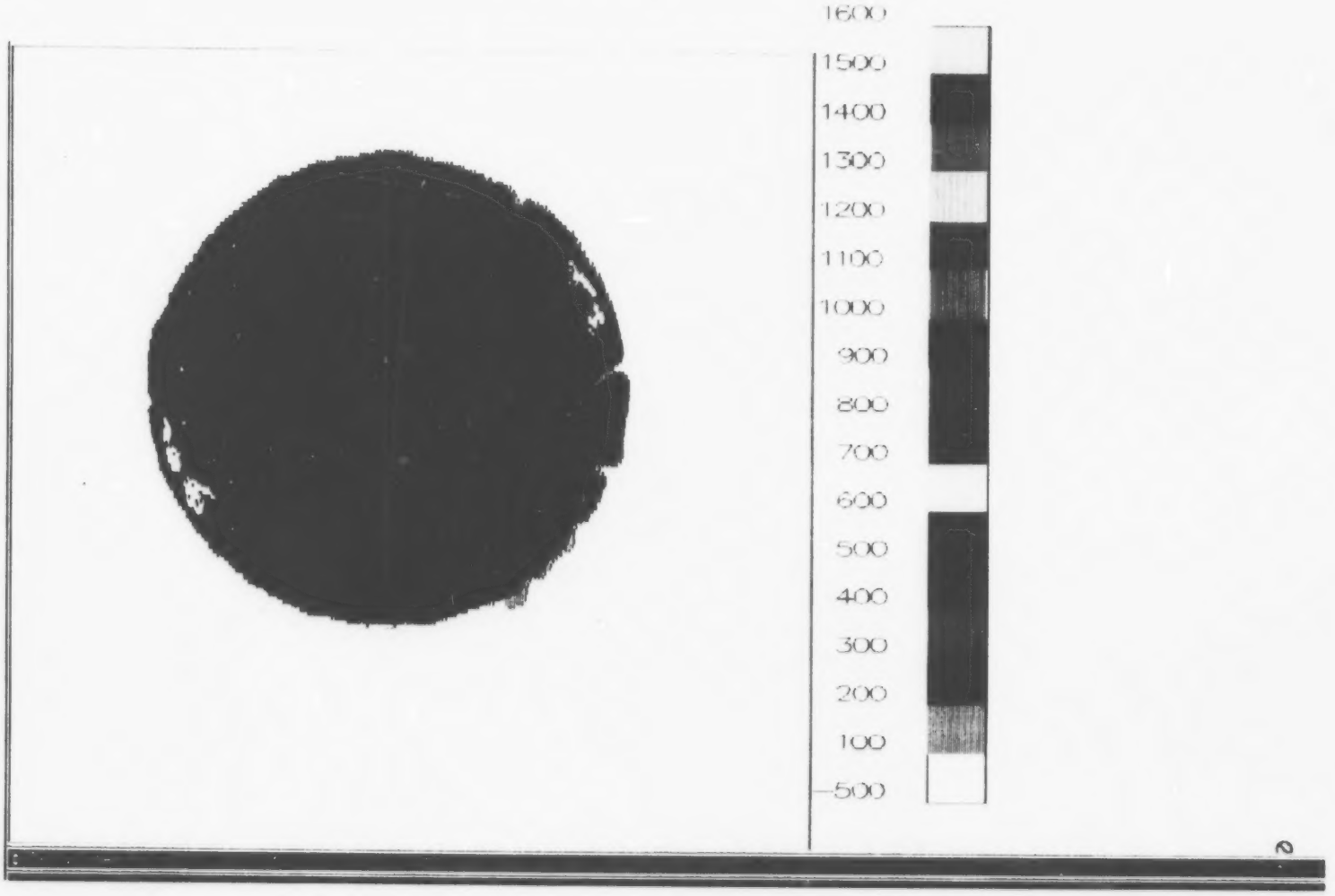

© 1988 NOVA HUSKY RESEARCH CORPORATION

Figure 5.3 CT number image of Cold Lake Core. Example of core damage. The left hand side of the core is missing.

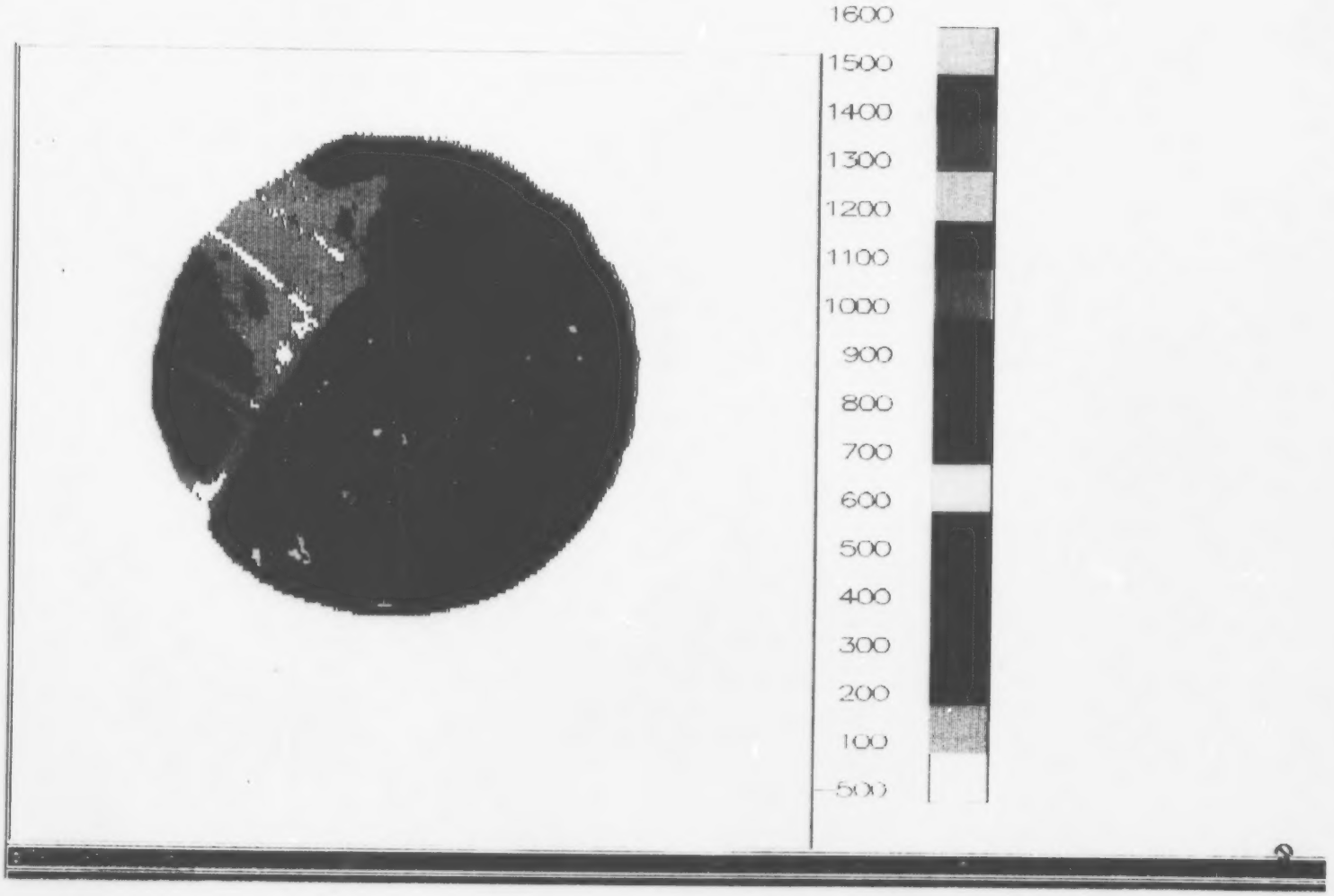

© 1990 NOVA HUSKY RESEARCH CORPORATION

Figure 5.4 CT number frequency distribution for the image of Figure 5.3.

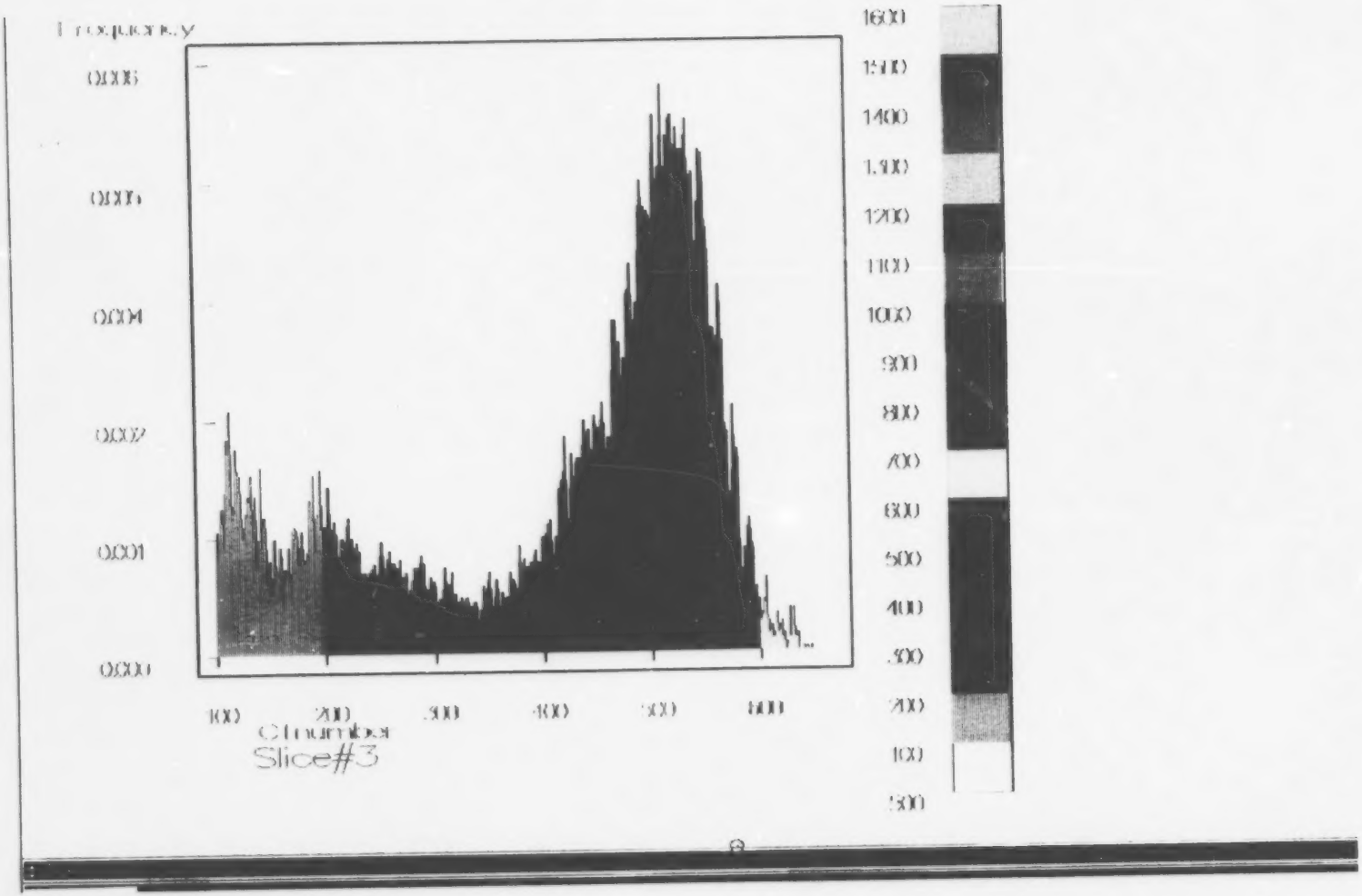

© 1990 NOVA HUSKY RESEARCH CORPORATION

Figure 5.5 CT number image of Cold Lake Core. Example of a layer where bedding planes meet.

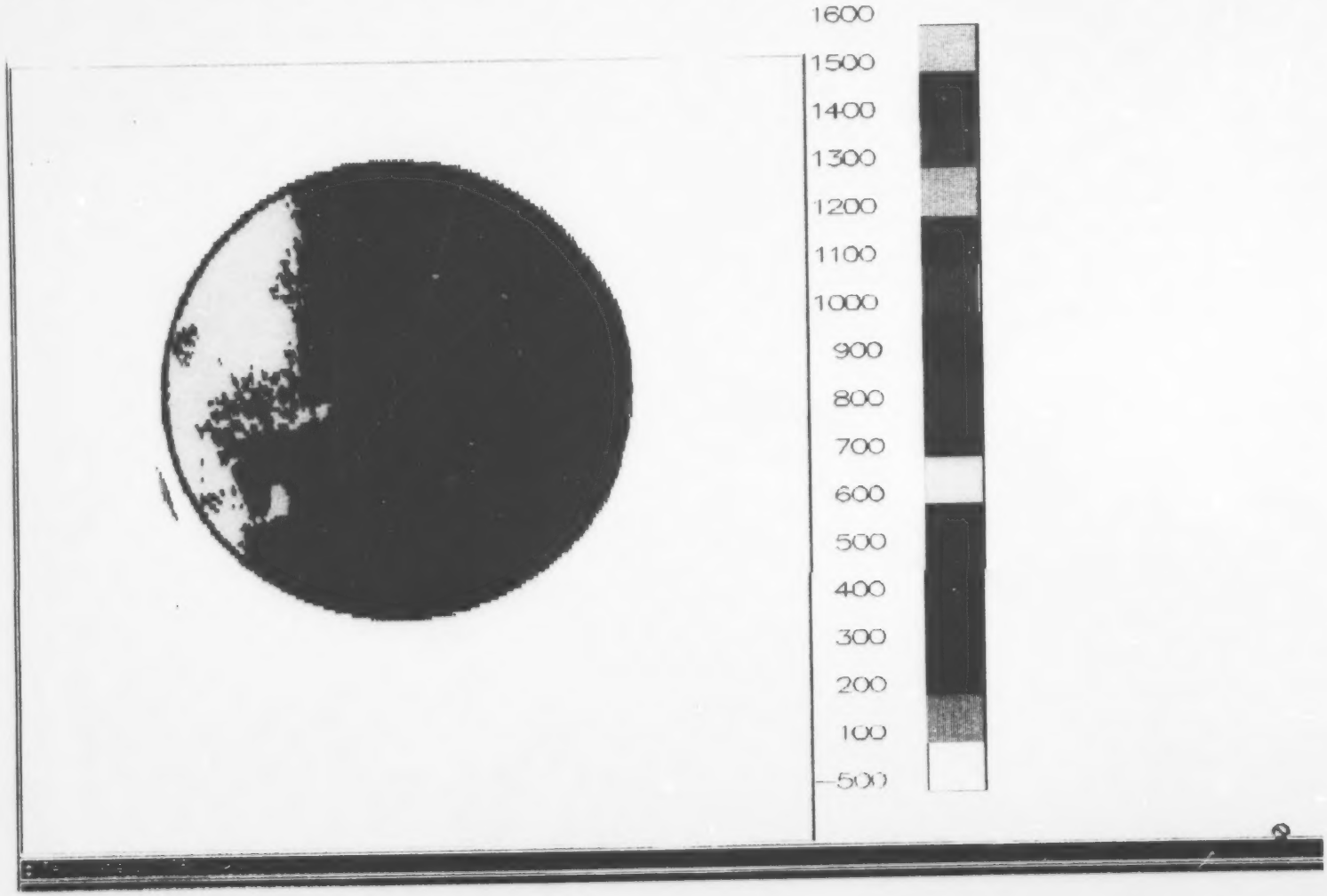

© 1990 NOVA HUSKY RESEARCH CORPORATION

Figure 5.6 CT number frequency distribution for the image of Figure 5.5.

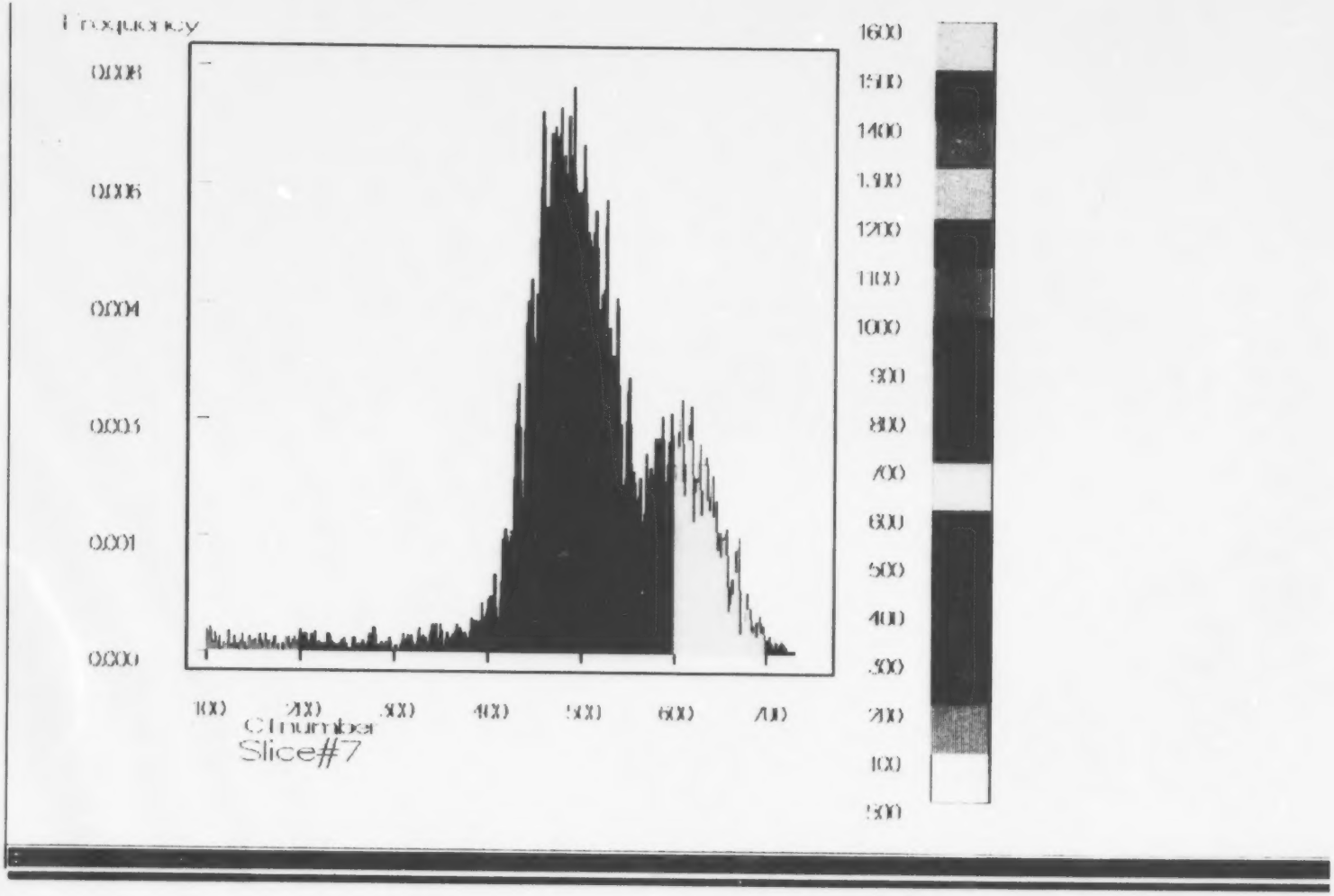

© 1990 NOVA HUSKY RESEARCH CORPORATION

Figure 5.7 CT number image of Cold Lake Core. Idenfication of clay clast inclusions in the boundary between shale and sand. Indication of core damage at the top right side.

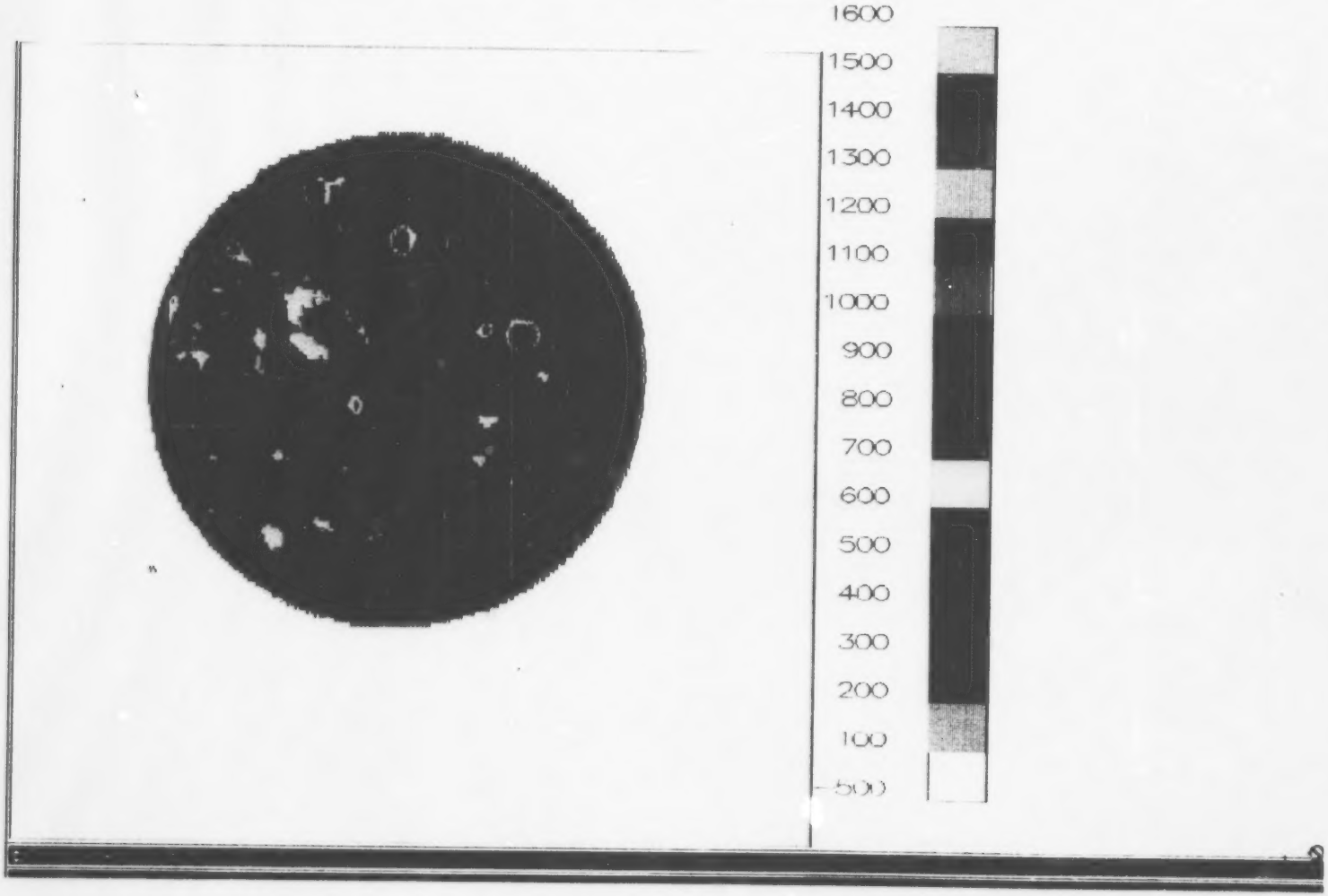

© 1990 NOVA HUSKY RESEARCH CORPORATION

Figure 5.8 CT number image of Cold Lake Core 0.01m deeper than the image of Figure 5.7.

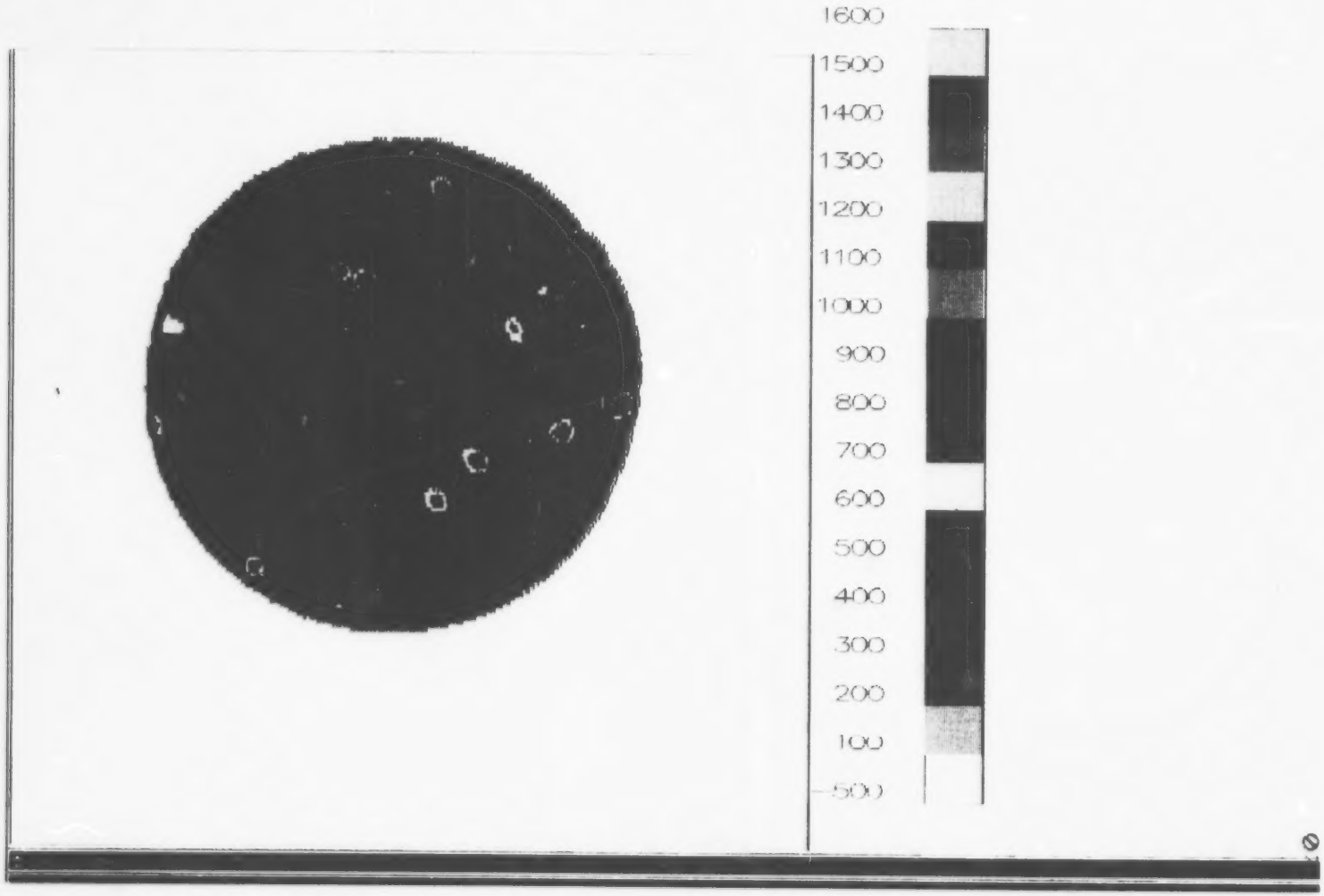

©1990 NOWA HUSKY RESEARCH CORPORATION

Figure 5.9 CT number image of Cold Lake Core. Idenfication of fractures and clay clasts in a uniform sand.

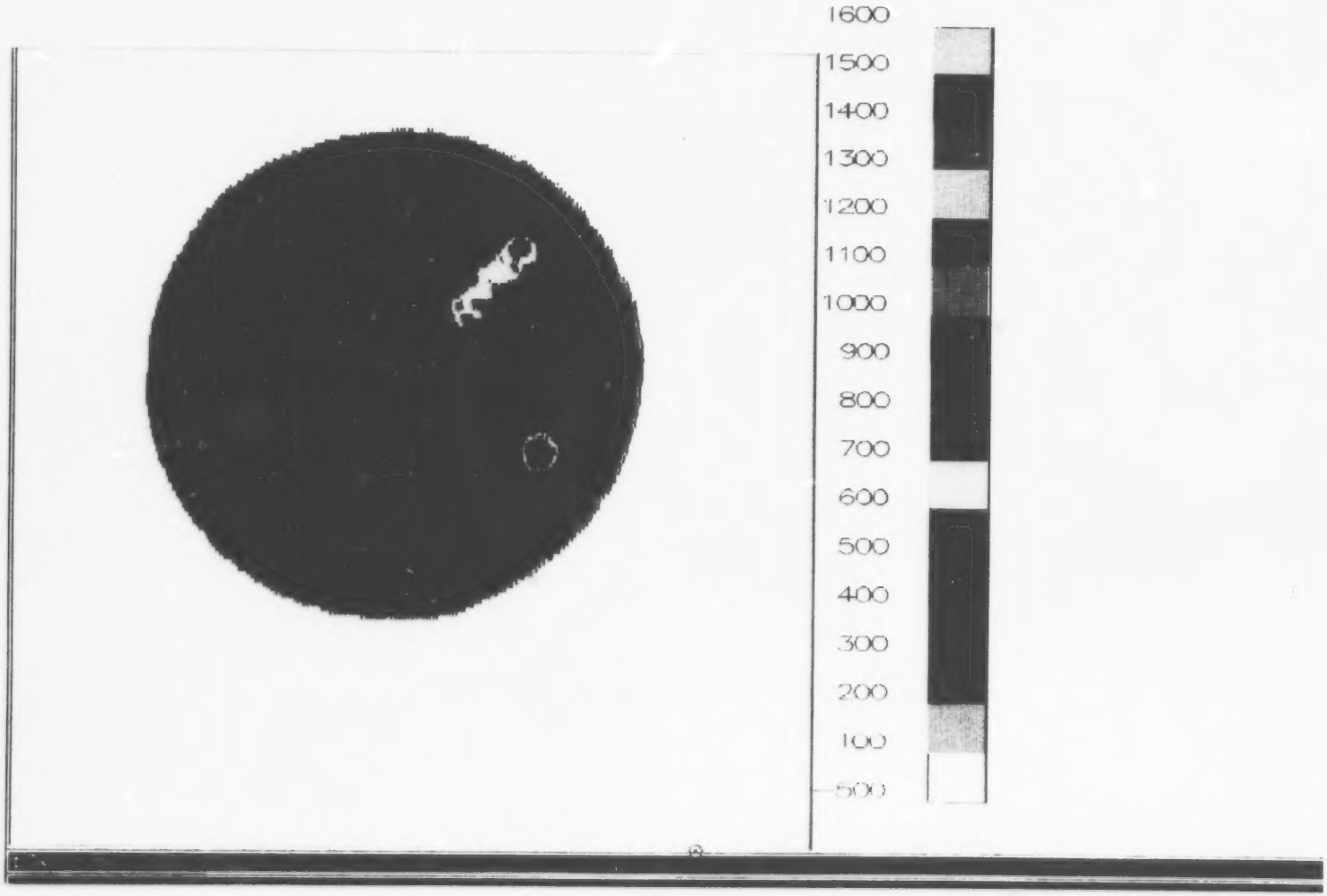

© 1990 NOVA HUSKY RESEARCH CORPORATION

Figure 5.10 Longitudinal reconstruction of Cold Lake Core. Clay clasts, shales and mud invasion can be identified.

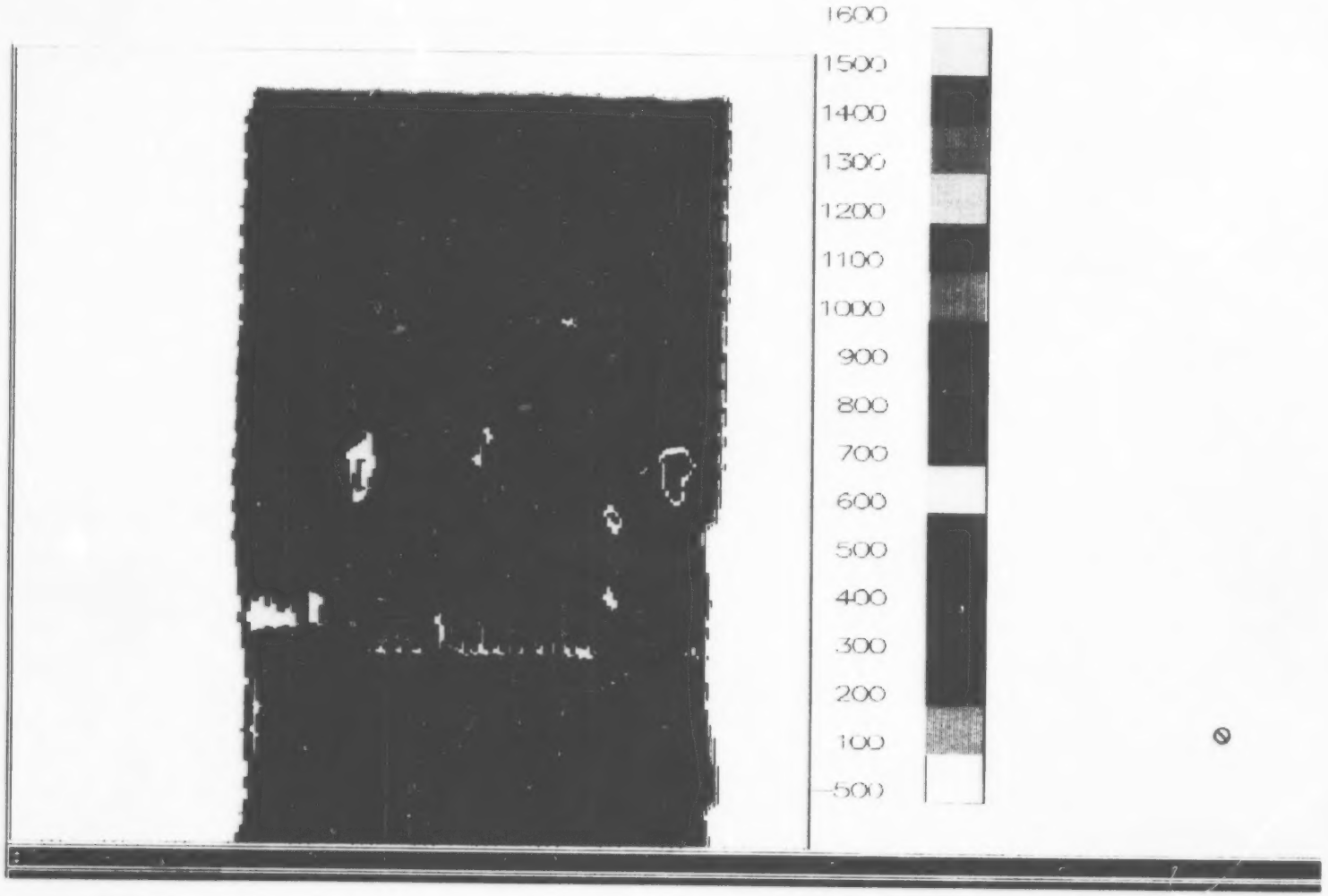

© 1990 NOVA HUSKY RESEARCH CORPORATION

Figure 5.11 Longitudinal reconstruction of Cold Lake core. Shales, mud invasion and missing core can be seen.

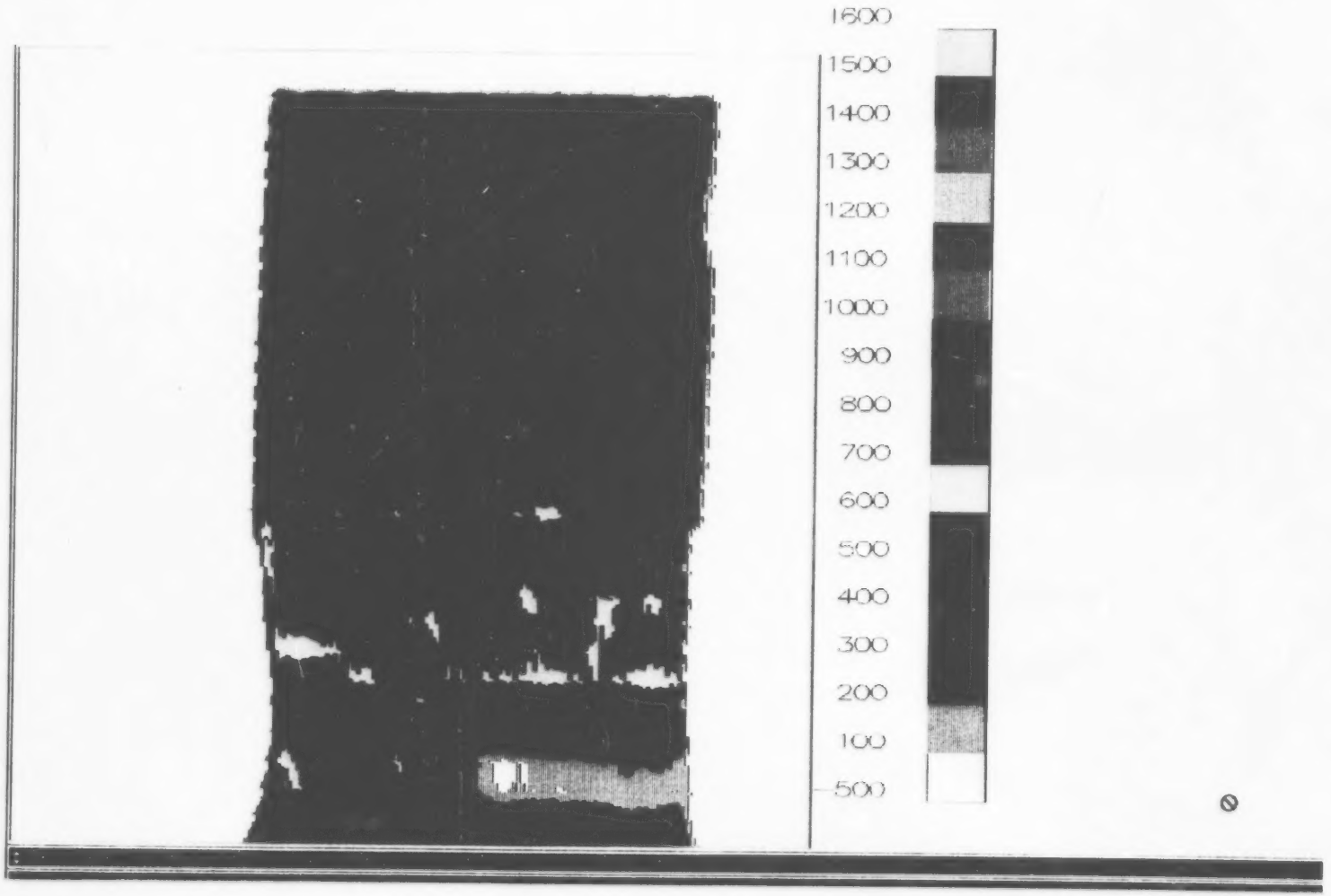

© 1990 NOVA HUSKY RESEARCH CORPORATION

Figure 5.12 Core from Provost area. Identification of possible bedding planes.

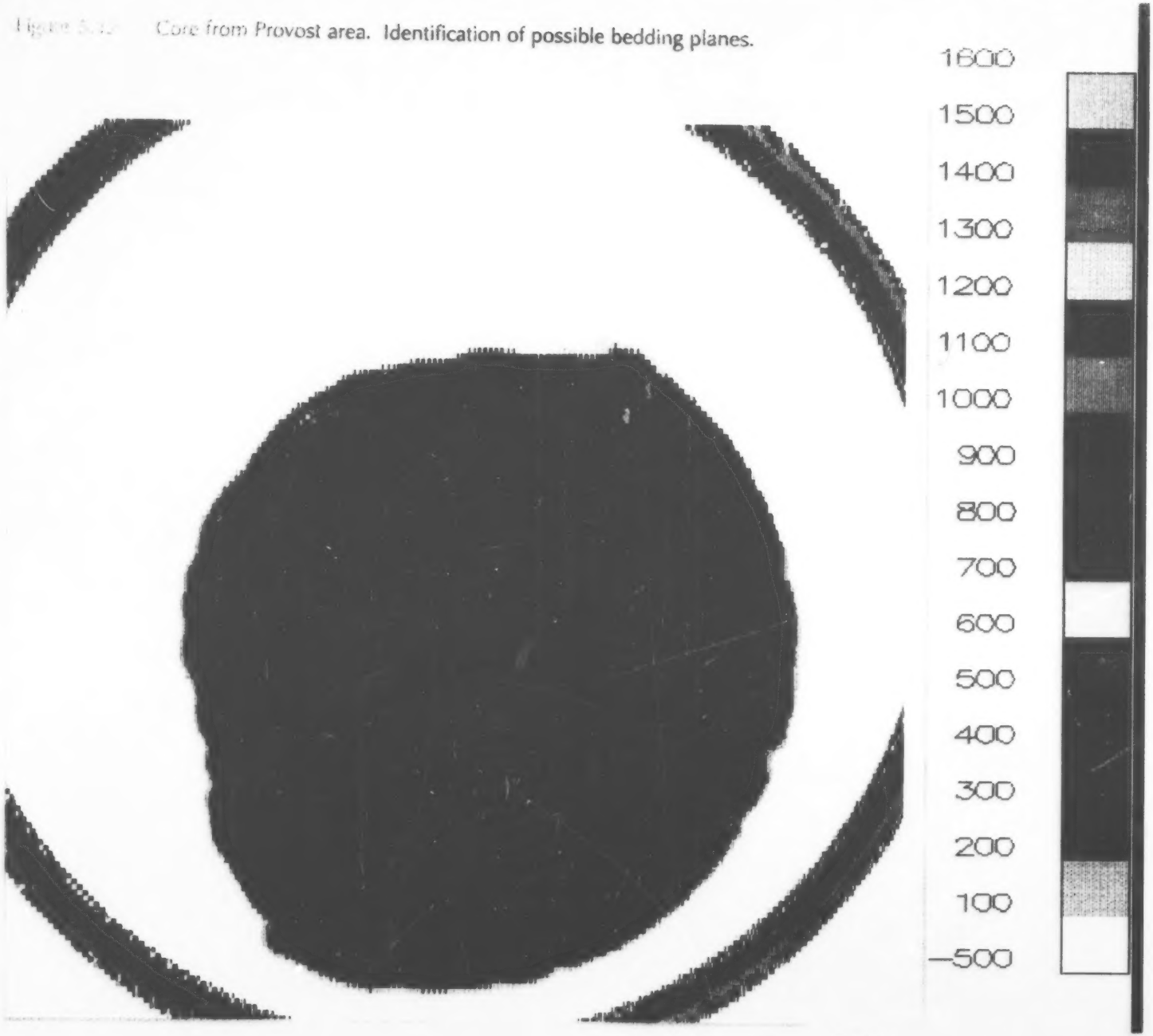

© 1990 NOVA HUSKY RESEARCH CORPORATION

Figure 5.13 CT number image of Provost core. Relatively uniform sand with a presence of clay clast.

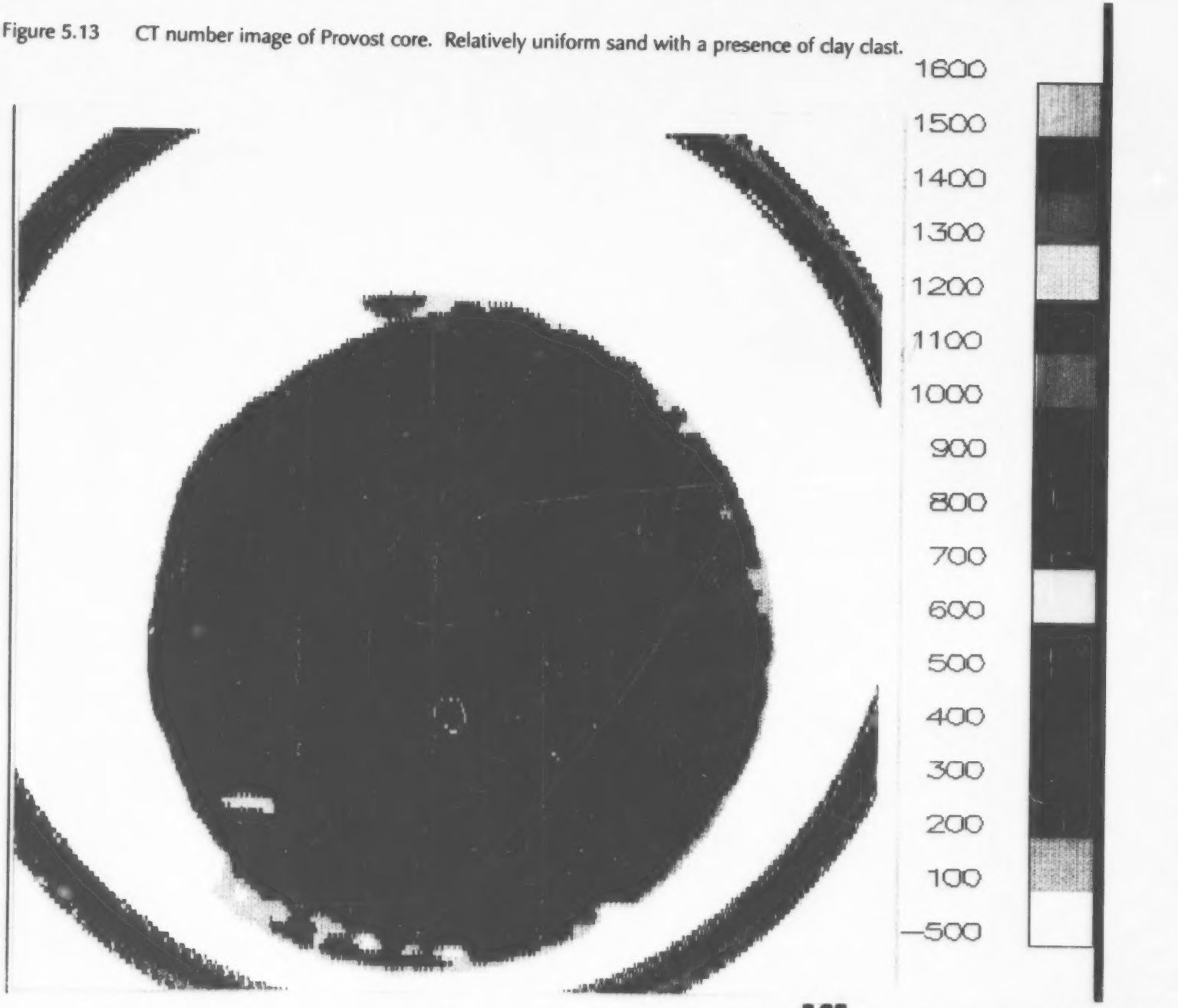

© 1990 NOVA HUSKY RESEARCH CORPORATION

Figure 5.14 Core from Provost area. Uniform shale or consolidated sand.

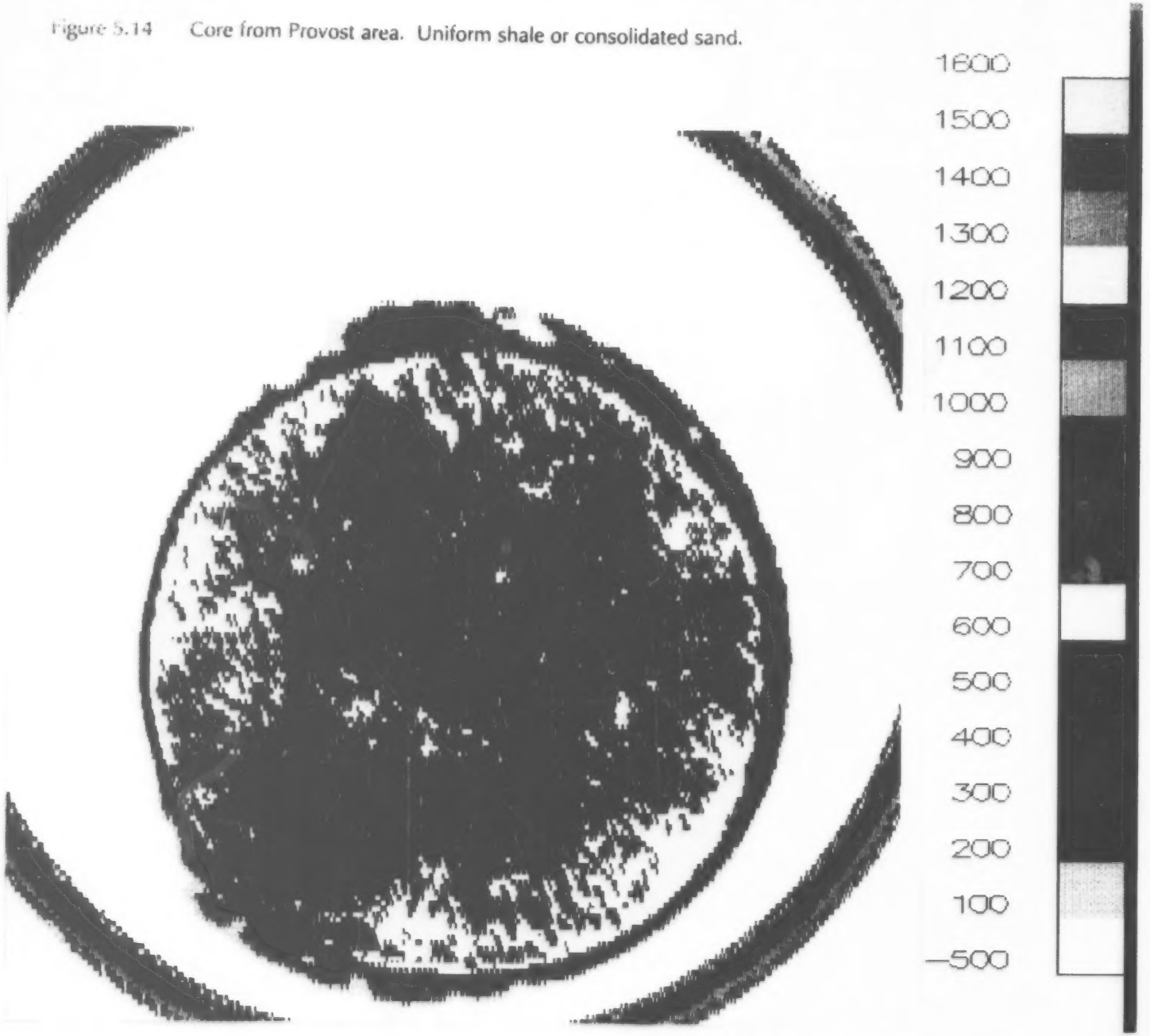

© 1990 NOVA HUSKY RESEARCH CORPORATION

Figure 5.15 CT number image of damaged core from the Provost area.

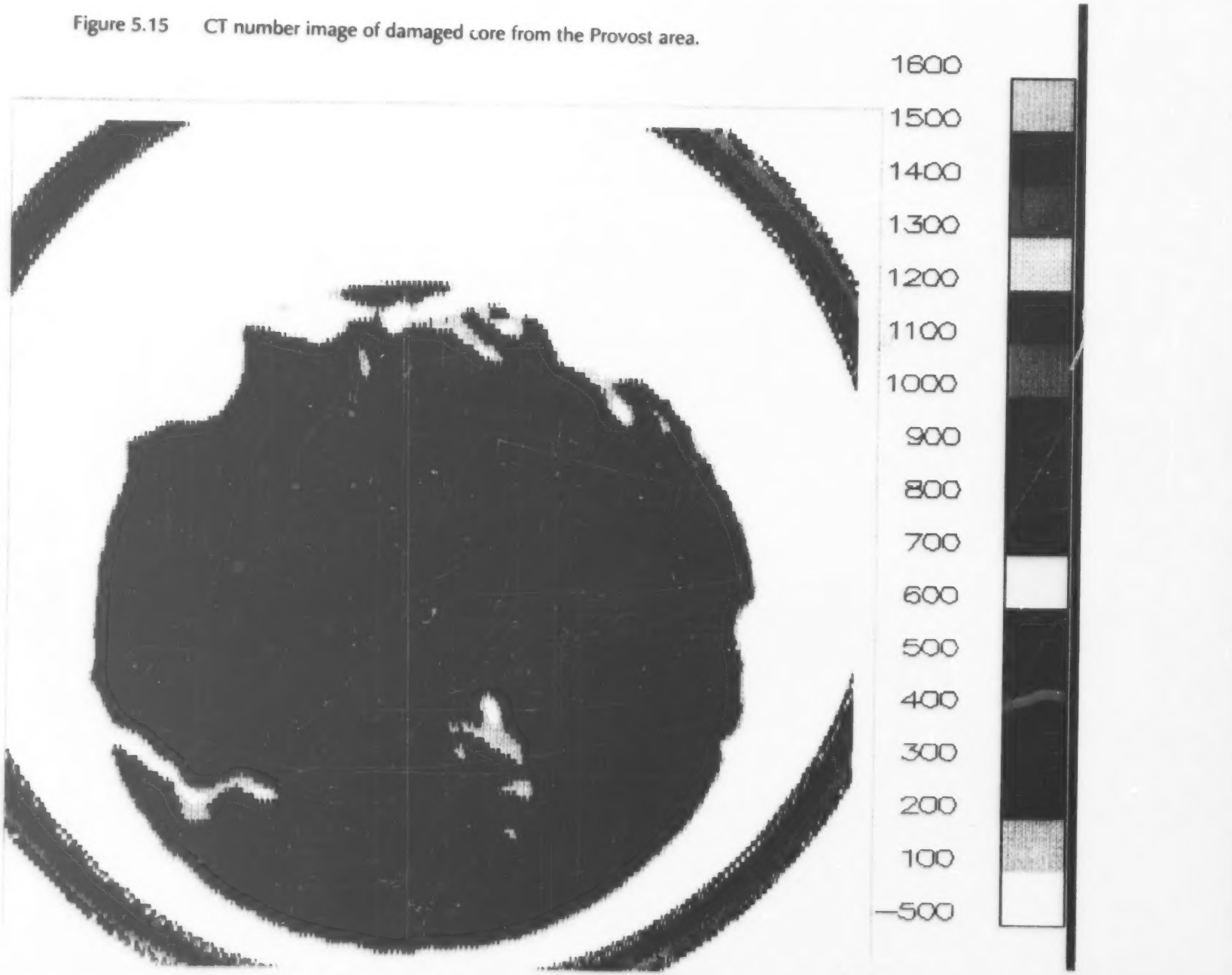

Figure 5.16 Core from Provost area. Consolidated core broken by unconsolidated material.

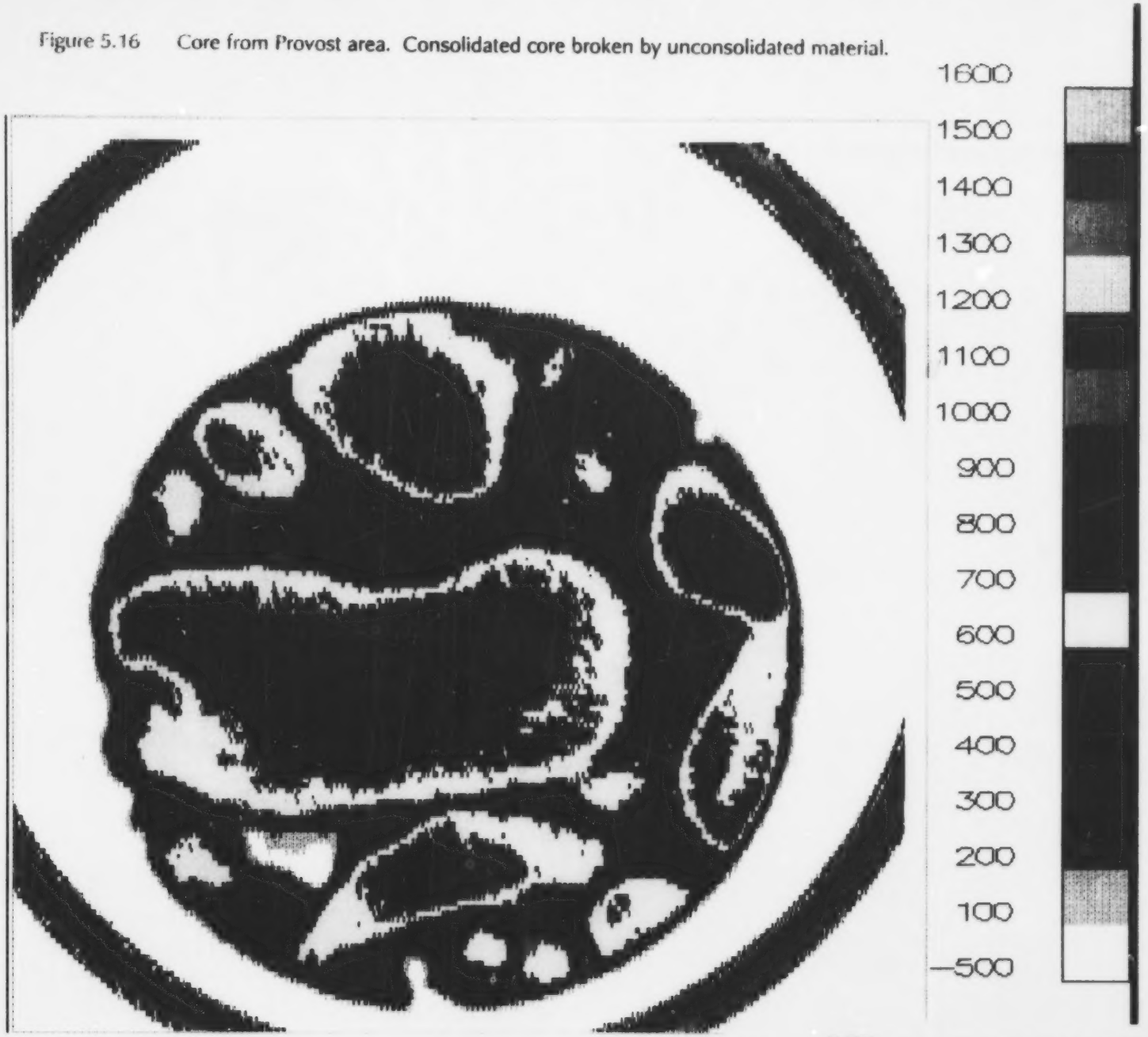

© 1990 NOVA HUSKY RESEARCH CORPORATION

Figure 5.17 CT number image of damaged shale piece of core from Provost area.

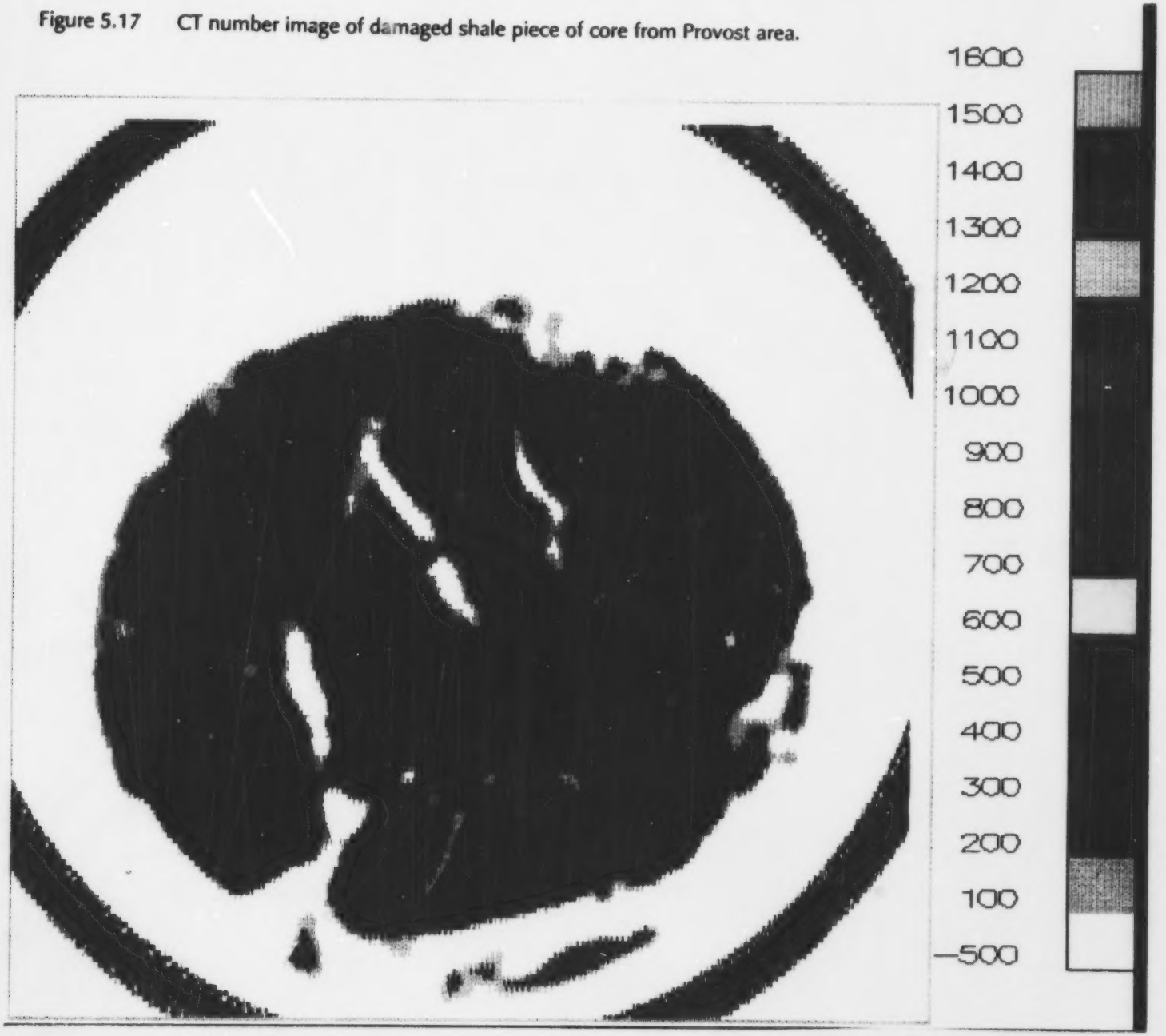

© 1990 NOVA HUSKY RESEARCH CORPORATION

Figure 5.18 Provost core image. Highly consolidated pieces of rock connected by loose material.

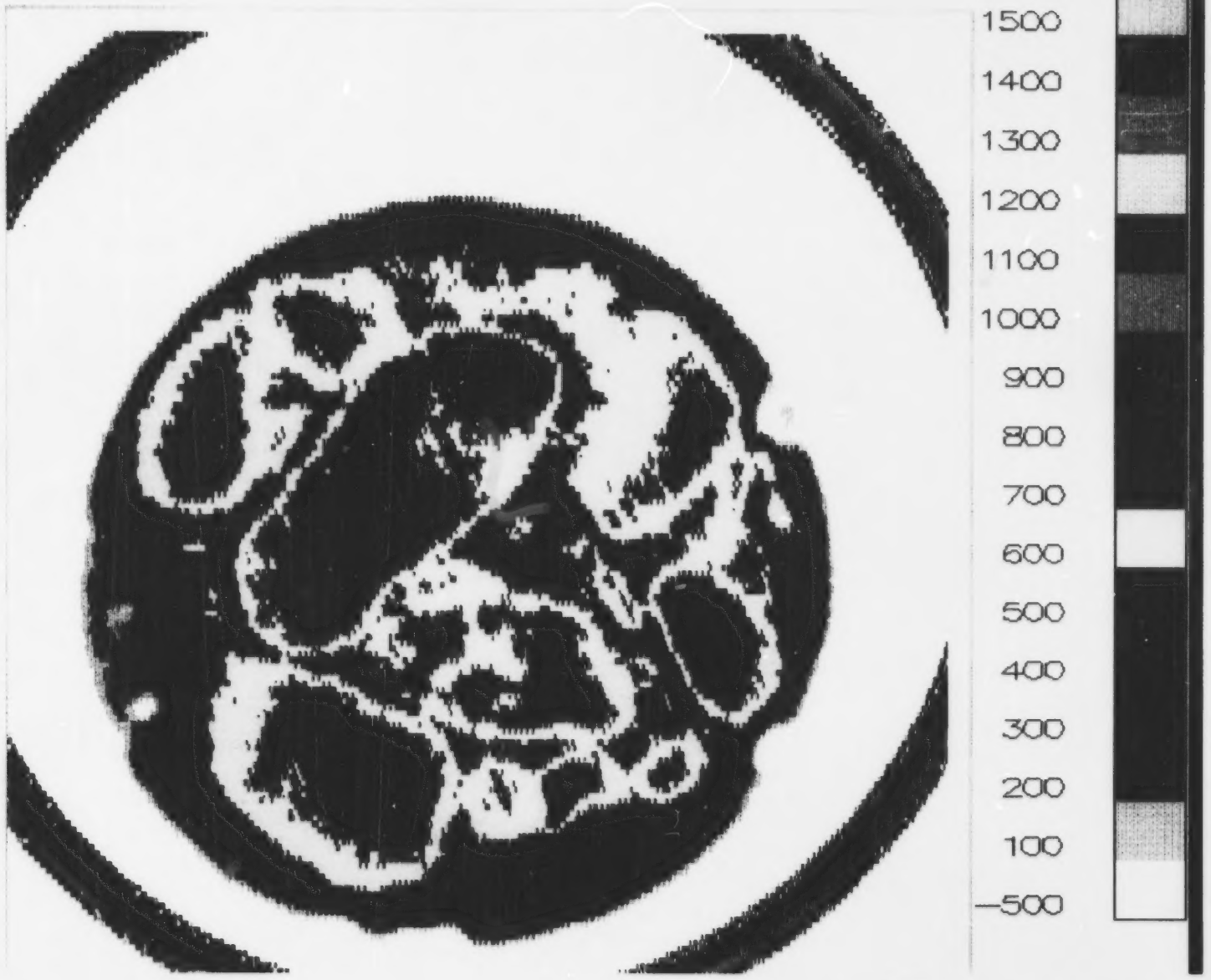

©1990 NOVA HUSKY RESEARCH CORPORATION

Figure 5.19 CT image of Provost core. Fractured semi-consolidated material.

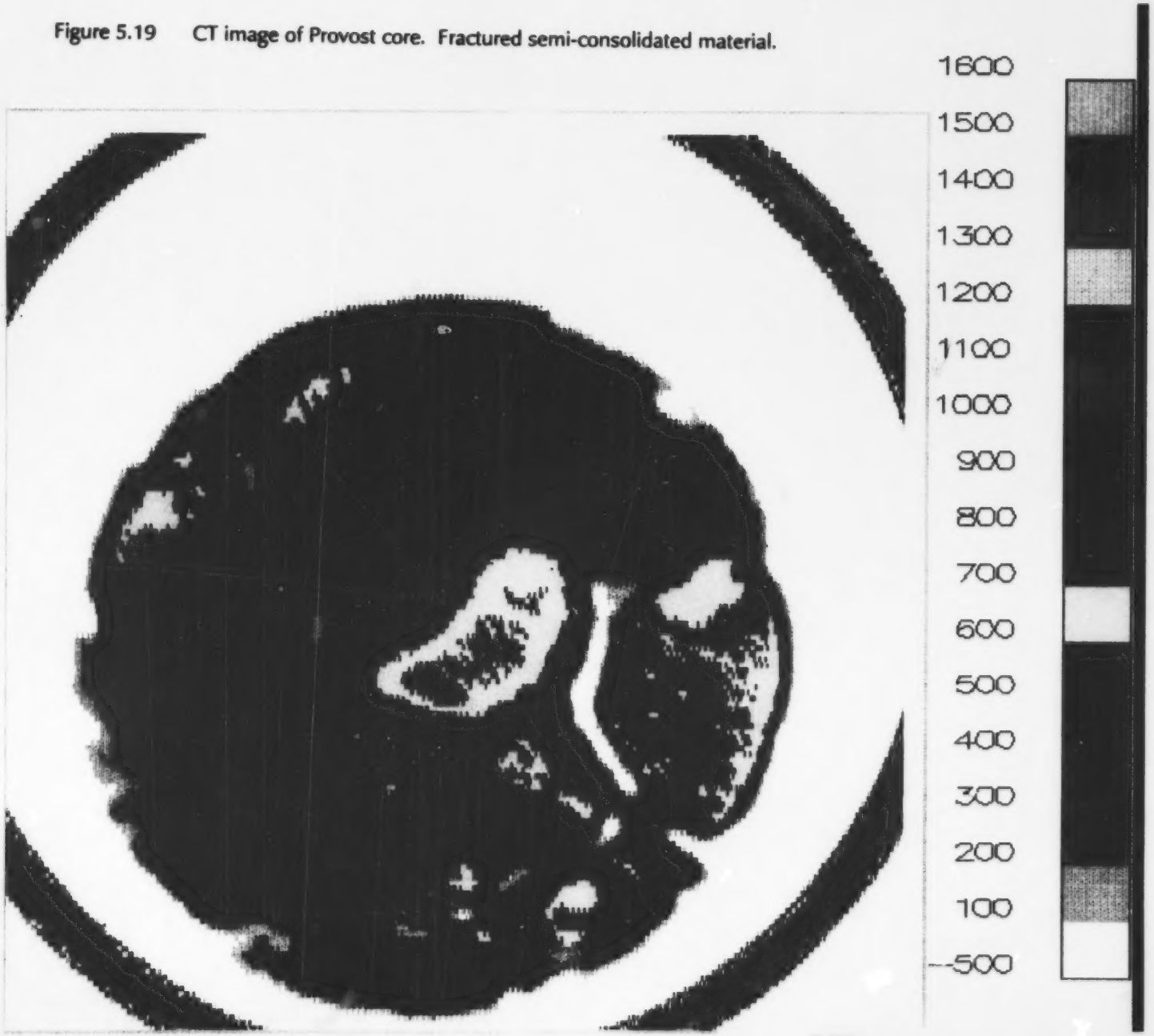

© 1990 NOVA HUSKY RESEARCH CORPORATION

Figure 5.20 Deudritic fracture pattern of semi-consolidated Provost core.

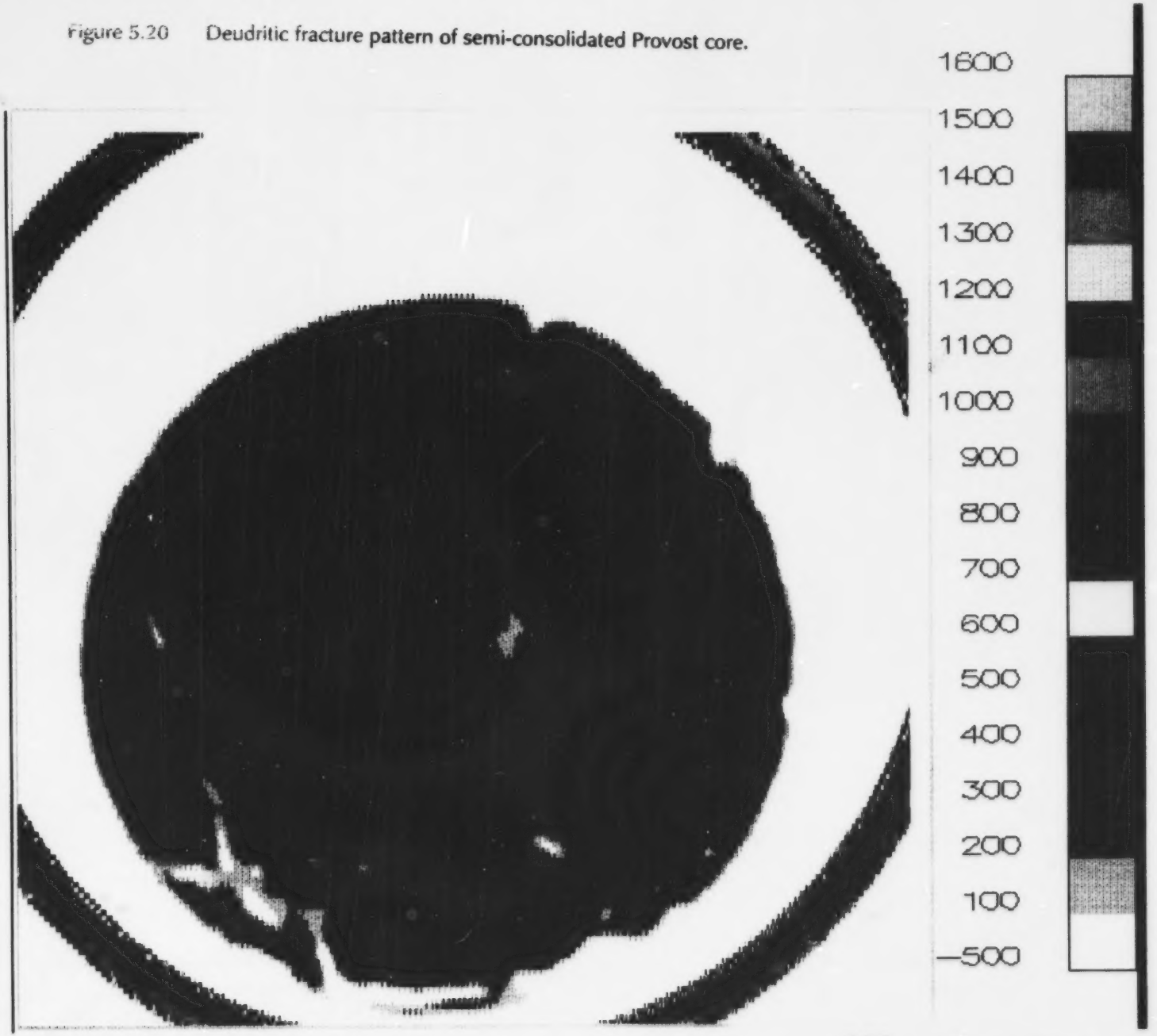

©1990 NOVA HUSKY RESEARCH CORPORATION

Figure 5.21 Radial fracture pattern of shale or consolidated core from Provost area.

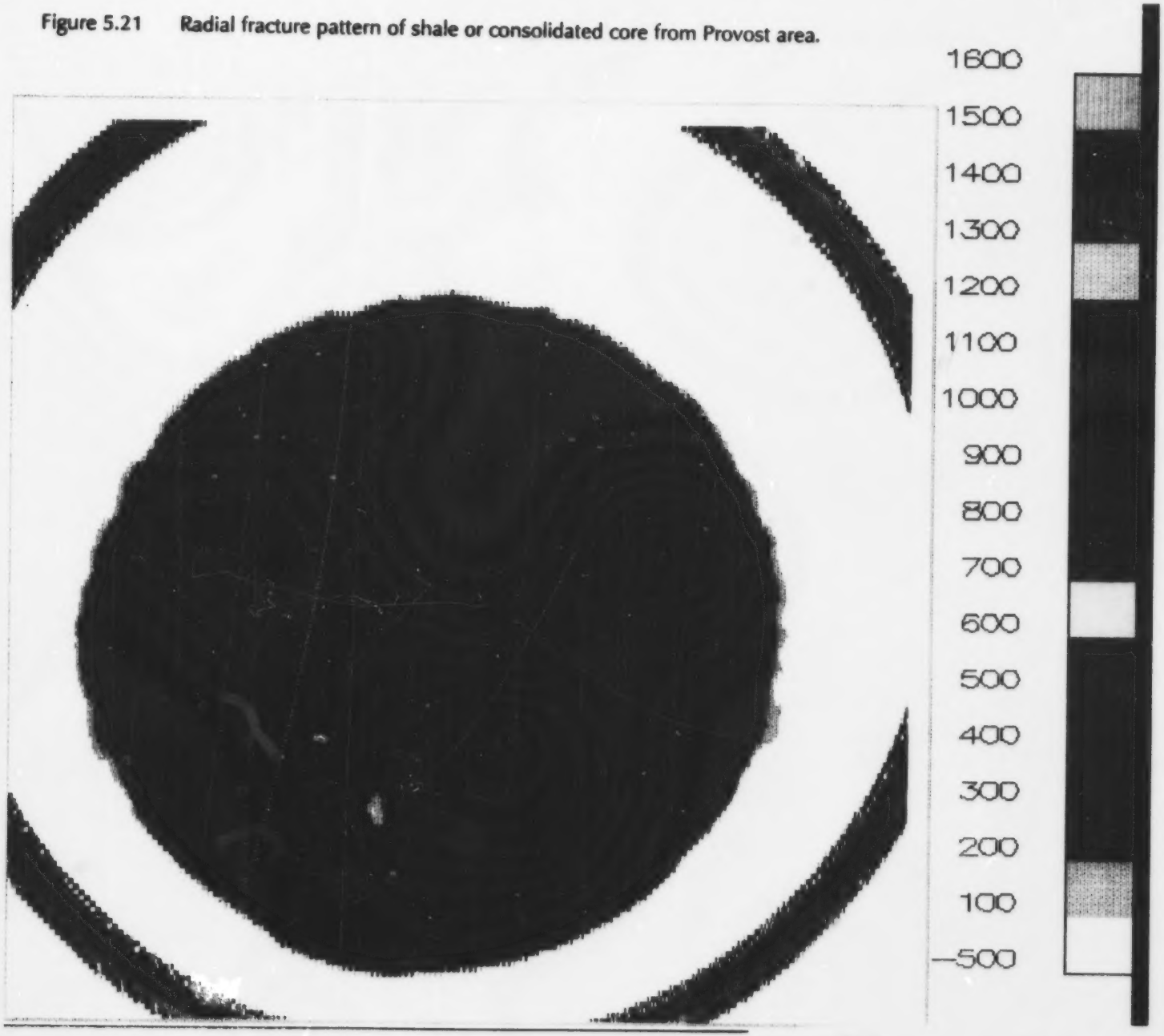

© 1990 NOVA HUSKY RESEARCH CORPORATION

Figure 5.22 Core from Provost area. Identification of core cracking.

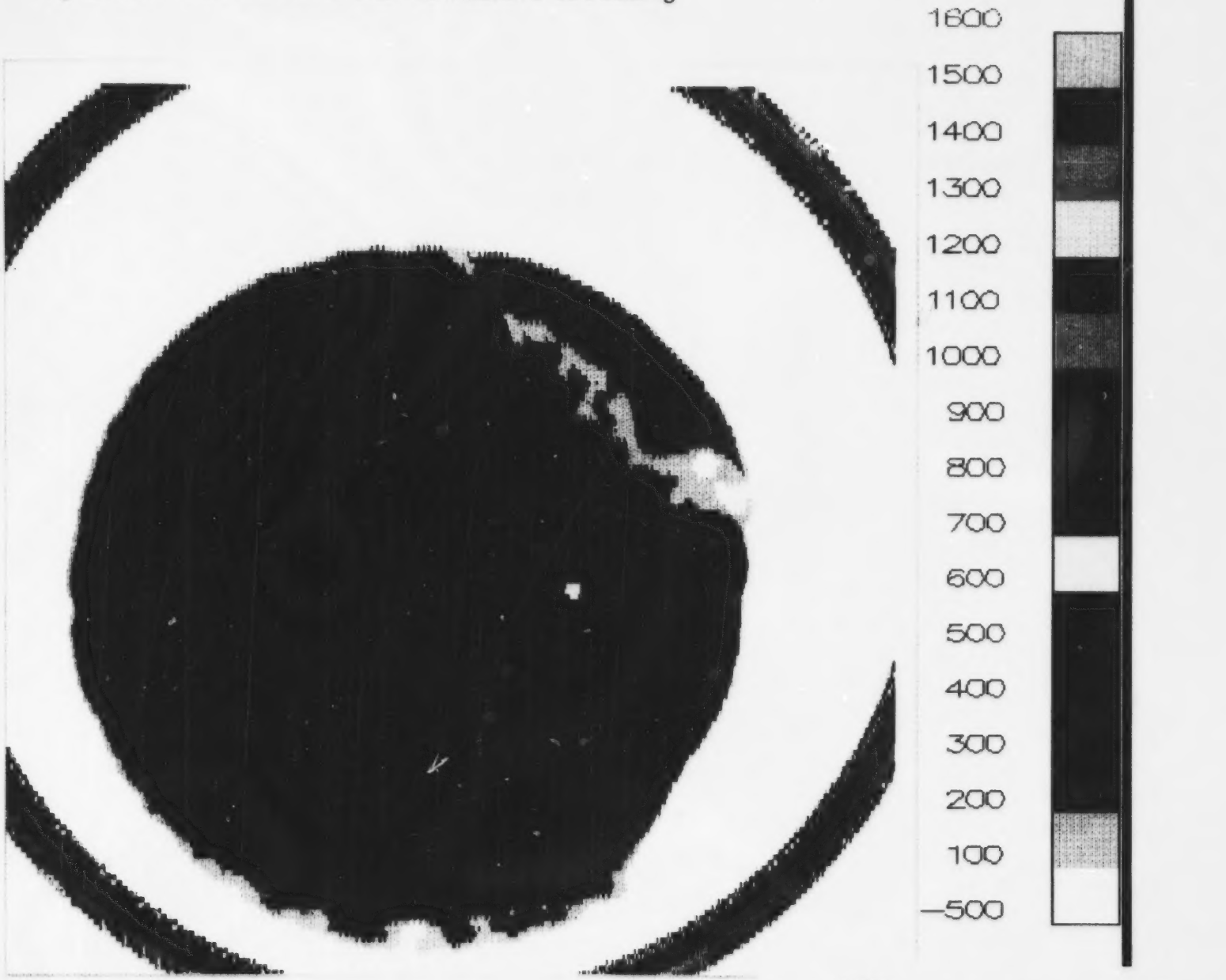

© 1990 NOVA HUSKY RESEARCH CORPORATION

Figure 5.23 CT image of Provost area. Area of very loose sand.

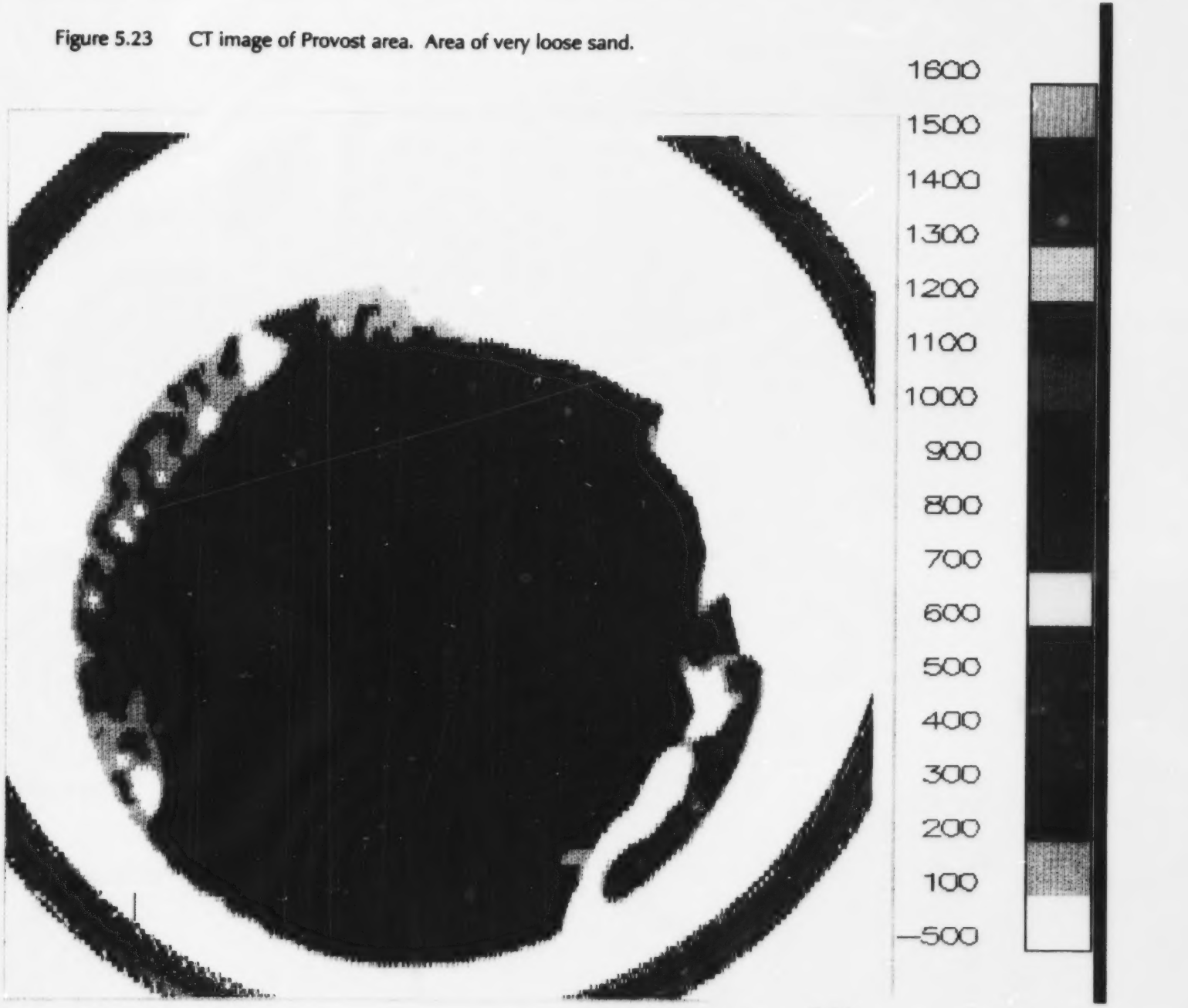

© 1990 NOVA HUSKY RESEARCH CORPORATION

Figure 5.24 Longitudinal representation of Provost core #1; shale laminations and damaged areas are seen.

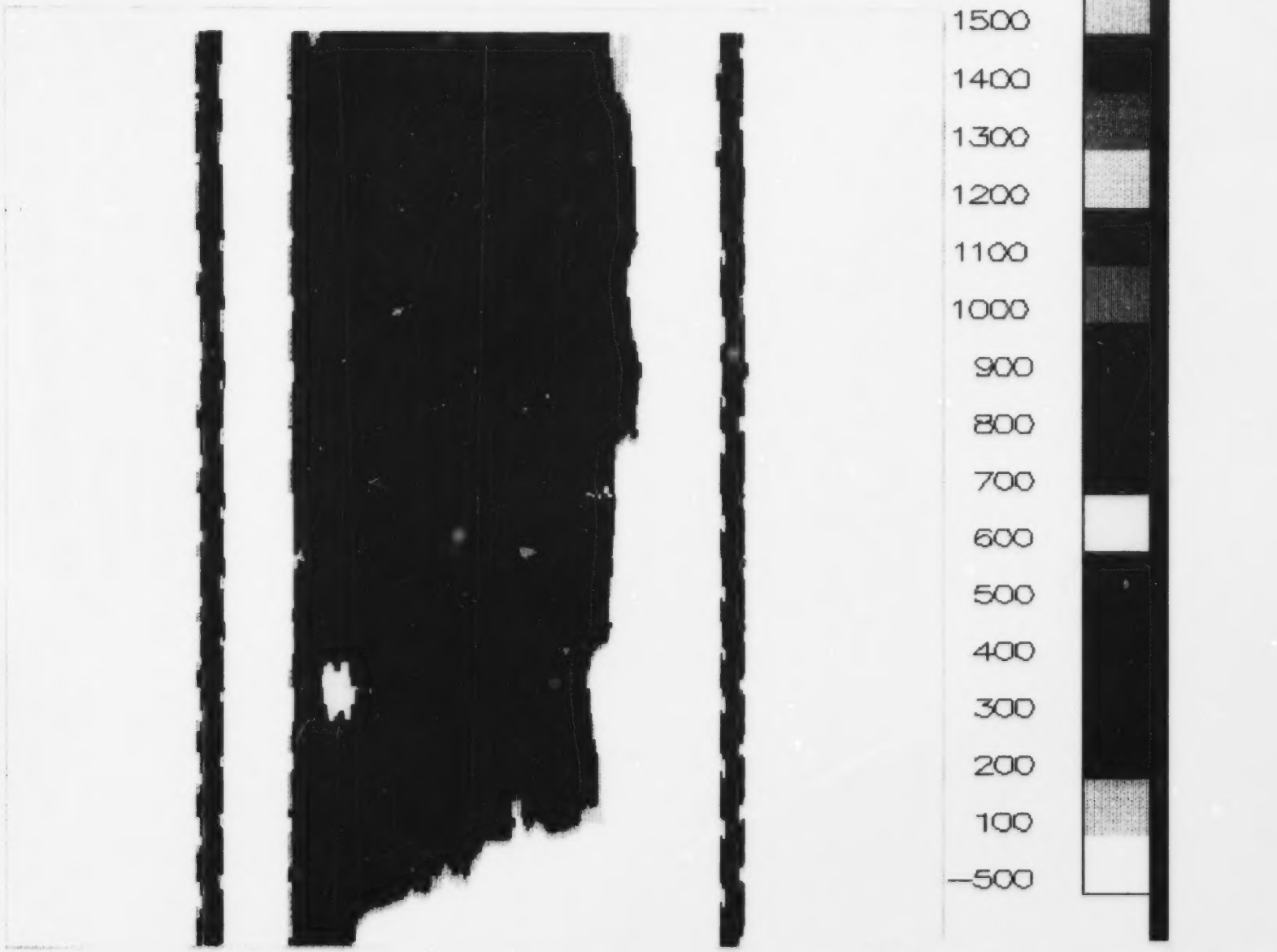

© 1990 NOVA HUSKY RESEARCH CORPORATION

Figure 5.25 Longitudinal representation of Provost core #2. The consolidated layers and cement material are shown along with core damage.

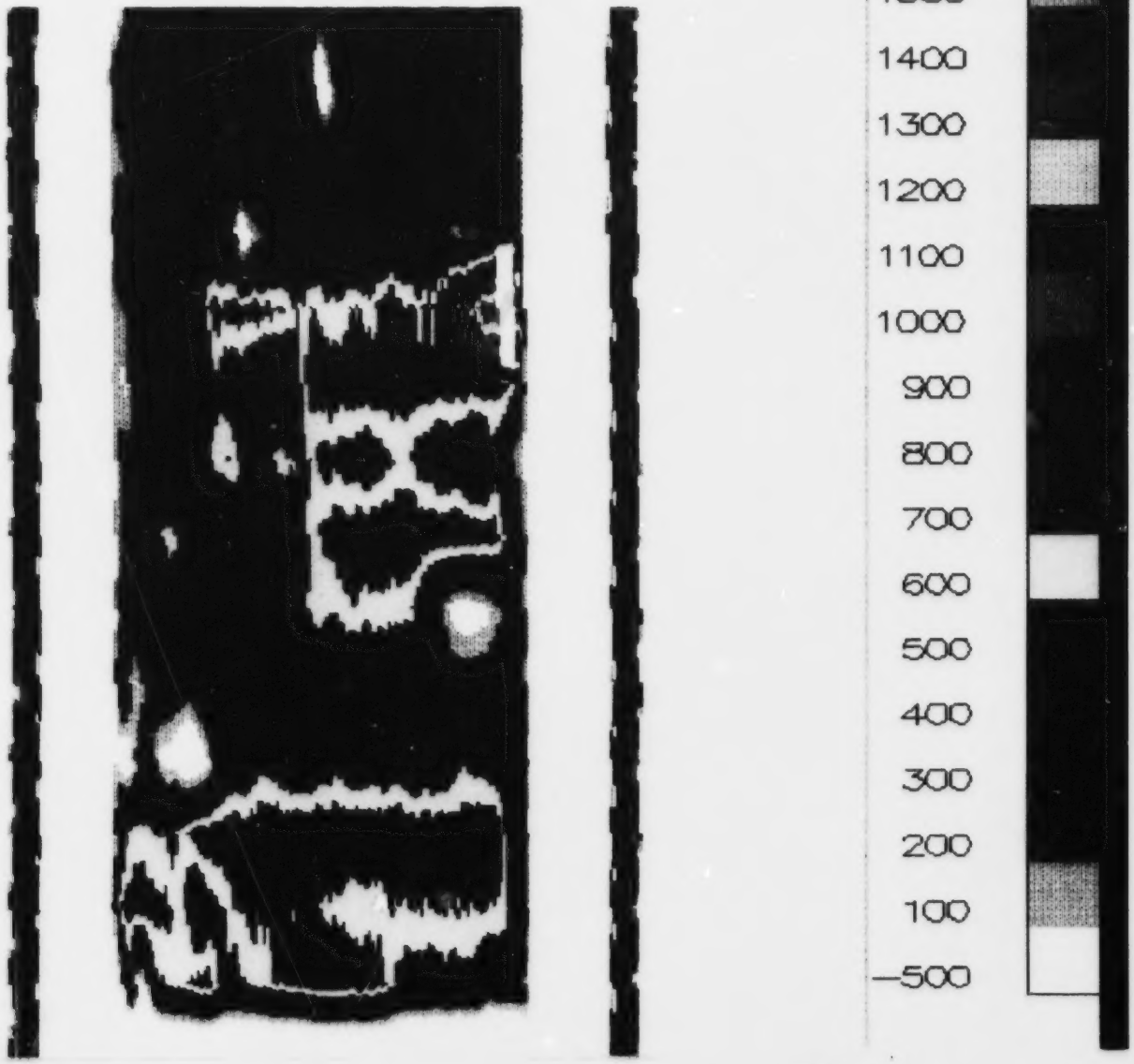

© 1990 NOVA HUSKY RESEARCH CORPORATION

Figure 5.26 Longitudinal representation of Provost core #3. Two consolidated layers with clay clasts are shown.

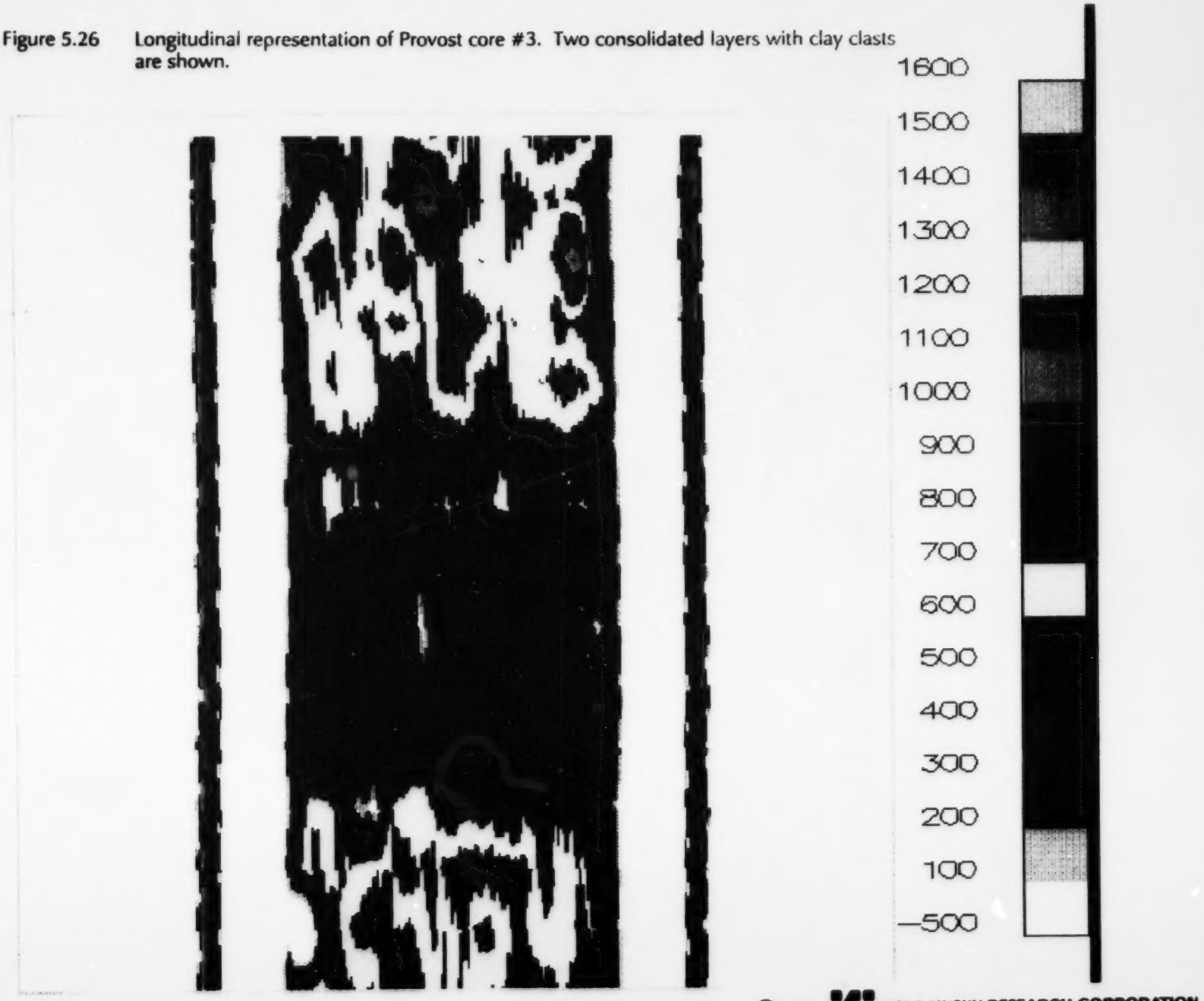

© 1990 NOVA HUSKY RESEARCH CORPORATION

Figure 5.27 Longitudinal representation of Provost core #4. Unconsolidated and damaged sand.

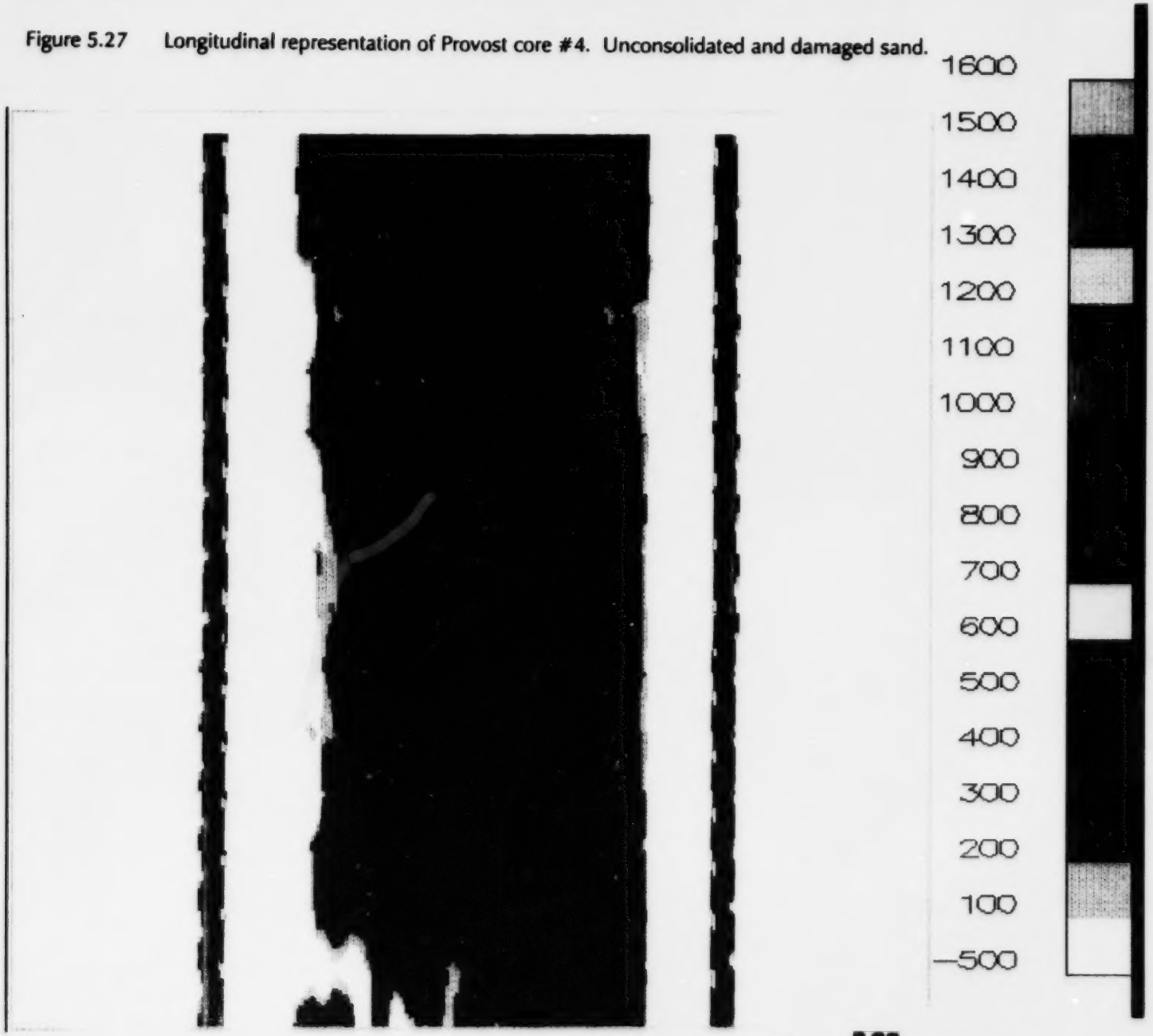

© 1990 NOVA HUSKY RESEARCH CORPORATION

Figure 5.28 Longitudinal representation of Provost core #5. Unconsolidated and damaged sand; presence of a shale layer.

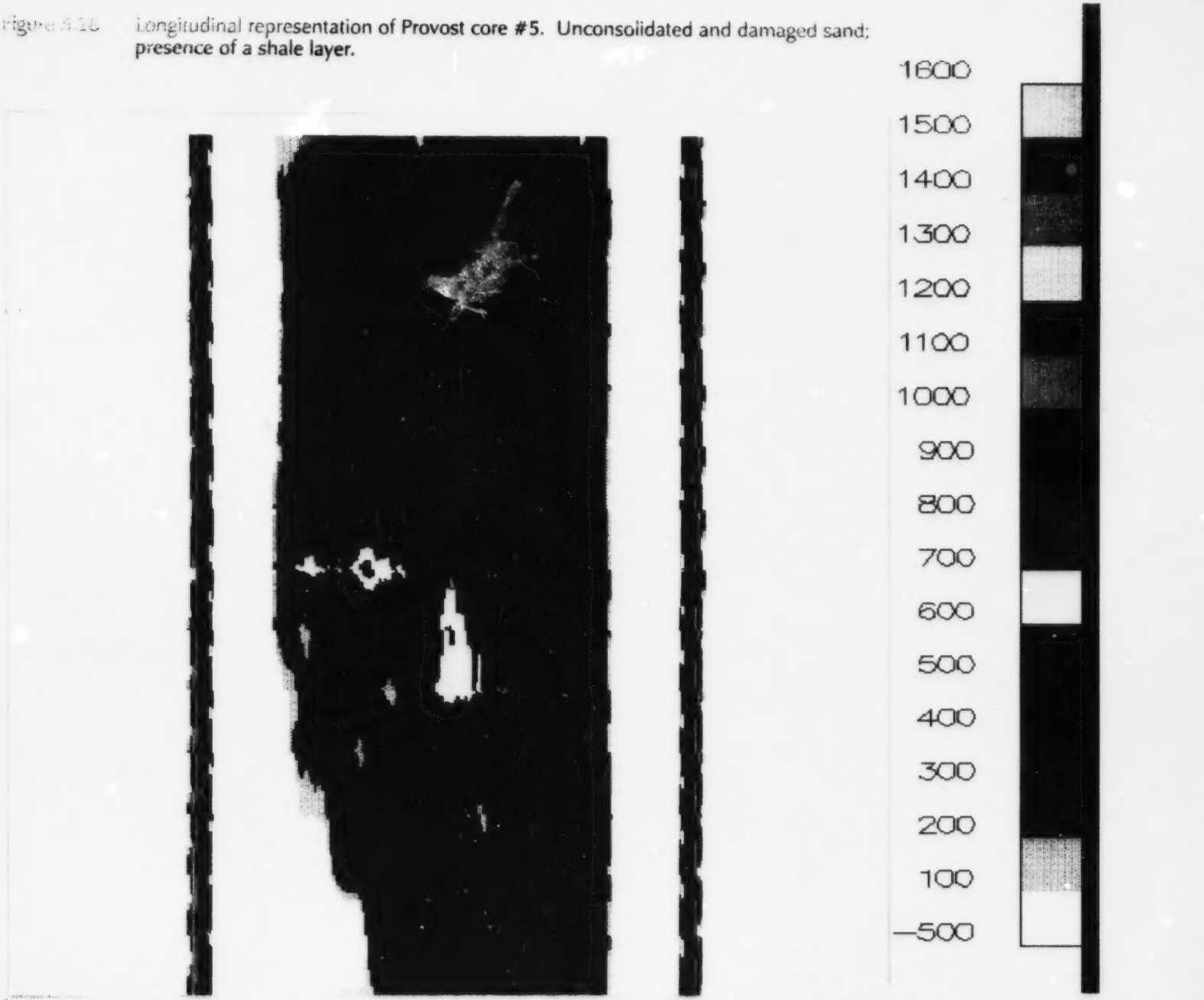

© 1990 NOVA HUSKY RESEARCH CORPORATION

Figure 5.29 Longitudinal representation of Provost core #6. Unconsolidated loose and damaged sand.

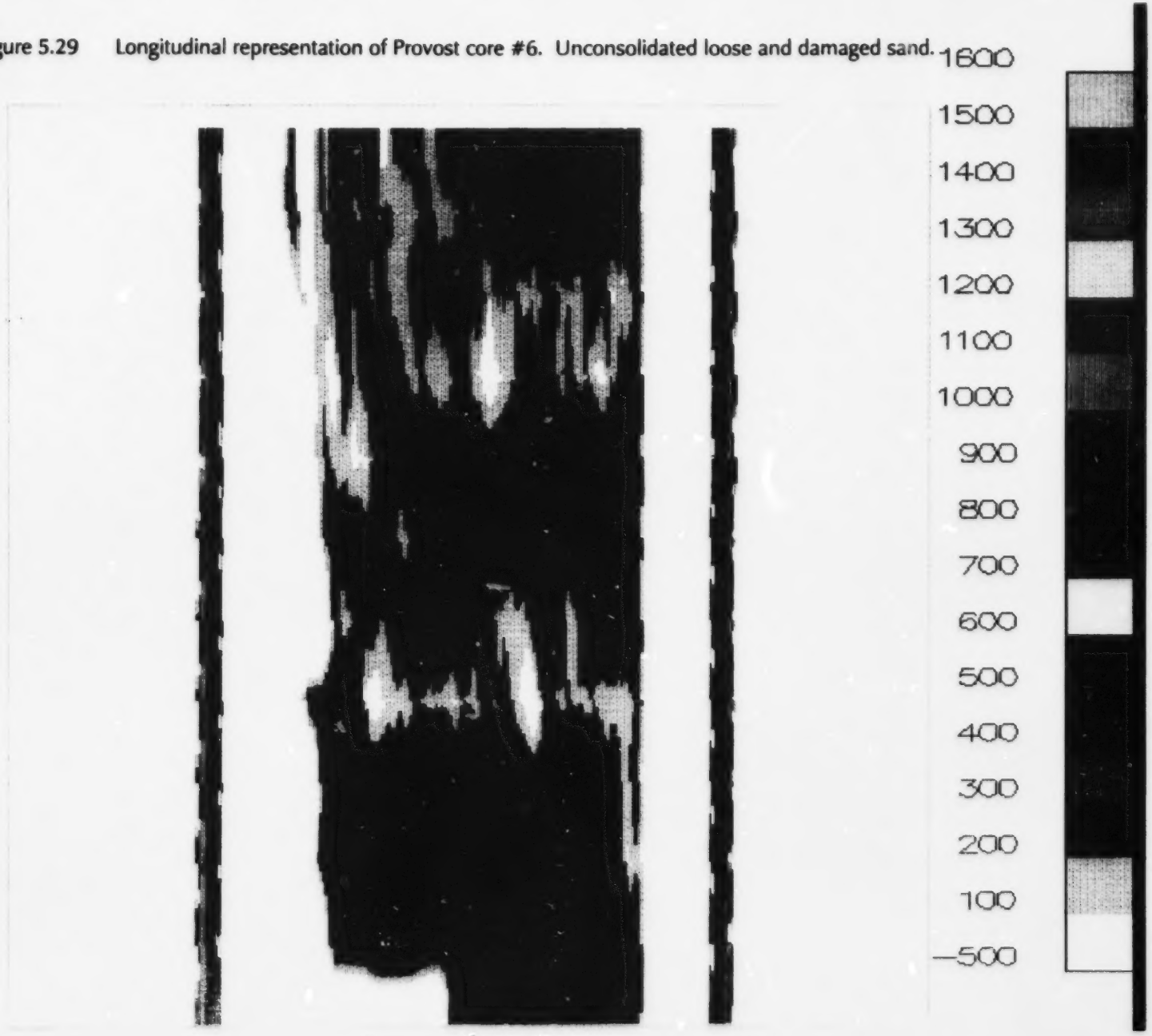

© 1990 NOVA HUSKY RESEARCH CORPORATION

Figure 5.30 Longitudinal representation of the whole Provost core as a function of depth (in m).

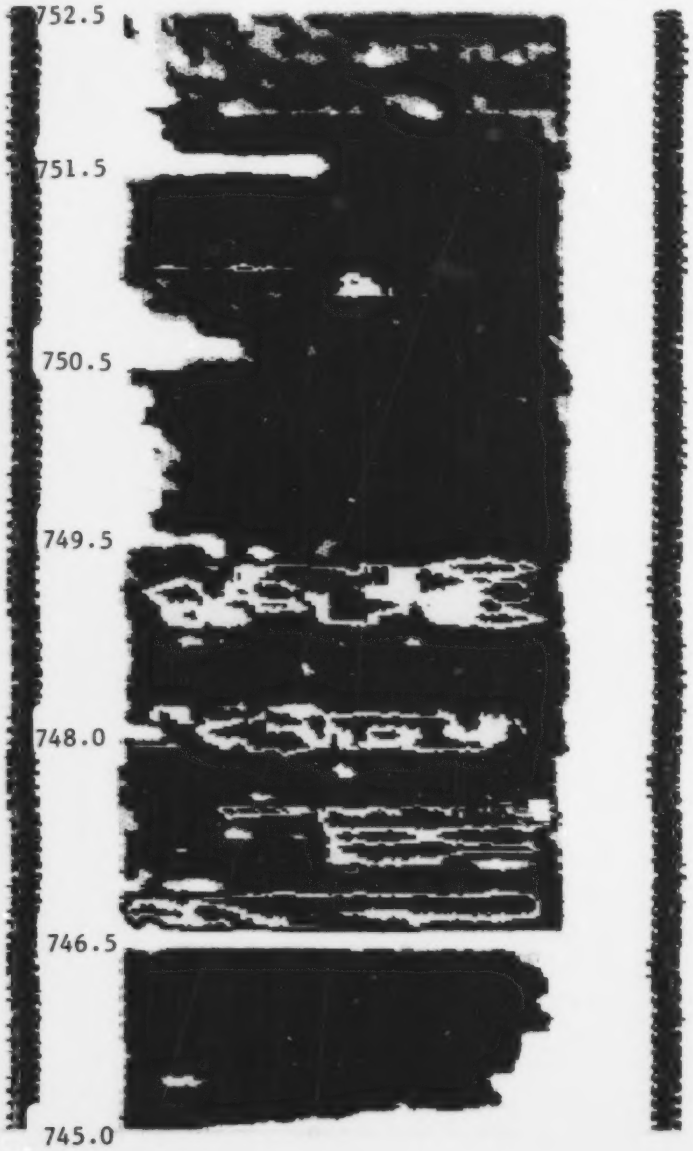

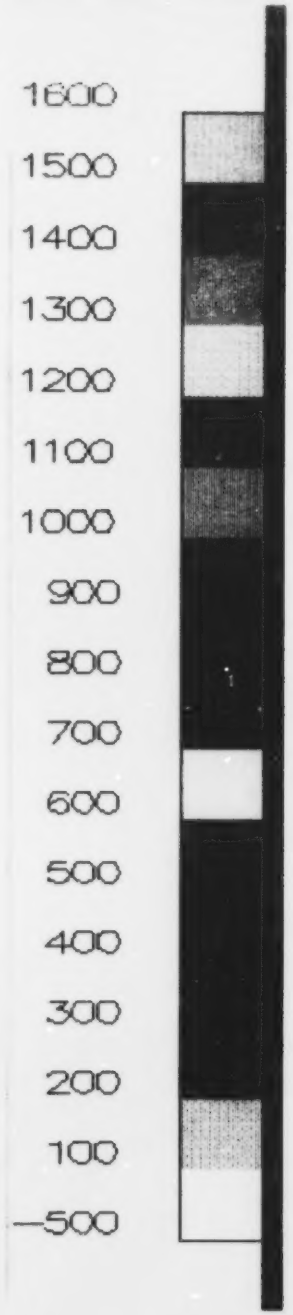

©1990 NOVA HUSKY RESEARCH CORPORATION

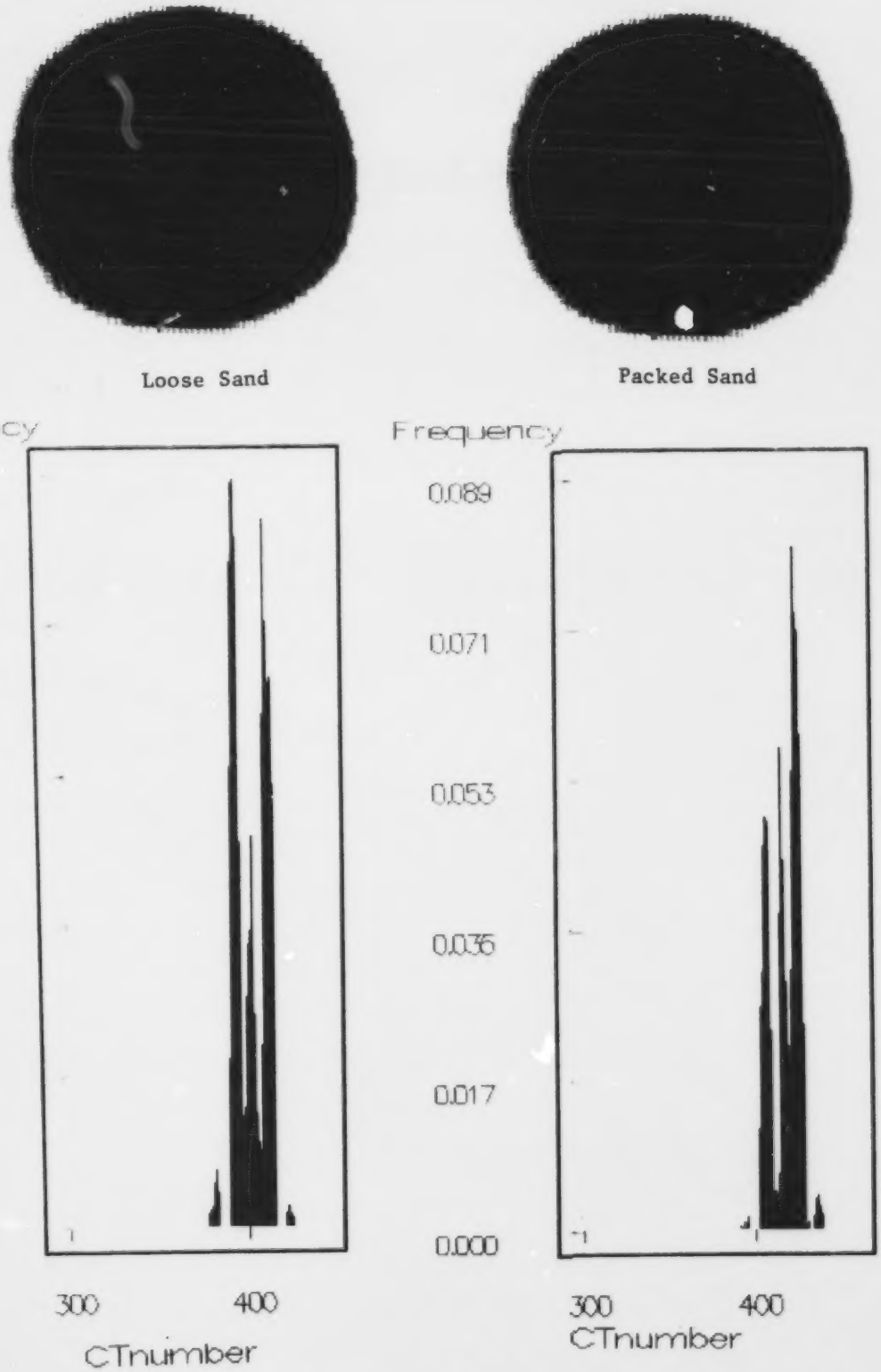

Figure 5.31 Image of sandpack prepared in the laboratory.

© 1990 NOVA HUSKY RESEARCH CORPORATION

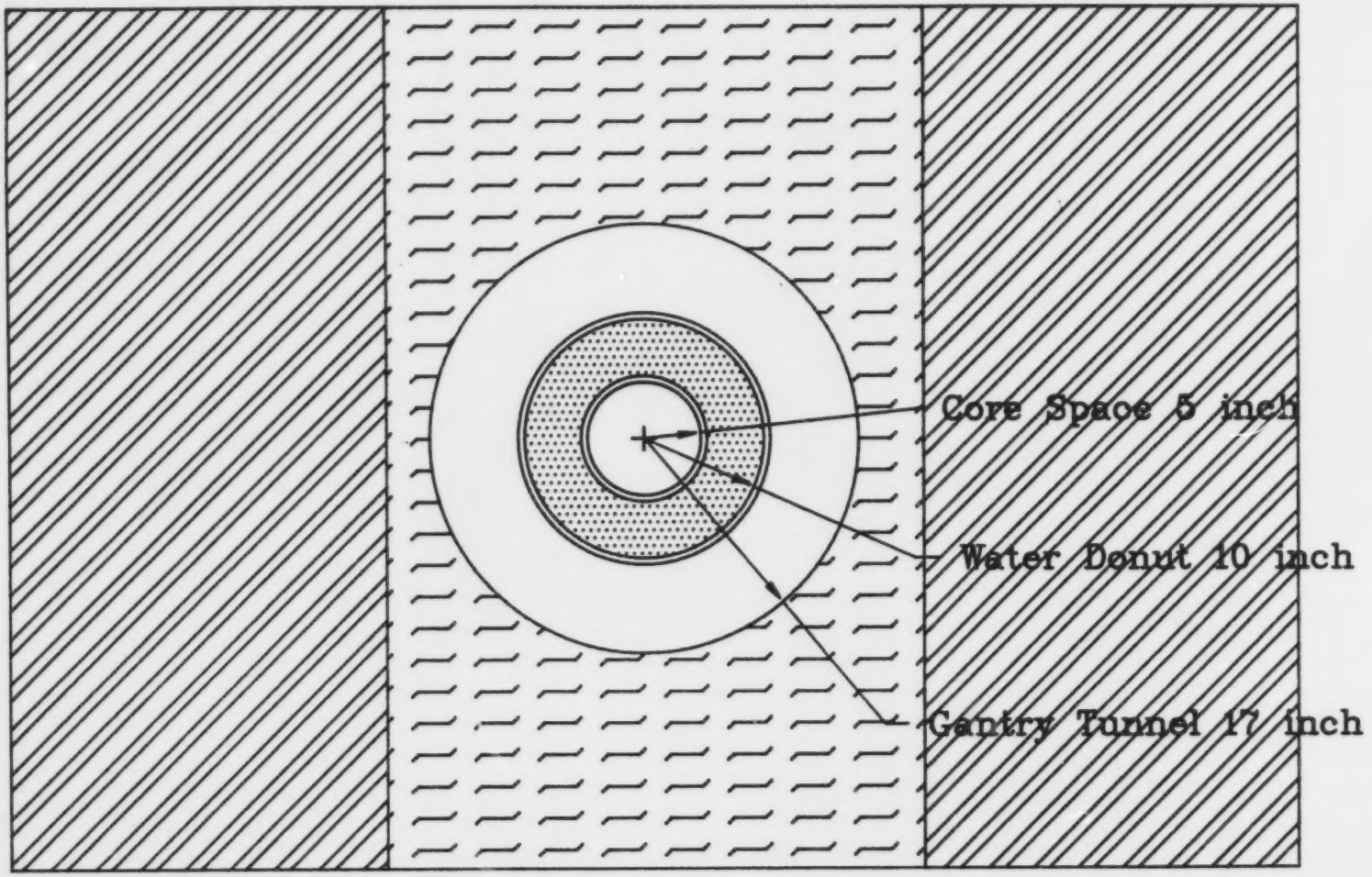

Figure 6.1 Schematic of the x-ray scanner gantry.

©1989 NOVA HUSKY RESEARCH CORPORATION

Figure 6.2 Image of the Halkirk sandstone. Presence of high density inclusions. The color code at the right hand side indicates the range of CT numbers for each color. The range is 100 CT numbers.

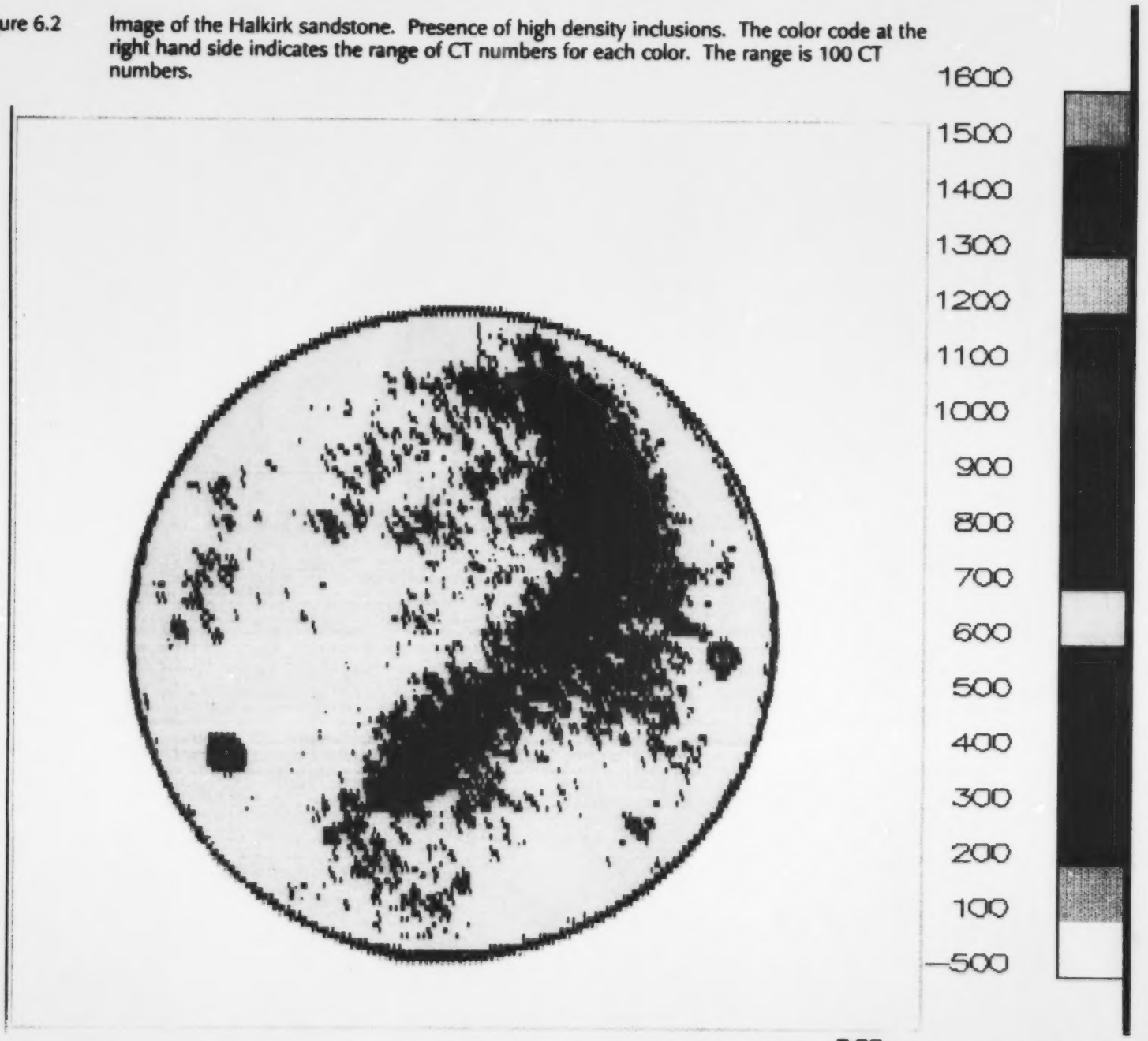

©1990 NOVA HUSKY RESEARCH CORPORATION

Figure 6.3 Image of the Halkirk sandstone. Uniform sample. Color code same as in Figure 6.2.

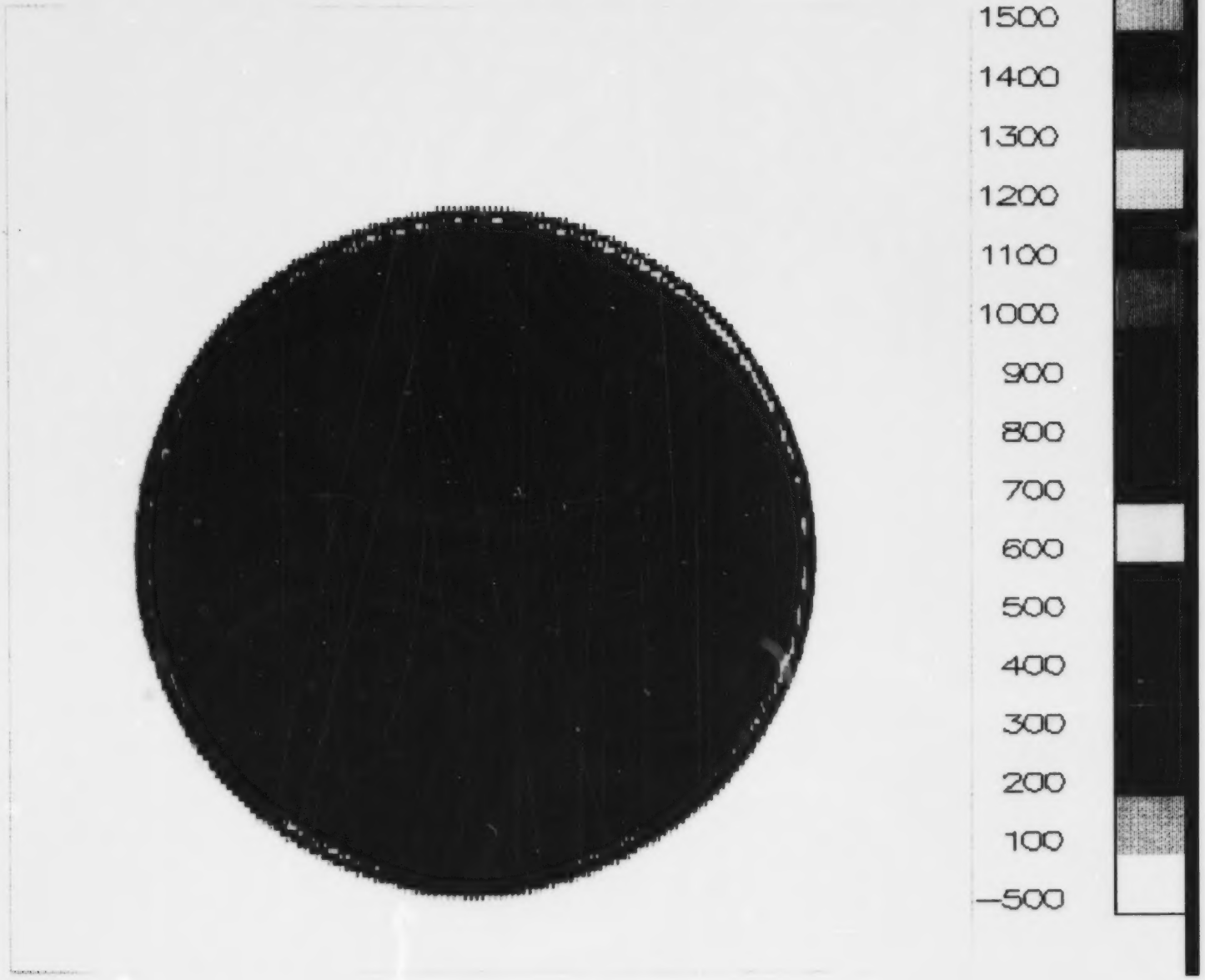

Figure 6.4 Longitudinal view of Halkirk core #1. Uniform sand. Color code same as in Figure 6.2.

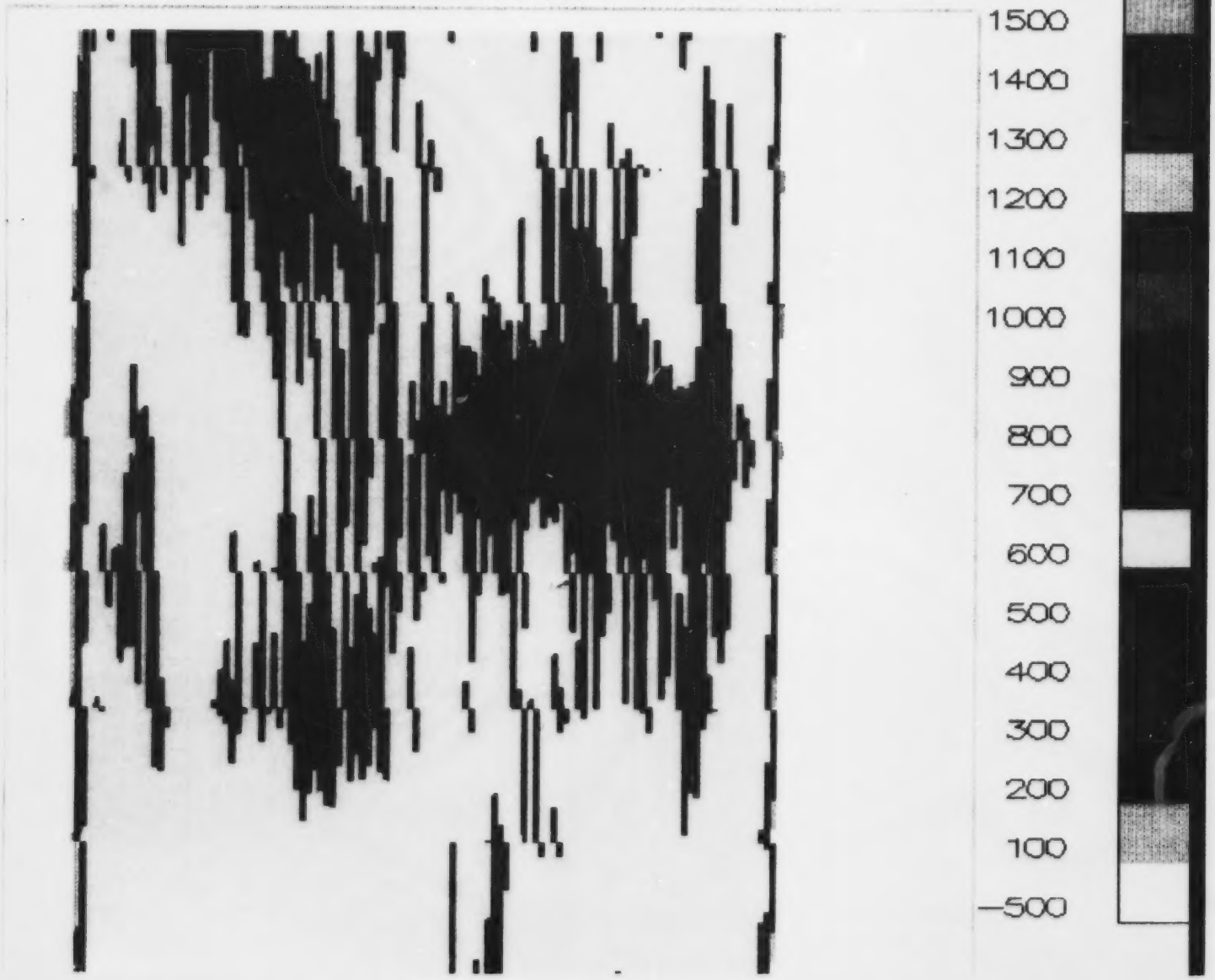

Figure 6.5 Longitudinal view of Halkirk core #2. Color code same as in Figure 6.2.

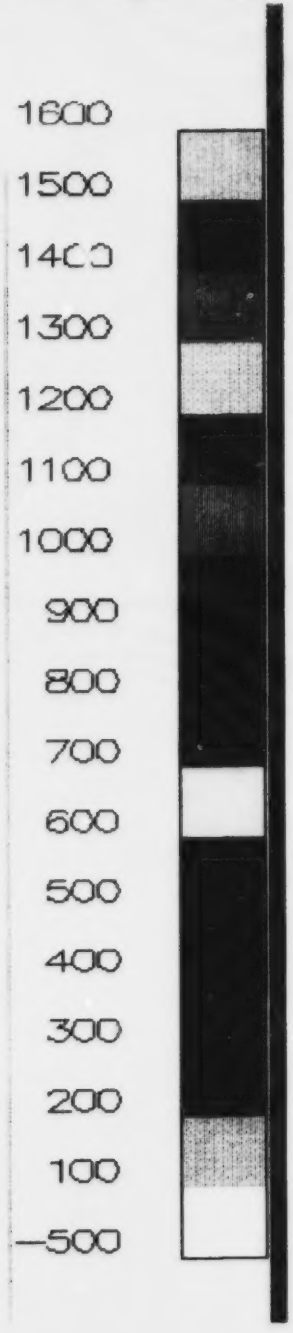

Figure 6.6 Longitudinal view of Halkirk core #3. Uniform sand with few high density inclusions. Color code as in Figure 6.2.

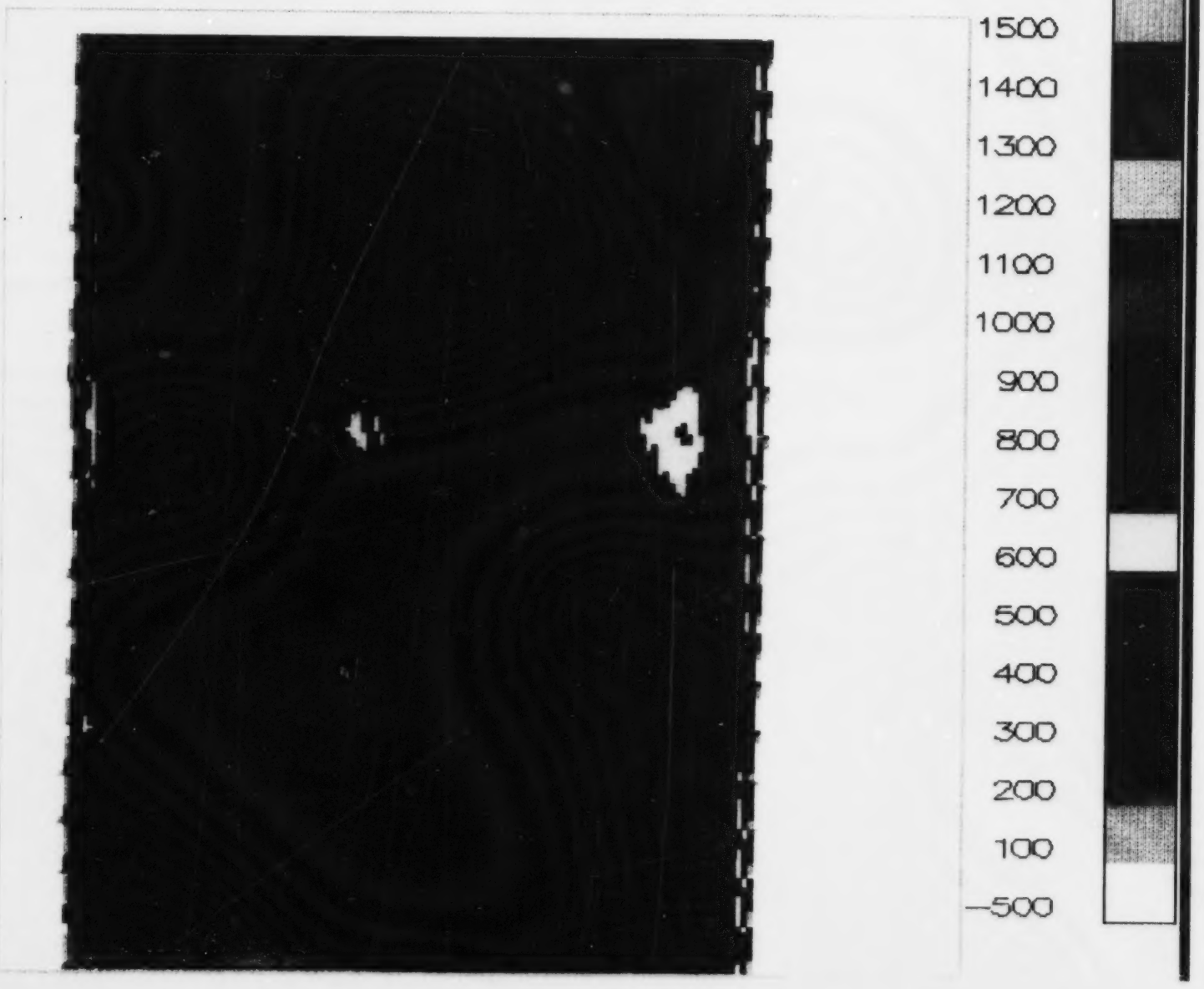

CAT SCAN VIEWS

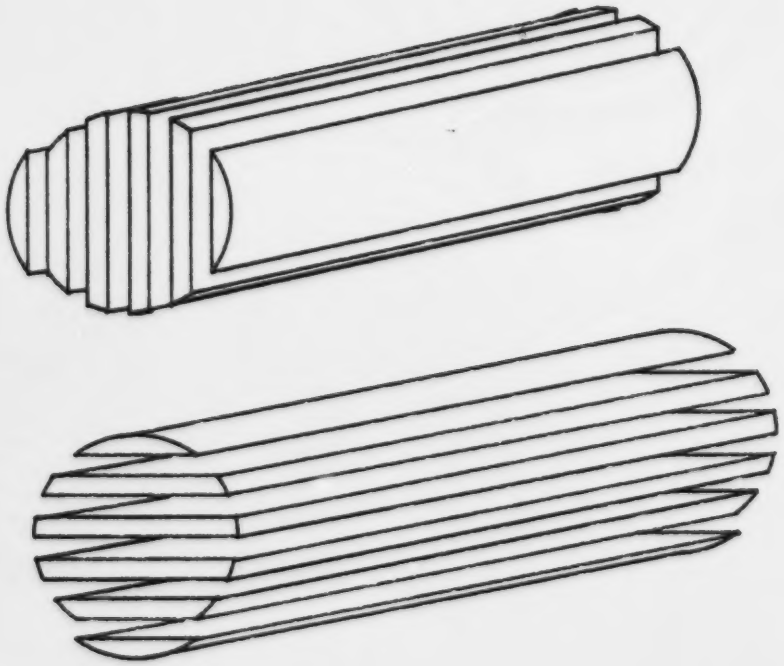

Saggital

Coronal

JPB/CORDAL3VG/MARCH/89

Figure 6.7 Different longitudinal type views of core samples.

©1989 NOVA HUSKY RESEARCH CORPORATION

Figure 6.8 CT number image of Bluesky formation. Dolomitic sandstone. Color code same as in Figure 6.2.

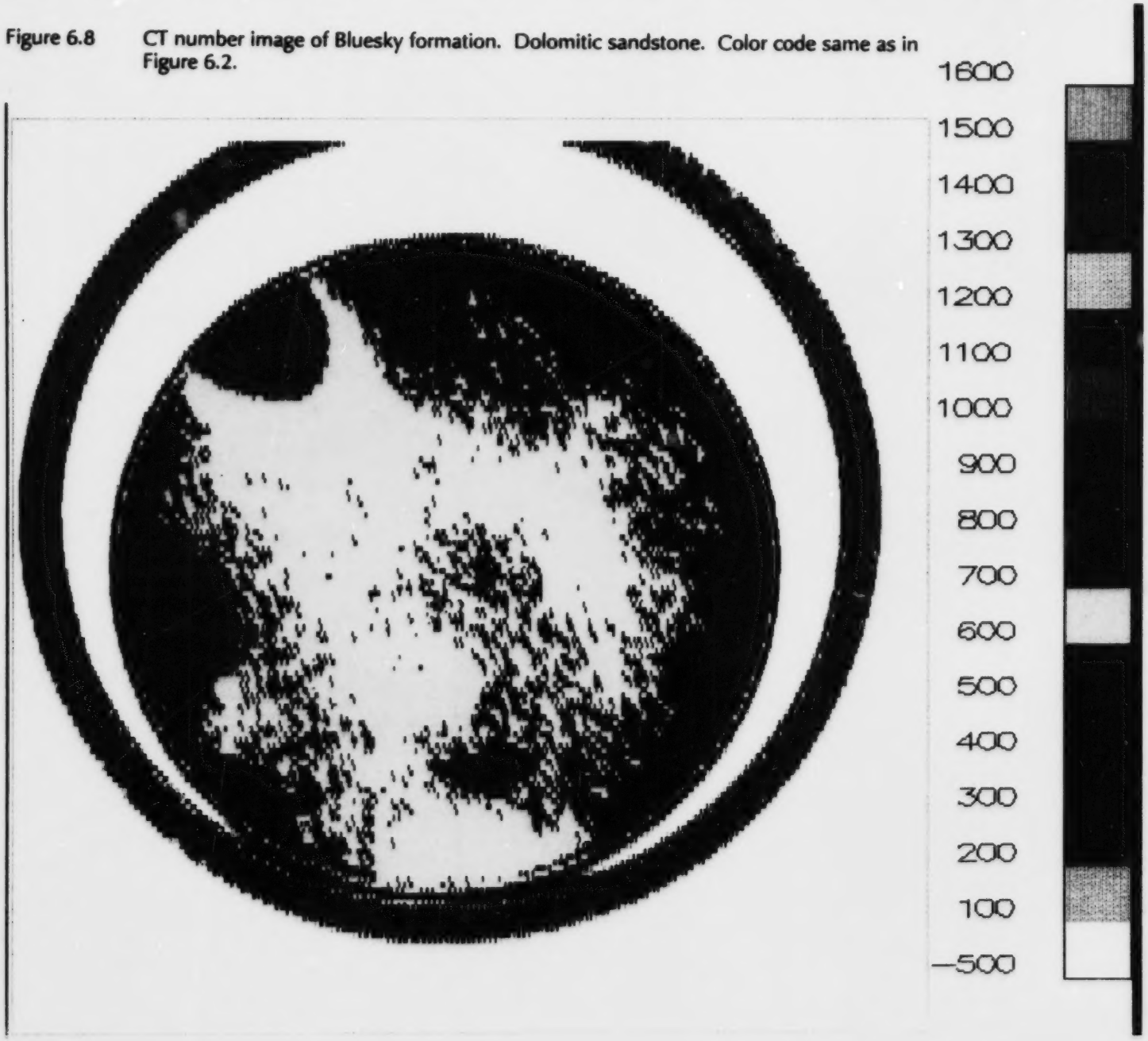

Figure 6.9 CT number image of Bluesky formation. Dolomite. Color code as in Figure 6.2.

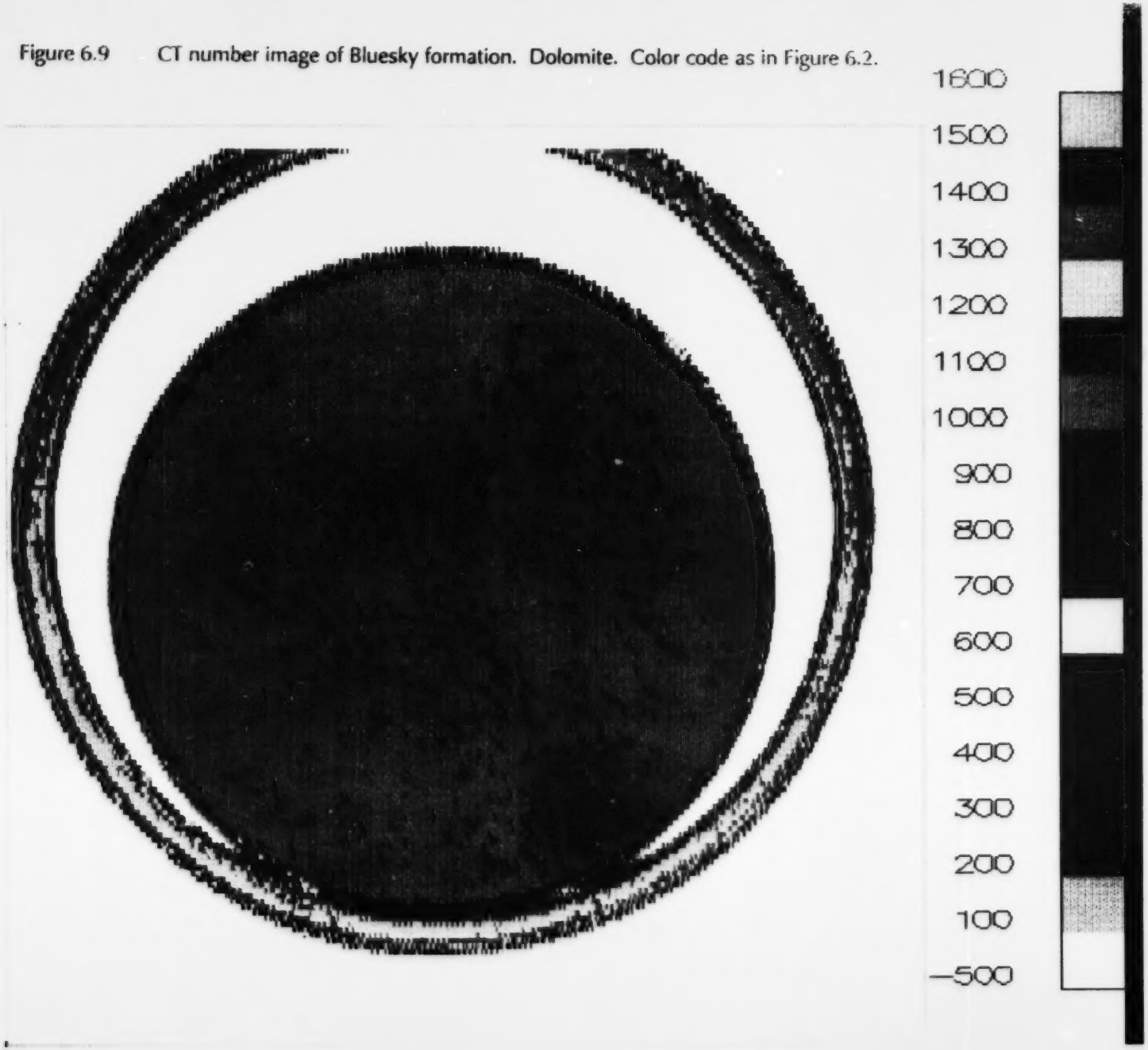

Figure 6.10 CT number image of Bluesky formation. 2/3 slabbed core with 1/3 Berea Cap. Uniform dolomitic sandstone. Color code as in Figure 6.2.

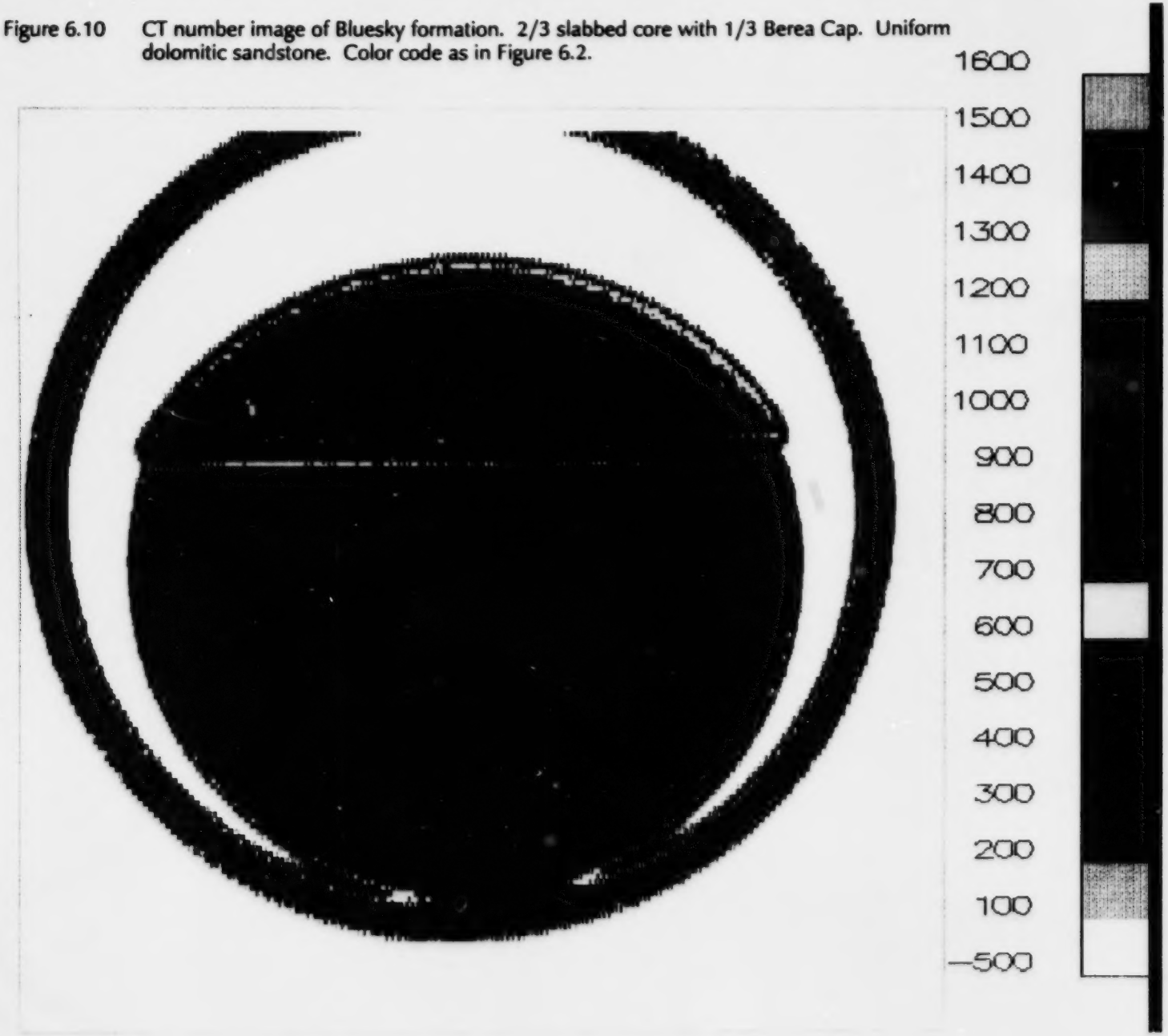

Figure 6.11 CT number image of Bluesky formation. 2/3 slabbed core with 1/3 Berea cap. Non-uniform dolomitic sandstone. Color code as in Figure 6.2.

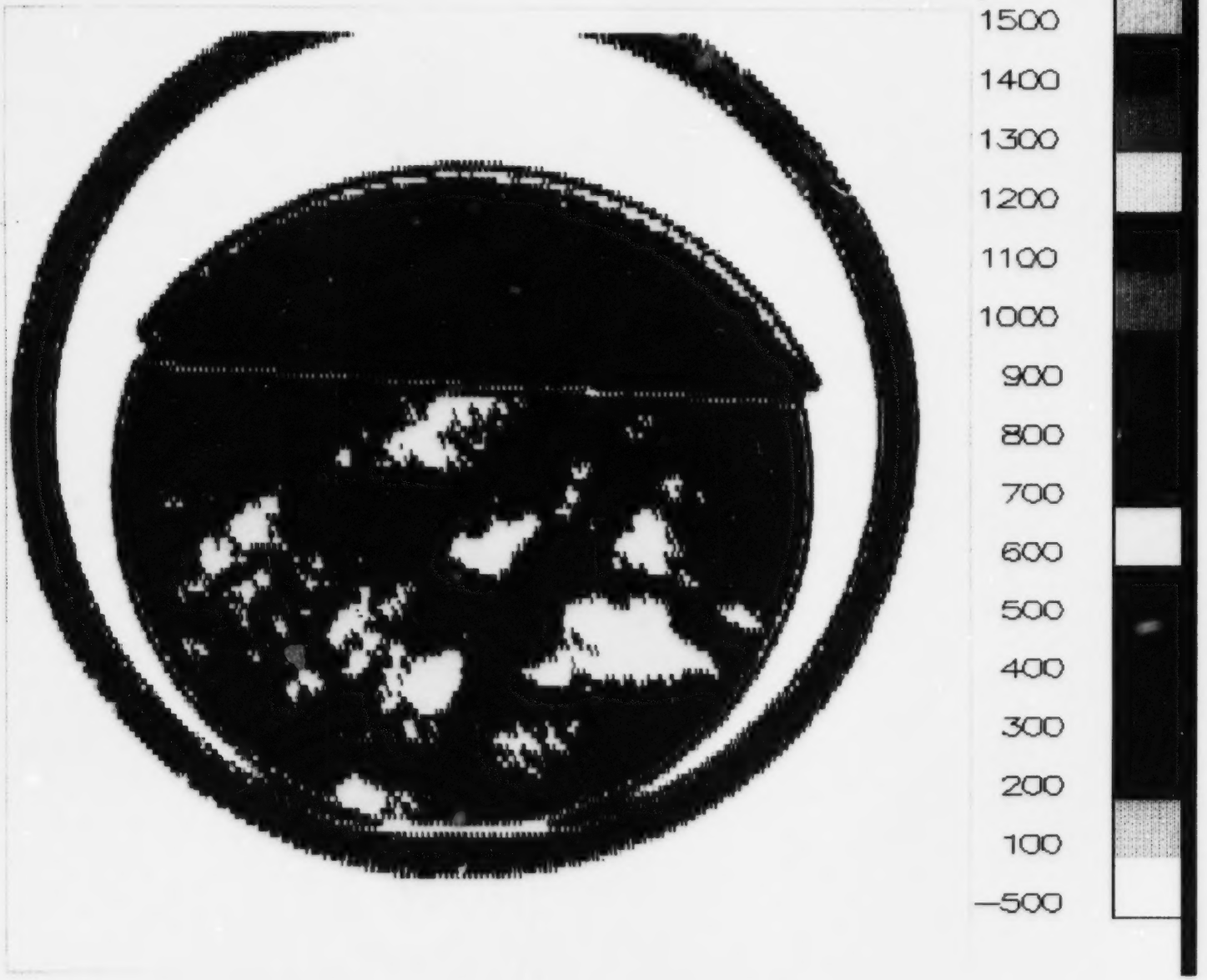

Figure 6.12 Saggital view of Rainbow Keg River "A" Pool core 52. Color code as in Figure 6.2.

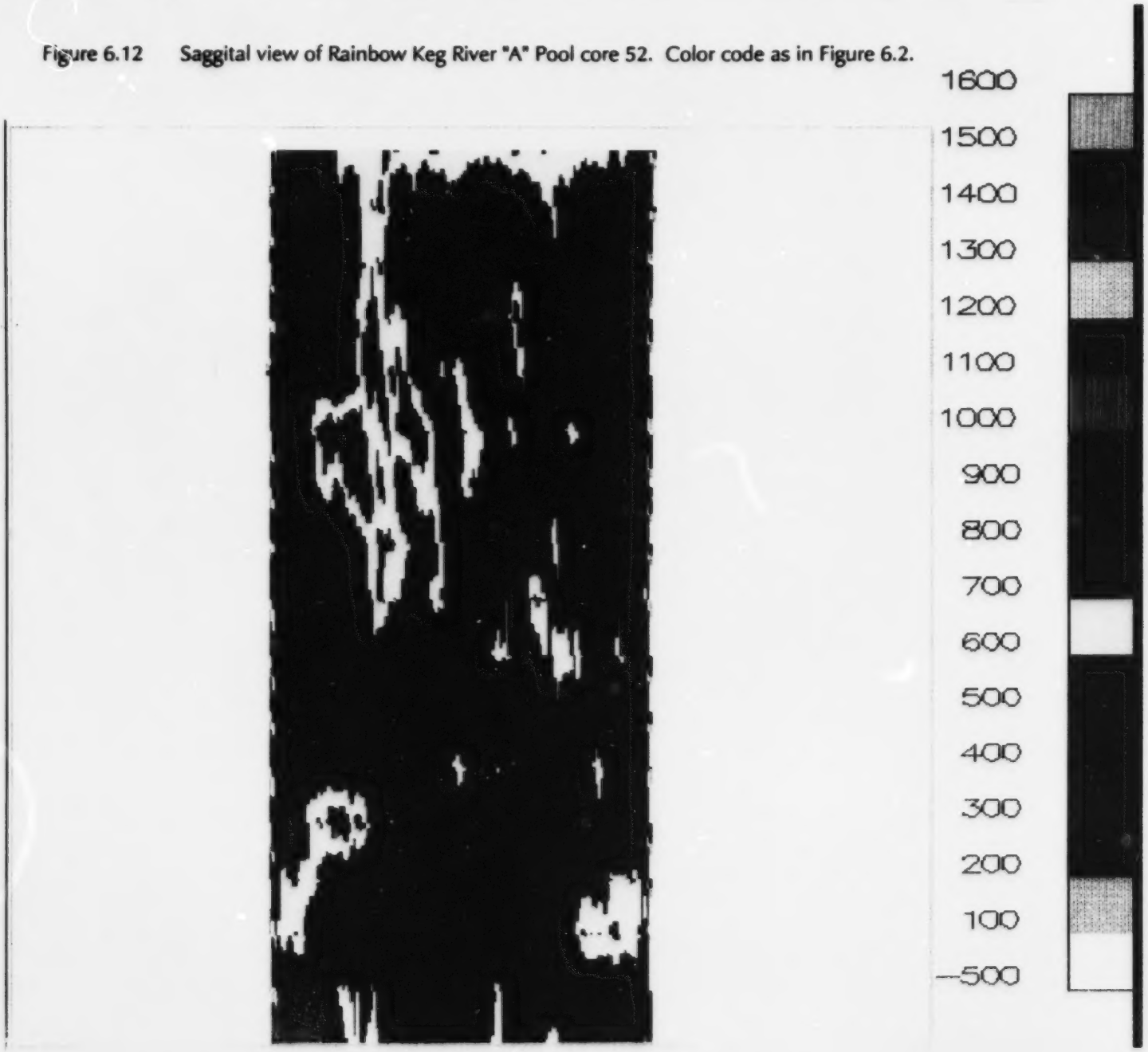

Figure 6.13 Saggital view of Rainbow Keg River "A" Pool core 56. Color code as in Figure 6.2.

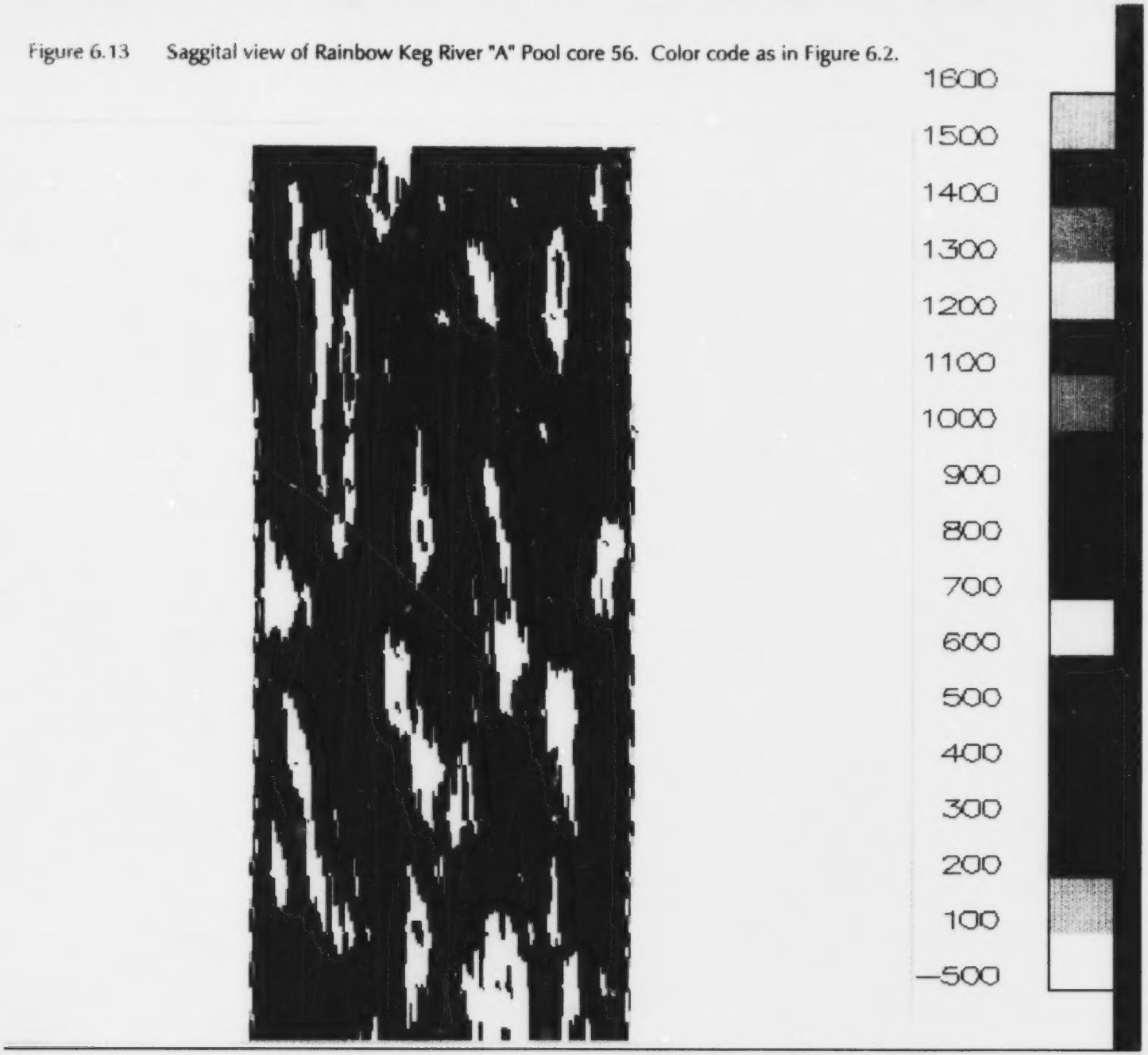

Figure 6.14 Core from Rainbow Keg River "G" Pool. Directional vugs. Evidence of mud invasion. Color code as in Figure 6.2.

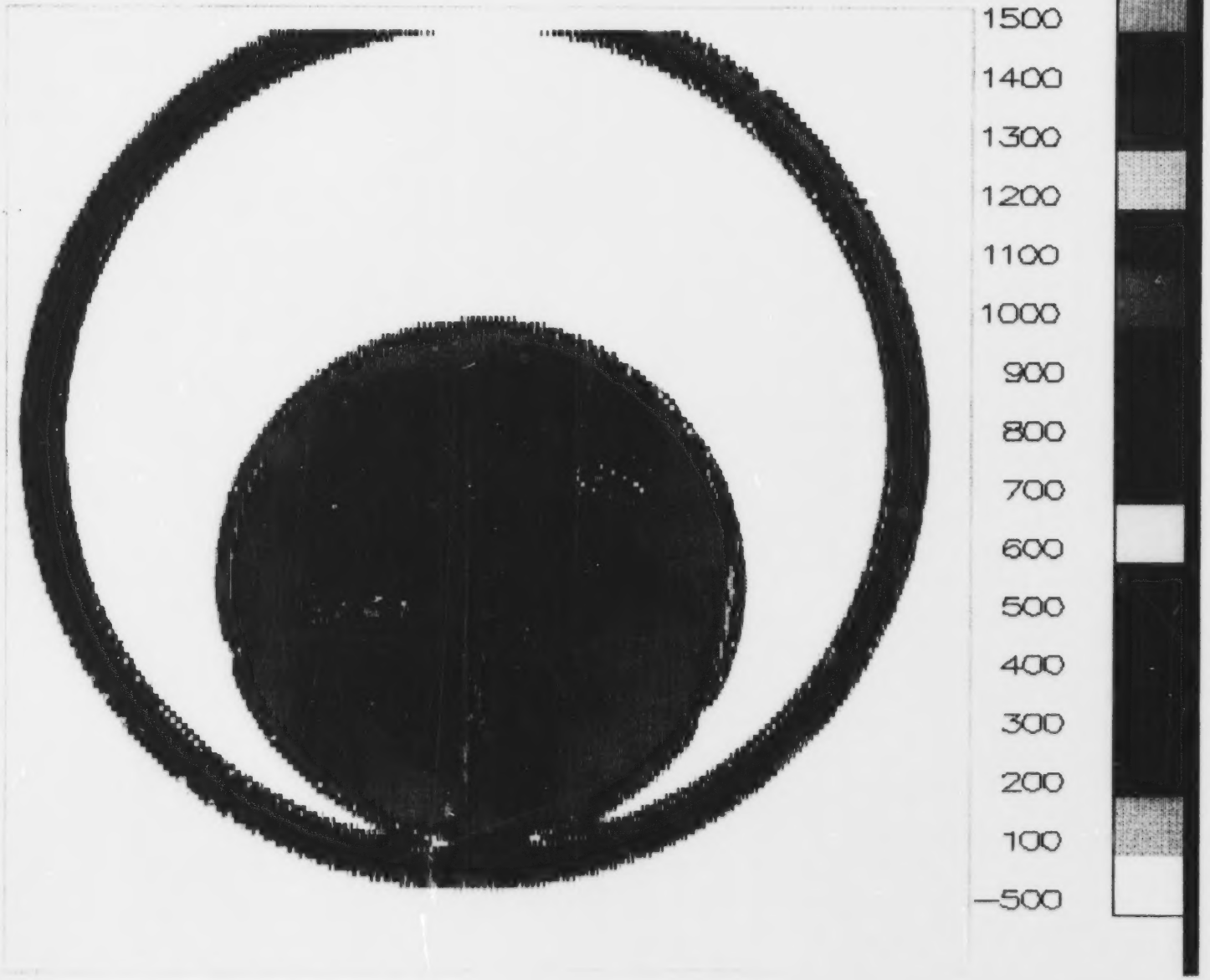

Figure 6.15 Rainbow Keg River "G" Pool core. Evidence of mud invasion. Color code as in Figure 6.2.

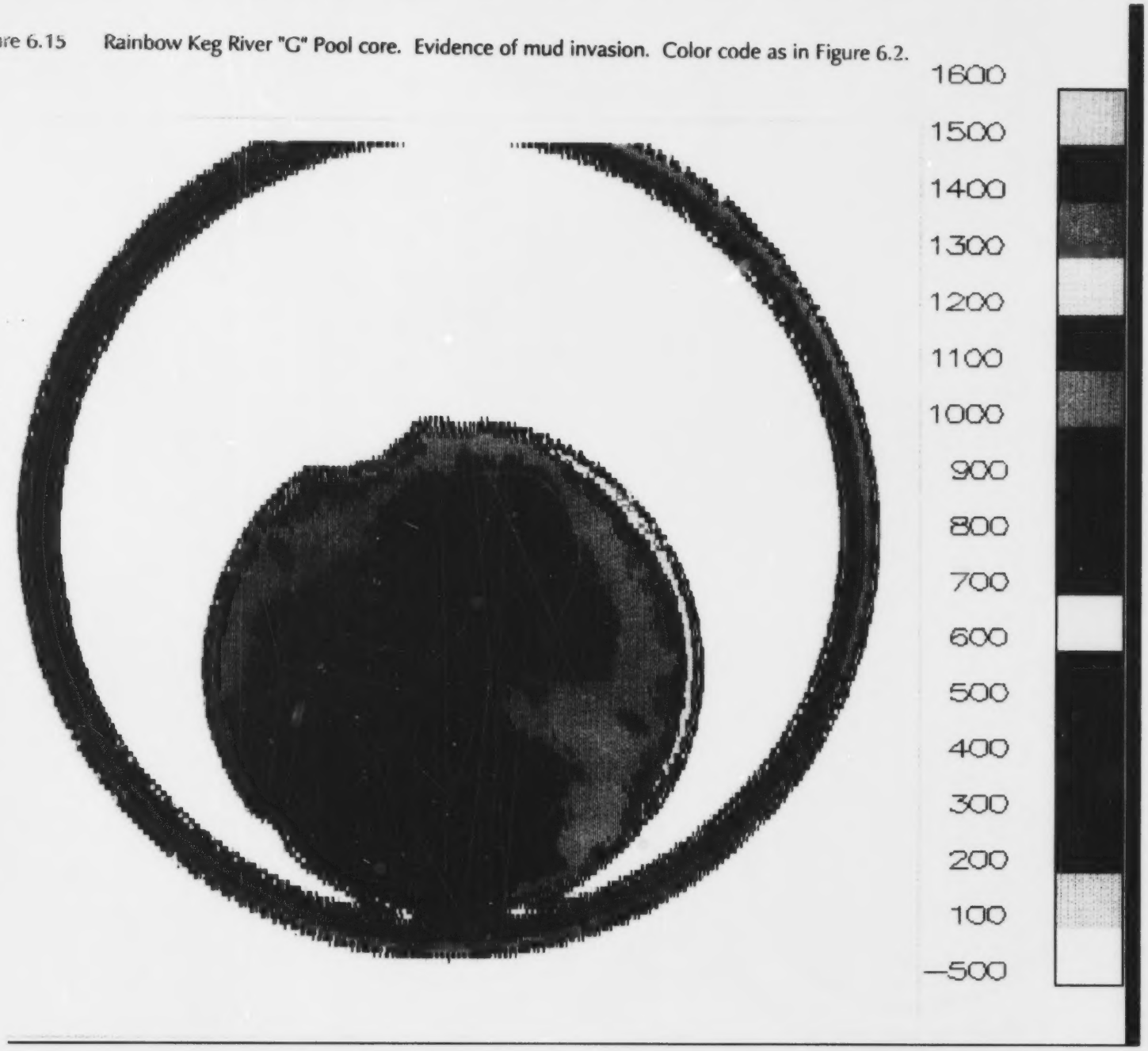

Figure 6.16 Image of vuggy core in Rainbow Keg River "C" Pool. Color code as in Figure 6.2.

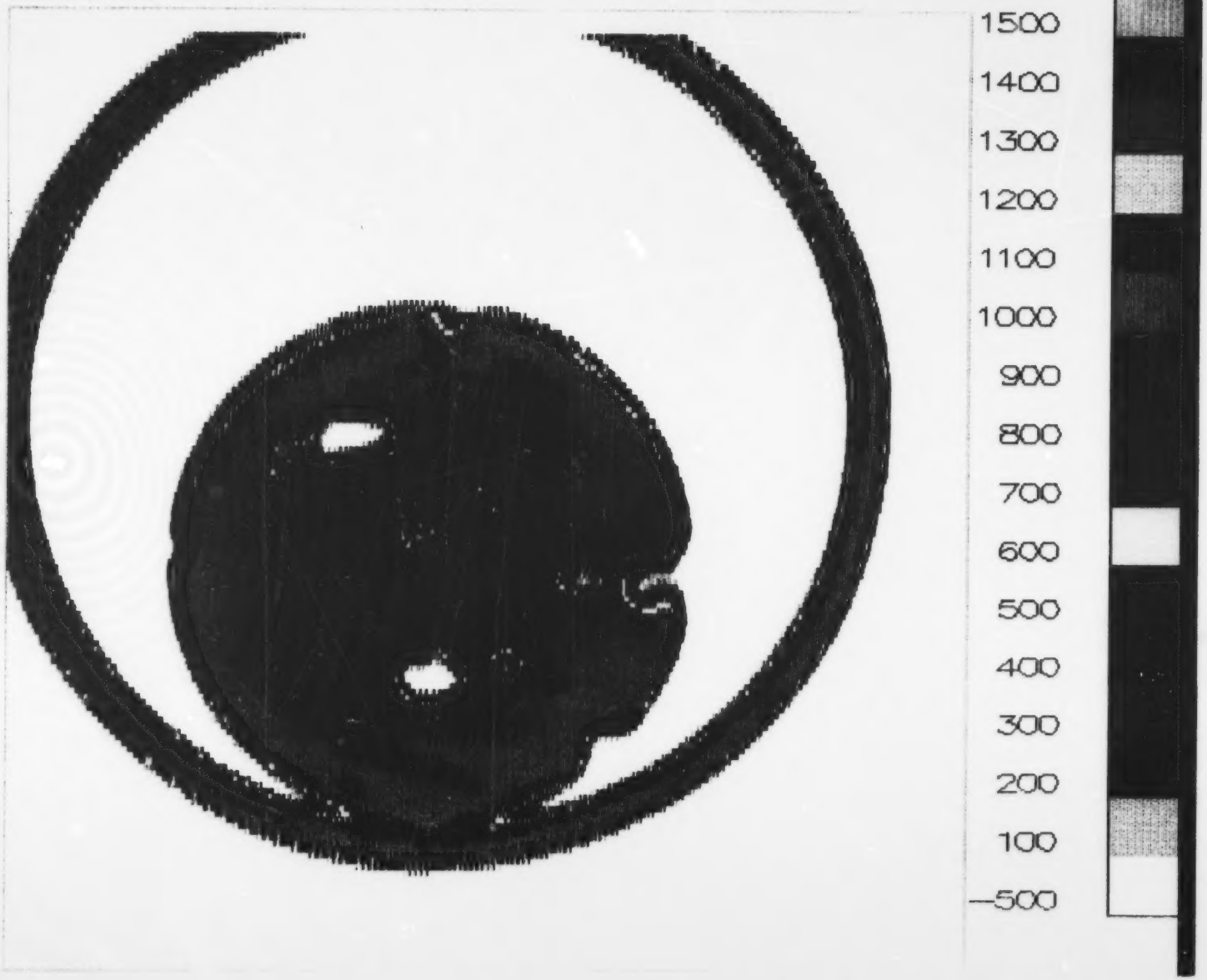

Figure 6.17 Core from Rainbow Keg River "C" Pool. Presence of fracture. Evidence of mud invasion. Color code as in Figure 6.2.

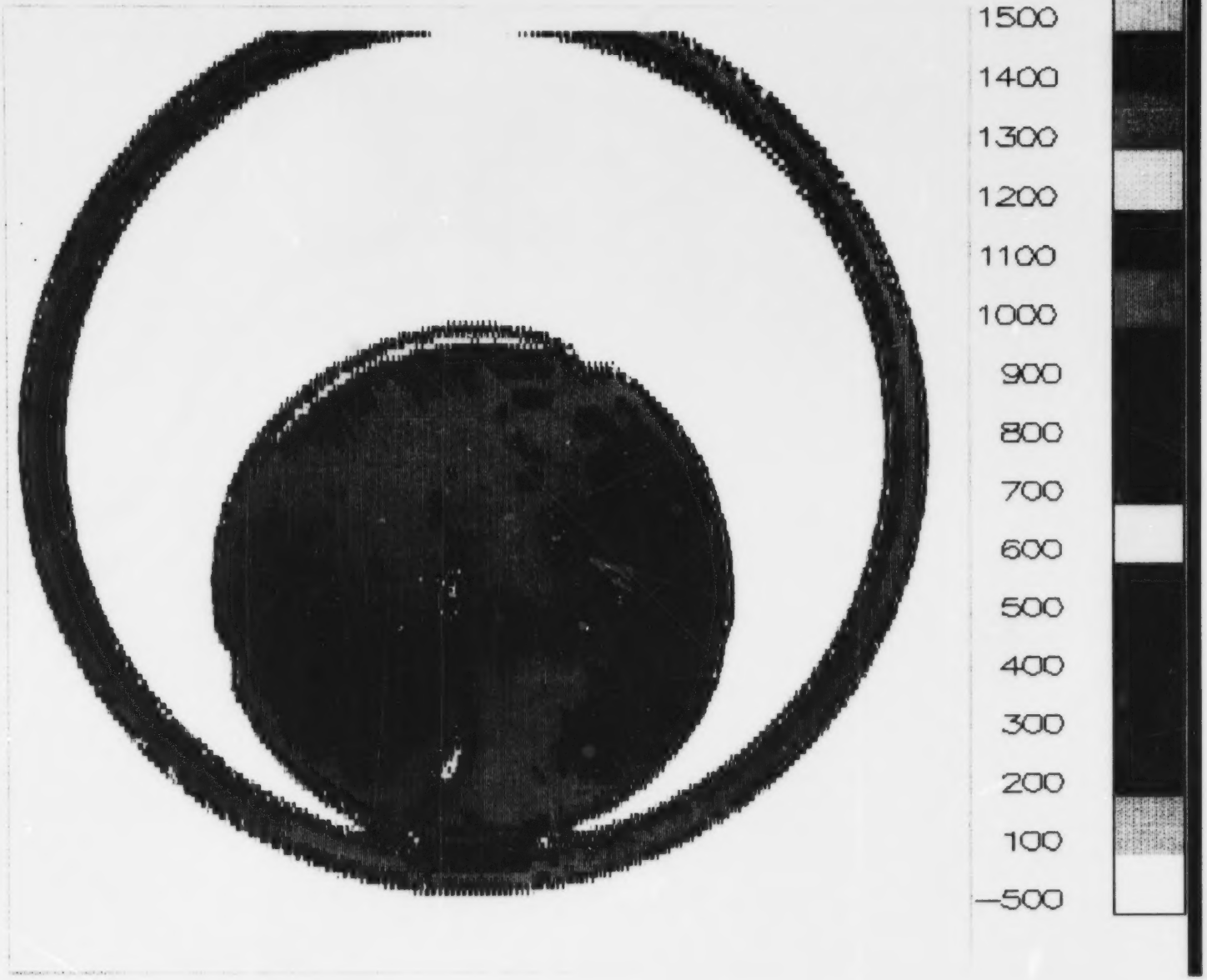

Figure 6.18 Core from Rainbow Keg River "G" Pool. Layered structure (stromatoporoids). Color code as in Figure 6.2.

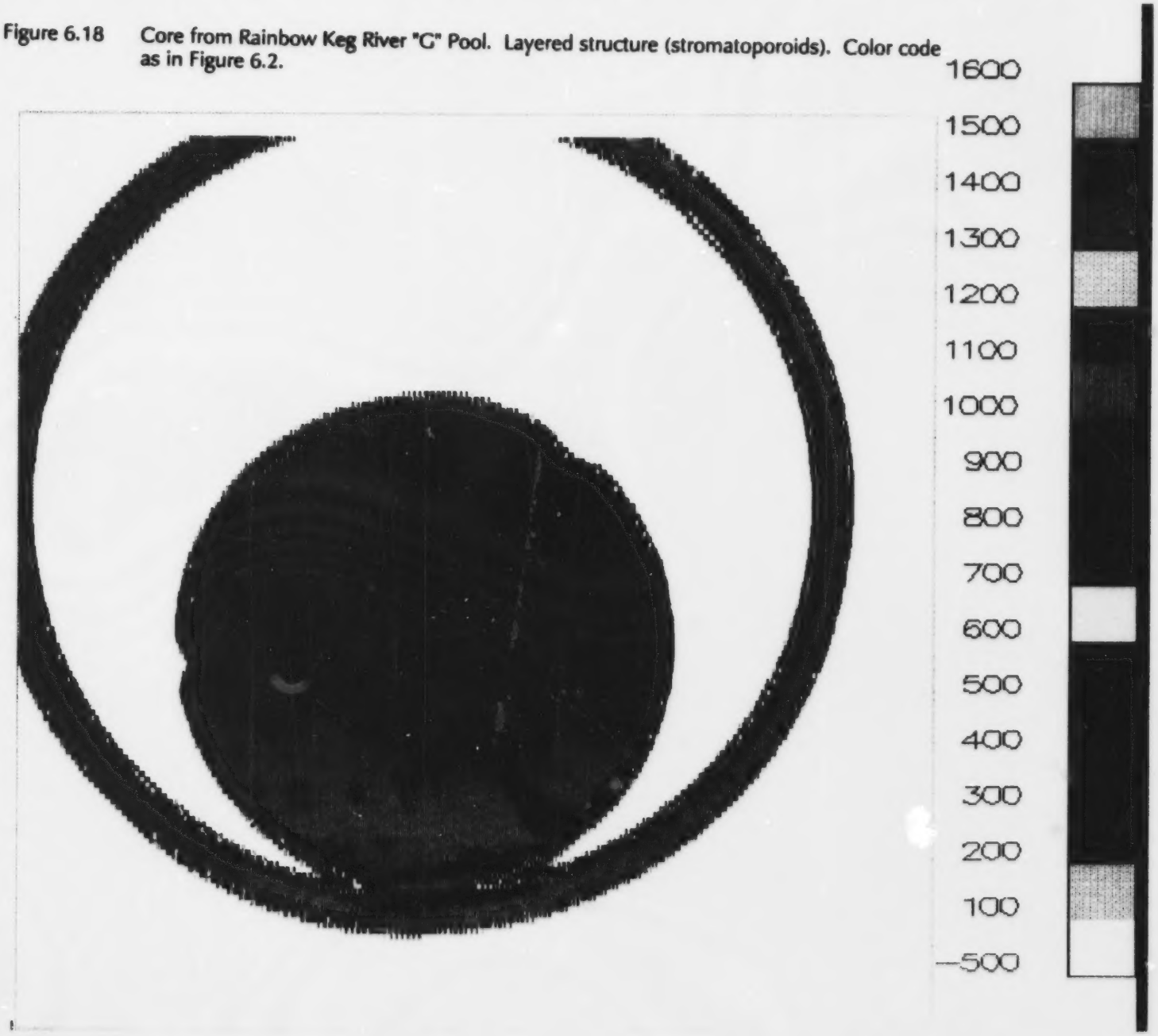

Figure 6.19 More stromatoporoids from Rainbow Keg River "G" Pool. Color code as in Figure 6.2.

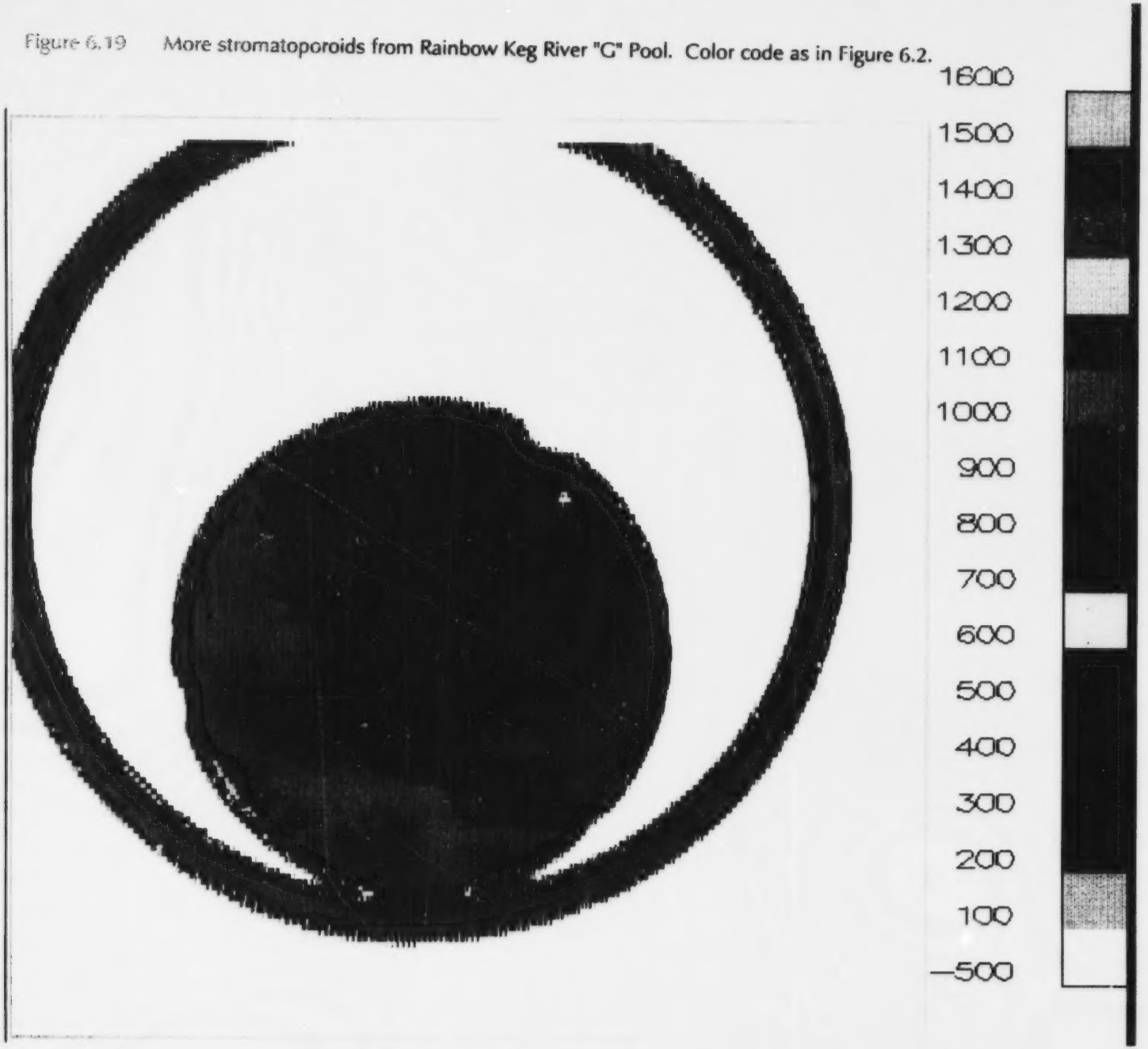

Figure 6.20 Continuation of stromatoporoids from Rainbow Keg River "G" Pool. Color code as in Figure 6.2.

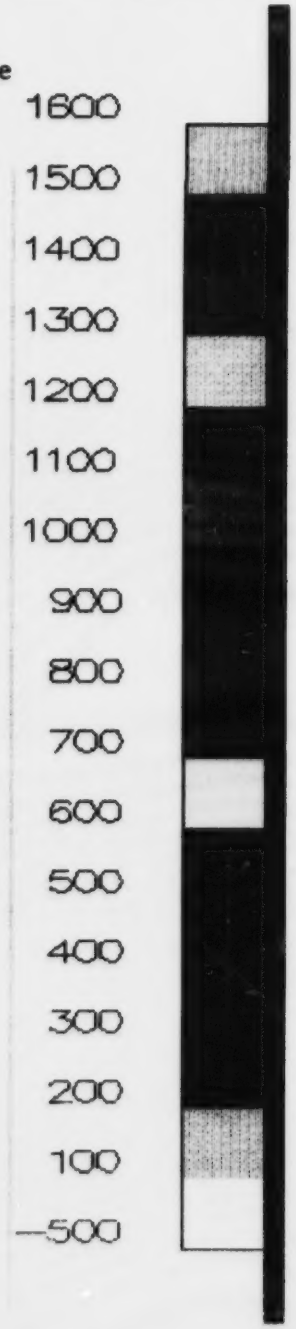

Figure 6.21 Mud invaded piece of Rainbow Keg River "G" Pool core. Color code as in Figure 6.2.

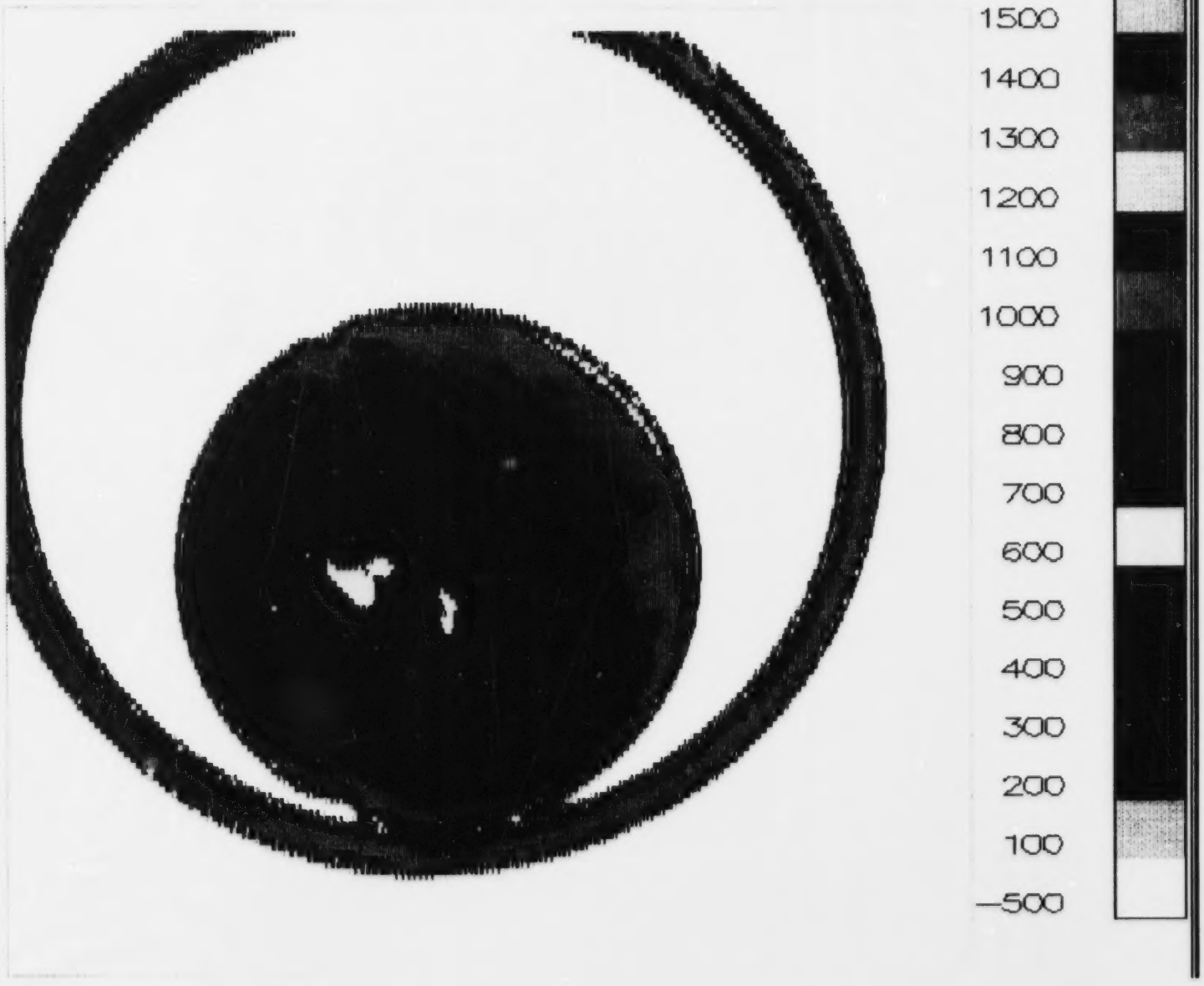

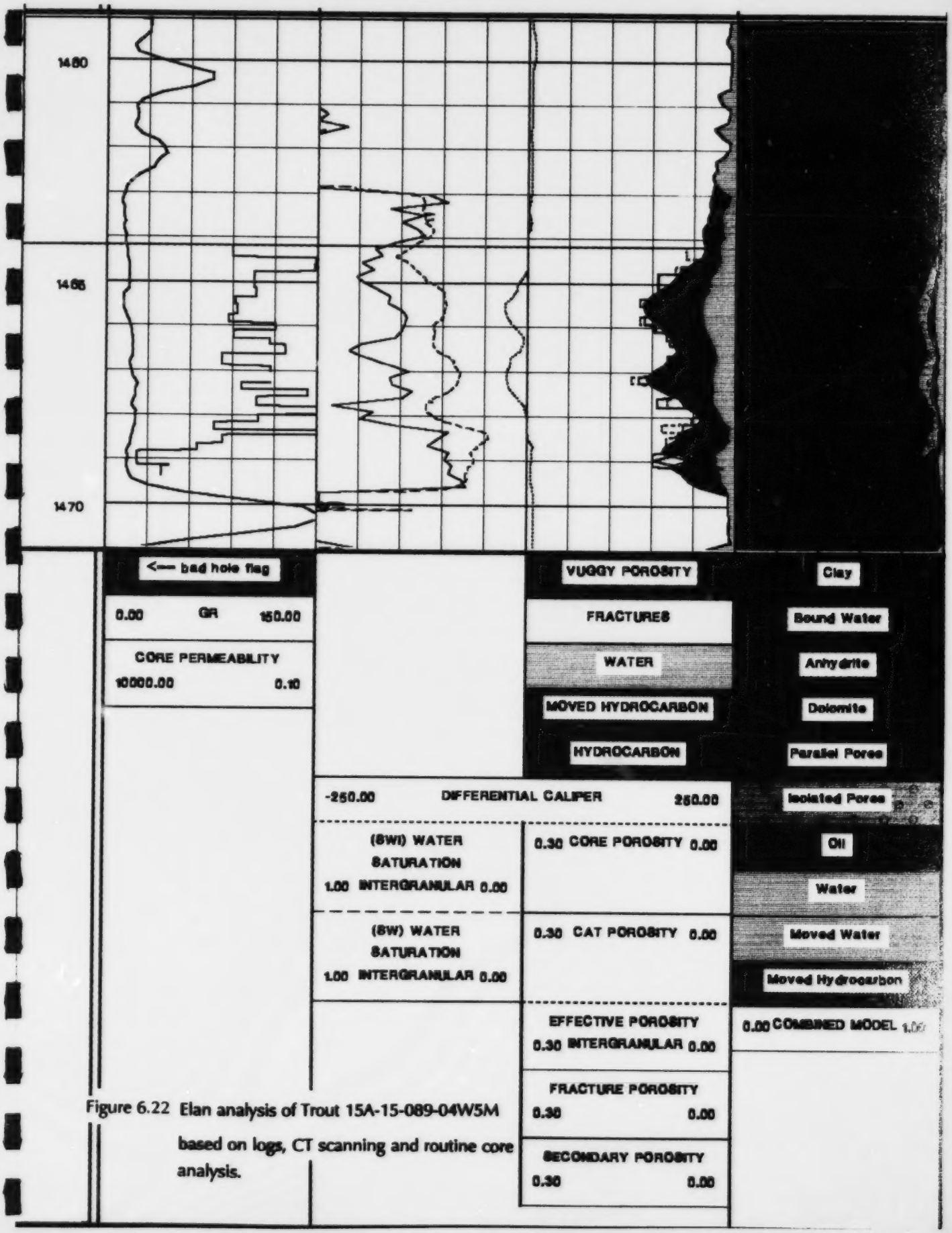

Figure 6.22 Elan analysis of Trout 15A-15-089-04W5M based on logs, CT scanning and routine core analysis.

Figure 6.23 CATscan of intergranular core piece with some pinpoint vugs (bulk density map). Color code in intervals of.2 g/cm^3 - core piece 2.

Figure 6.24 CATscan of core piece with leached fossils (bulk density map, piece 6b; color codes as for Figure 6.23).

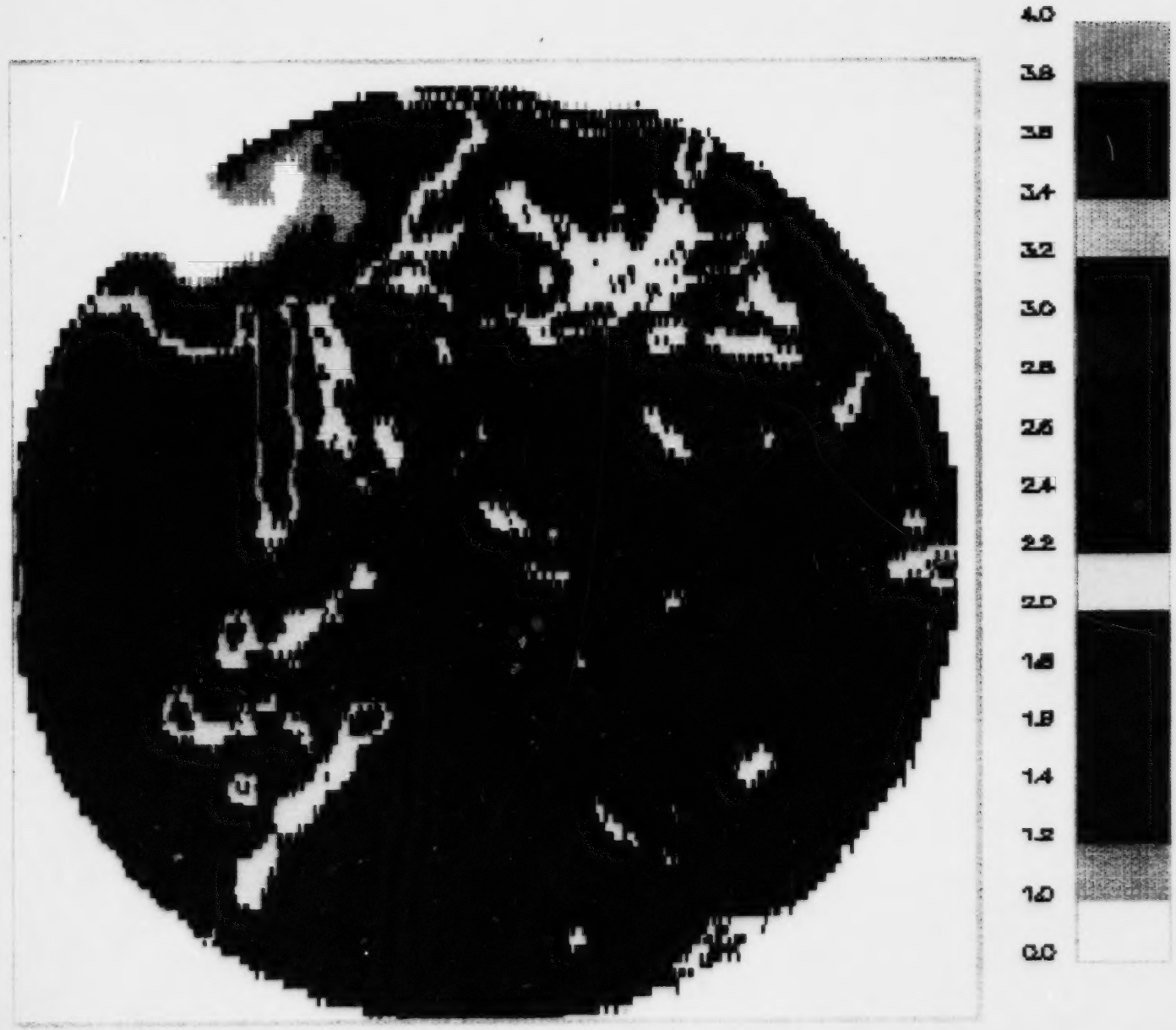

Figure 6.25 CATscan of core piece with fractures (bulk density map, piece 5p; color codes as for Figure 6.23).

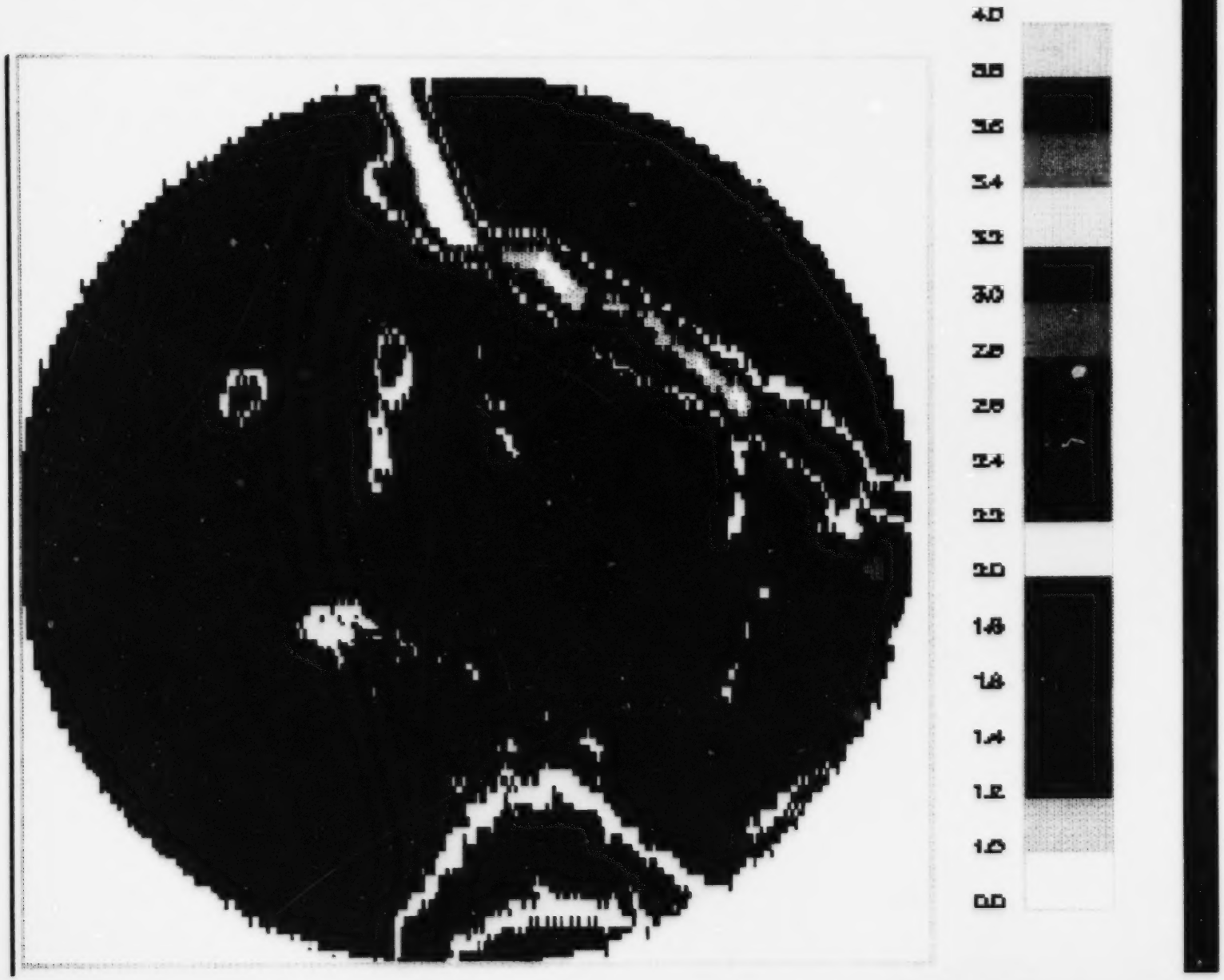

Figure 6.26 CATscan of core piece with leached vugs and anhydrite (bulk density map, piece 5p; color codes as for Figure 6.23).

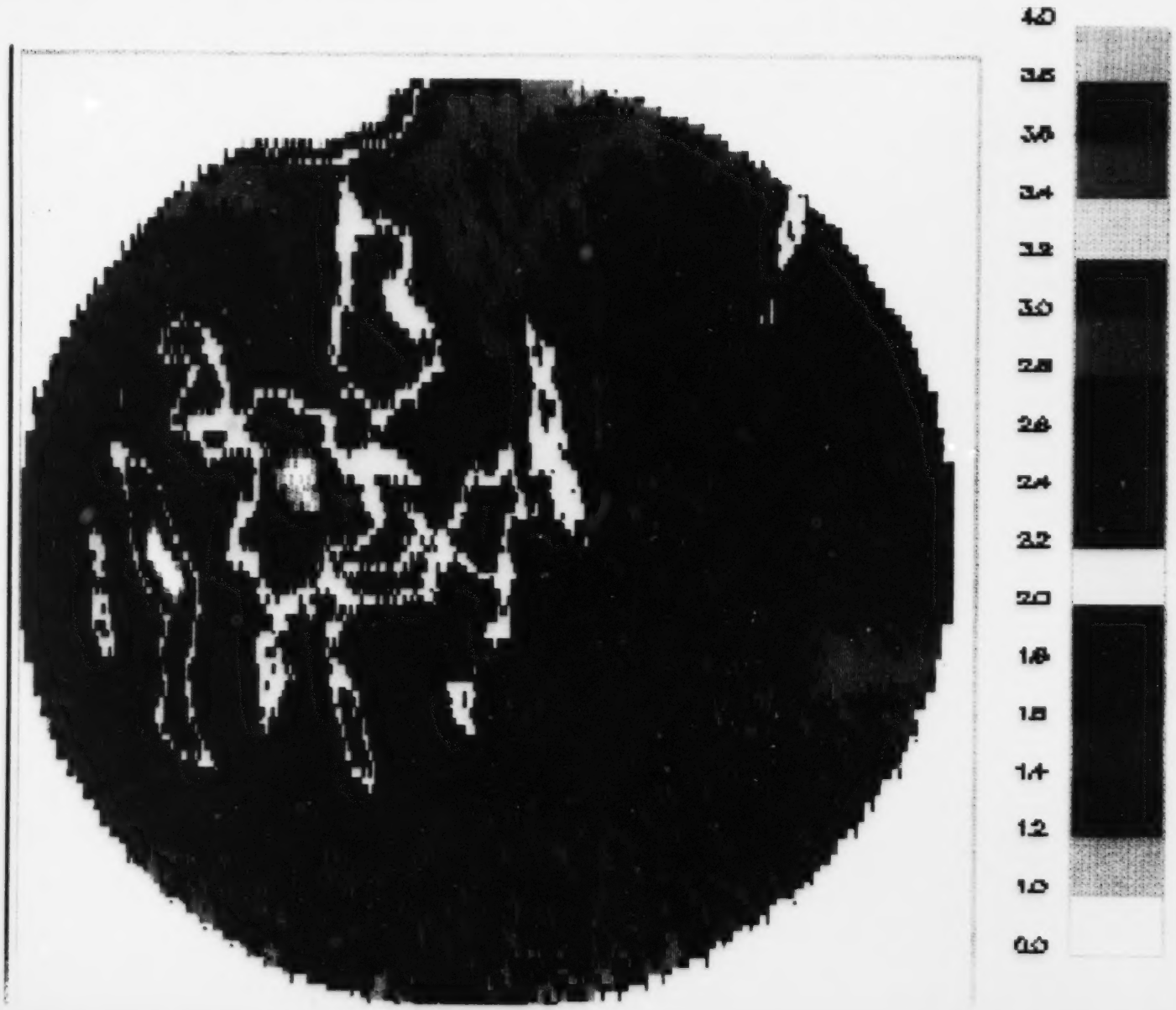

Figure 6.27 CATscan of core piece with leached vugs and anhydrite (CT number map color code 100 CT numbers per color change, piece 7p)

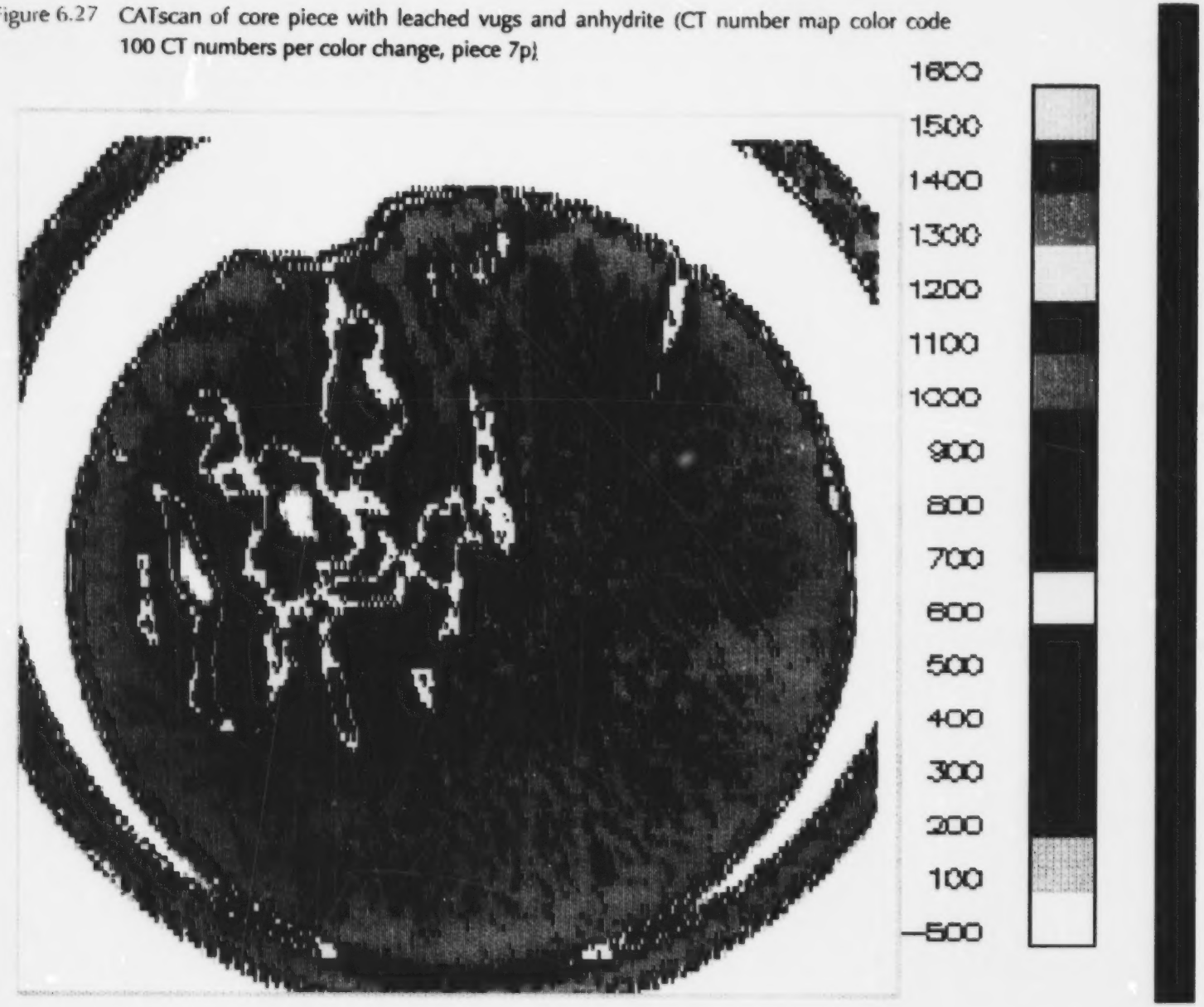

Figure 6.28 CATscan of core piece with leached vugs and anhydrite (effective atomic number map colorcode 1.0 effective atomic number unit, piece 7p).

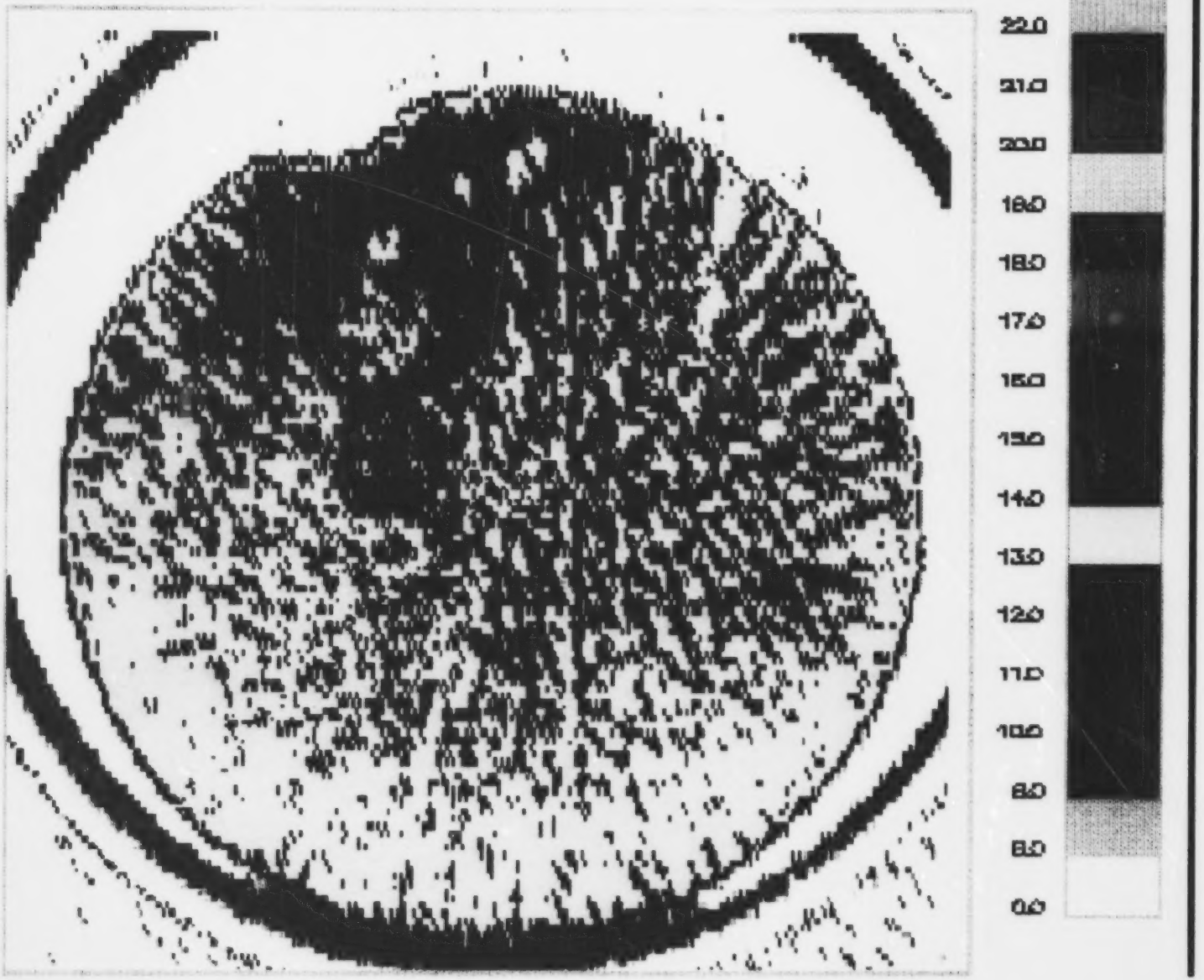

Figure 6.29 Bulk density map of slice with small vuggs (piece 9bp; color codes as for Figure 6.23).

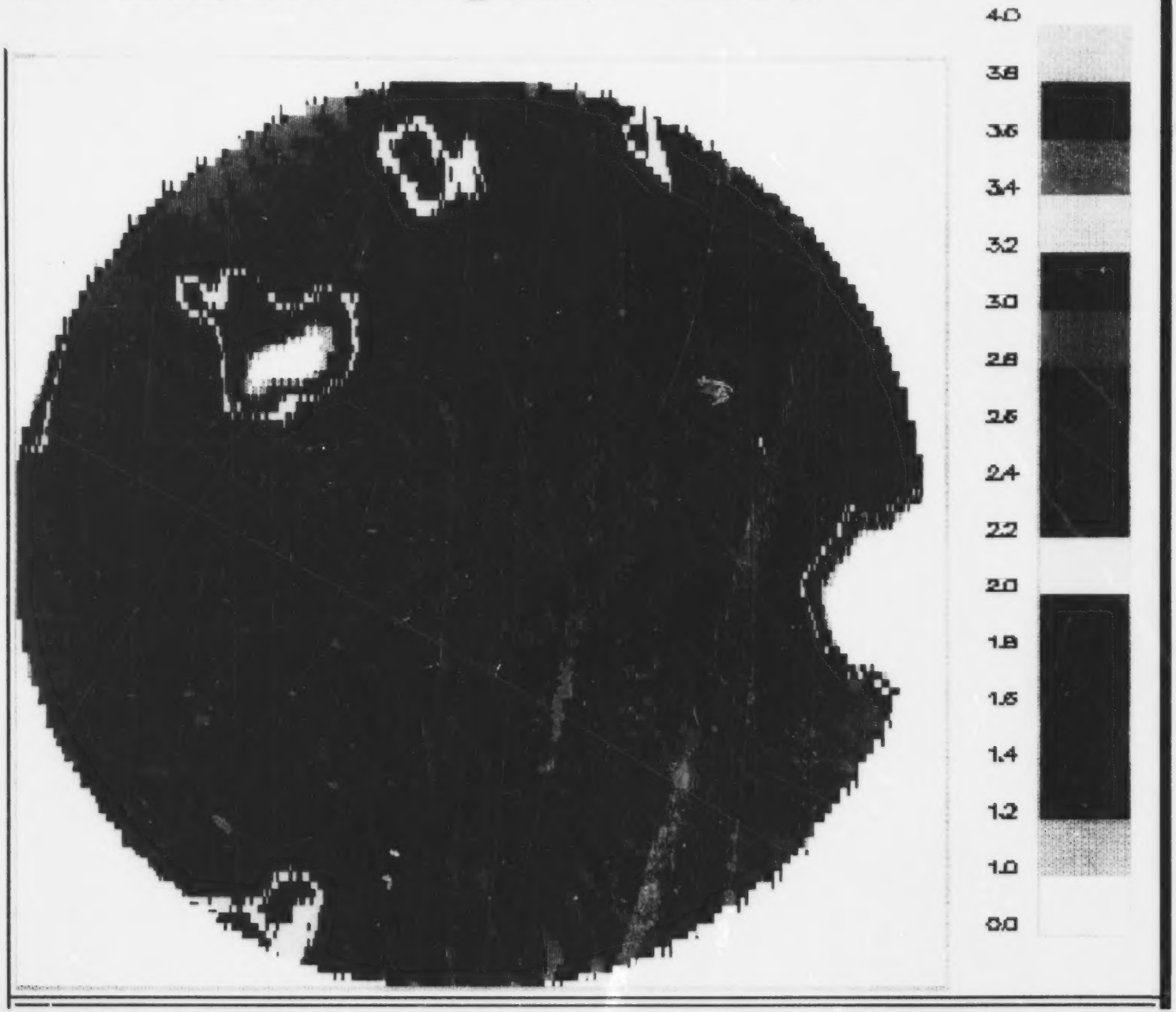

Figure 6.30 **Bulk density map of slice with small leached fossils (piece 4b; color codes as for Figure 6.23).**

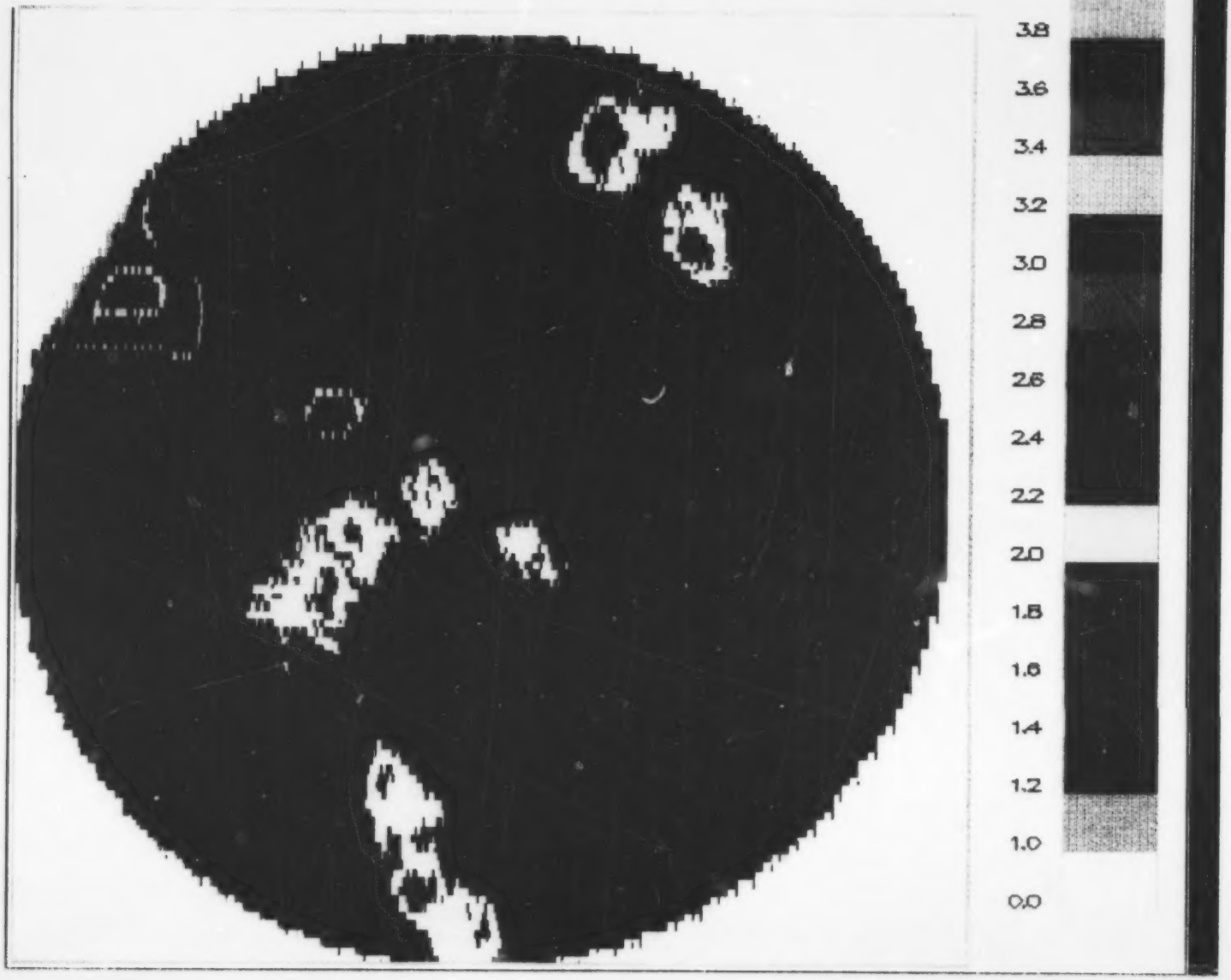

Figure 6.31 Bulk density map showing anhydrite presence in vugs (piece 8p; color codes as for Figure 6.23).

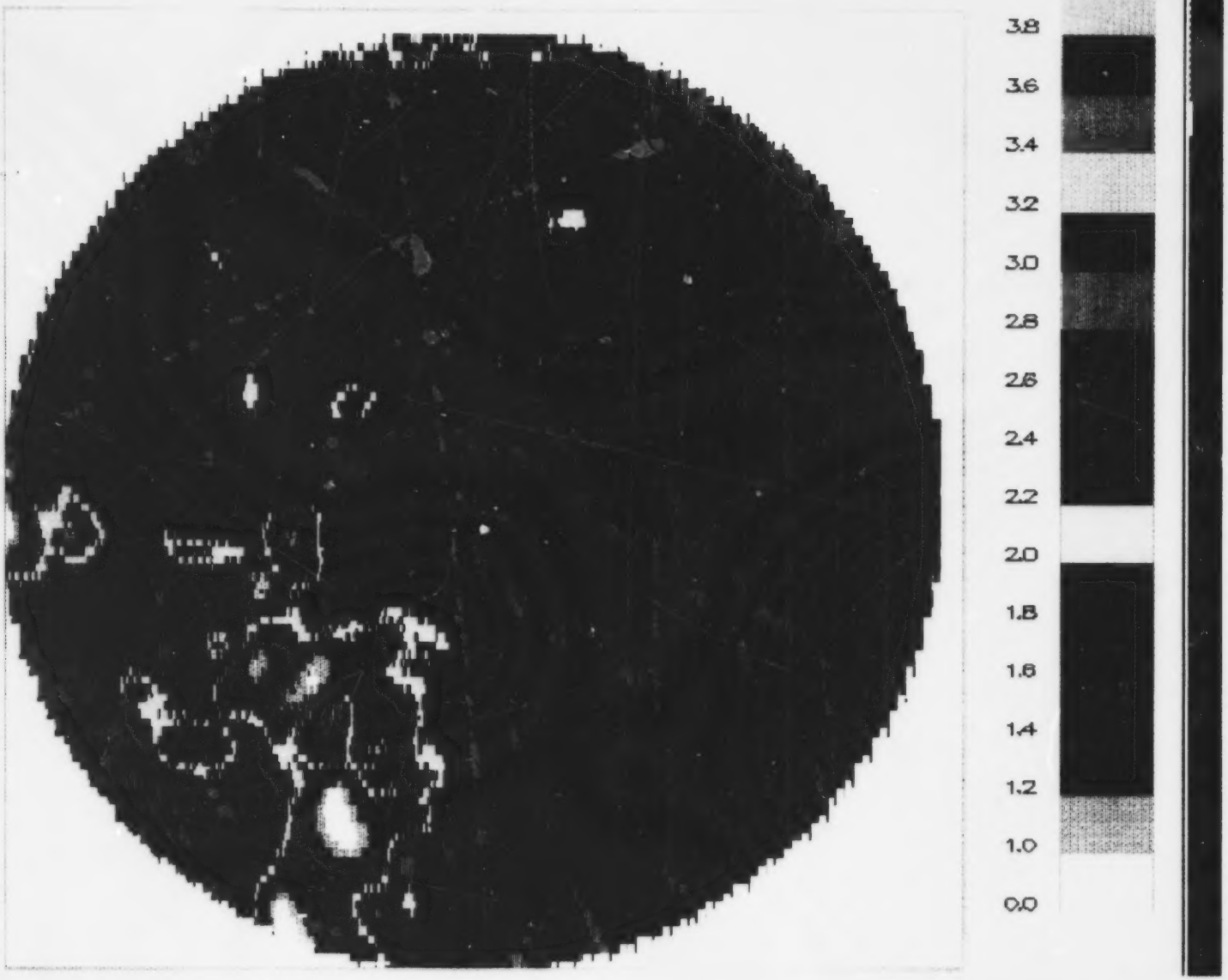

Figure 6.32 **Bulk density map showing leached fossils example (piece 3p; color codes as for Figure 6.23).**

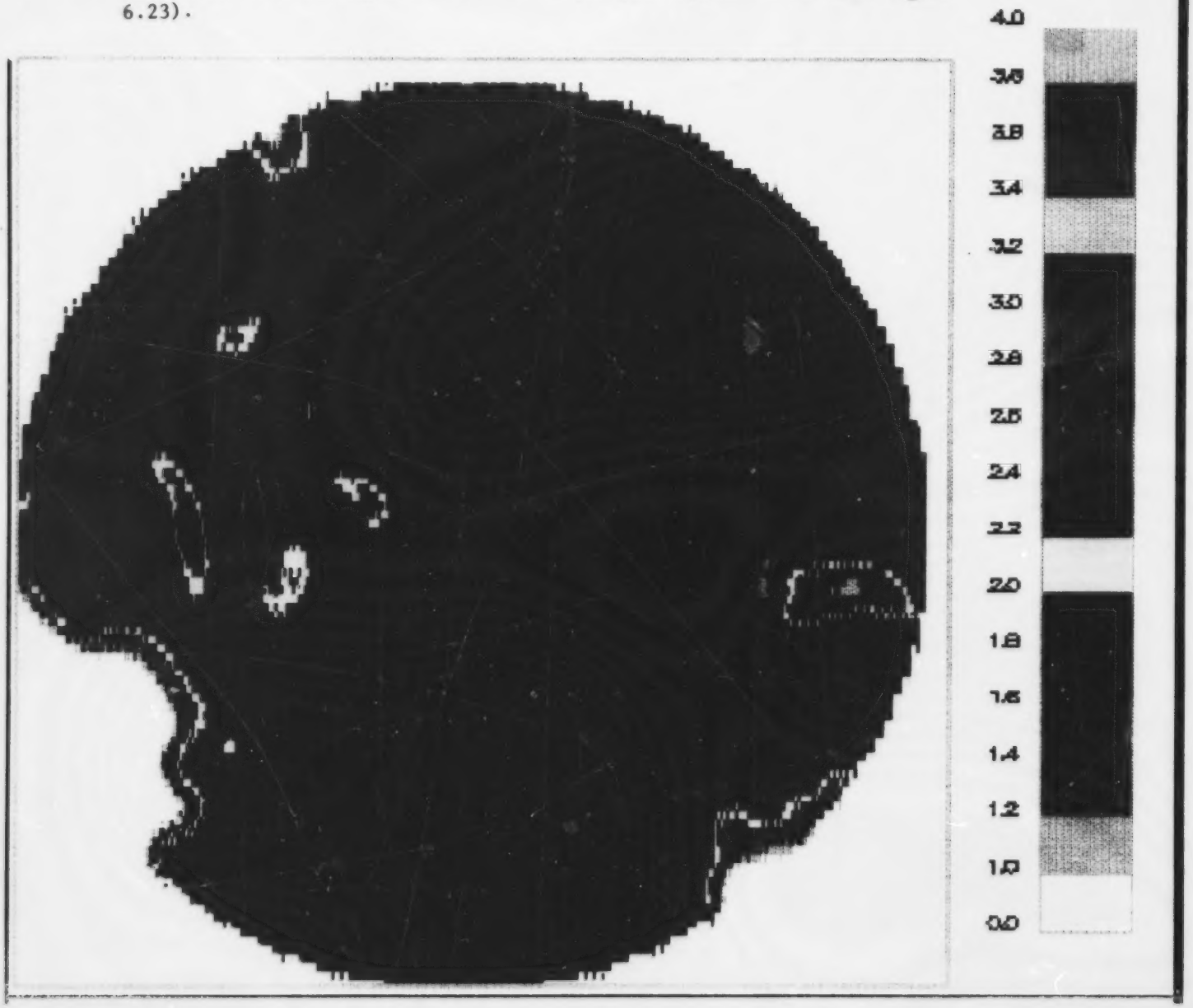

Figure 6.33 Bulk density map of slice with small and medium vugs (piece 16; color codes as for Figure 6.23).

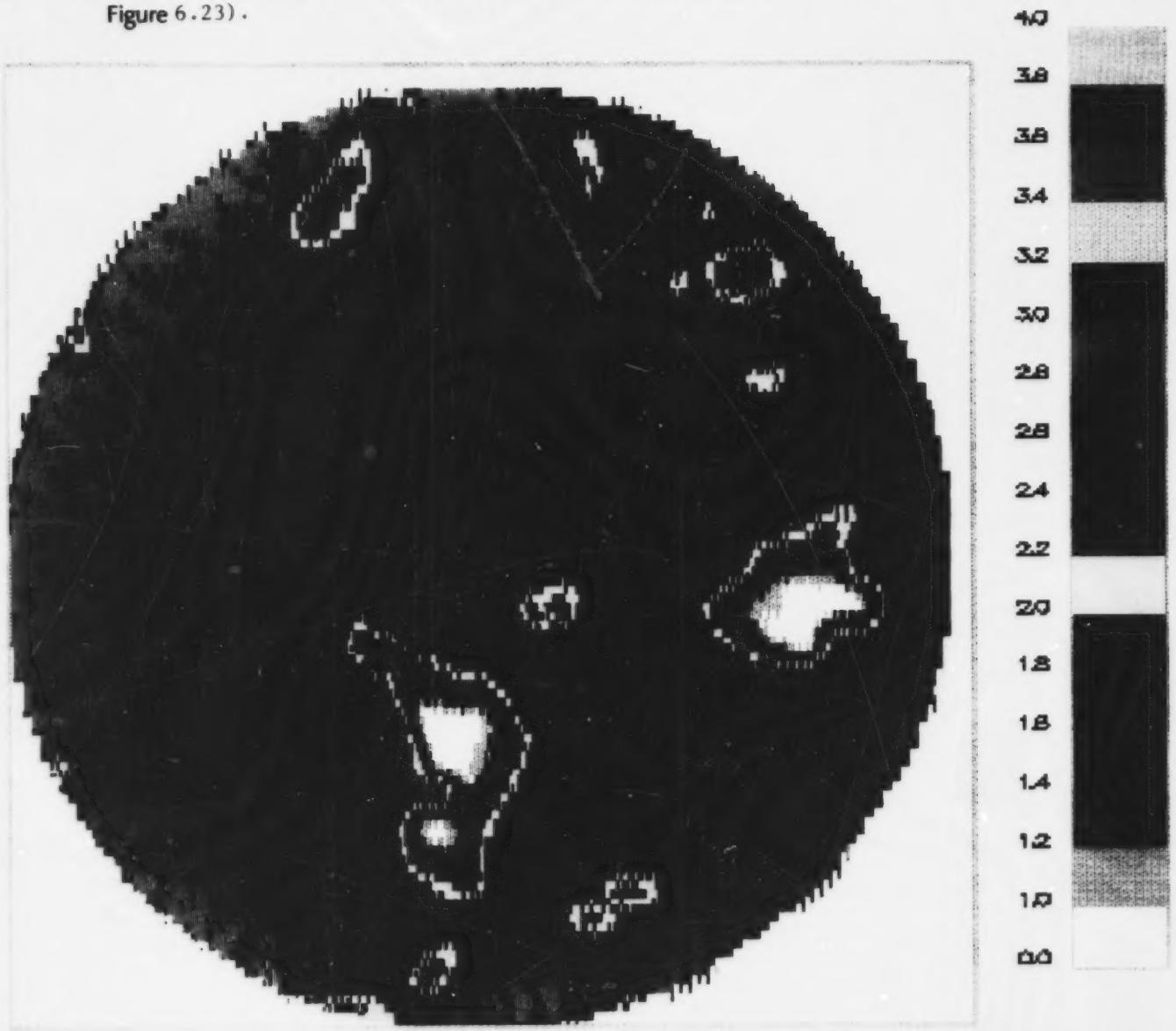

Figure 6.34 Bulk density map of slice with large vugs (piece 3b; color codes as for Figure 6.23).

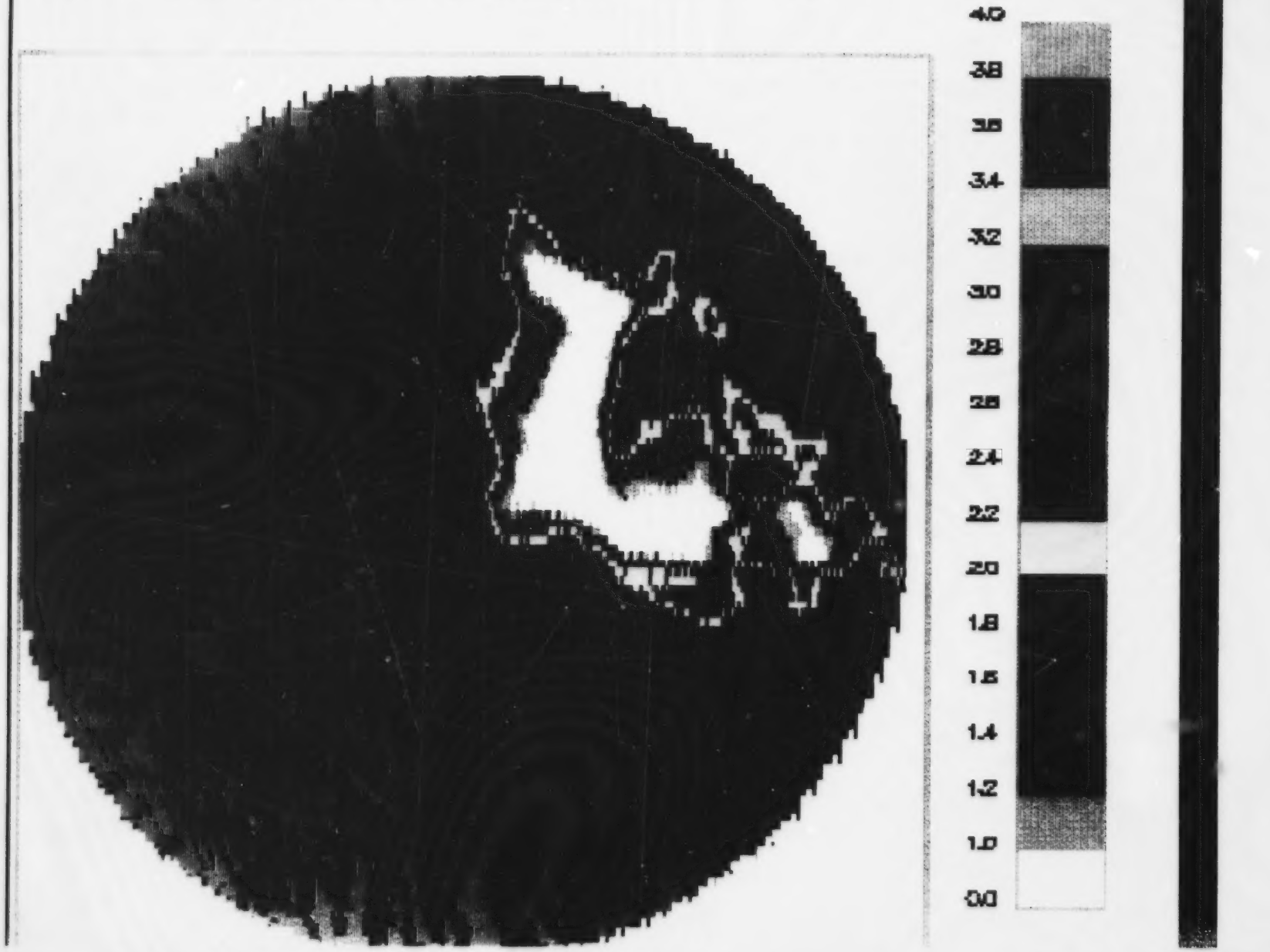

Figure 6.35 Bulk density map of slice with intercrystalline porosity and small vugs (piece 1p; color codes as for Figure 6.23).

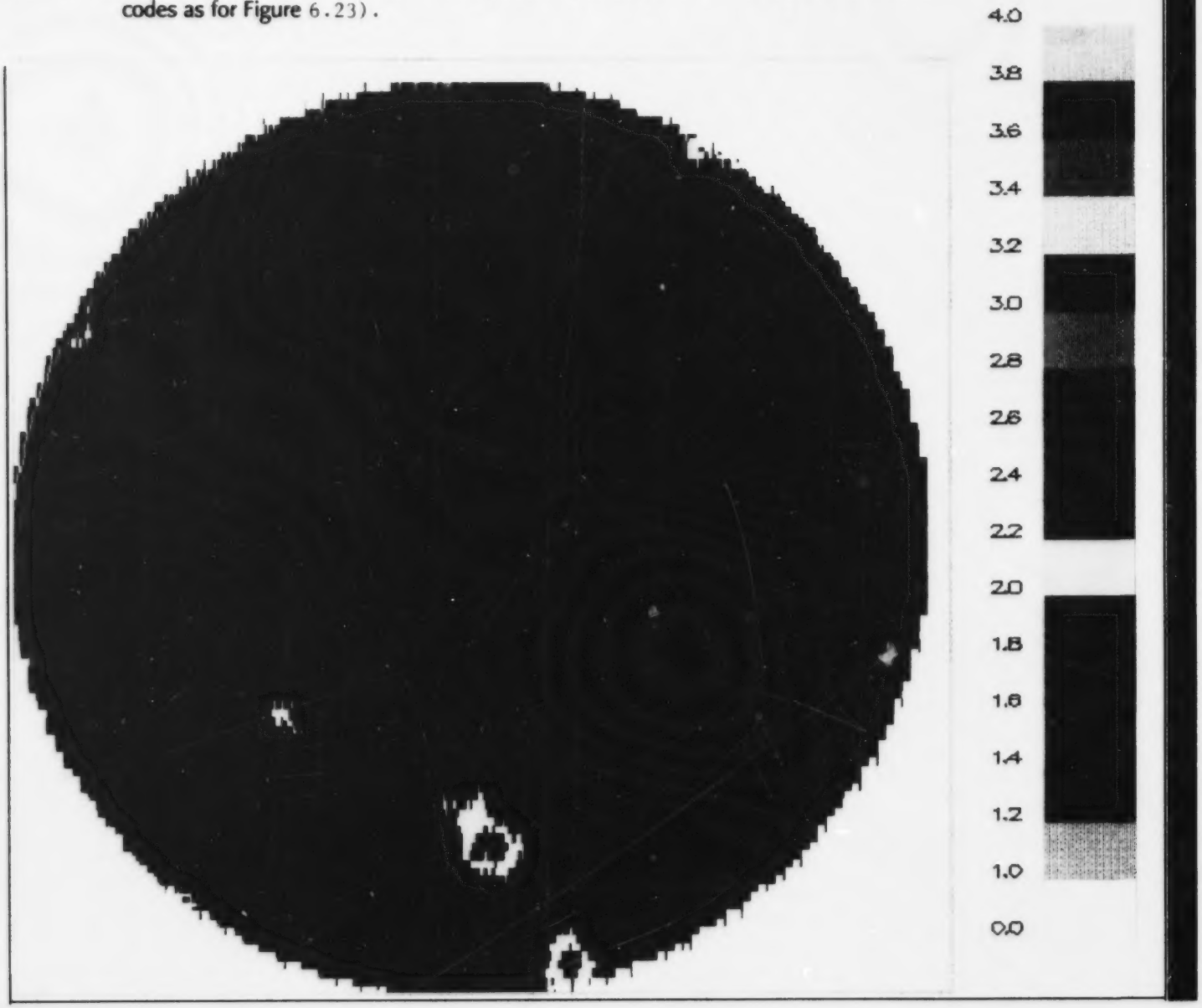

Figure 6.36 Bulk density map of slice with intercrystalline porosity (piece 3t). Effect of hardening artifact, which is shown as a black annulus. Care is being taken to avoid such effects by careful calibration of photomultiplex tubes (scale as for Figure 6.23).

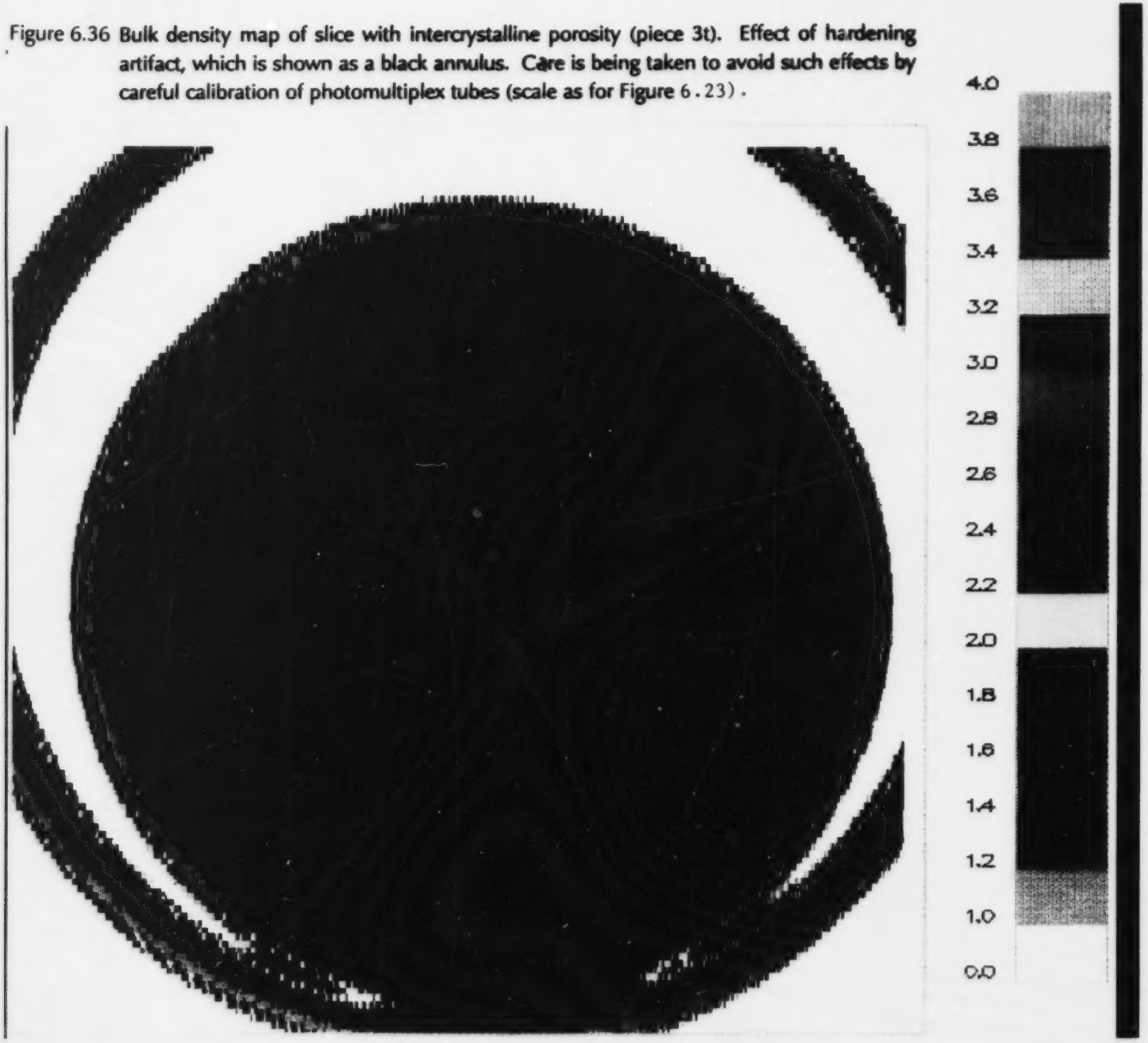

Figure 6.37 **Longitudinal CT number map of a uniform core piece (piece 7).**

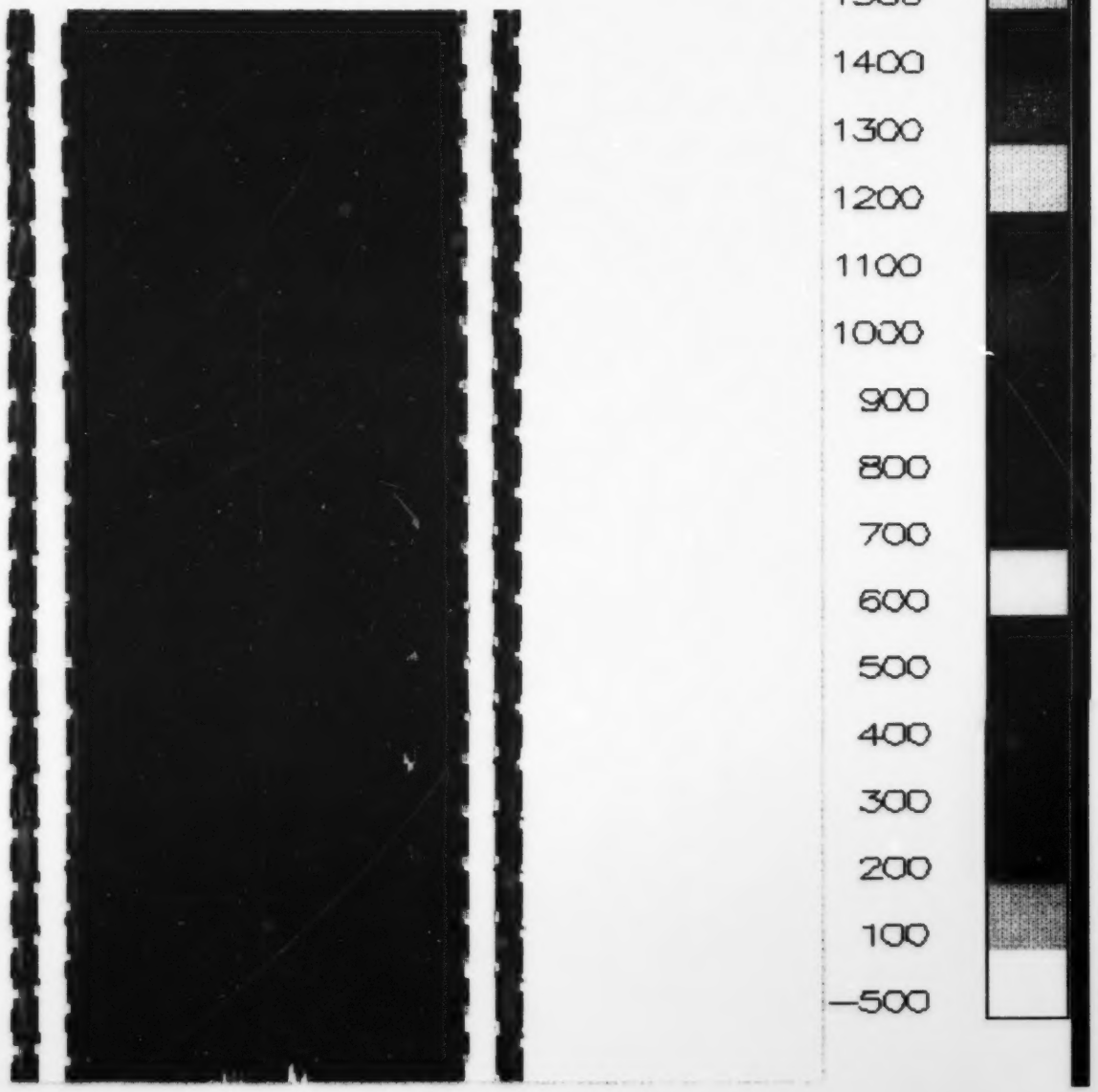

Figure 6.38 Longitudinal CT number map of a vuggy core piece (piece 7p).

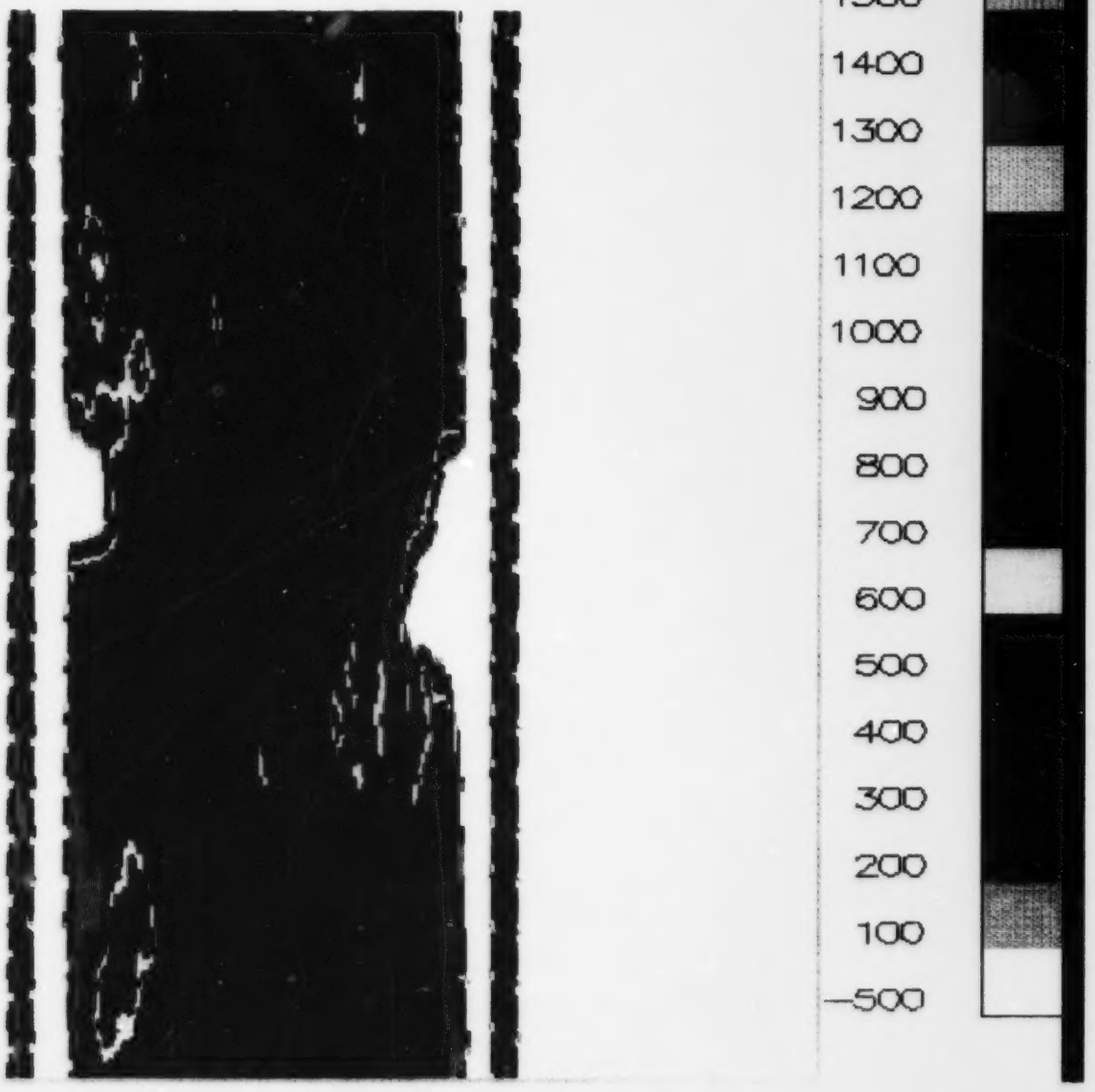

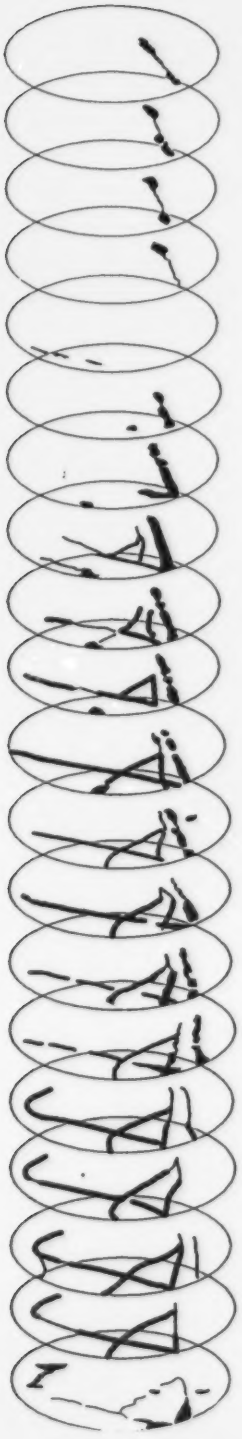

Figure 6.39 Three dimensional fracture map of core #4 from Wabamun formation.

Figure 6.40 Coronal view of Wabamun core #4. Two fractures can be seen. The color code indicates the range of CT numbers (100 CT numbers per color).

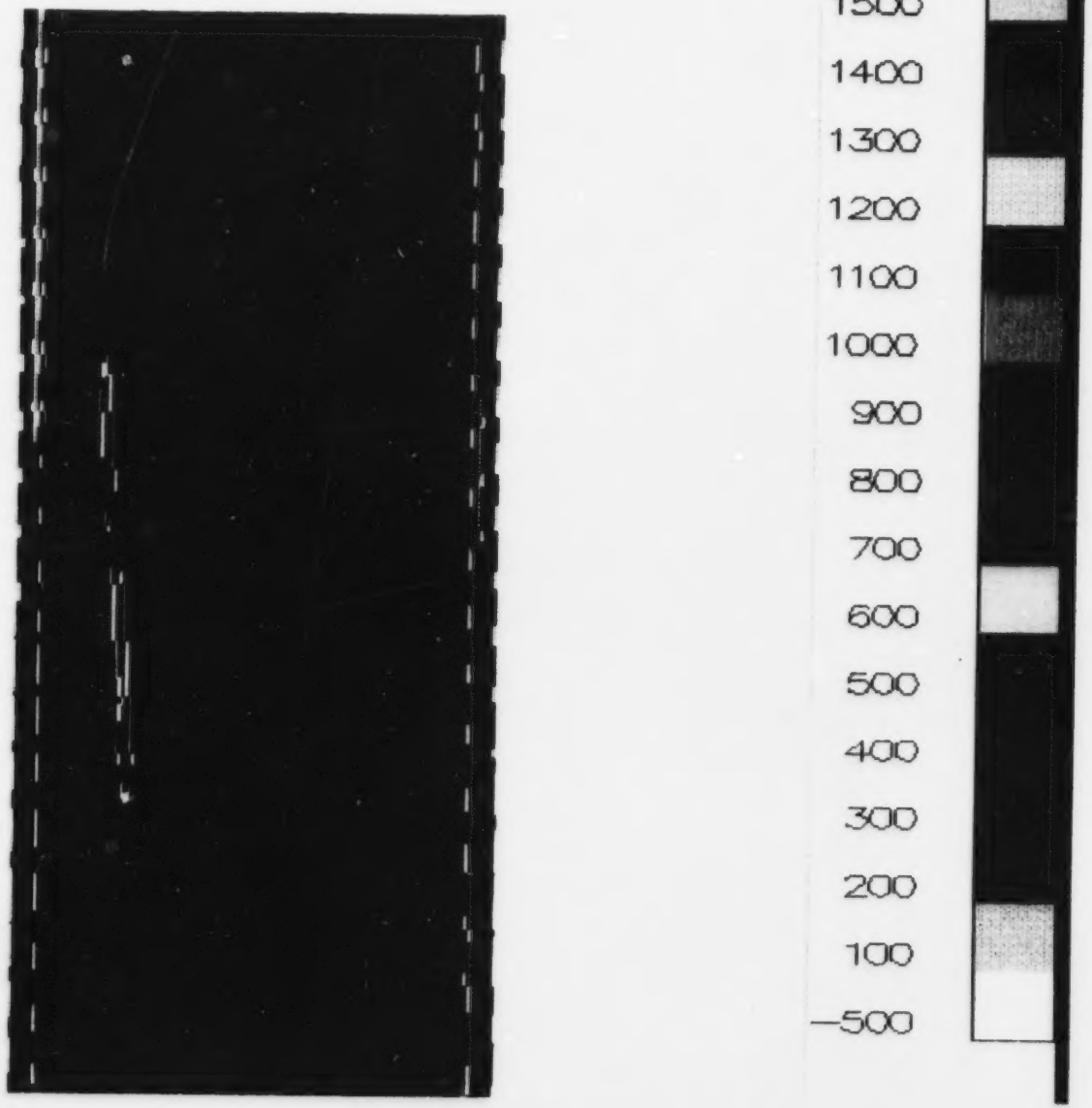

Figure 6.41 Image of fracture core from Wabamun formation. Color code as in Figure 6.40. The core is 2/3 slabbed with a 1/3 Berea cap.

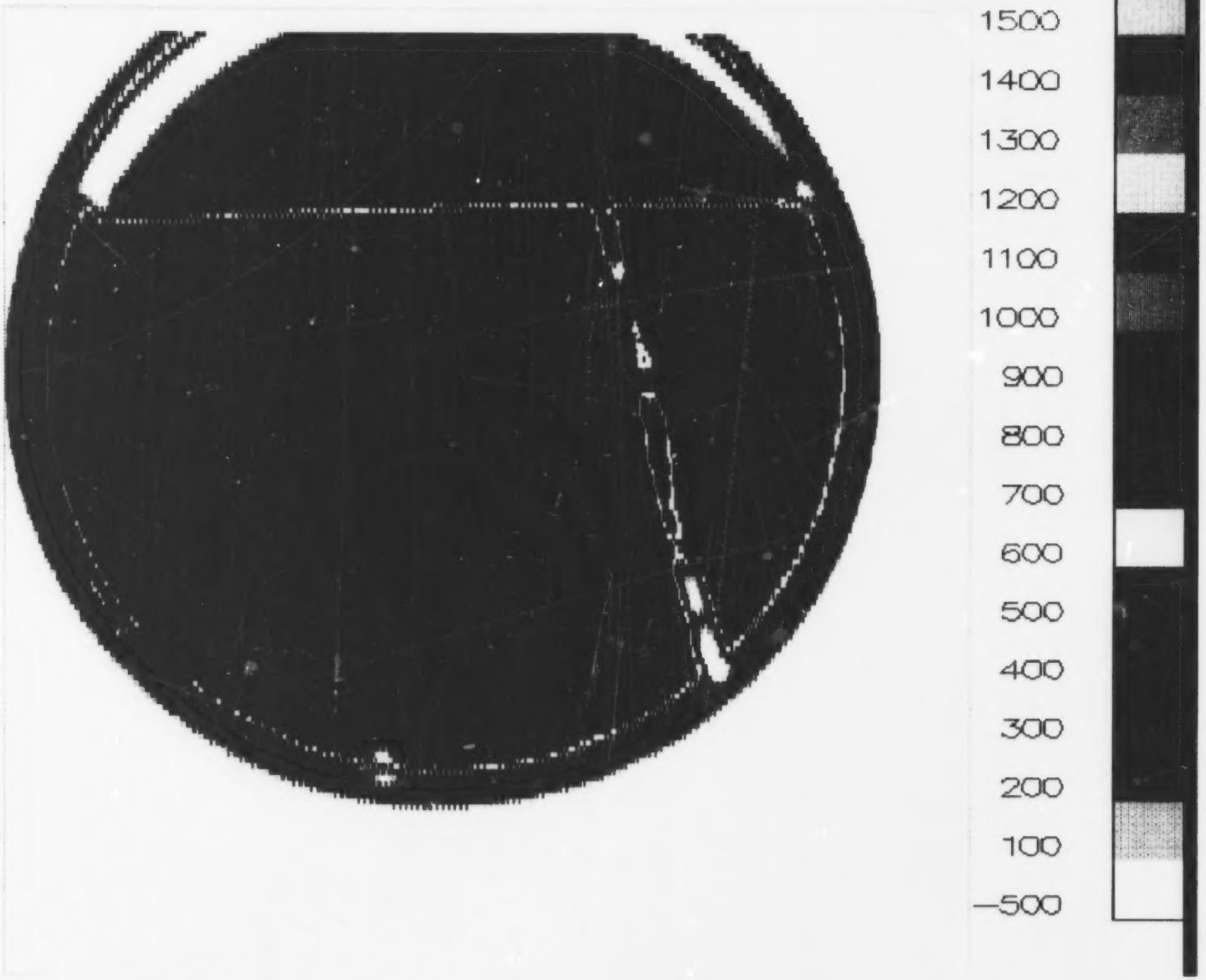

Figure 6.42 Coronal view of Wabamun core #5. The core is much more vuggy than #4. Color code as in Figure 6.40.

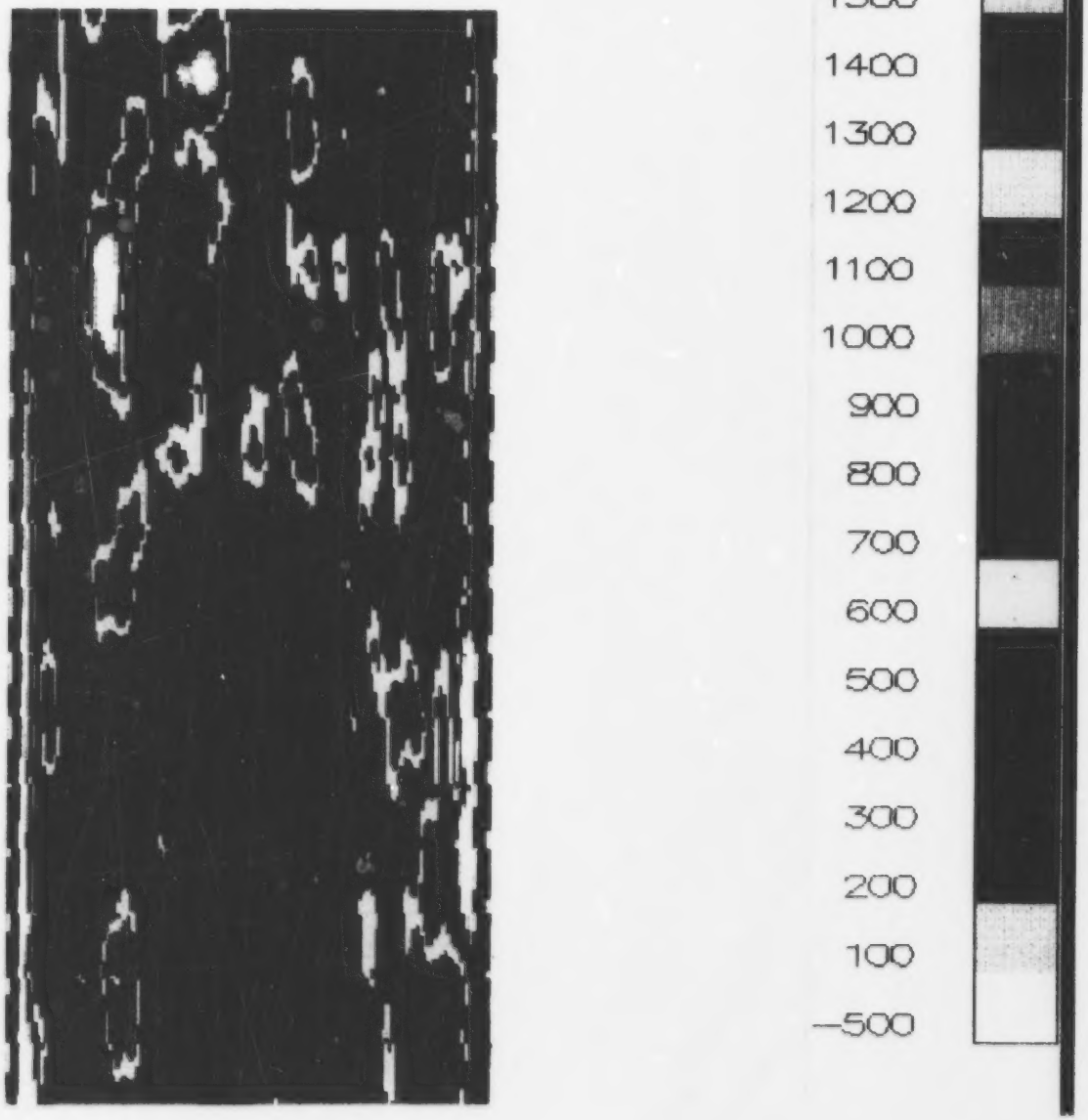

Figure 6.43 Vuggy core piece from Wabamun formation. Color code is in Figure 6.40.

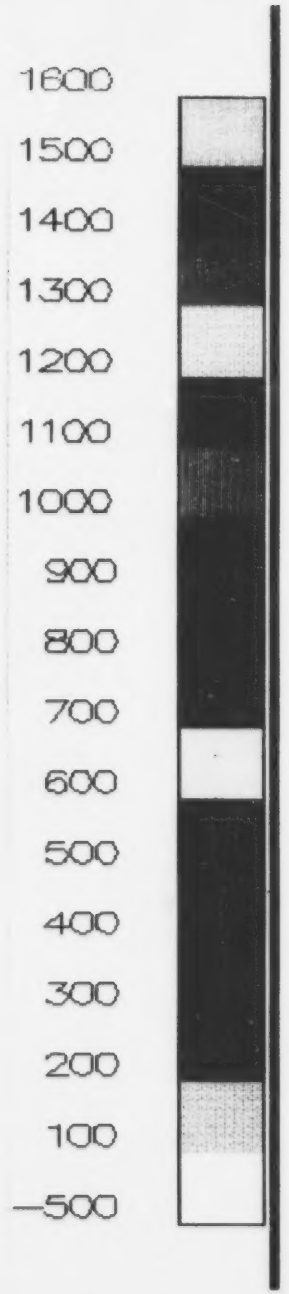

Figure 6.44 Coronal view of Wabamun core #6. Presence of large vugs. Color code as in Figure 6.40.

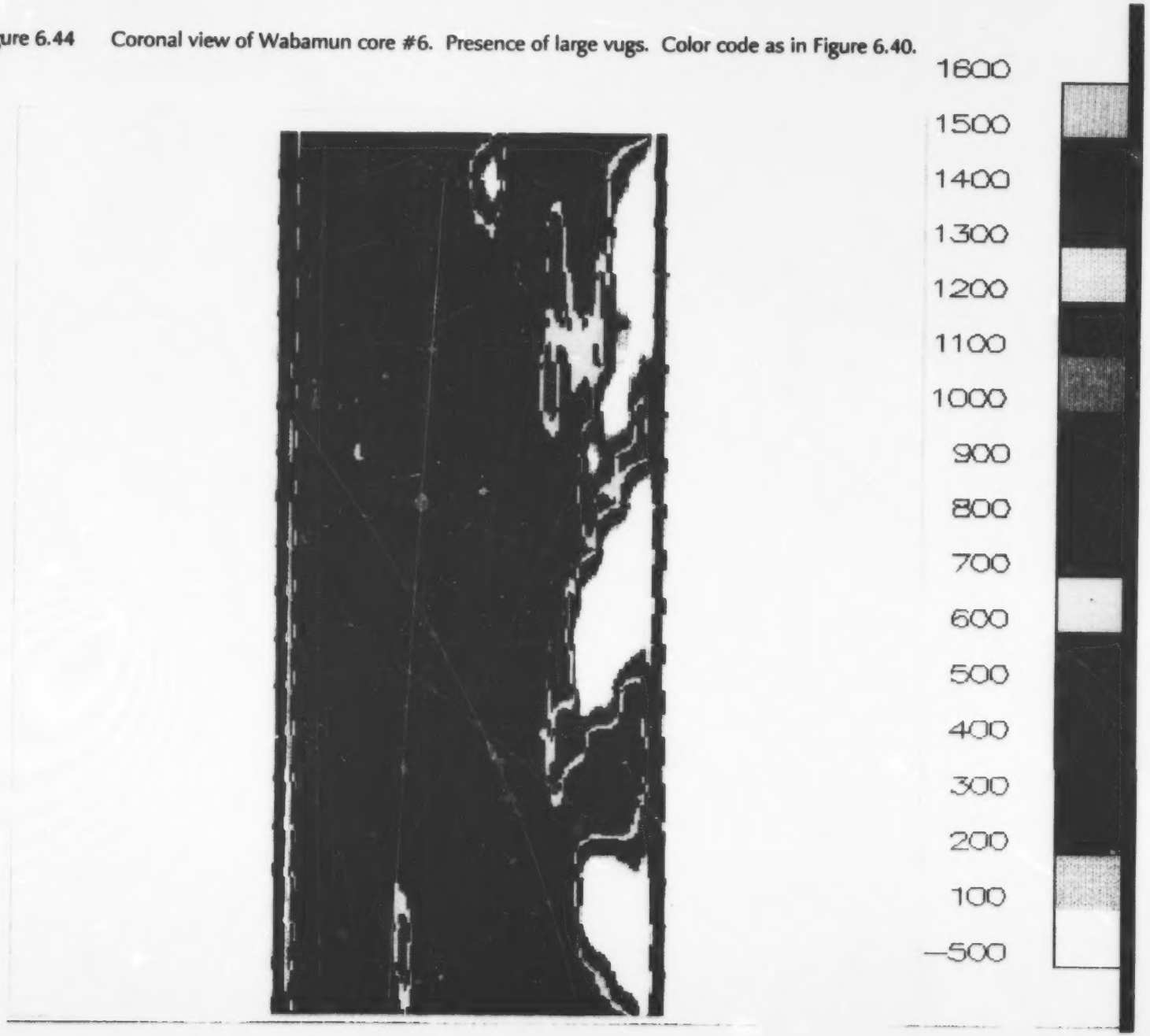

Figure 6.45 Image of vuggy and fracture piece from Wabamun core. Color code as in Figure 6.40.

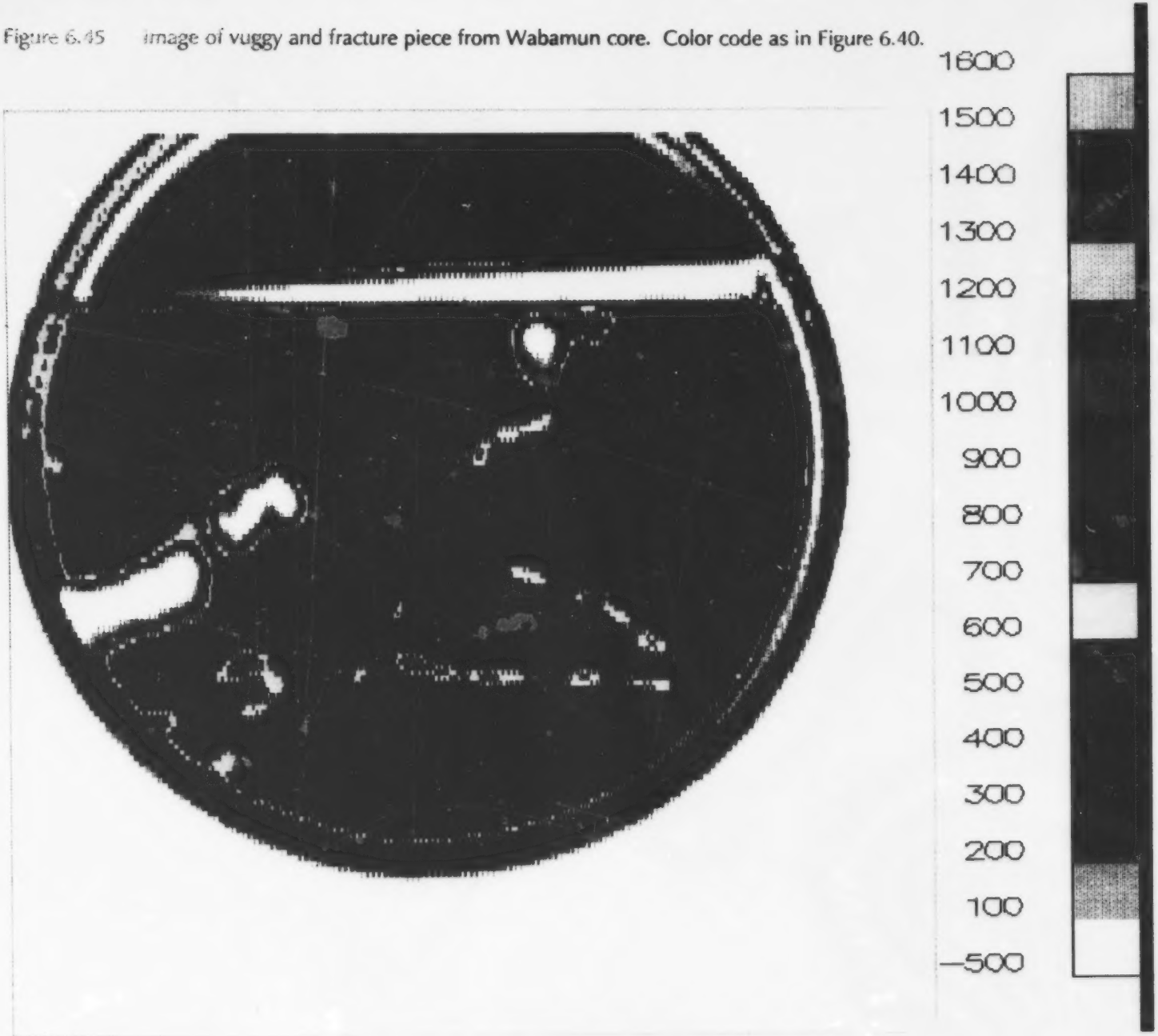

Figure 6.46 Image of vuggy and fractured piece from Wabamun core. Multiple fracture pattern. Color code as in Figure 6.40.

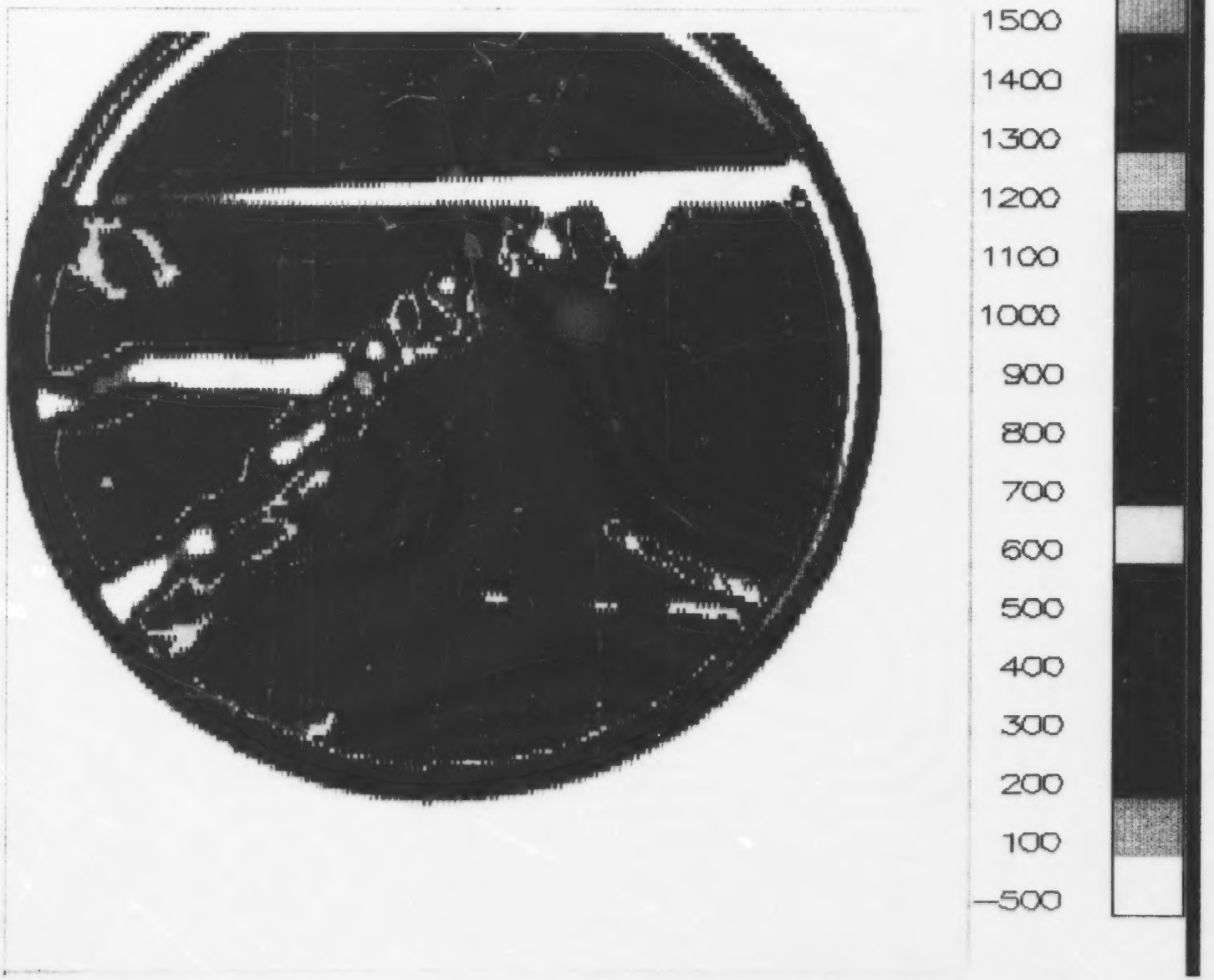

Figure 6.47 Image of fractured piece from Wabamun core. Color code as in Figure 6.40.

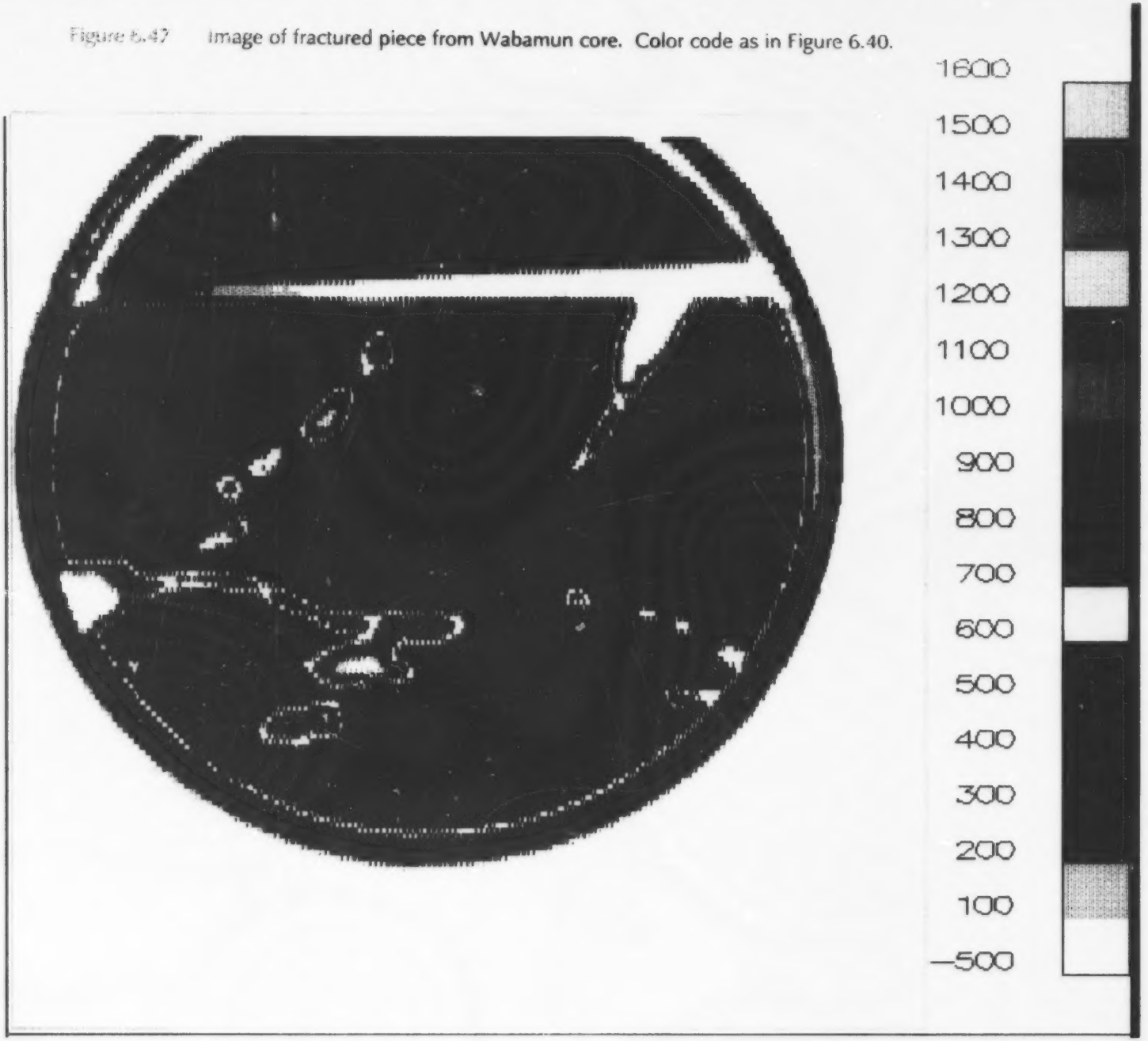

Figure 6.48 Bedding planes on Berea sandstone. Each color correponds to CT numbers.

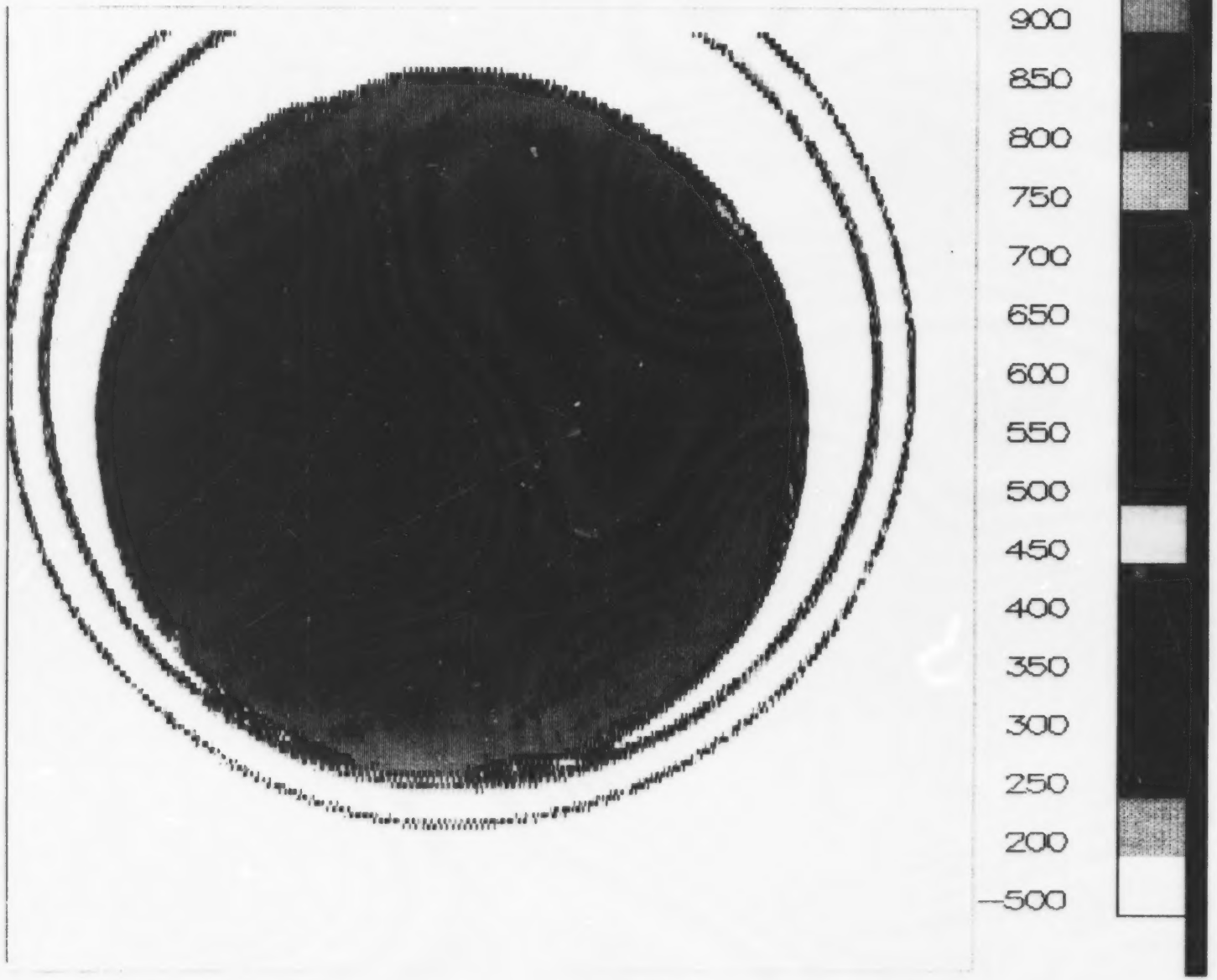

Figure 6.49 More bedding planes on Berea sandstone. Color code as in Figure 6.48.

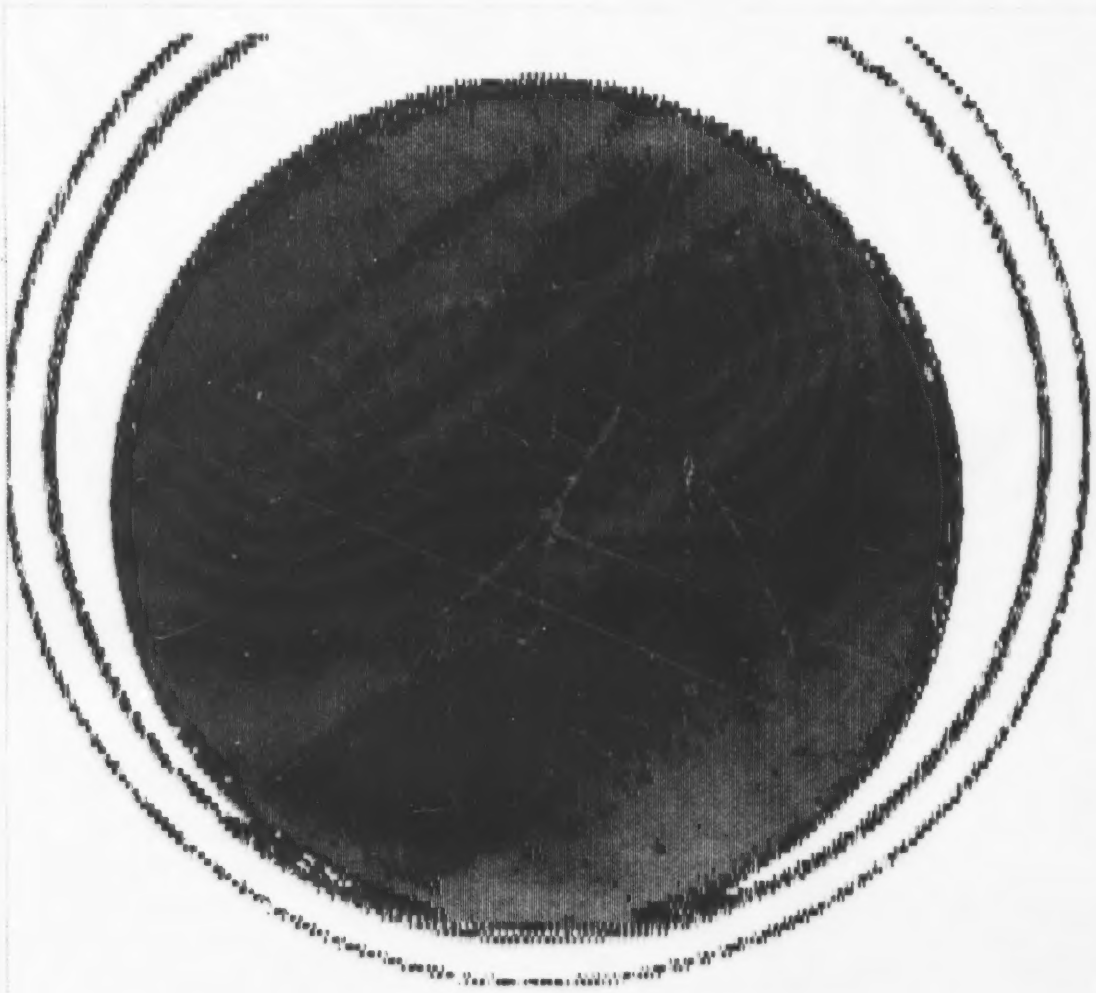

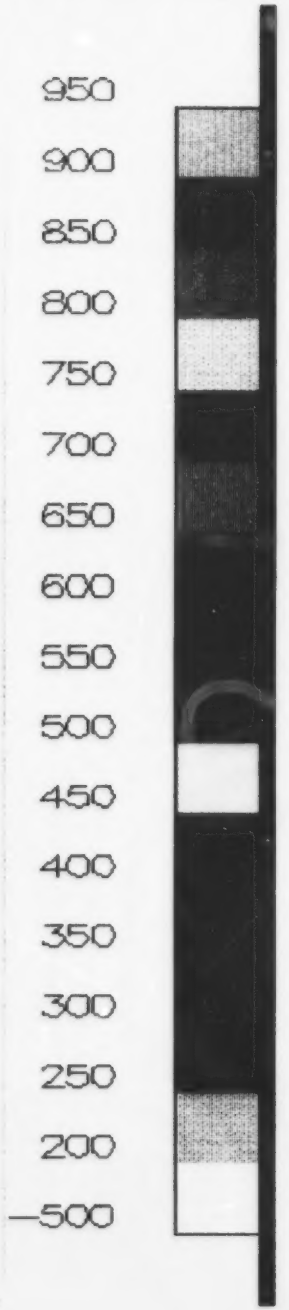

Figure 6.50 Saggital view of layered Berea sandstone. Color code as in Figure 6.48.

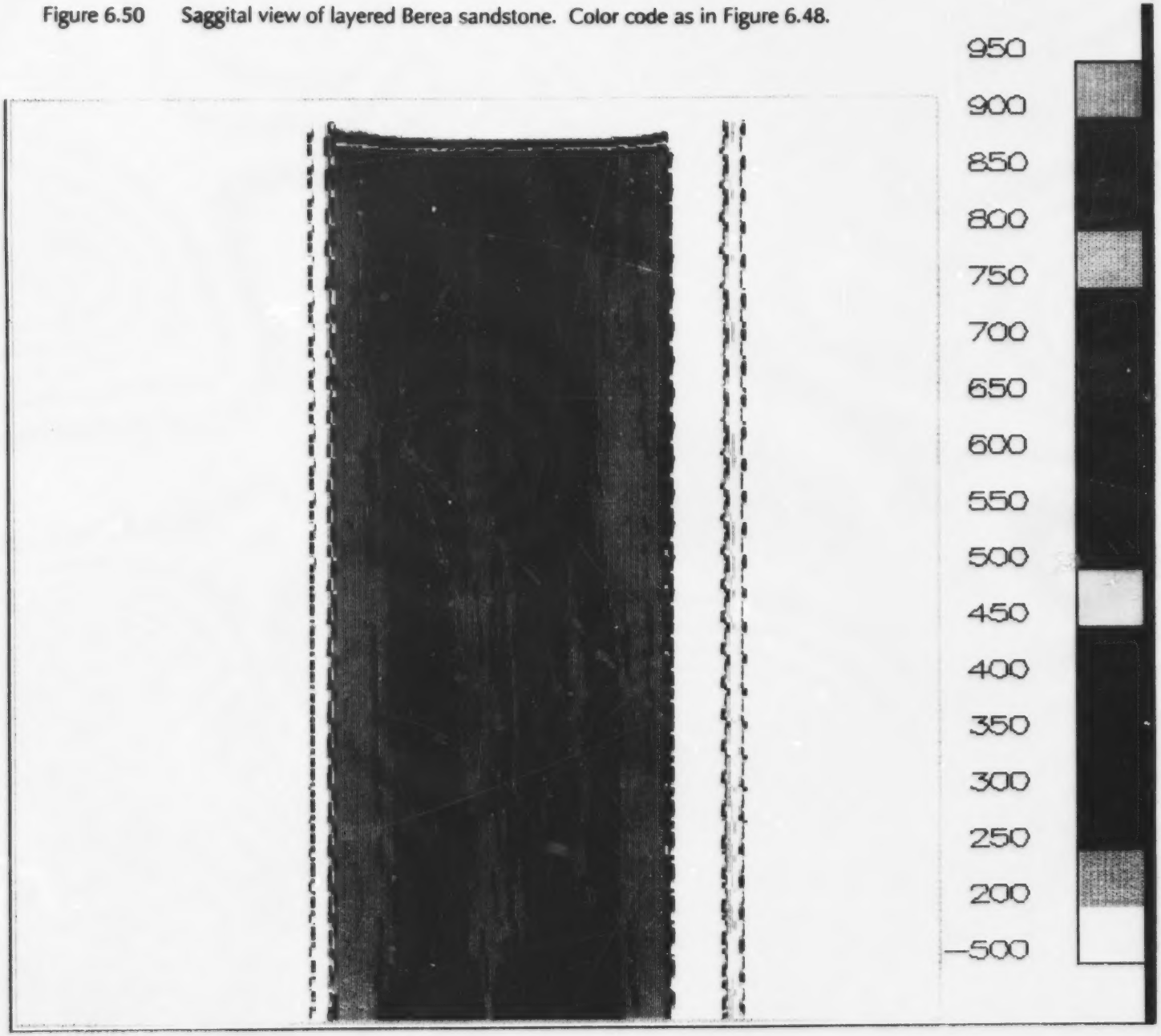

Figure 6.51 Coronal view of layered Berea sandstone. Color code as in Figure 6.48.

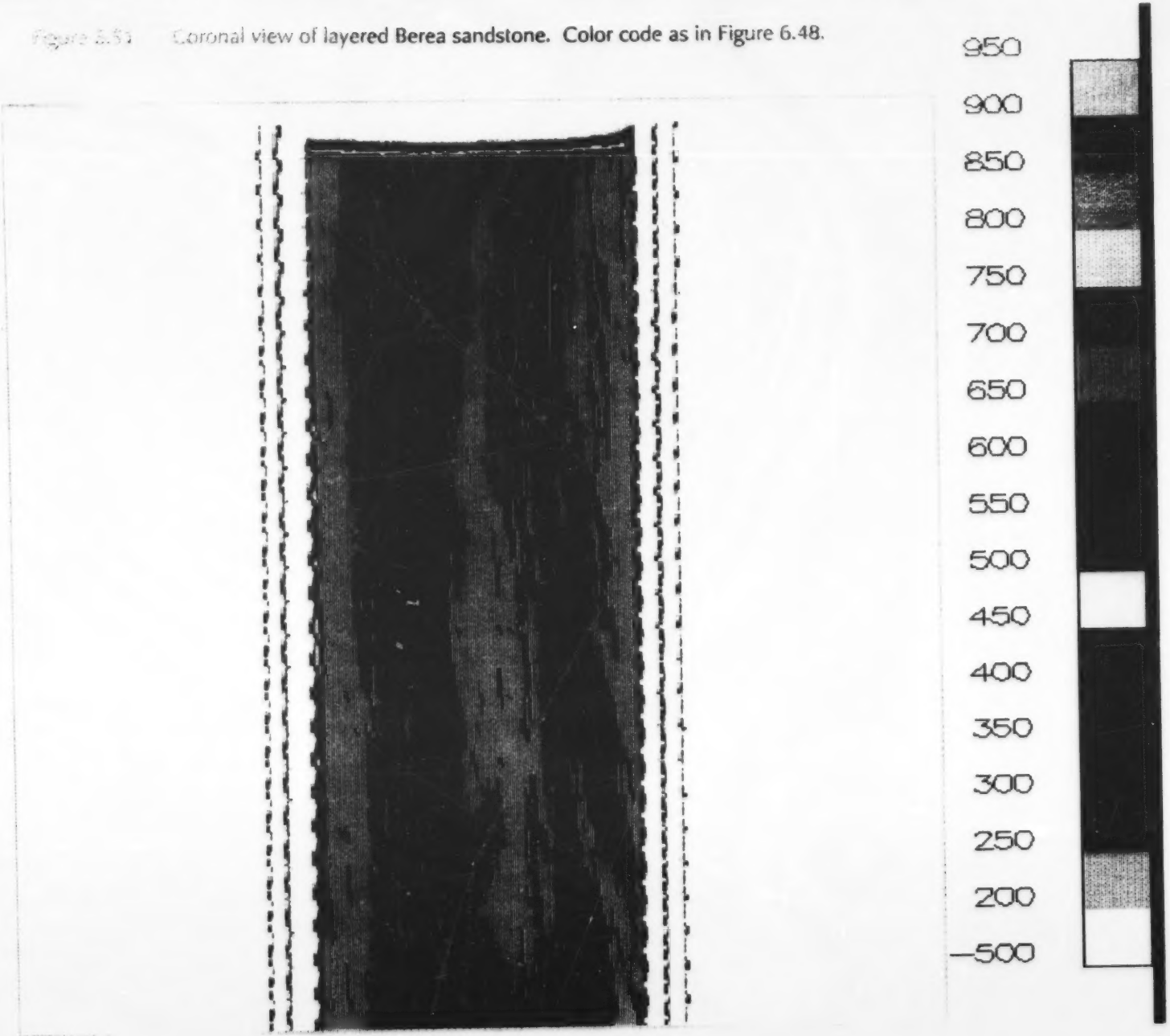

Figure 7.1 Effect of overburden pressure on dry sand #3(coarse, high permeability)using a teflon shrink tube.

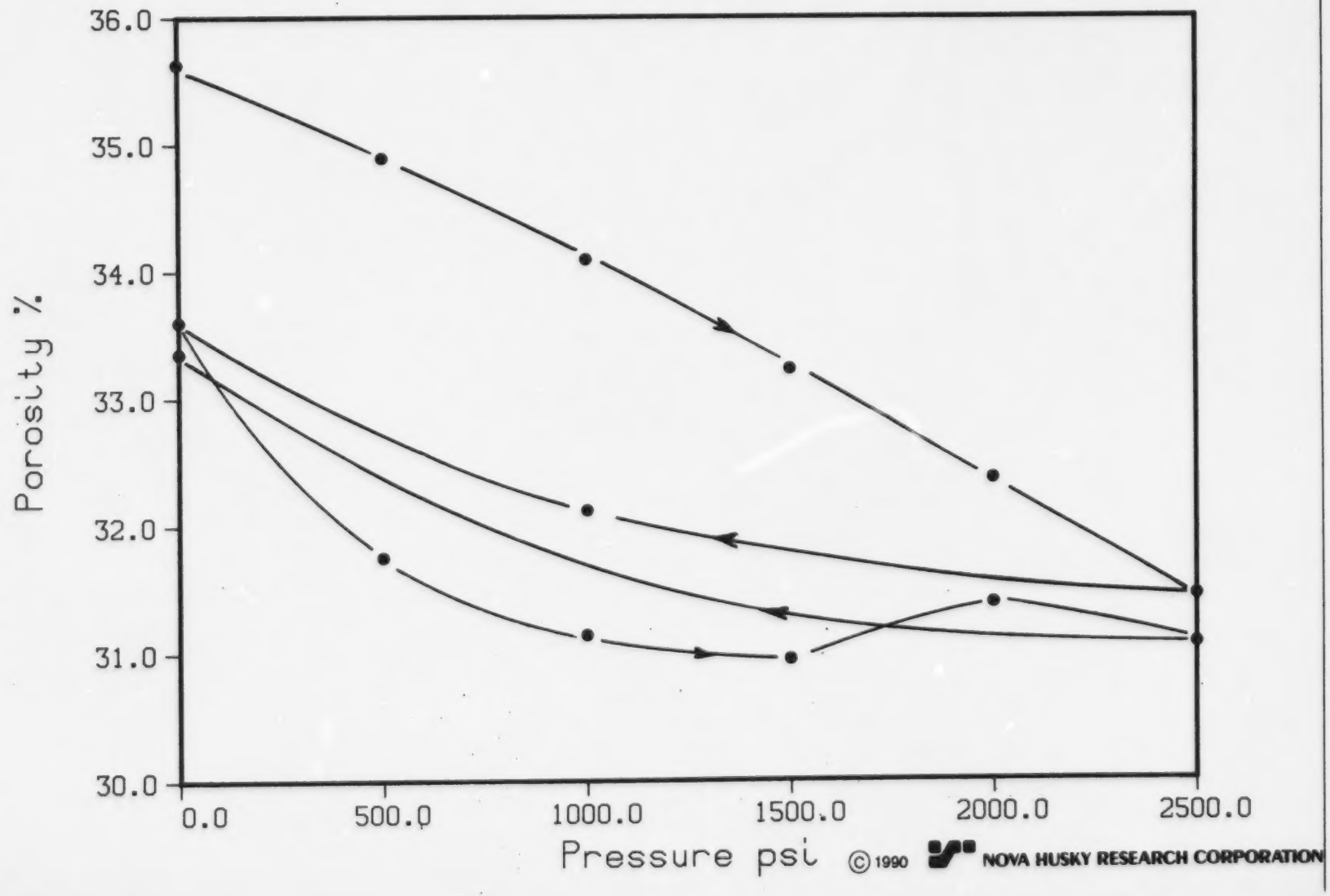

Figure 7.2 Repeat run on sand #3.

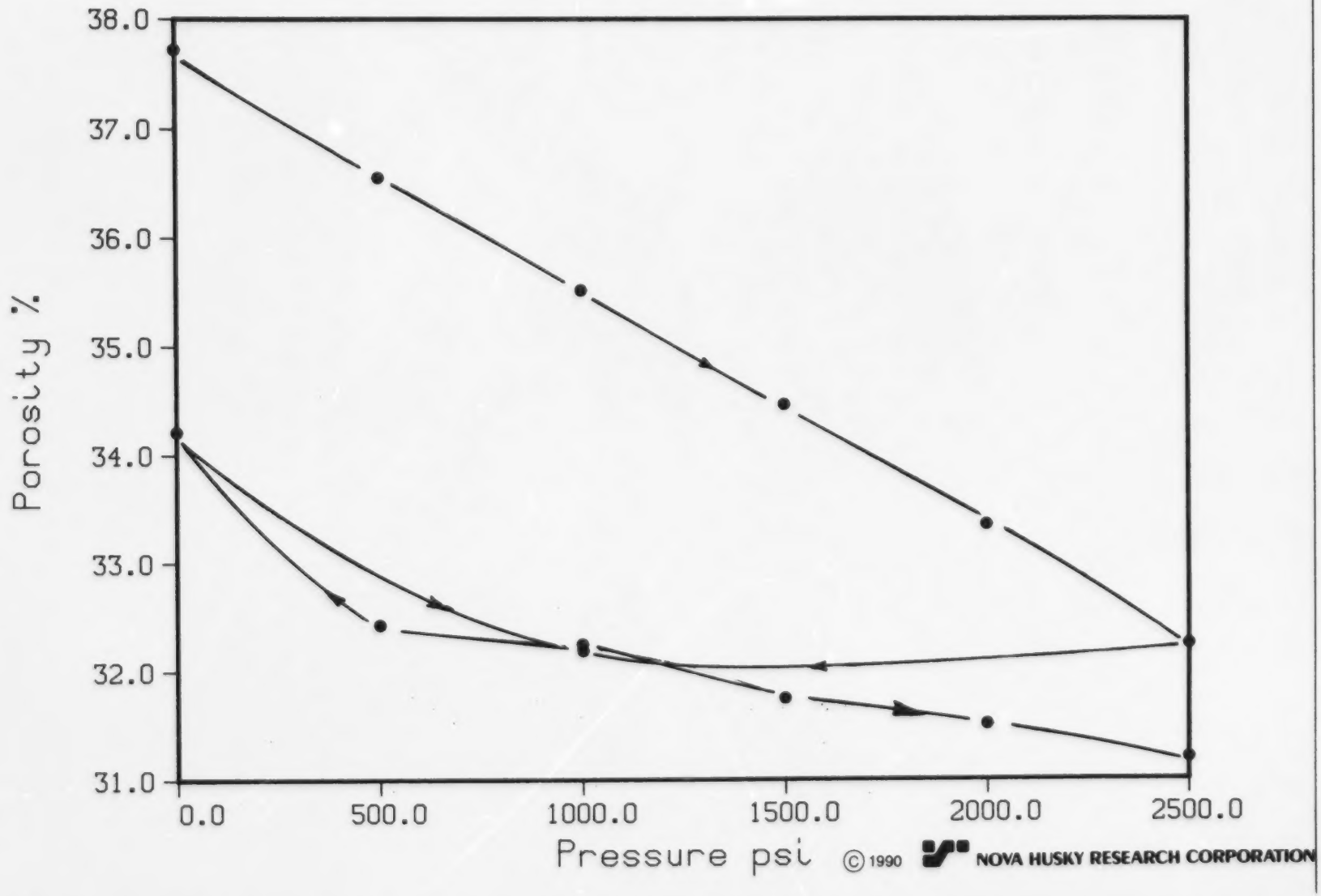

Figure 7.3 Repeat run on sand #3 using a rubber shrink tube.

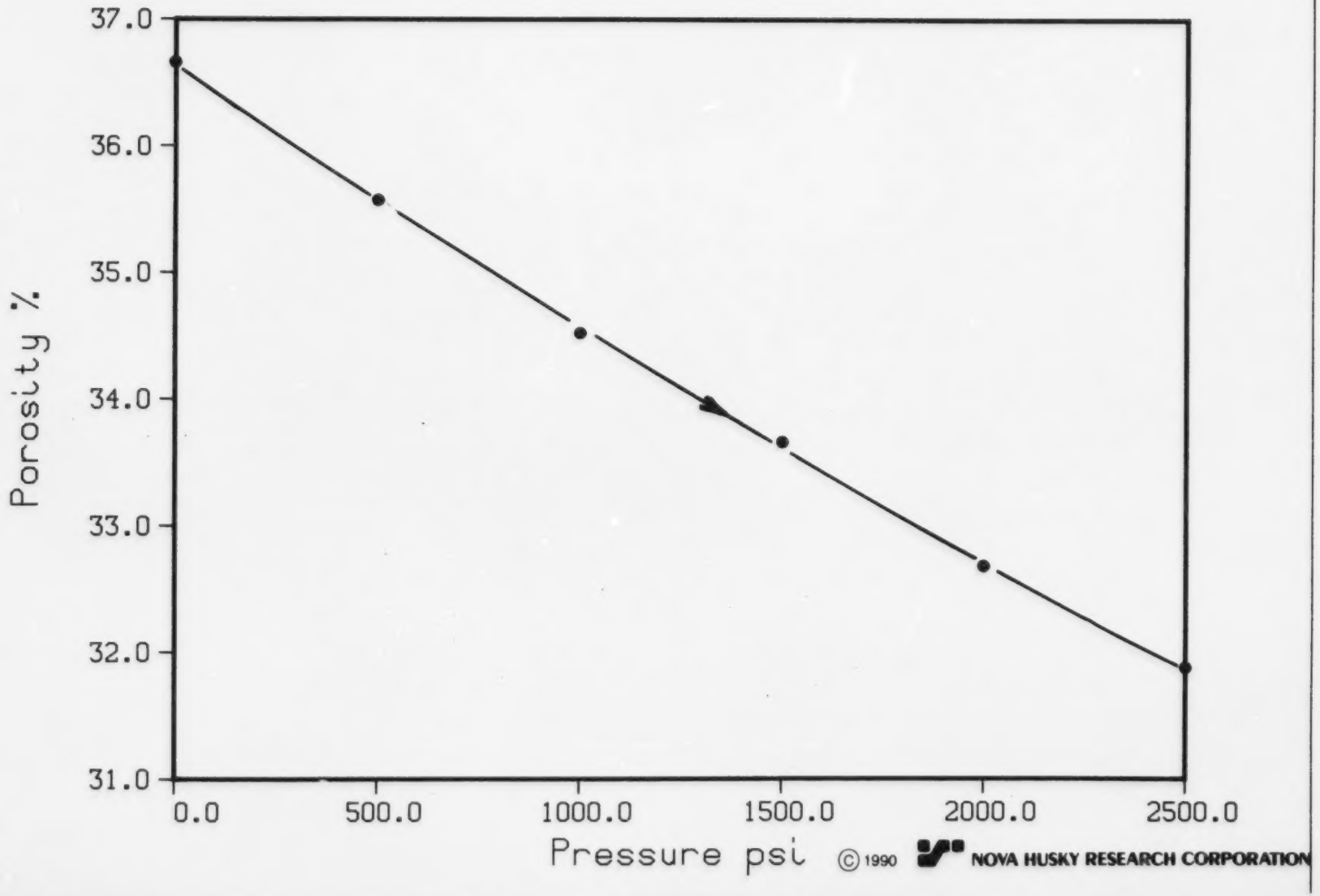

Figure 7.4 Effect of overburden pressure on water saturated sand #3.

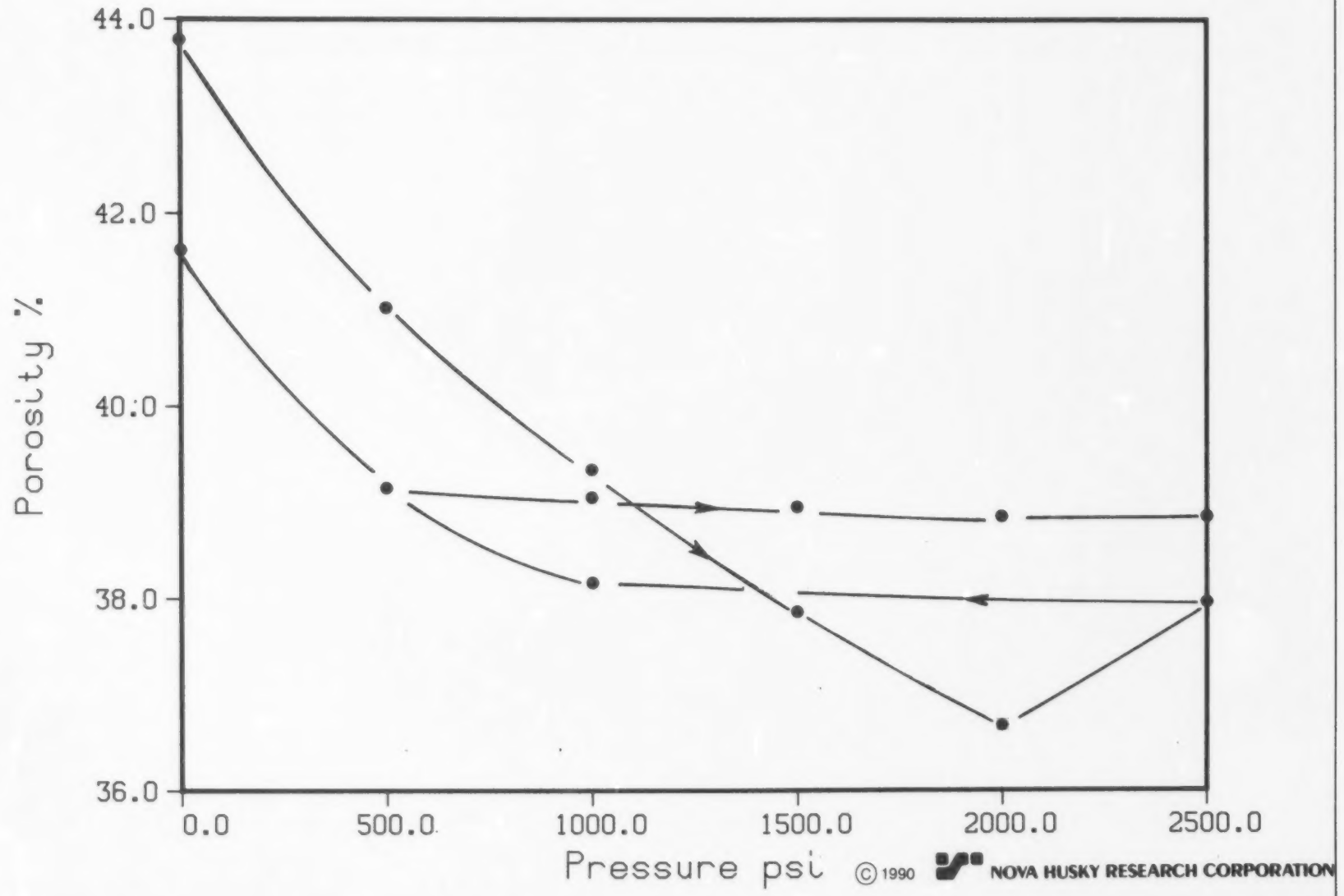

Figure 7.5 Effect of overburden pressure on dry sand #16 (fine, low permeability).

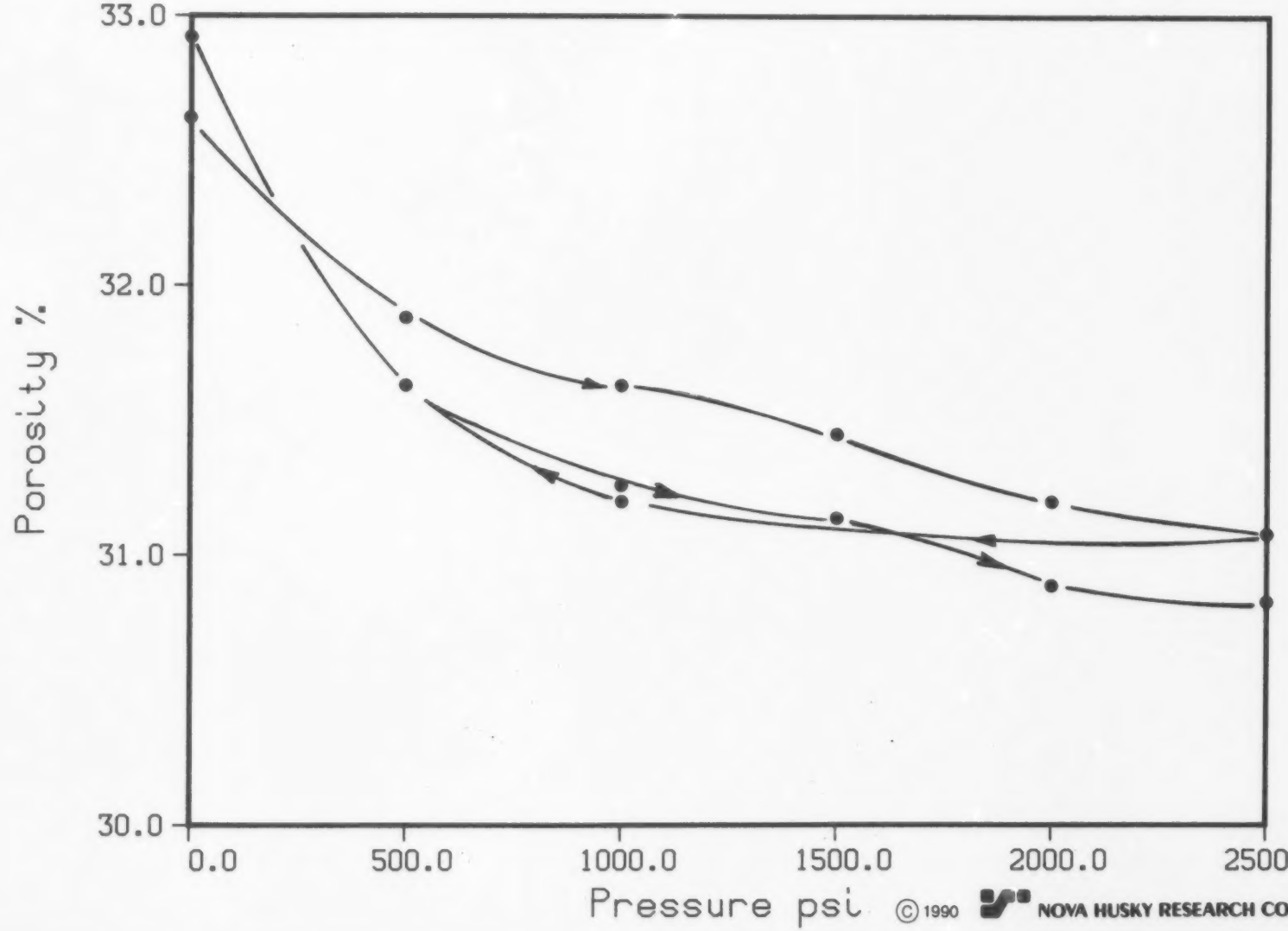

Figure 7.6 Effect of overburden pressure on Berea sandstone.

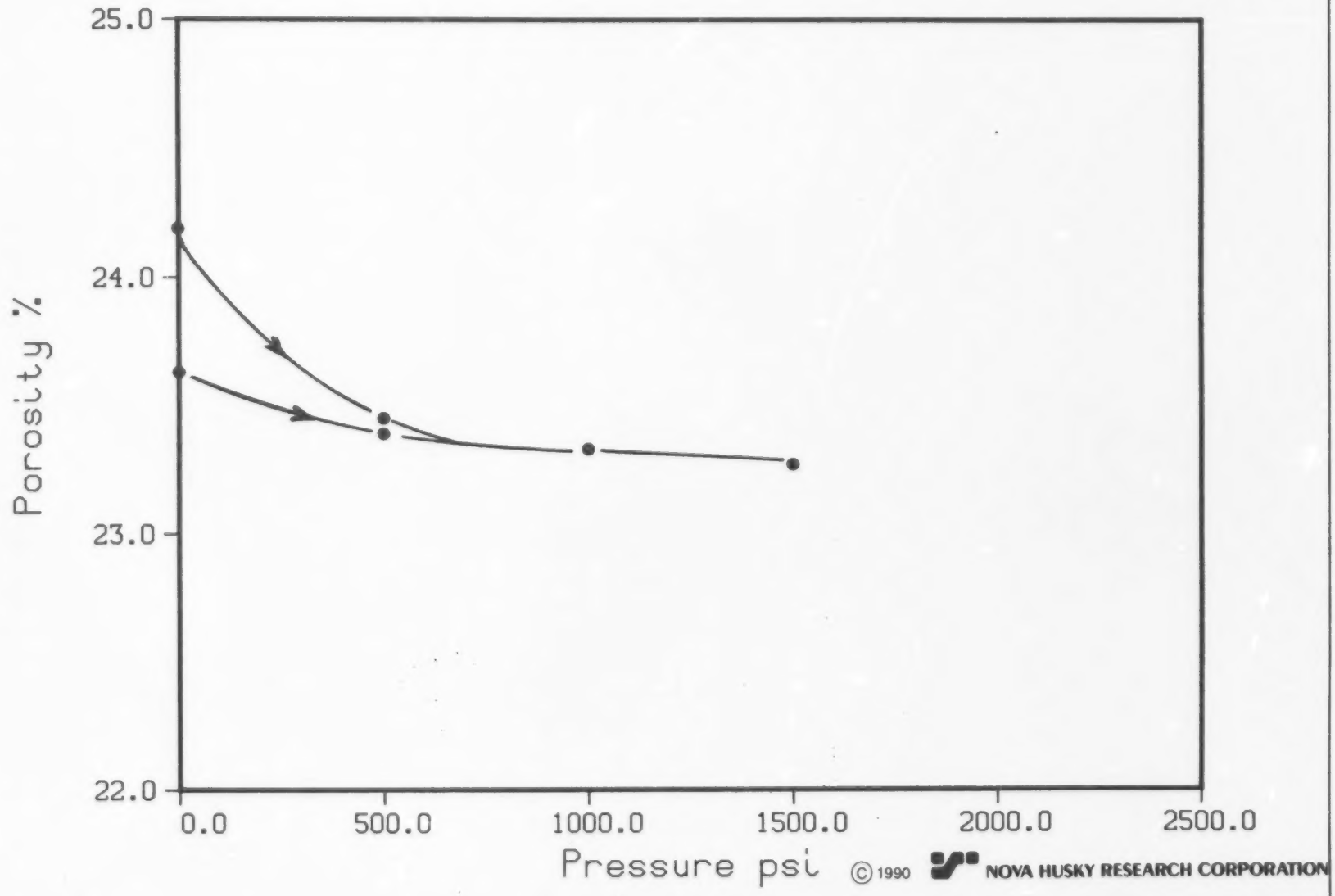

Figure 7.7 Low pressure cycles for sand #3.

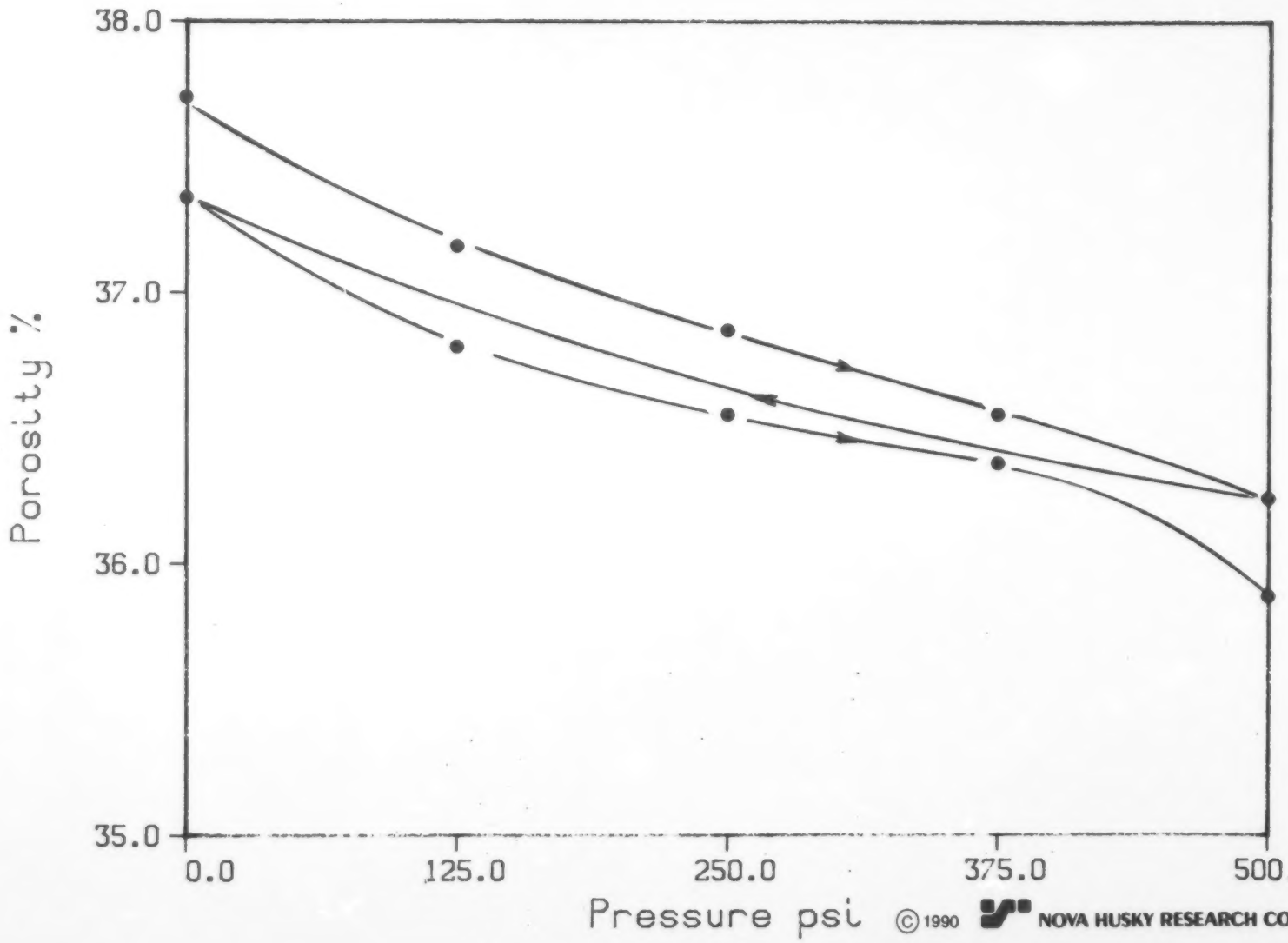

Figure 3.1 Bulk density map of the slice of core piece #12 at 18mm from the top face. The color code at the right hand side indicates the range of densities for each color. The density values, displayed next to the code, are in g/cm^3.

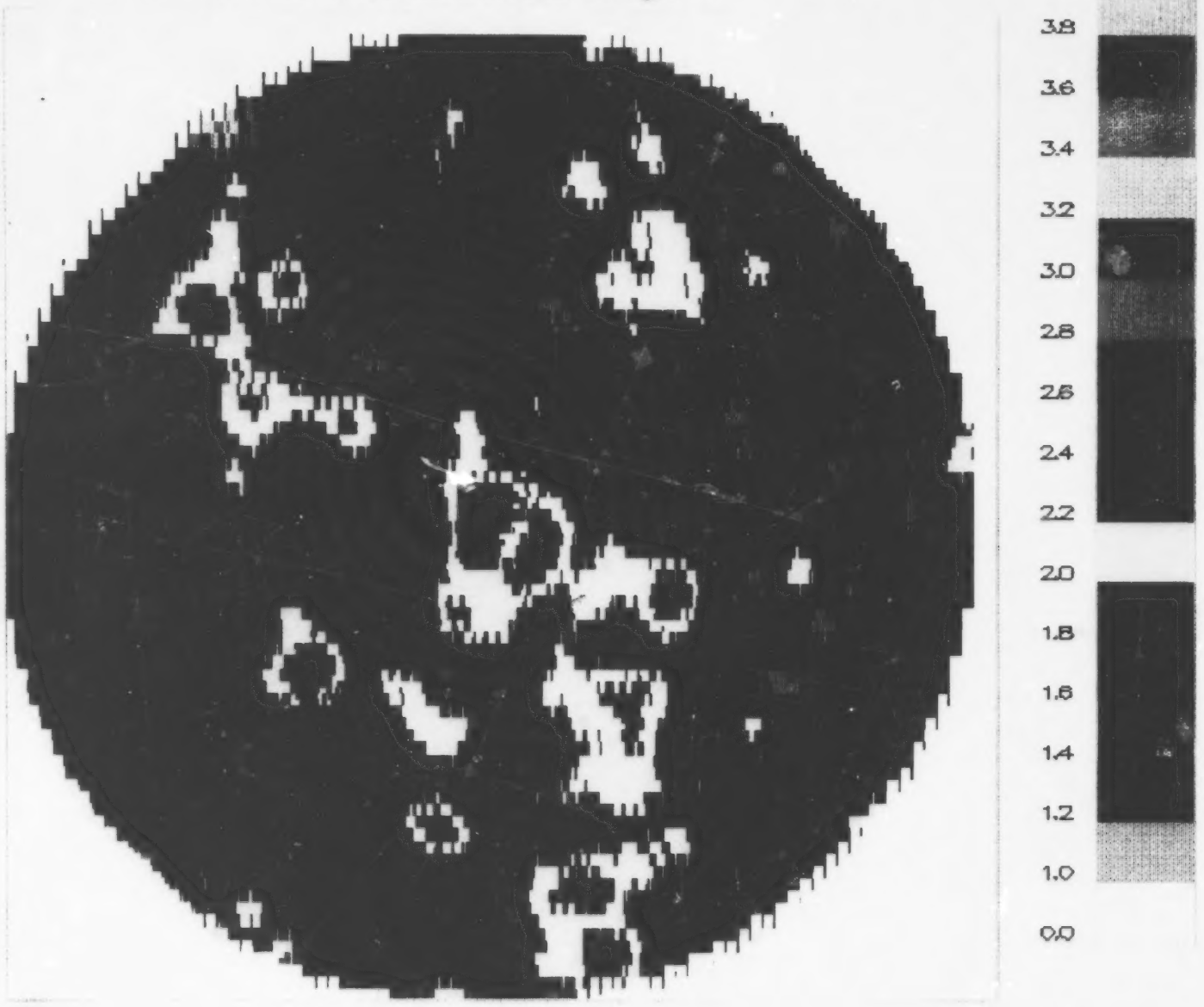

Figure 9.2 Bulk density map of the slice of core piece #12 at 20mm from the top face. Color code same as in Figure 9.1

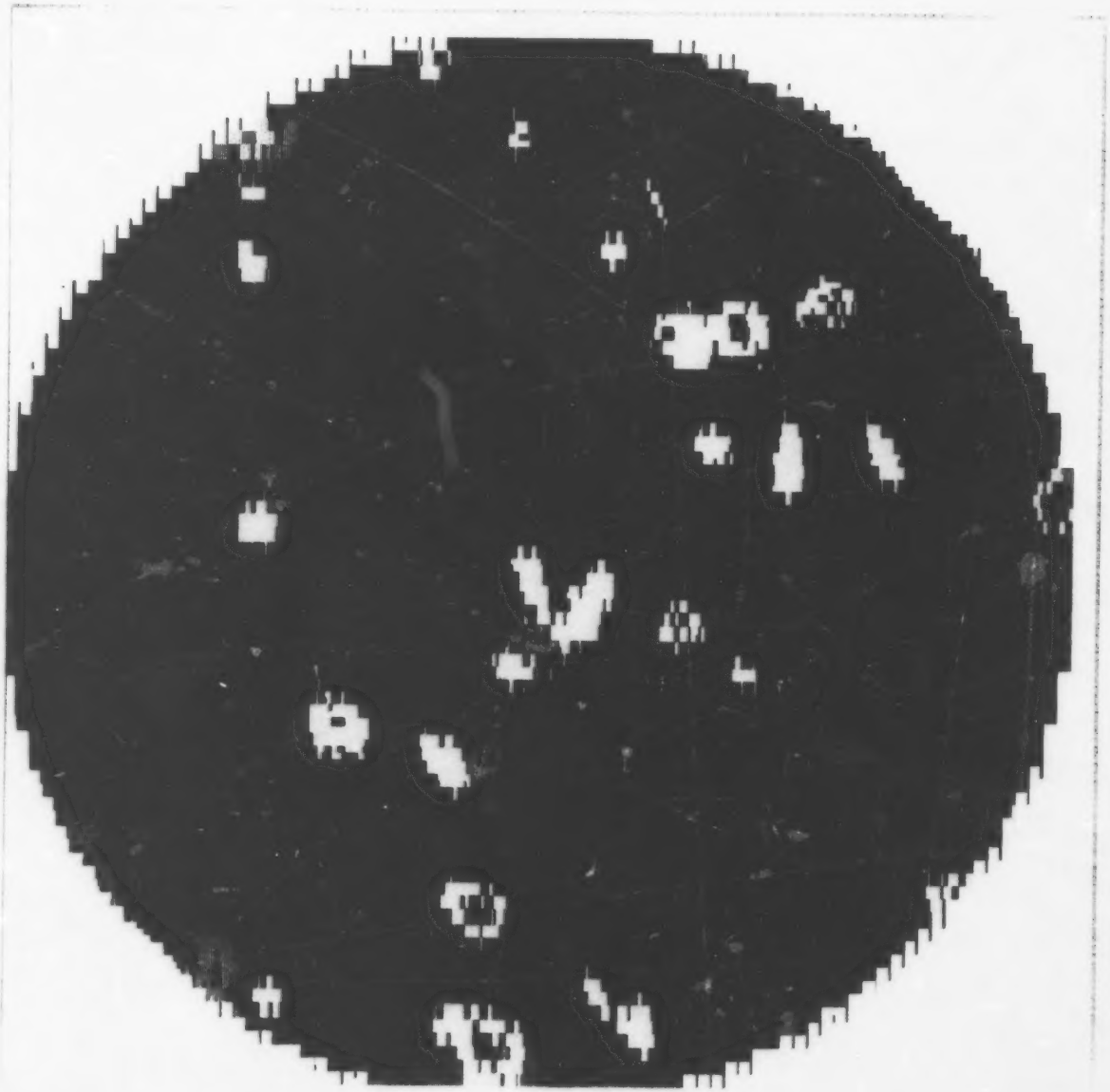

Figure 9.3 Bulk density map of the slice of core piece #12 at 21mm from the top face. Color code same as in Figure 9.1

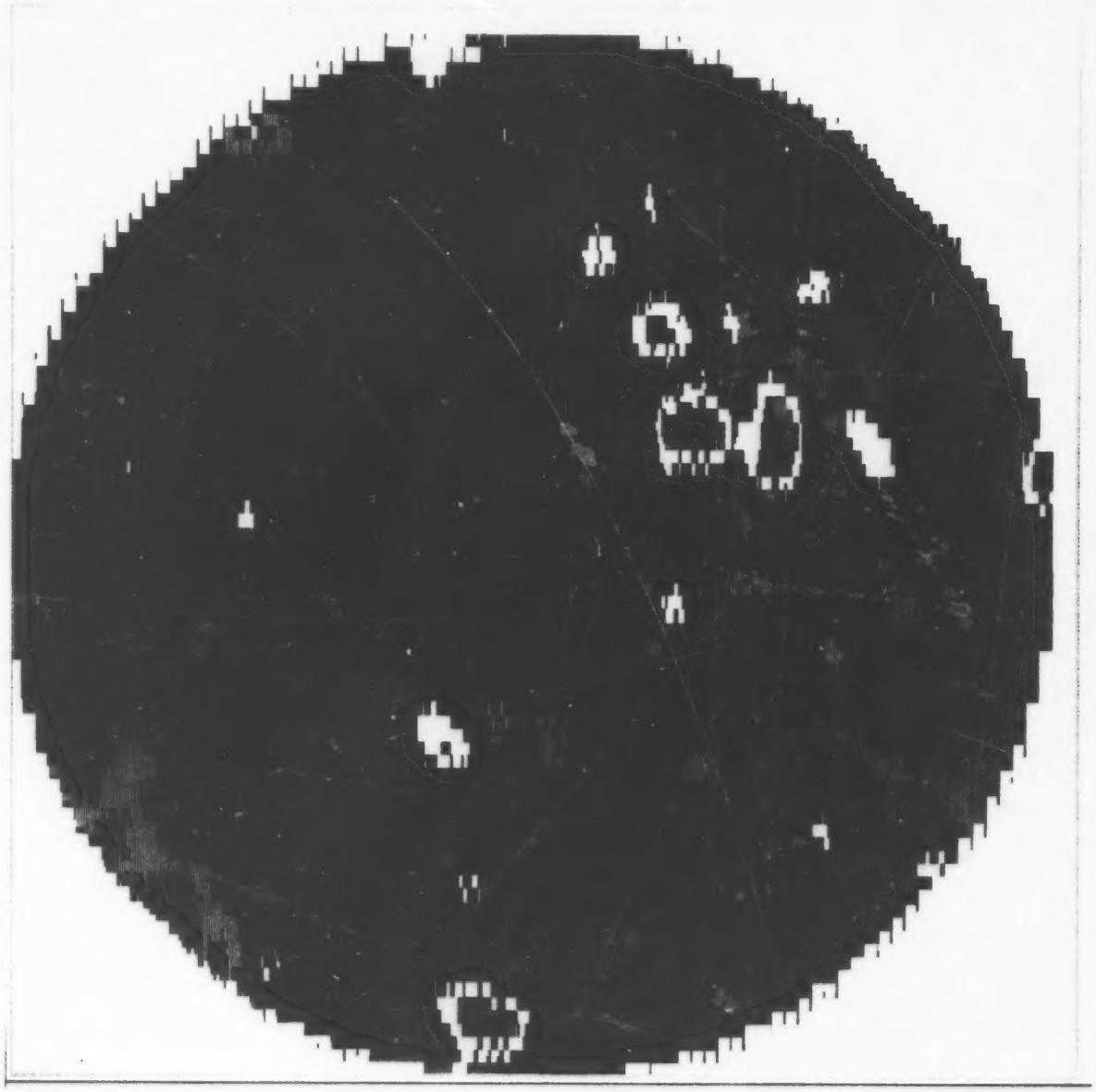

Figure 9.4 Bulk density map of the slice of core piece #12 at 24mm from the top face. Color code same as in Figure 9.1

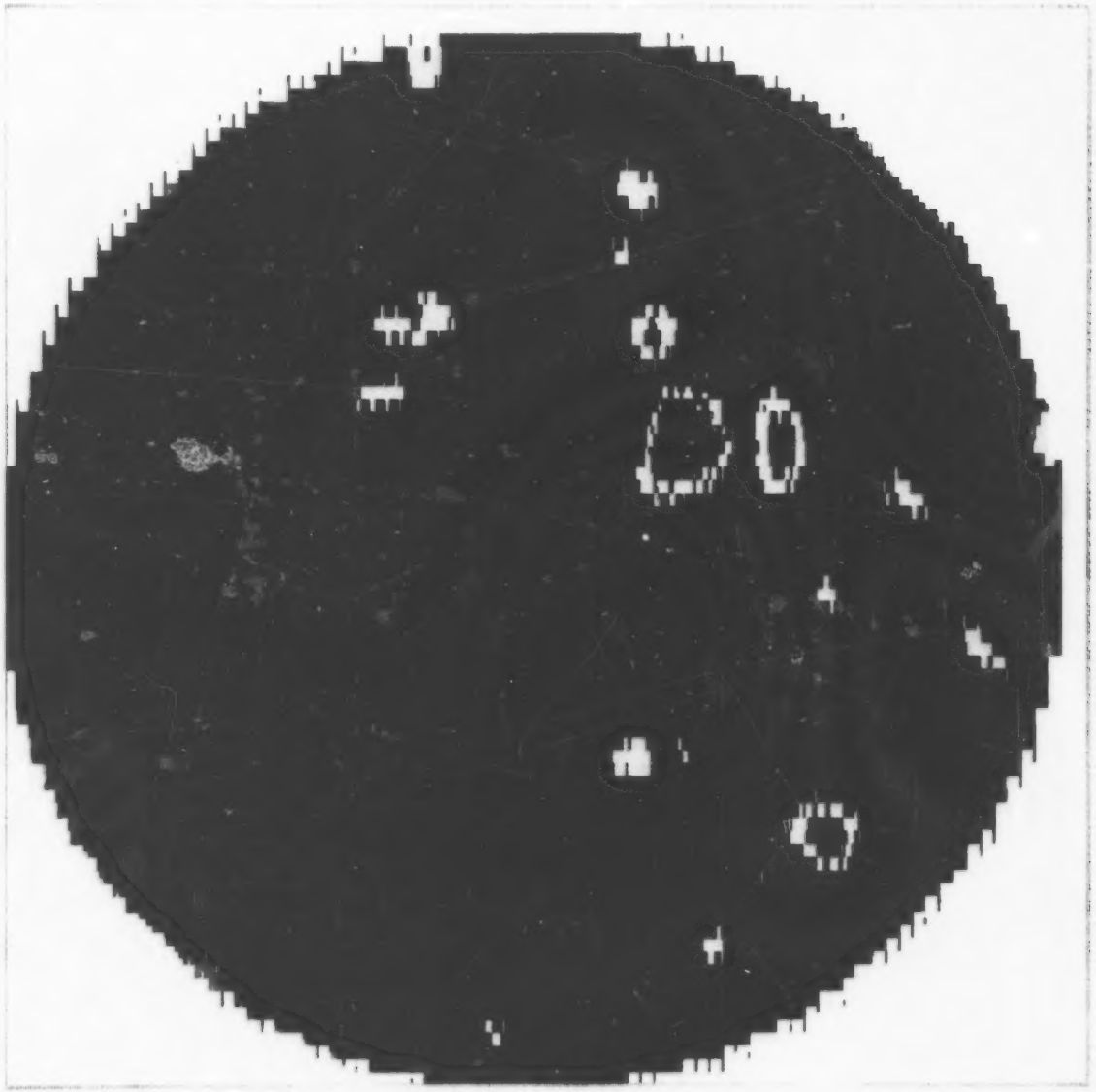

Figure 9.5 Bulk density map of the slice of core piece #12 at 25mm from the top face. Color code same as in Figure 9.1

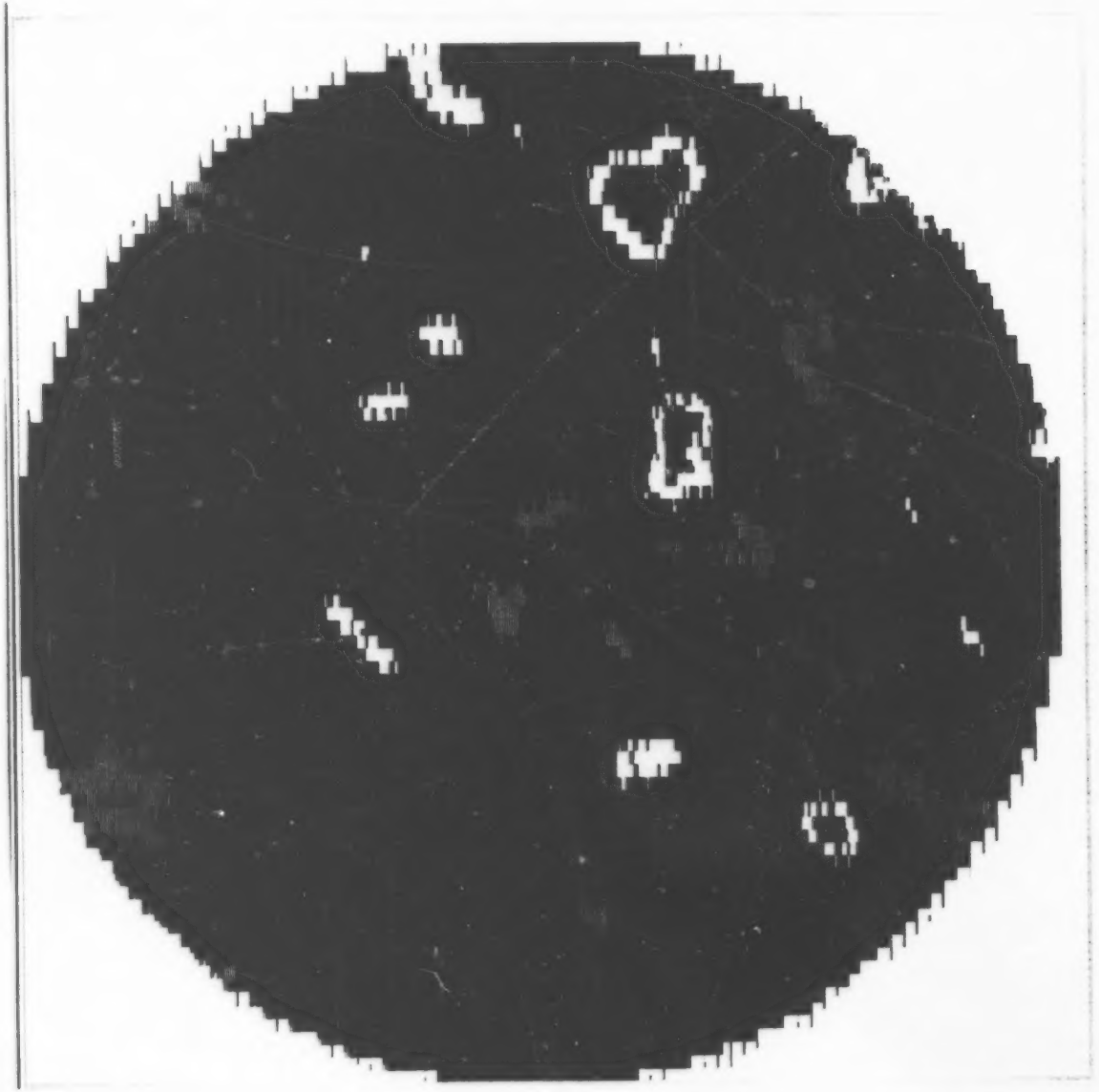

Figure 9.6 Bulk density map of the slice of core piece #12 at 27mm from the top face. Color code same as in Figure 9.1

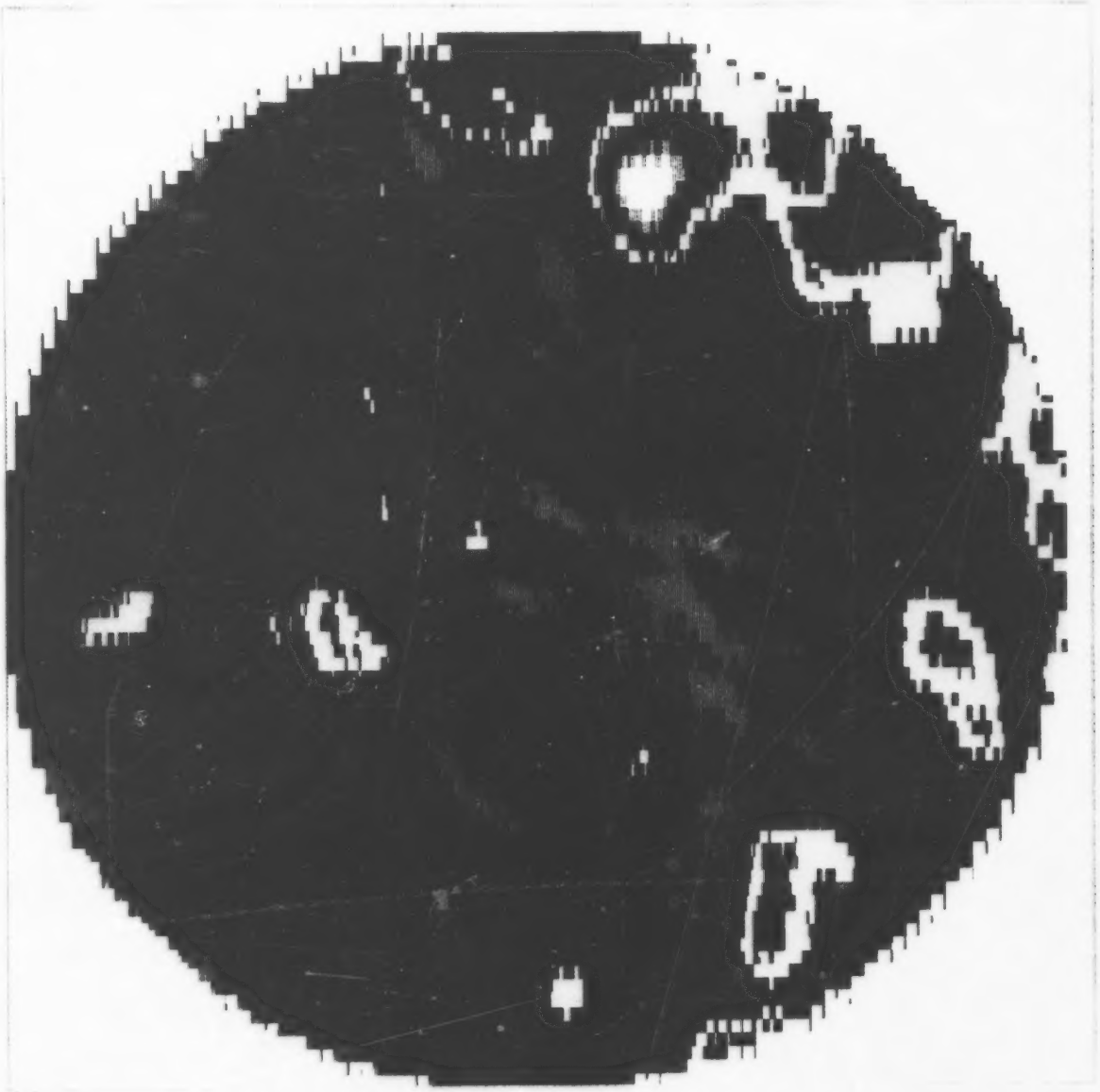

Figure 9.7 Bulk density map of the slice of core piece #12 at 30mm from the top face. Color code same as in Figure 9.1

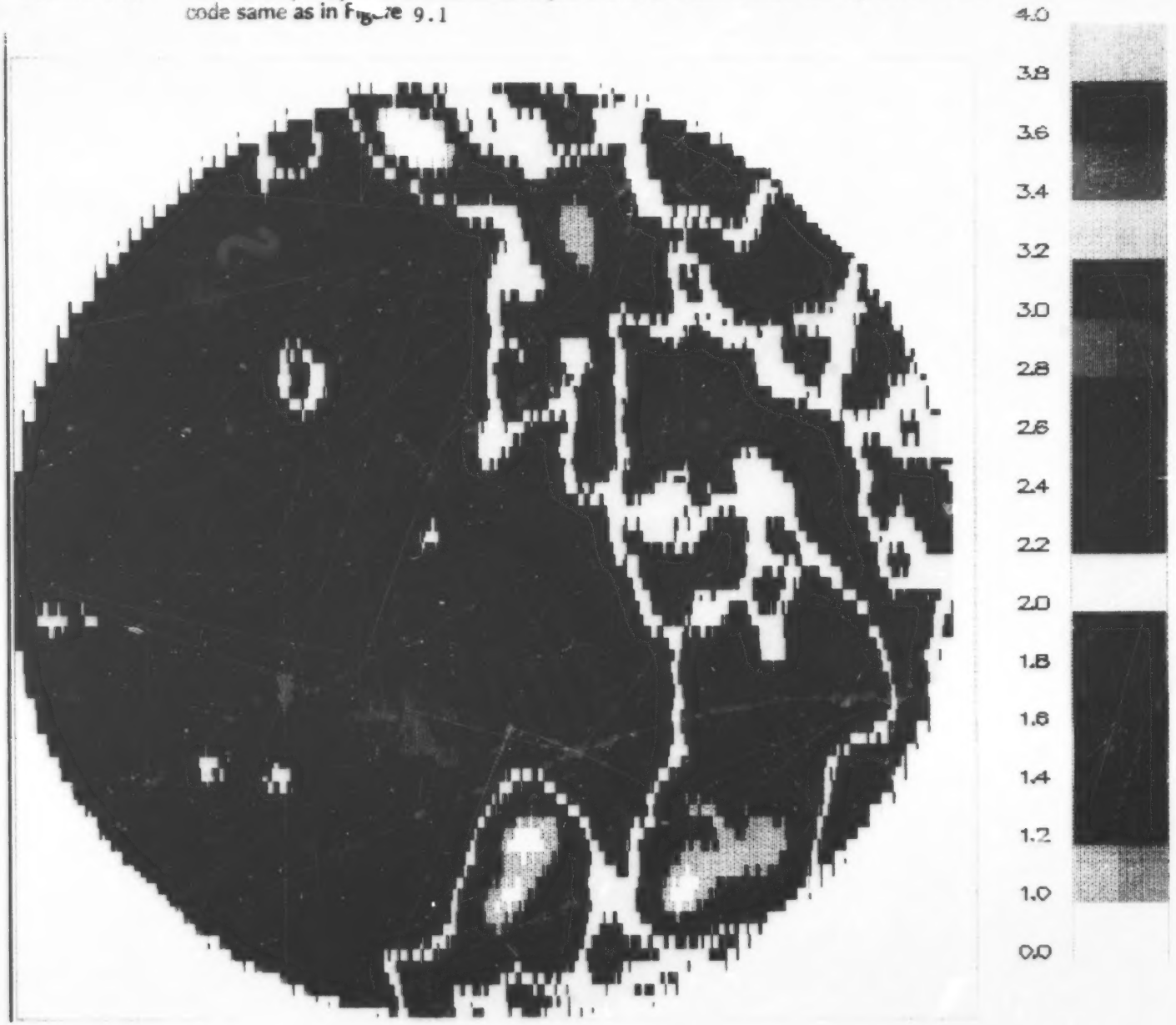

Figure 9.8 **Bulk density map of the slice of core piece #52 at 15mm from the undamaged face. Color code same as in Figure 9.1**

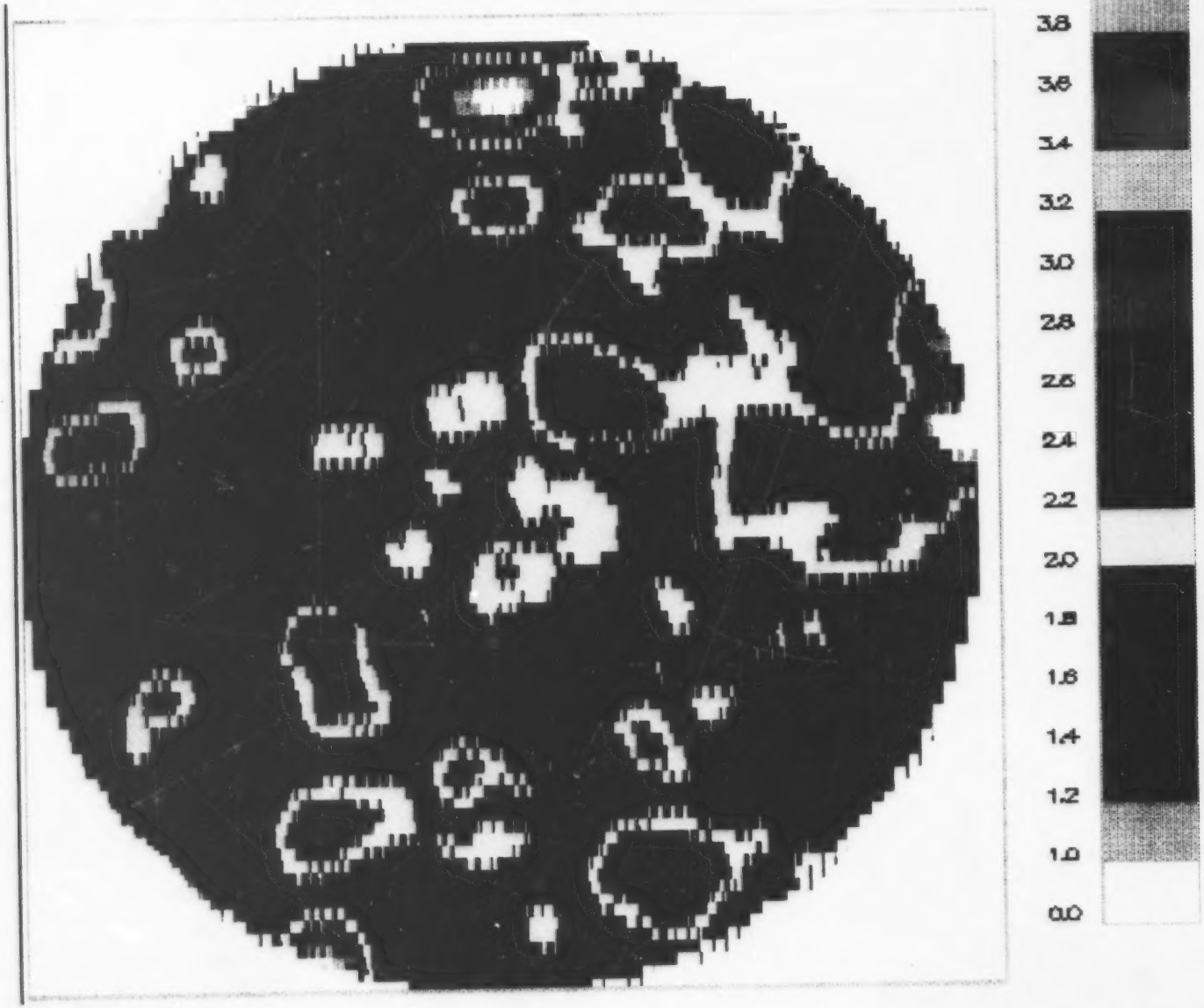

Figure 9.9 Bulk density map of the slice of core piece #52 at 35mm from the undamaged face. Color code same as in Figure 9.1

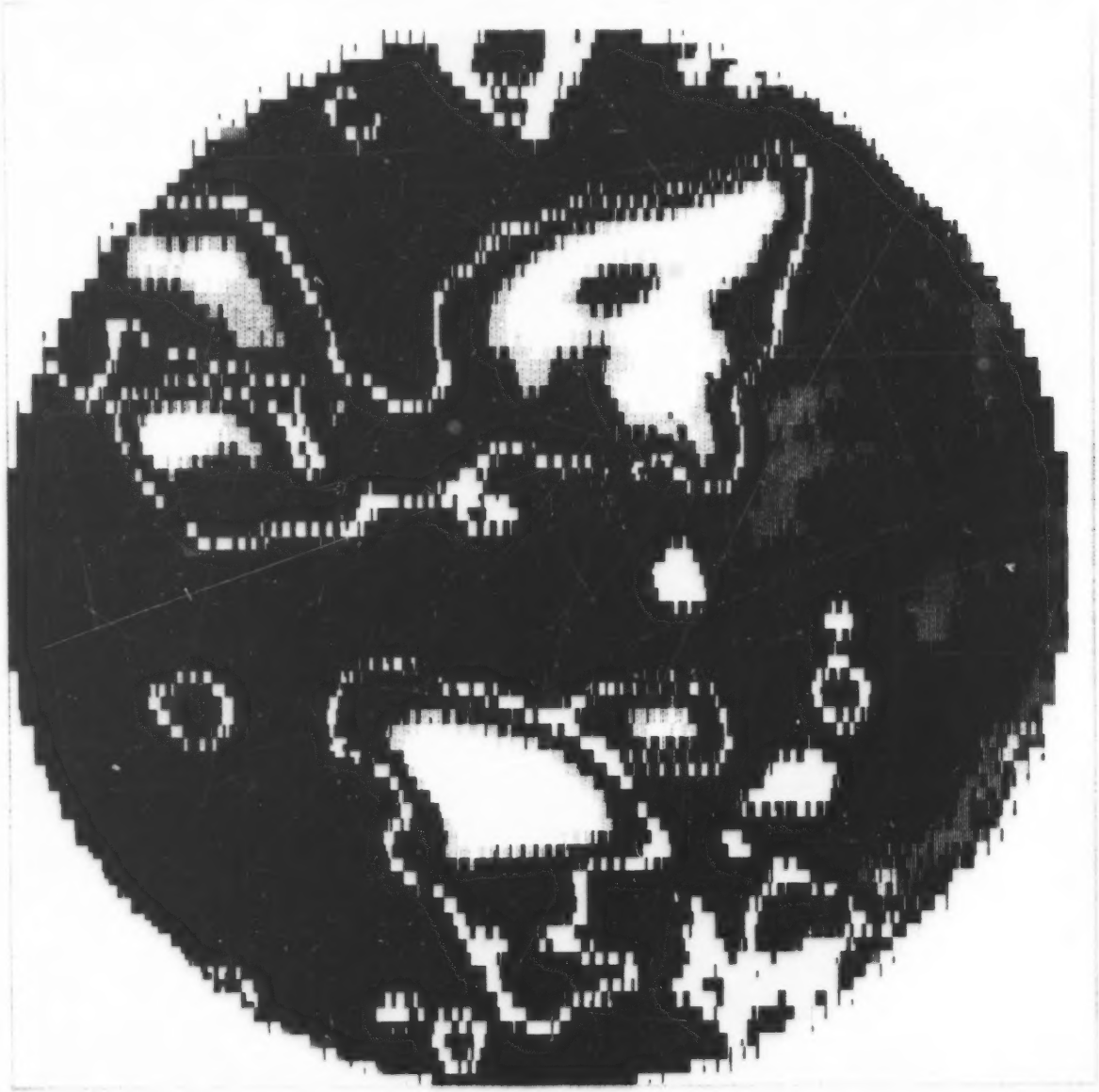

Figure 9.10 Bulk density map of the slice of core piece #52 at 55mm from the undamaged face. Color code same as in Figure 9.1

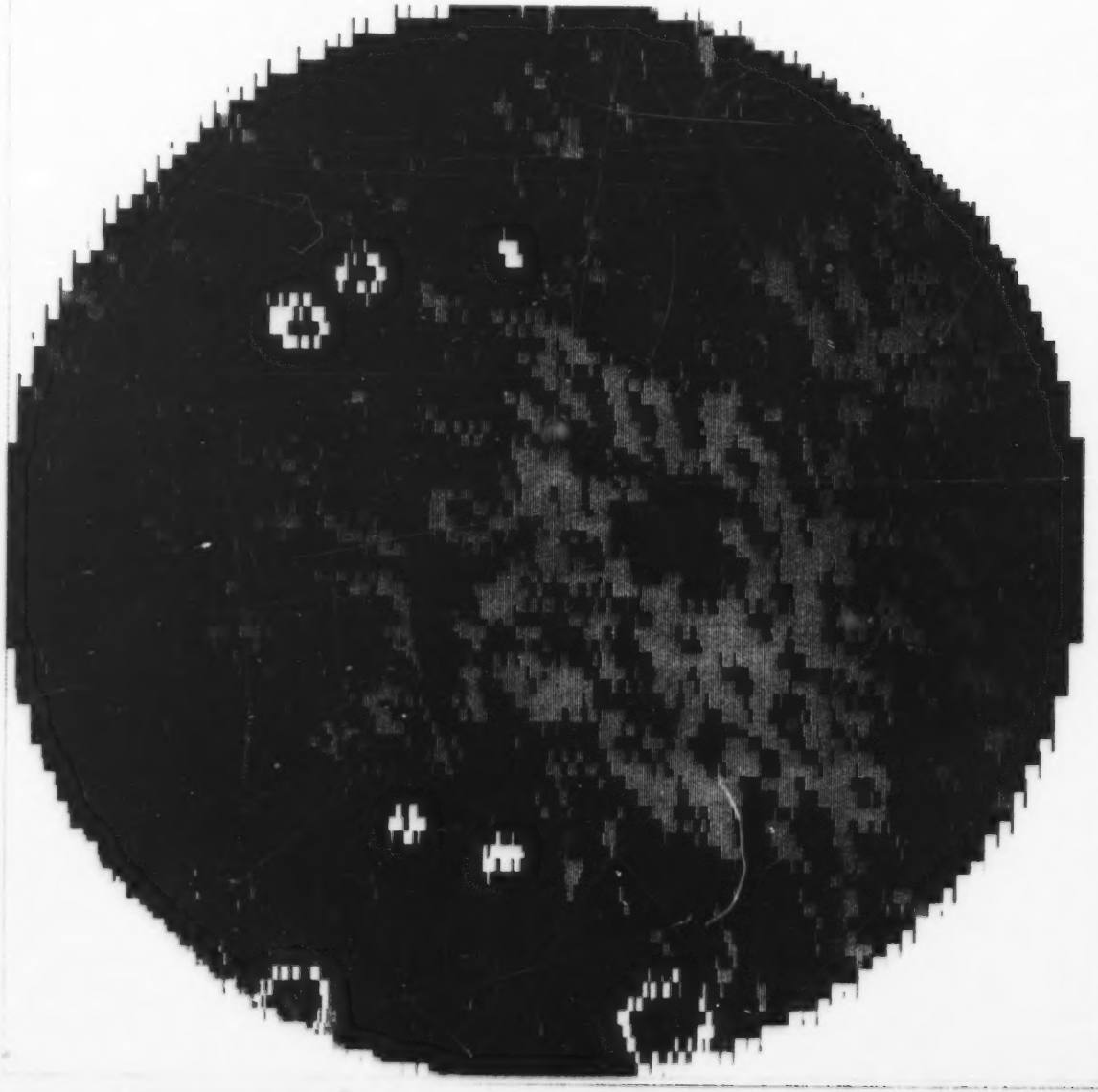

Figure 9.11 Bulk density map of the slice of core piece #52 at 75mm from the undamaged face. Color code same as in Figure 9.1

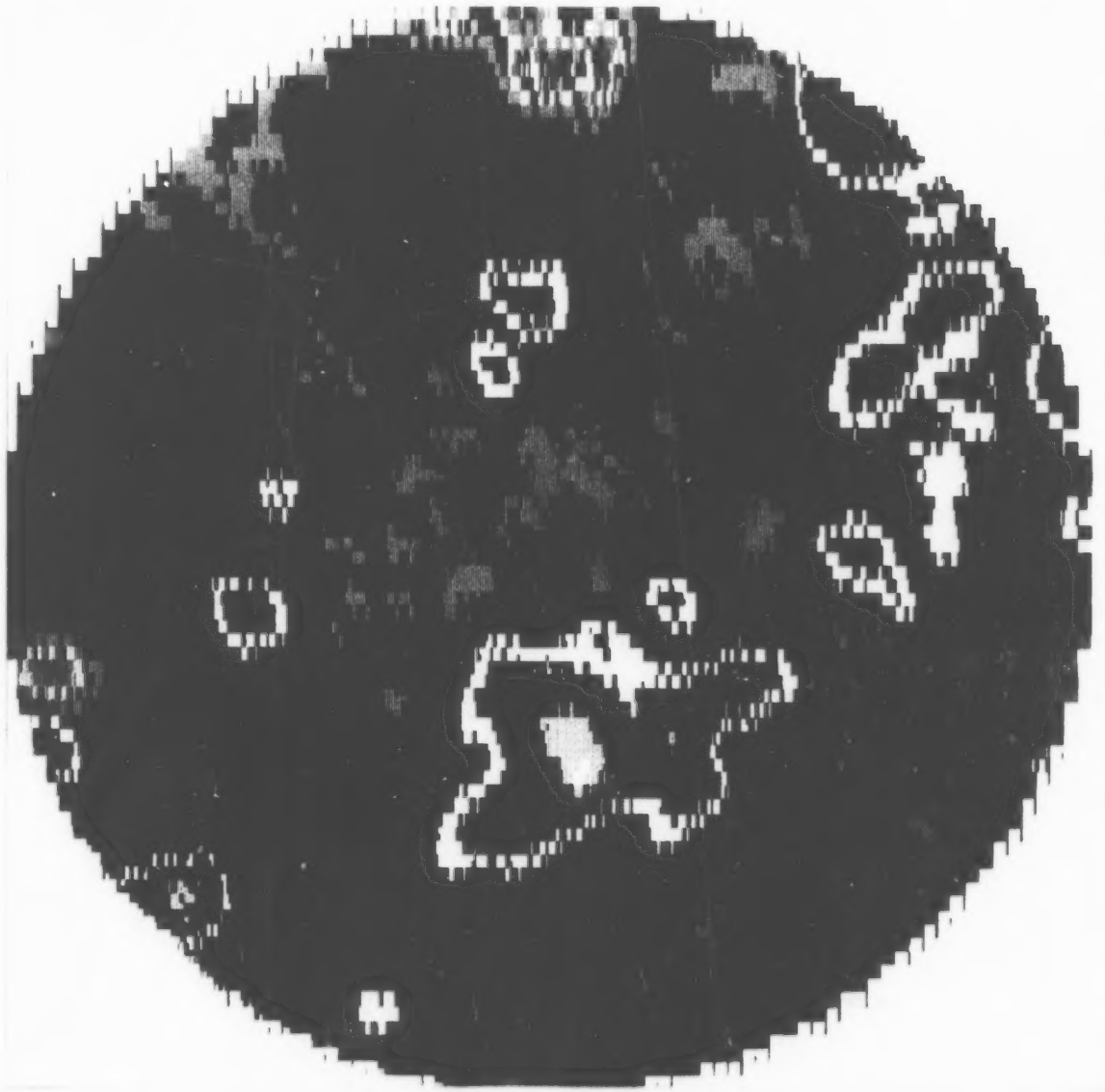

Figure 9.12 Bulk density map of the slice of core piece #52 at 95mm from the undamaged face. Color code same as in Figure 9.1

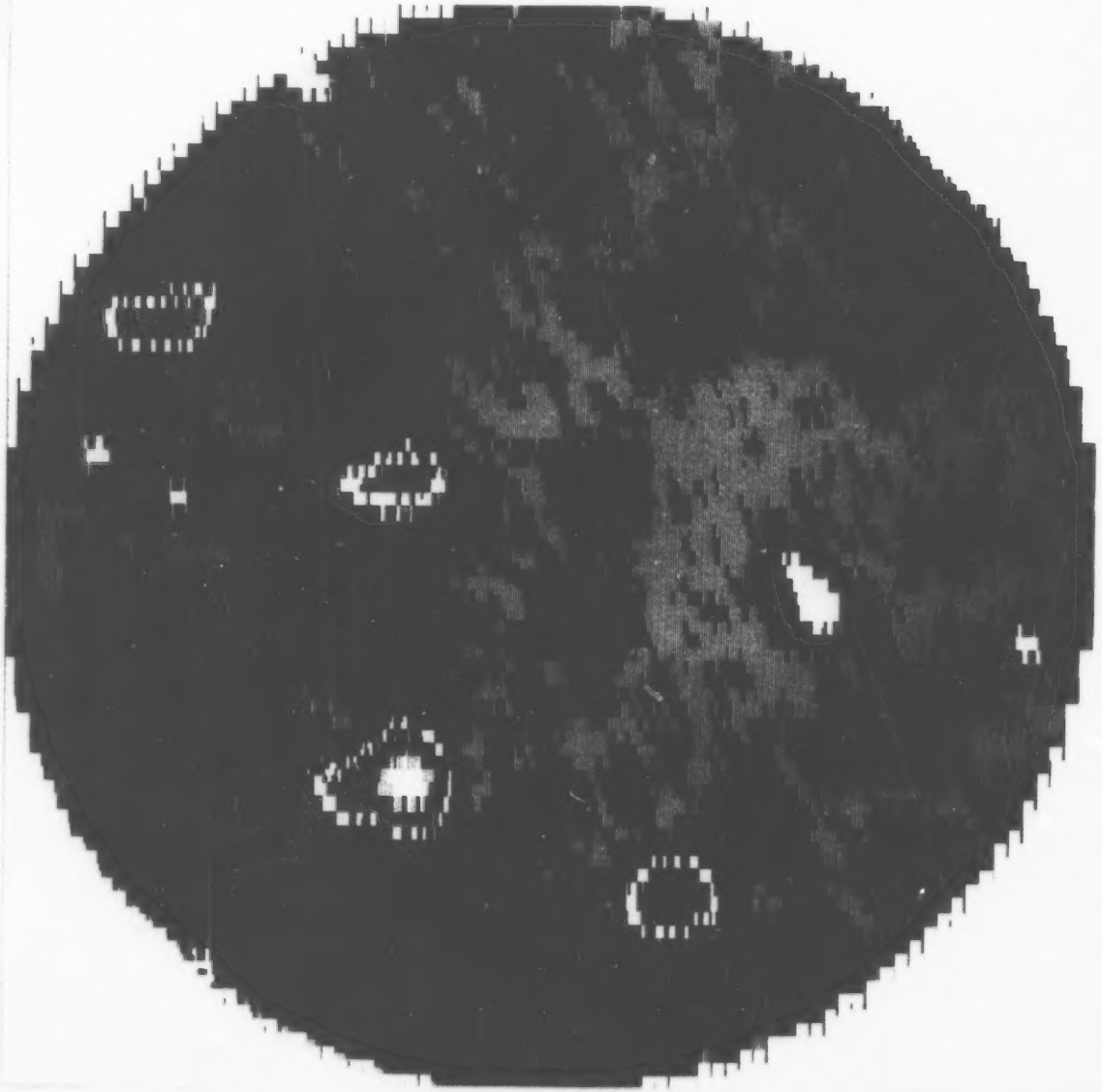

Figure 9.13 Bulk density map of the slice of core piece #52 at 115mm from the undamaged face. Color code same as in Figure 9.1

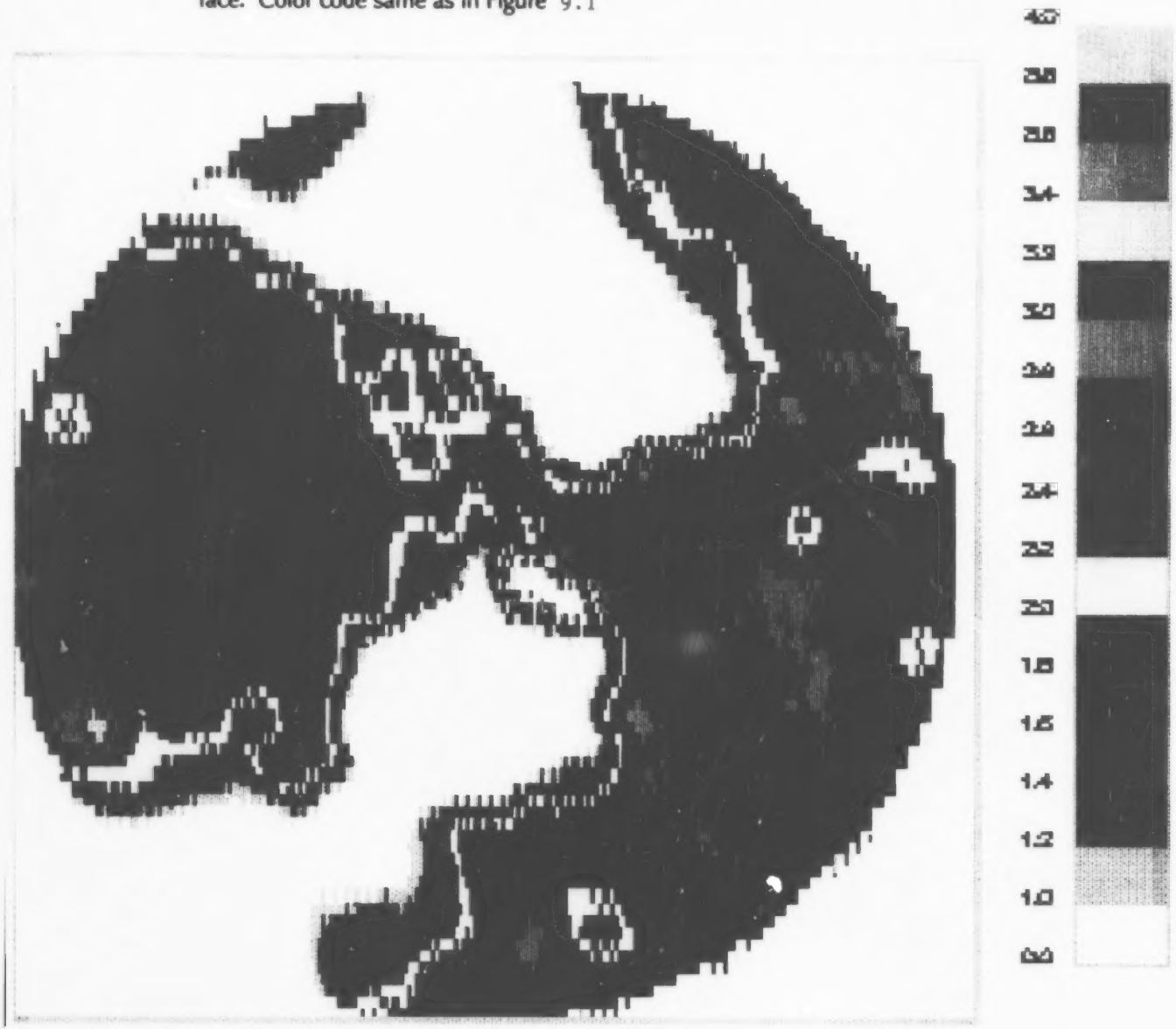

Figure 10.1 CAT scanner and core analysis prediction comparisons of bulk density (units in g/cm^3).

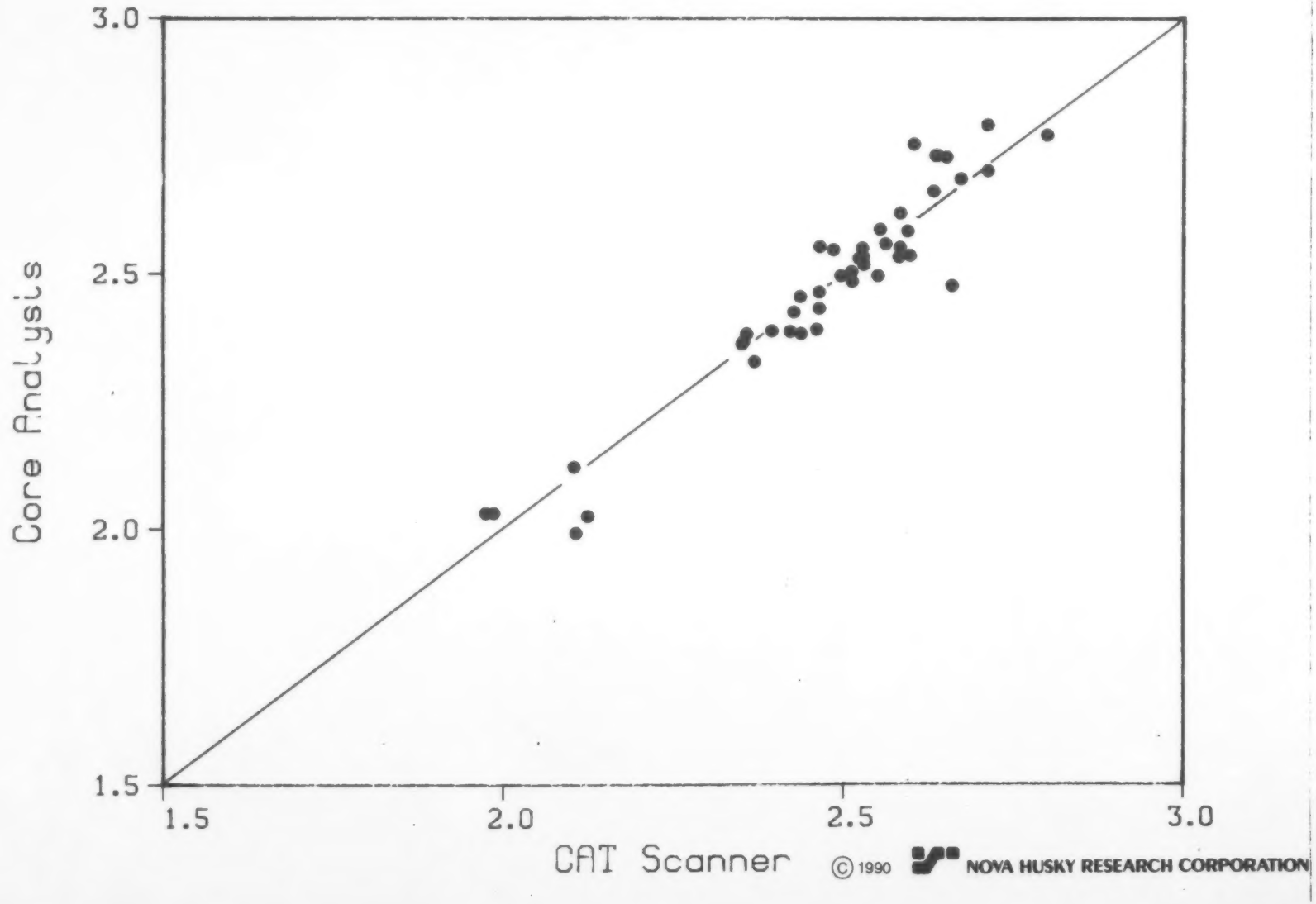
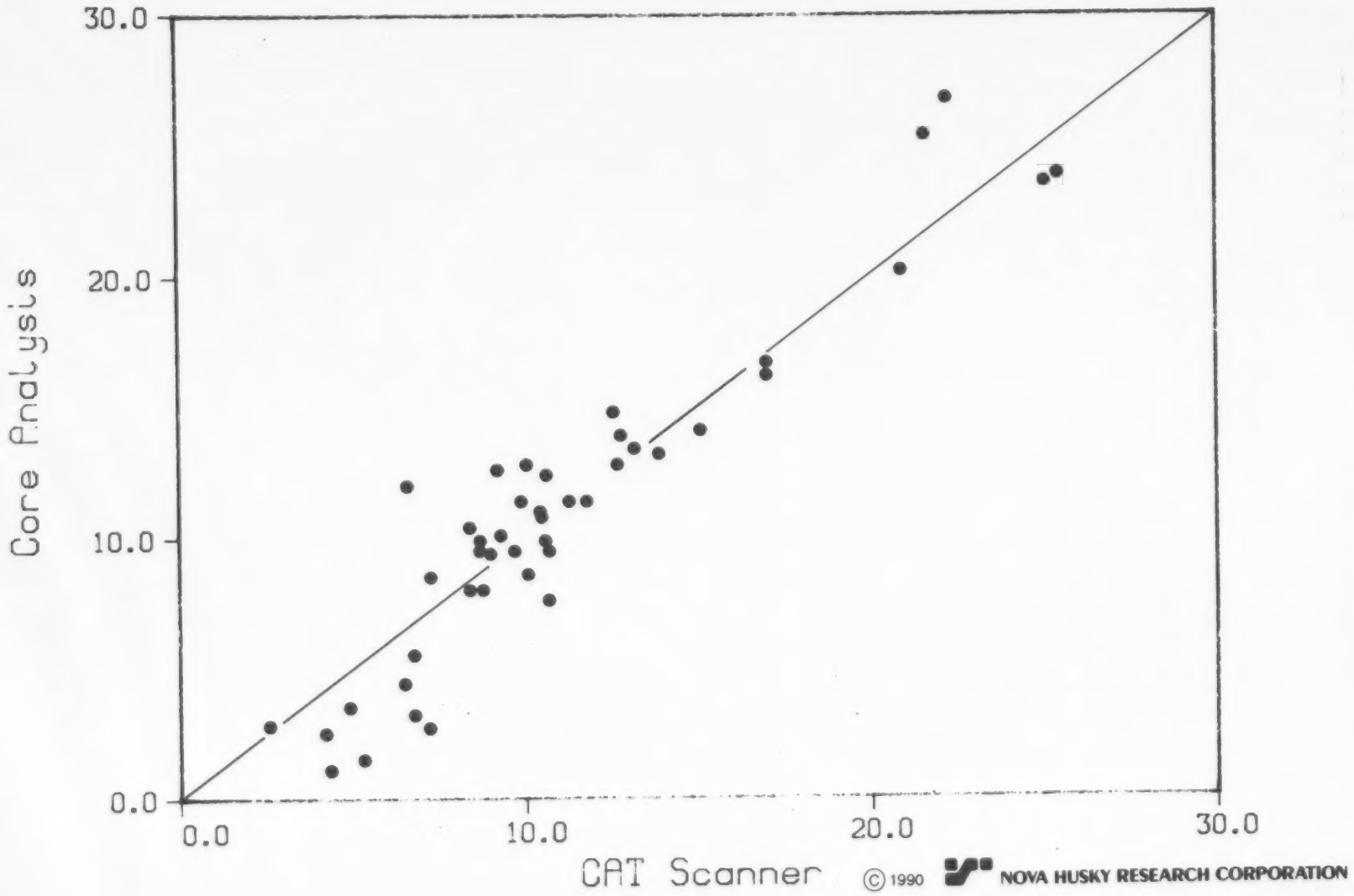
Figure 10.2 CAT scanner and core analysis prediction comparison of porosity (units in % pore volume).